VNIVERSITAT DE VALÈNCIA

Departamento de física atómica, molecular y nuclear

DOCTORADO EN FÍSICA

Dosimetric studies through Monte Carlo methods in surface high-dose-rate electronic brachytherapy

PhD thesis dissertation by:

Christian Valdés Cortez

Under the supervision of:

Facundo Ballester Pallarés

Javier Vijande Asenjo

Valencia, September 2020

Declaración

Facundo Ballester Pallarés.
Catedrático en el Dpto. de Física Atómica, Molecular y Nuclear.
Javier Vijande Asenjo.
Catedrático en el Dpto. de Física Atómica, Molecular y Nuclear.

Certifican:

Que la presente memoria titulada "Dosimetric studies through Monte Carlo methods in surface high-dose-rate electronic brachitherapy" ha sido realizada bajo su dirección en la Universidad de Valencia por Christian Valdés Cortez, constituyendo su Tesis Doctoral para optar al grado de Doctor en Física en el Departamento de Física Atómica, Molecular y Nuclear de la Universidad de Valencia. Y para que así conste, en cumplimiento de la legislación vigente, firman el presente certificado.

Facundo Ballester Pallarés Javier Vijande Asenjo

Agradecimientos / Acknowledgments

A mis profesores Facundo y Javier, por su magnífica guía, apoyo y confianza; nunca dudaron en compartir sus conocimientos y recursos en mi beneficio, y de incluirme en sus actividades científicas como uno más. A José, cuyas ideas y experiencia tanto aportaron a esta tesis; una persona muy ocupada, pero que siempre se dio el espacio para colaborar en este proyecto. A mi esposa Viviana, por hacer posible este maravilloso viaje; por su apoyo, cariño y por ser mi sostén en tierras lejanas. A mi madre, luchadora incansable cuyos esfuerzos me permitieron llegar hasta aquí. Mi querida hermana, ¿qué sería de mí sin su ternura e incondicionalidad? A mi querida Meche, tía preciosa, siempre presente. Y por último mis agradecimientos van para Raúl, por su ayuda en momentos claves de mi vida.

To my supervisors Facundo and Javier for their excellent guidance, support, and confidence; they never hesitated to share their

knowledge and resources in my favor, and to include me in their scientific activities. To José, whose outstanding ideas and experience make an enormous contribution to this thesis; a very busy person, but always available to help in this project. To my wife Viviana, for making this incredible journey possible; for her support, love, and for being my foundation in such distant lands. To my mother, a tireless fighter whose efforts allowed me to get here. My dear sister, what would become of me without your tenderness and unconditionality? To my dear Meche, my beautiful aunt, always present. And finally, my thanks go to Raul, for his help at crucial moments of my life.

Contents

List of Tables

List of Figures

List of abbreviations and acronyms

AAPM American Association of Physicists in Medicine. 36, 62, 66, 68, 74, 88, 94, 97, 101, 102, 106, 107, 128, 148

APP$_{\mathbf{10mm}}$ Applicator of 10 mm diameter. ix, x, xiii, 28, 31, 34, 38, 41, 42, 44, 45, 46, 47, 48, 51, 69, 74, 76, 79, 82, 83, 91, 108, 112, 113, 114, 118, 122, 124, 128, 132, 139, 143, 144, 145, 150, 154, 179, 180

APP$_{\mathbf{30mm}}$ Applicator of 10 mm diameter. ix, xiii, 28, 31, 34, 38, 39, 40, 41, 42, 44, 45, 46, 47, 48, 50, 55, 58, 74, 76, 78, 79, 82, 83, 118, 122, 124, 132, 139, 143, 144, 145, 154

BQI Beam Quality Index. 6, 88, 89, 127, 128, 130, 131, 148, 149, 151, 152, 155

BT Brachytherapy. 2, 3, 7, 8, 118, 126

CPE Charge Particle Equilibrium. 67, 68, 79

DD Absorbed Depth-Dose. 34, 35, 45, 50, 51, 52

DHFS Dirac-Hartree-Fock-Slater. 16, 17

DP Off-axis Dose Profile. 31, 35, 36, 47, 48, 49, 50, 51, 52, 56, 57, 58, 121, 141

EBRT External Beam Radiation Therapy. 2, 6, 88, 126, 127, 147, 148

eBT Electronic Brachytherapy. 3, 4, 5, 6, 7, 8, 9, 10, 16, 23, 24, 27, 28, 57, 59, 65, 66, 67, 69, 73, 84, 85, 88, 89, 90, 113, 114, 115, 116, 117, 118, 119, 120, 121, 122, 125, 126, 127, 128, 130, 131, 132, 133, 134, 135, 136, 137, 138, 139, 140, 141, 142, 147, 149, 151, 152, 153, 154, 155, 179, 180

EFEN Efficiency-Enhancing Technique. 18, 19, 28, 29, 41, 54, 58, 119, 139

EPoM Effective Point of Measurement. 61, 62, 64, 70, 72, 77, 78, 79, 80, 81, 85, 122, 124, 125, 126, 142, 144, 146

$\mathbf{EPoM_{man}}$ Effective Point of Measurement recommended by the manufacturer. 64, 65, 68, 70, 71, 72, 74, 77, 78, 79, 81, 83, 123, 125, 126, 144, 146

FF Flattening Filter. 90, 91, 93, 98, 104, 105, 116, 120, 121, 125, 128, 129, 130, 131, 132, 136, 140, 141, 146, 149, 150, 151, 152, 154

FFF Flattening Filter-Free. 91, 93, 102

FWHM Full Width at Half Maximum. 37, 91, 95

GES Gaussian Energy Source. 29, 34, 35, 37, 41, 42, 44, 54

GIS Gaussian Intensity Source. 29, 37, 42, 48, 56, 69, 91, 95, 120, 122, 123, 129, 140, 143, 150, 180

HDR High-Dose-Rate. 2, 3, 4, 23, 126

HVL Half-Value Layer. xii, xiii, xiv, 6, 31, 33, 34, 43, 44, 50, 52, 54, 55, 56, 89, 91, 92, 93, 94, 97, 99, 100, 101, 102, 103, 104, 105, 106, 107, 108, 109, 111, 112, 113, 120, 123, 127, 128, 129, 130, 131, 132, 134, 140, 144, 148, 149, 150, 151, 153, 154, 155

IAEA International Atomic Energy Agency. 64, 66, 88, 92, 127, 128

ICRU International Commission on Radiation Units and Measurements. 8, 66

IG Ideal Geometry. 90, 91, 93, 96, 97, 98, 99, 101, 103, 105, 106, 107

IS Ideal Source. 29, 32, 34, 35, 37, 41, 42, 44, 46, 48, 55, 56

MC Monte Carlo. xii, 7, 8, 9, 11, 12, 16, 27, 29, 36, 39, 62, 65, 67, 75, 81, 84, 91, 94, 116, 117, 118, 119, 133, 136, 137, 138, 139, 154

MCDF Multi-configuration Dirac-Fock. 16, 17

NG Negative Geometry. 90, 94

PDD Percentage absorbed Depth-Dose. ix, xiii, 31, 35, 45, 46, 47, 50, 51, 52, 55, 56, 57, 74, 83, 85, 121, 127, 128, 129, 141, 148, 149, 150

PEN14 PENELOPE-2014. ix, 11, 12, 16, 17, 24, 25, 28, 34, 37, 93, 95, 118, 128, 138, 139, 150, 177, 181, 182

PEN18 PENELOPE-2018. ix, 11, 12, 14, 16, 17, 24, 25, 64, 69, 70, 118, 122, 138, 143, 177, 181, 182

PENELOPE PENetration and Energy LOss of Positrons and Electrons. ix, 4, 12, 13, 14, 15, 16, 17, 18, 20, 21, 52, 67, 68, 69, 95, 117, 118, 129, 133, 137, 138, 151, 154, 177, 179

PG Positive Geometry. 90

PRSC Pratt's Renormalization Screening Correction. 16, 17, 75, 124

PSF Phase-Spase File. ix, 28, 30, 31, 33, 34, 37, 38, 39, 40, 41, 119, 120, 139, 140

RT Radiation Therapy. 1, 2, 7

SpS Spread Source. 29, 37, 42

SSD Source to Sourface Distance. 23, 98, 118, 131, 138, 152

SSo Simplified Source. 180

TG Task Group. 7, 36, 62, 66, 68, 74, 85, 88, 91, 94, 97, 98, 100, 102, 103, 106, 107, 109, 110, 113, 126, 127, 129, 130, 131, 132, 133, 146, 147, 150, 151, 152, 153, 154

TPS Treatment Planning System. 5

TRS Technical Report Series. 64, 66, 74, 88, 126, 127

VRIF Variance Reduction Interaction Forcing. 19, 20, 30, 38, 39, 41, 52, 53, 67, 95, 119, 139

VRPS Variance Reduction Particle Splitting. 19, 34, 42, 67, 95

VRT Variance Reduction Technique. 19, 20, 22, 37, 52, 53, 54, 58, 67, 69, 95

Glossary

$\overline{E}$: Average photon energy in PENELOPE. 31, 32, 34, 41, 42, 43, 44, 51, 52, 56

ϵ : efficiency of the simulation (dependent of time). 19, 39

τ : intrinsic efficiency of the simulation (dependent of the number of primary particles N). 19, 38, 39

Ψ : Energy fluence . 33, 177, 178, 179

μ_{Al} : Linear attenuation coefficients for aluminum . 93

μ_{FF} : Linear attenuation coefficients for the flattening filter . 93

μ_{air} : Linear attenuation coefficients for air . 93

λ_{el} : mean free path of electron elastic interactions. 13, 14, 15

$\lambda_{el,1}$: first transport mean free path of electron elastic interactions. 13, 14, 15

$\lambda_{el}^{(h)}$: mean free path of electron elastic hard interactions. 13, 14, 15

$(\overline{\mu_{en}/\rho})_{w,air}$: Mean mass energy-absorption coefficients for water to air . xiv, 66, 68, 69, 70, 74, 75, 76, 81, 82, 91, 92, 96, 99, 100, 102, 103, 105, 106, 107, 108, 109, 110, 111, 113, 122, 123, 125, 126, 127, 129, 133, 143, 144, 145, 147, 150, 151, 154, 177, 178, 179, 181

$(\Psi_{FFF})^{free-space}$: Energy fluence obtained with a flattening filter-free geometry in vacuum . 93, 94, 95

$(\mu_{en}/\rho)_{air}$: Mass energy-absorption coefficients for air . 34, 93, 179

$(\mu_{en}/\rho)_{w}$: Mass energy-absorption coefficients for water . 96, 98, 179

$(\mu_{tr}/\rho)_{w}$: Mass energy-transfer coefficients for water . 98

$(\Psi_{x_{FF\,\max}})^{free-air}$: Energy fluence obtained with the maximum flattening filter thickness of the positive geometry in free-air . 96, 97, 102

$(\Psi_{x_{FF\_IG}})^{free-air}$: Energy fluence obtained with the flattening filter thickness of the ideal geometry in free-air . 96, 102

$(\Psi_{x_{FFmin}})^{free-air}$: Energy fluence obtained with the minimum flattening filter thickness geometry in free-air . 95, 96, 97, 102

$(l)_w^{air}$: Distance traveled by photons in a small volume of water placed in-air . 97

$(l)_w^w$: Distance traveled by photons in a small volume of water placed at the surface of a water phantom . 97

B_w : Backscatter factor of the TG-61 calibration protocol . xiv, 91, 92, 98, 99, 100, 102, 103, 105, 106, 107, 108, 109, 110, 111, 113, 126, 127, 129, 133, 147, 150, 151, 154

$C1$: average angular deflection for multiple elastic scattering between two consecutive hard elastic events. 12, 13, 14, 15, 22, 30, 37, 38, 39, 41, 53, 67, 95

$C2$: maximum average fractional energy loss between two consecutive hard elastic events. 12, 13, 14, 15, 22, 30, 37, 38, 39, 41, 53, 67, 95

DSMAX : cutting energy loss for bremsstrahlung emissions. 13, 15, 30

D_{cav} : Depth-dose in the sensitive volume of the ionization chamber . 66, 68, 71, 74, 78, 82, 122, 123, 133, 143, 144, 154

D_w : Depth-dose in water . 66, 68, 69, 71, 74, 77, 78, 80, 82, 122, 123, 133, 143, 144, 154

$D_{z,3}$: Ratio of dose obtained at z to 3 mm depth . 99, 100, 108, 109, 110, 129, 130, 131, 150, 151, 153

WGMIN : Minumum particle weight in which a variance reduction technique will be applied in PENELOPE. 41

W_{cc} : cutting energy loss for hard inelastic collision. 13, 22, 30, 41

W_{cr} : cutting energy loss for bremsstrahlung emissions. 13, 22, 30, 41

k_{Q,Q_0} : Beam quality correction factor if the IAEA calibration protocol . 92, 100, 109, 112, 126, 132, 147, 154

p_{glob} : Perturbation correction factor, considering all depths maintaining the effective point of measurement recommended by the ionization chamber's manufacturer.. 123, 124, 125, 144, 146

p_{shift} : Perturbation correction factor, considering all depths using an optimized effective point of measurement in the sensitive volume of the ionization chamber.. 123, 124, 125, 144, 146

p_{surf} : Perturbation correction factor at the phantom surface, maintaining the effective point of measurement recommended by the ionization chamber's manufacturer. . 123, 124, 143, 144

x_{Al} : Aluminum thickness in mm . 92

x_{FF} : Flattening filter thickness . 91, 93, 94, 98, 102, 103, 104, 105, 111

x_{FF_IG} : Flattening filter thickness of the ideal geometry . 96, 111

$x_{FFextra}$: Thickness of the additional material added to x_{FFmin} . 96, 97

x_{FFmax} : Maximum flattening filter thickness . 91, 93, 96, 97

x_{FFmin} : Minimum flattening filter thickness . 91, 93, 94, 96, 97

Chapter 1

Introduction

1.1 Surface high-dose-rate electronic brachytherapy

Radiation therapy (RT) has a long history in the treatment of cancer. Currently, depending on the region of the world they live in, up to 65% of all cancer patients could benefit from radiotherapy as part of their treatment management (Aird *et al.*, 2016). RT consists of the irradiation of malignant cells to deactivate their replication capacities (Joiner and van der Kogel, 2009). Despite the technological advances over the years, it is impossible to irradiate cancer cells without damaging healthy tissues, existing a delicate balance between benefits and complications (therapeutic ratio) (Joiner and van der Kogel, 2009). Several organizations rec-

ommend maintaining as low as possible the uncertainties in the dose determination (Almond *et al.*, 1999; Andreo *et al.*, 2000), an important point to associate dose distributions with cure and complication rates (Aird *et al.*, 2016).

RT is classified into two branches depending on the position of the radiation source regarding the treatment site: external beam radiation therapy (EBRT) and brachytherapy (BT). EBRT usually uses a linear particle accelerator to generate x-rays or electrons at a considerable distance from the tumor (often at 100 cm). On the other hand, the BT sources, traditionally composed of a radioisotope contained in a sealed seed, are placed very close (less than a few centimeters) to the disease (Podgorsak, 2005).

The use of BT has been increasingly growing in this century, with expectations that this trend continues in the future (Guedea, 2014). It is the treatment of choice for some gynecological malignancies (Gerbaulet *et al.*, 2002) and plays an important role in a variety of other sites like prostate, breast (Beaulieu *et al.*, 2012), and skin (Ouhib *et al.*, 2015; Guinot *et al.*, 2018). Depending on the absorbed dose-rate in the prescription structure, BT is classified into low-dose-rate (0.4 Gy/h - 2 Gy/h), medium-dose-rate (2 Gy/h - 12 Gy/h), and high-dose-rate (HDR, more than 12 Gy/h) (Chassagne *et al.*, 1985). According to the source location, BT is classified in intracavitary (inside natural cavities in the body), interstitial (in organ interstice), and superficial (skin surface) (Gerbaulet *et al.*, 2002).

HDR BT consists of a millimetric source of high activity (in

the order of hundreds of GBq), attached to the tip of a wire remotely controlled by an afterloader machine (see figure 1.1). The afterloader has two main functions: store the source in a shielded container (safe position) when it is not being used; and control the extension of the wire, positioning the source at a specific distance from its safe position. Nowadays, two HDR radioisotopes are widely used as HDR source, the ^{192}Ir (half-life = 73.83 d), and the ^{60}Co (half-life = 1925.28 d) (NUDAT 2.8, 2020), whose average energies are 350 and 1252.9 keV, respectively (Perez-Calatayud *et al.*, 2012). Due to the high activities (shorter treatment times) and smaller sizes of its sources, HDR BT has become the preferred technique (Guedea, 2014), replacing the low-dose-rate sources in intracavitary and interstitial applications (Perez-Calatayud *et al.*, 2012).

However, the important amount of radiation delivered combined with photon energies above 350 keV, generate the necessity to handle the HDR sources in highly shielded facilities (Kubo *et al.*, 1998). Furthermore, radioisotopes must be changed periodically due to the radioactive decay, which imposes logistics and safety challenges (IAEA, 2003). To solve those problems, in the past decade, a new type of HDR BT machine has been developed, replacing the radioactive material by a small low-energy (< 100 kV) x-ray source (Eaton, 2015; Nath *et al.*, 2016). This technique, called electronic BT (eBT), is already used in gynecological, breast, and surface skin treatments of non-melanoma malignancies (Tom *et al.*, 2018).

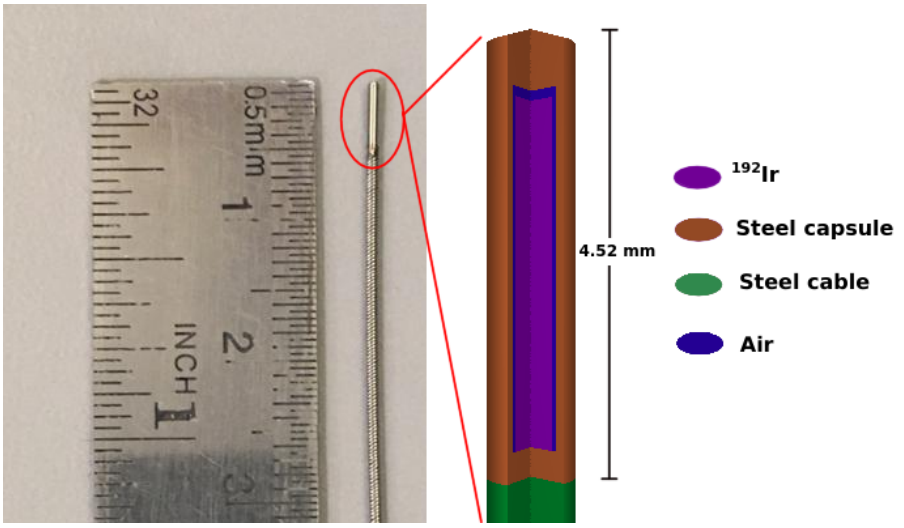

Figure 1.1: Example of an ^{192}Ir HDR brachytherapy source, corresponding to the Varian GammaMed Plus model. Left: image of a *dummy* source, kindly provided by Harold Novoa from Centro Oncológico del Norte. Right: same HDR source modeled in PENELOPE.

Non-melanoma skin cancers (or keratinocyte carcinomas) are one of the most common human malignancies (Madan *et al.*, 2010; Nehal and Bichakjian, 2018), presenting a continuous increase in their incidence around the world (Perera *et al.*, 2015; Rogers *et al.*, 2015; Rubió-Casadevall *et al.*, 2016; Leiter *et al.*, 2017). While it is true that surgical ablation is the first therapeutic option (Nehal and Bichakjian, 2018), surface HDR eBT has become an effective treatment, achieving excellent control rates and good cosmetic results (Bhatnagar, 2013; Ouhib *et al.*, 2015; Ballester-Sánchez *et al.*, 2017; Guinot *et al.*, 2018).

Surface eBT systems consist basically of two components: an x-ray tube and an applicator attached. The x-ray tube accelerates electrons in the energy range between 50 and 70 keV, producing flattened x-ray beams. The eBT applicator serves as a collimator positioned directly in contact with the skin, producing conical beams of 10 to 50 mm diameter. The flattening filter may or may not be included in the applicator, depending on the eBT system design (Candela-Juan *et al.*, 2015b).

1.2 General drawbacks of eBT

Despite its benefits, eBT is far from being a drawbacks-free technique. Low-energy x-rays present several dosimetric challenges across the entire treatment process. The high dose gradient with depth increases the dose averaging over the sensitive volume of the detectors, affecting the accuracy of absorbed dose measurements. The photoelectric cross-sections, interaction predominant at these energies, have a strong dependency on the atomic number. Furthermore, the characteristics of the beam can suffer noticeable changes with depth, affecting the detector response. Those characteristics have a twofold effect: make the detector performance highly sensitive to its materials composition, design, and depth (Hill *et al.*, 2014; Watson *et al.*, 2017); and increase the need for developing sophisticated treatment planning systems (TPS) able to consider the differences in the composition of the human tissues (Beaulieu *et al.*, 2012).

Beam calibrations and depth-dose measurements represent an essential part of an eBT quality control program (Thomadsen *et al.*, 2009; Candela-Juan *et al.*, 2015a; Eaton, 2015; Thomadsen *et al.*, 2019). However, there exists a lack of absorbed dose-to-water standards for low- and medium-energy x-rays. In many cases, it is still necessary to use conversion factors (e.g., mass energy-absorption coefficients and backscatter factors) to obtain the dose in water from air kerma (Andreo, 2019). Those factors would explain, at least in part, the higher uncertainty estimated for eBT (less than 4%) compared to EBRT beam calibrations (less than 2%) (Castro *et al.*, 2008; Candela-Juan *et al.*, 2015b; Aird *et al.*, 2016).

The most widely used calibration protocols for low-energy x-rays beams use the half-value layer (HVL) as a beam quality index (BQI) (Andreo *et al.*, 2000; Ma *et al.*, 2001). This measurement is carried out through a cumbersome procedure that requires elements not always available in the hospital environment. Furthermore, the HVL has no other practical use in the clinical practice, a clear disadvantage compared with EBRT, which obtains its BQI from depth-dose measurements (Andreo *et al.*, 2000; Almond *et al.*, 1999), a quantity intensively used in the clinical process (Podgorsak, 2005).

1.3 Monte Carlo methods in BT

The drawbacks discussed in the previous section, and the complexity of the physics underlying the eBT systems, difficult their study through experimental or analytical approaches. In this context, the random nature of the radiation interactions makes Monte Carlo (MC) a useful tool. Historically, the use of MC in radiation therapy has been used mainly for research. The time required to complete the simulation of a real treatment (with acceptable uncertainties) left MC out of the clinical practice. However, technological advances, together with improvements in the MC codes, have made it possible to incorporate the MC tools into the treatment processes in RT (Beaulieu *et al.*, 2012; Famulari *et al.*, 2018; Ma *et al.*, 2019; Vidal *et al.*, 2019).

A significant part of the knowledge we have about dose distribution around BT radioisotope sources, either in water or in a heterogeneous medium, comes from MC studies (Beaulieu *et al.*, 2012; Perez-Calatayud *et al.*, 2012). The TG-43 formalism (Nath *et al.*, 1995), which dominates the water dosimetry at the clinical context, is feed with parameters obtained almost exclusively from MC studies (Perez-Calatayud *et al.*, 2012). The model-based dose calculation algorithms (MBDCAs), whose recently introduction allows dose calculation in an inhomogeneous medium, are based in MC methods or are benchmarked against MC simulations (Beaulieu *et al.*, 2012).

Some of the most used and benchmarked MC codes in BT are EGSnrc, GEANT4, MCNP, and PENELOPE (Perez-Calatayud *et al.*, 2012). There exists a good agreement between them (typically better than 0.5%) when comparing results for radioisotope sources with photon energies higher than 200 keV (Vijande *et al.*, 2013; 2012; Ballester *et al.*, 2015). MC also has been extensively applied to eBT studies (Rivard *et al.*, 2006; Clausen *et al.*, 2012; Croce *et al.*, 2012; Fulkerson *et al.*, 2014; Hiatt *et al.*, 2015; Watson *et al.*, 2017) but, at the best of our knowledge, without MC codes intercomparisons (beyond comparing specific factors). However, there is evidence suggesting that the good agreement achieved for higher photon energies may worsen due to uncertainties in the photoelectric cross-sections of photons with energies lower than 100 keV (Andreo *et al.*, 2012; Seltzer *et al.*, 2014).

The International Commission on Radiation Units and Measurements (ICRU) has estimated the uncertainty of the photoelectric cross-sections between 2% and 3% for photons with energies between 1 keV and 100 keV. For incoherent scattering, the uncertainty estimated is within 0.5% for energies over 50 keV, increasing to 2% for photons of 10 keV (Seltzer *et al.*, 2014). Although the current cross-sections uncertainties are well established, more studies are needed to evaluate their effects on the different quantities used in radiation dosimetry obtained from MC simulations.

1.4 Objectives and outline of this thesis

This thesis aims to study some of the drawbacks, mentioned in the previous sections, of the surface eBT treatments. The focus will be on the uncertainties arising in the dosimetry of 70 kV beams, range of energy with a lack of published information. The study will be carried out mainly through MC methods, assessing three main aspects: characterizing the eBT unit of interest, evaluating the response dependence of the detector recommended to in-water dosimetry, and proposing alternative procedures to facilitate and reduce uncertainties in beam calibrations.

This memory has been performed as an article compendium. According to the University of Valencia, this format shall include three or more scientific publications, provided that the articles were published (or accepted) in international indexed journals. Chapters 1 to 3 give the context and deliver the information necessary to understand the problems studied in chapters 4 to 6, where the scientific publications were presented. Those chapters were modified regarding the original articles, which are included in Appendix C, to adapt them to this memory. Finally, Chapter 7 summarizes the findings, highlighting their relevance and consistency to the goals proposed to this work.

Regarding the published original contributions, in Chapter 4 is presented a complete dosimetric study of the eBT device performed through MC simulations. The methodologies and findings obtained

were the base ground for the following two chapters. Chapter 5 studies the correction factors needed by the only (at the time of writing this thesis) parallel-plate ionization chamber recommended for in-water dosimetry of eBT beams. A complete analysis of the uncertainties associated with the system composed of the eBT unit and the detector device is performed. Chapter 6 illustrates some of the challenges found during eBT beam calibrations, proposing solutions and improvements through a deep analysis of their uncertainties.

Chapter 2

Monte Carlo system

2.1 Introduction

This thesis presents a series of data obtained from MC simulations performed with the PENELOPE system (Salvat *et al.*, 2015; Salvat, 2019). When this work was started, the version available was PENELOPE-2014 (PEN14) (Salvat *et al.*, 2015). However, in 2019, the developers released a new version: PENELOPE-2018 (PEN18) (Salvat, 2019). PEN18 includes a series of new features beneficial for this research, with a negligible impact on the simulations results (see below). For that reason, this research group decided to switch to PEN18 in the last part of this work. This chapter discusses the main characteristics of PENELOPE shared by both versions. A comparison to ensure the constancy between

PEN14 and PEN18 simulations is presented in Appendix A.

2.2 PENELOPE code system

PENELOPE is an open-source code system for MC simulations developed at the Universitat de Barcelona. The PENELOPE official package is distributed (under demand) by the OECD Nuclear Energy Agency.[1] It contains a complete set of Fortran modules that allow simulating the transport of electron and photons, from 50 eV to 1 GeV, through complex geometries.

2.2.1 Electron transport

Six user-defined parameters (henceforth called transport parameters) determine the electrons transport:

- *EABS*: energy threshold to stop the particle tracking (electrons, photons, and positrons), asumming a local energy depositio.
- $C1$: average angular deflection for multiple elastic scattering between two consecutive hard elastic events.
- $C2$: maximum average fractional energy loss between two consecutive hard elastic events.

[1] `https://www.oecd-nea.org/tools/abstract/list`

- W_{cc}: cutting energy loss for hard inelastic collisions.
- W_{cr}: cutting energy loss for bremsstrahlung emissions.
- *DSMAX*: it is the maximum jump allowed for electrons, before recording the energy losses due to soft interactions and the resampling of the next event.

When $C1 = C2 = W_{cc} = W_{cr} = 0$, PENELOPE performs a detailed (Class I) simulation of the electrons transport; otherwise, it changes to a mixed (Class II) simulation. In the Class I simulation, all events are treated individually, regardless of whether they are soft or hard. The Class II algorithm only simulates hard events with energies greater than W_{cc} and W_{cr}, treating all the remainder interactions as soft events in a multiple-scattering approximation. This approach allows condensing all the soft interactions, between two continuous hard collisions, in a single (hinge) event (Salvat, 2019).

In practice, the specification of the mean free path of elastic hard interactions, $\lambda_{el}^{(h)}$, will define the Class II algorithm, where

$$\lambda_{el}^{(h)}(E) = max\left\{\lambda_{el}(E), min\left[C1\lambda_{el,1}(E), C2\frac{E}{S(E)}\right]\right\}. \quad (2.1)$$

Here, $\lambda_{el}(E)$ is the mean free path for elastic interactions, $\lambda_{el,1}(E)$ is the first transport mean free path, and $S(E)$ is the electron stopping power, all dependent on the electron energy E. Roughly

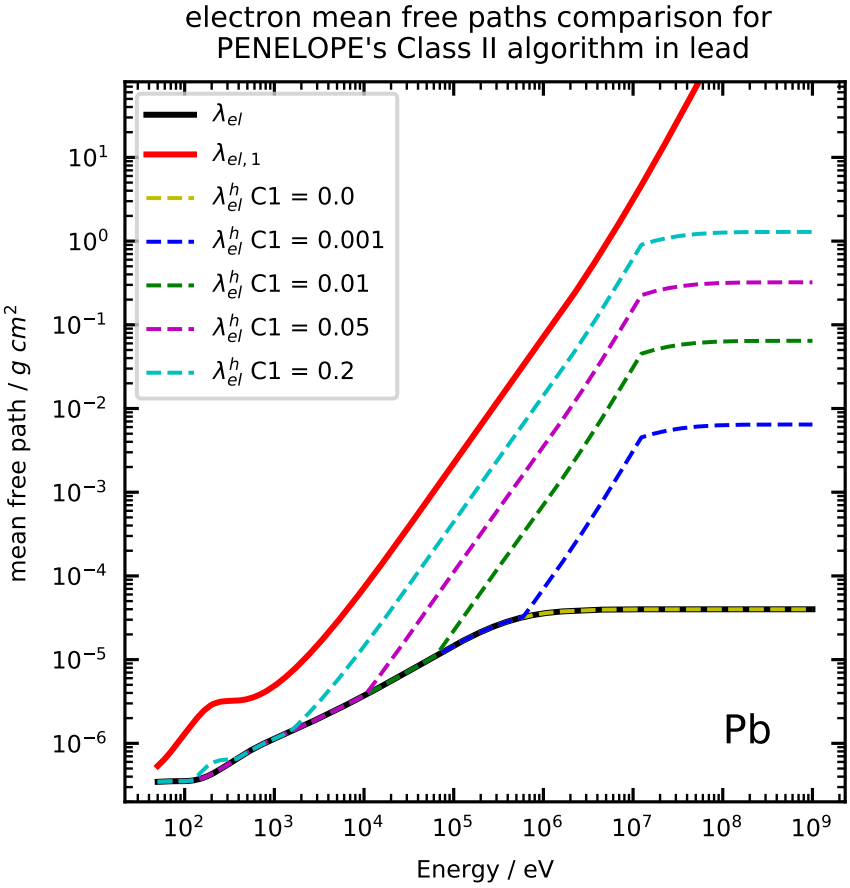

Figure 2.1: Electron mean free paths relevant in PENELOPE's class II algorithm calculated with PEN18. Solids lines correspond to the elastic (black), λ_{el}, and the first transport (red), $\lambda_{el,1}$, mean free paths. Dashed lines correspond to the mean free paths for hard elastic events, $\lambda_{el}^{(h)}$, calculated with Equation 2.1, using different $C1 = C2$ transport parameters. A perfect overlay it can be seen between λ_{el} and $\lambda_{el}^{(h)}$ with $C1 = 0$ (dashed yellow), which denotes a detailed (Class I) simulation.

speaking, for medium- and high-energies (where the electron mean angular deflection becomes small), $C1$ and $C2$ determine the simulation time modifying $\lambda_{el}^{(h)}$. An increment of $\lambda_{el}^{(h)}$ increases the number of events included in the hinge event, saving computation time. For lower energies, $\lambda_{el}^{(h)}$ tends to λ_{el}, in which case the simulation becomes detailed (Class I, see Figure 2.1).

Equation 2.1 clearly illustrates the domain operation of $C1$ and $C2$. While $C1$ acts as a weight factor for $\lambda_{el,1}$, which is related to the average angular deflection, $C2$ does it for the energy spent in the electron step. According to the PENELOPE user manual, those parameters should not have any influence in the simulation accuracy, while their values (allowed range between 0 and 0.2) are kept small enough. However, the user should be aware that small non-zero values can affect the electron angular deflection, which, depending on the simulation setup, can introduce a noticeable bias in the results, see Section 4.4.1 and Rodriguez *et al.* (2015). Class II algorithm adopts artificial probability distributions to sample the hinge events. Such distributions need a relatively large number of events (more than ten) to dismiss any effect over the simulation outcome. For thick bodies, this condition is automatically satisfied. However, for thin bodies, the user needs to adjust *DSMAX* to a tenth of the body thickness to ensure an appropriate number of hinge events (Salvat, 2019).

2.2.2 Photon transport

The dominant interactions in eBT beams are photoelectric absorption and Rayleigh and Compton scatterings. Effects that, unlike the electrons transport, PENELOPE always simulates considering all the events separately. For this reason, when the transport of charged particles is not required, the user only needs to define *EABS*, setting all other transport parameters equal to 0.

PEN14 and PEN18 obtain the photoelectric libraries from PHOTACS (Sabbatucci and Salvat, 2016), a Fortran program that calculates subshell cross-sections for arbitrary atomic potentials (Salvat *et al.*, 2015; Salvat, 2019). PHOTACS uses the independent-electron model with the Dirac–Hartree–Fock–Slater (DHFS) self-consistent potential (Sabbatucci and Salvat, 2016). This approximation considers a single electron in a central potential, interacting with a photon without taking into account the influence of the electrons in other orbitals. This approach facilitates the calculations, but it is expected to deliver less accurate results than a more elaborate atomic model such as multi-configuration Dirac-Fock (MCDF), which involves a non-local potential, different for each sub-shell. Those considerations complicate the calculations needed, making them unavailable for a MC simulation of a realistic experimental setup (Sabbatucci and Salvat, 2016; Seltzer *et al.*, 2014). To solve this problem, PHOTACS includes Pratt's renormalization screening approximation (PRSC). This method corrects the DHFS cross-sections by the ratio of the electronic densities cal-

culated with MCDF and DHFS at the limit when the radius tends to 0 (Sabbatucci and Salvat, 2016). Both versions of PENELOPE include photoelectric libraries with PRSC as default. However, the improvement of this correction is debatable (Seltzer *et al.*, 2014; Basaglia *et al.*, 2020). For that reason, unlike PEN14, PEN18 allows switching to a simulation without PRSC (Salvat, 2019).

Raighley atomic cross-sections and form factors (used in the calculation of the probability function distribution of the angular deflection) are obtained from EPDL97 (Cullen *et al.*, 1997), calculated using non-relativistic perturbation theory. EPDL97 includes the dispersion corrections to the form factors (or anomalous scattering factors), which take into account the fast variation in cross-sections with photons energies near the absorption edges (Salvat *et al.*, 2015; Salvat, 2019).

PENELOPE calculates the Compton cross-sections using the relativistic impulse approximation, considering the contributions of atomic electron subshells separately. As the impulse approximation considers electrons in movement with a certain momentum distribution, PENELOPE takes into account the Doppler broadening of the Compton line (Salvat *et al.*, 2015; Salvat, 2019).

2.2.3 Simulation uncertainty, efficiency and variance reduction tools

Technically, the statistic calculations are made in the main steering program (see below). However, as their computation is highly related to the use of efficiency-enhancing techniques (EFEN) and with the core of the PENELOPE system, they will be discussed here.

This work uses the history-by-history method (Walters *et al.*, 2002; Sempau *et al.*, 2001) to estimate the uncertainty of a given quantity Q, which considers the contribution, q, of each particle:

$$\overline{Q} = \frac{1}{N}\sum_{i=1}^{N} q_i, \tag{2.2}$$

$$\sigma = \sqrt{\frac{1}{N}\left[\frac{1}{N}\sum_{i=1}^{N} q_i^2 - \overline{Q}^2\right]}. \tag{2.3}$$

The proportionality of the variance with $1/\sqrt{N}$, where N is the total number of primary particles, implies that, over a determined limit, the effect of an increase of N does not significantly improves the statistics, resulting in an inefficient simulation (Chetty *et al.*, 2007).

The figure of merit that relate the variance with the simulation

time is

$$\epsilon = \frac{1}{\sigma^2 t}, \tag{2.4}$$

where ϵ is the efficiency (or absolute efficiency) of the simulation. Equation 2.4 shows that efficiency should be independent of N. However, this relation may not be valid in simulations with a small N due to statistical fluctuations (Salvat, 2019). To evaluate the limits in which the efficiency stabilizes regarding N, one can use

$$\tau = \frac{1}{\sigma^2 N}, \tag{2.5}$$

where τ is called the intrinsic efficiency.

As it is possible to observe from Eq. 2.4, efficiency can be increased, either by decreasing the simulation time for a given variance or by decreasing the variance for a given time. The EFENs can be divided into two groups: variance reduction tools (VRTs) and approximation-based strategies. VRTs reduce the variance for a given time without biasing the results; however, increasing the time for the computation of a single history. On the other hand, the approximation-based strategies (e.g., Class II algorithm in electron transport, see section 2.2.1) aim to decrease the time for computing a single history, through the introduction of a negligible but yet existing bias (Chetty *et al.*, 2007). This work uses two VRTs: the particle splitting (VRPS) and the interaction forcing (VRIF).

The VRPS philosophy is to increase the radiation flux to the

Table 2.1: Code number (*ICOL*) for various interaction events in PENELOPE

ICOL	Electrons	Photons
1	artificial soft event (hinge)	coherent (Rayleigh) scattering
2	hard elastic collision	incoherent (Compton) scattering
3	hard inelastic collision	photoelectric absorption
4	hard bremsstrahlung emission	electron-positron pair production
5	inner-shell impact ionization	

region of interest. When the particle reaches some user-defined material, with a weight w_0 and a particular state, it is transformed into a number $S > 1$ of particles with the same state, but a weight $w = w_0/S$. On the other hand, VRIF aims to increase the frequency of a specific interaction of the particle with matter. The mean free path of interaction A, λ_A, is replaced by a shorter one, λ_A/F with $F > 1$, generating $1 - F$ forced A interactions. The state of the particle only changes when a "real" (not forced) interaction occurs. Each particle resulting from a forced interaction will receive a weight w_0/F. Both S and F are user-defined parameters (Salvat, 2019). Table 2.1 enumerates the interactions considered by PENELOPE in the VRIF.

The use of a VRT generates a shower of secondary particles from a primary one. To maintain unbiased the simulation, the

contribution of the j-th particle of the shower, coming from the i-th primary particle, must be corrected by its weight:

$$\overline{Q} = \frac{1}{N} \sum_{i,j} w_{i,j} q_{i,j}. \tag{2.6}$$

which can be considered in the uncertainty calculation through:

$$\sigma = \sqrt{\frac{1}{N} \left[\frac{1}{N} \sum_{i} \left(\sum_{j} w_{i,j,} q_{i,j} \right)^2 - \overline{Q}^2 \right]}. \tag{2.7}$$

2.3 The penEasy main program

PENELOPE needs a steering main program to get access to the physics and coordinating the particle transport through the desired geometry. Users can develop their program from scratch; however, the distribution package comes with some examples of main programs ready to be used. Nonetheless, in this work, we used penEasy (Sempau *et al.*, 2011): a main modular program developed at the Universitat Politècnica de Catalunya, distributed by the Institute of Energy Technologies,[2] outside the official PENELOPE package distribution.

penEasy has five main functions:

1. Set the global simulation parameters (e.g., initial seeds, time

[2] `https://inte.upc.edu/en/downloads/peneasy`

of execution, the maximum number of N, among others).

2. Set the initial state of the primary particles (particle type, energy, position and direction) and modeling the radiation source.

3. Manage the simulation geometry and stablish the transport parameters (i.e., $EABS$, $C1$, $C2$, W_{cc} and W_{cr}) for each material in the simulation setup.

4. Tally and report the quantities of interest with an adequate estimation of the uncertainties.

5. Manage the VRTs.

Chapter 3

The electronic brachytherapy system

The Esteya® eBT system (Elekta Brachytherapy, Veenendaal, The Netherlands) is specially designed for surface treatments (see Fig. 3.1). This device presents a maximum absorbed dose rate of 198 Gy/h, above the lower limit of 12 Gy/h specified for an HDR treatment (Chassagne *et al.*, 1985). Its x-ray tube accelerates electron at 69.5 kV toward a tungsten target, generating a bremsstrahlung beam flattened by a 1.6 mm thick (measured at the beam axis) aluminum filter (flattening filter), collimated by applicators from 10 mm to 30 mm diameter. A plastic cap covers the exit of the applicators in order to reduce the electronic contamination of the beam, leaving a constant source to surface distance (SSD) of 60

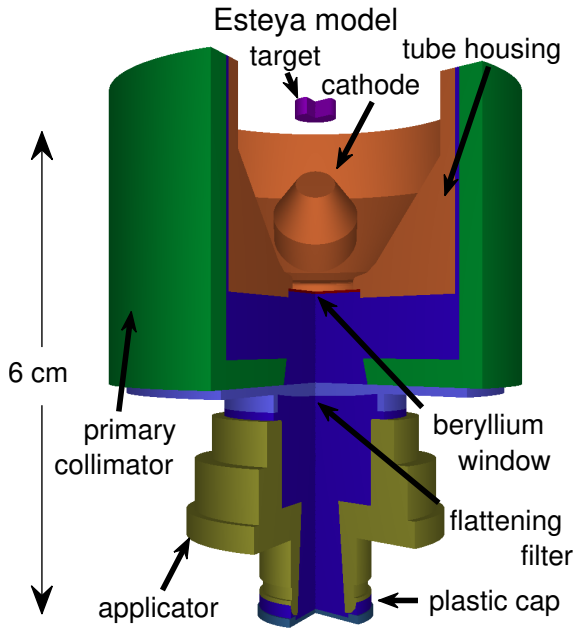

Figure 3.1: Model of the Esteya system in PEN14 and PEN18 for its 10 mm diameter applicator.

mm (Candela-Juan *et al.*, 2015b). It is worth mentioning that, unlike other surface eBT devices, the Esteya system only has one internal flattening filter.

The specifications of the Esteya system have been provided by the manufacturer. As far as we know, this is the most updated information for this eBT system at the time of writing this thesis. A comprehensive list of all materials and their densities is given in Table 3.1 (their exact dimensions are not specified here because they are proprietary information). It is worth noting that this beam energy is in the highest range of all eBT devices (Eaton,

Table 3.1: Composition of the Esteya components and their densities used with PEN14 and PEN18.

Component	Material	Density (g/cm^3)
Target	W	19.3
X-ray tube window	Be	1.848
X-ray tube housing	EN 1.4301 / AISI 304	8.03
Primary collimator	Pb	11.35
Flattening filter	Al > 95%	2.6989
Applicator	Densimet® 176	17.6
Plastic cap	Polyfenilsulfone	1.29
Dry air	NIST[a,b]	1.205×10^{-3}

[a] Obtained at `https://physics.nist.gov/cgi-bin/Star/compos.pl?matno=104`

[b] C (0.01%), N (75.73%), O (23.18%), Ar (1.28%)

2015), and, at the best of our knowledge, the Esteya unit is the only machine operating at this energy limit.

Chapter 4

Dosimetric characterization of the Esteya eBT system

Most of the content of this chapter was published in the original research paper:

Valdes-Cortez, C., Niatsetski, Y., Perez-Calatayud, J., Ballester, F., & Vijande, J. (2019). A Monte Carlo-based dosimetric characterization of Esteya, an electronic surface brachytherapy unit. Medical Physics, 46(1), 356–369.

Kind permission was granted by the journal to reprint this article as a chapter of this dissertation.

4.1 Introduction

As we discussed earlier, the low-energy photon beams present several difficulties for experimental measurements and dosimetric calculations. Thus, it is imperative to obtain a better understanding of the dosimetric characteristics of the eBT systems. To accomplish that purpose, it is necessary to acquire a large amount of data, usually obtained through MC simulations, which is the theoretical gold standard.

The data required to dosimetrically characterize an eBT machine can be divided into two groups: the processes occurred inside (upward the applicator exit) and outside (e.g., water phantom) of the eBT device. Among those processes that occurred within the eBT device, the precise description of bremsstrahlung sources may be one of the most challenging MC calculations in radiation dosimetry (Hiatt *et al.*, 2016). Besides, the interactions of the x-ray beam with the matter, downward the applicator exits (e.g., the energy deposition in a water phantom), is essential to understand the clinical implications of the use of eBT systems in cancer treatments.

The computation time required to achieve results with an acceptable uncertainty is a major concern. To manage this situation, MC simulations are often performed in two stages. In the first step, the beam phase space is obtained through the simulation of a detailed model of the equipment under study. In the second step, the machine phase space, stored as a manageable phase-space file

(PSF), is used to reproduce the beam and simulate its interaction with different materials (Chetty *et al.*, 2007). This approach is advantageous when studying clinical cases, allowing variation in specific patient anatomy and body composition, or the study of dosimetric equipment for a particular energy spectrum (Watson *et al.*, 2017).

The Esteya eBT system has been studied by other authors, mainly experimentally (Candela-Juan *et al.*, 2015b; Ibanez-Rosello *et al.*, 2017; Garcia-Martinez *et al.*, 2014). The aim of this chapter is divided into three main objectives: obtaining the phase space at the applicator exit of the Esteya system, exploring some EFEN strategies to achieve a good compromise between reliability and efficiency, and performing a dosimetric characterization of the Esteya system.

4.2 Material and method

4.2.1 Monte Carlo Esteya model

Two types of setups were implemented: the detailed setup, used to obtain the final PSF for the 10 mm (APP_{10mm}) and 30 mm (APP_{30mm}) diameter; and the simplified setup, used in the determination of the EFEN. Fig. 3.1 shows a schematic drawing of the detailed machine modeled with PEN14 using the data provided by the manufacturer. The simplified setup only includes the target

and the beryllium window, both surrounded by vacuum. The rationale for this choice is that EFEN strategies will only be applied over the target material and the window will be used as a detector.

We have performed MC calculations for four electron source models commonly used in the literature (Rivard *et al.*, 2006; Clausen *et al.*, 2012; Croce *et al.*, 2012; Safigholi *et al.*, 2012; Fulkerson *et al.*, 2014):

(a) The ideal source (IS): A mono-energetic electron beam of 69.5 keV with a homogeneous electron distribution over the focal spot.

(b) The Gaussian energy source (GES): Having its energy centered at 69.5 keV with a FWHM = 6.95 keV and a homogeneous electron distribution over the focal spot.

(c) The Gaussian intensity source (GIS): A mono-energetic electron beam of 69.5 keV, with a Gaussian electron distribution centered on the rectangular foil with a FWHM equal to the focal spot size of 1.8×1.3 mm^2, a value equal to the focal spot size kindly provided by the manufacturer.

(d) The spread source (SpS): A combination of GES and GIS.

Additionally, for the case of the simplified setup, we have looked for variations in the radiative yield due to the changes in the impingement angle of the electrons on the target. This allowed us to explore beam tolerances as reported by the manufacturer.

4.2.2 Efficiency enhancing

First, we have searched the optimum value for the VRIF factor F for the hard bremsstrahlung emission ($ICOL = 4$, see Table 2.1) and inner shell interactions ($ICOL = 5$, see Table 2.1) using the simplified setup. These simulations were performed using a cutoff of 1 keV for both electrons and photons. The remaining transport parameters, with the exception of *DSMAX*, were set equal to 0 to generate a detailed simulation. *DSMAX* was chosen to be equal to one tenth of the target thickness to assure a minimum of ten interactions within the target (Salvat *et al.*, 2015). The energy spectrum obtained here was stored and used as control. In a second step, we have evaluated the dependence of the efficiency with respect to $C1$ and $C2$, using the previously found F factor while keeping all the other parameters constant. For the sake of simplicity, we kept $C1$ equal to $C2$, and W_{cc} and W_{cr} were set to match *EABS* for electrons and photons, respectively.

The election of *EABS* implies determining cutoff energies large enough to speed up the simulations but small enough to avoid bias in the results. For this purpose, a control simulation ($EABS =$ 1 keV) of the detailed setup (see Section 4.2.1) was performed to generate a PSF (control PSF) scored at the exit of each applicator. For photons and electrons, *EABS* was taken as the energy where the intensity in the energy spectrum of the control PSF was less than 1% of its maximum. Furthermore, the ratio of the total energy scored by electrons to photons (electron contamination) in

the region of interest was registered. Afterwards, a new PSF (test PSF) was generated, simulating the detailed setup with the *EABS* previously determined. Finally, a comparison between the control and test PSFs was made, evaluating changes in both the photon energy spectra and the electron contamination.

4.2.3 Comparison with experimental data.

We have divided the comparison into two parts: spectral and clinical data for the APP_{10mm} and APP_{30mm}. The experimental data was obtained from Candela-Juan *et al.* (2015b) and Garcia-Martinez *et al.* (2014). In the spectral comparison, we have used two metrics obtained from the final PSFs, commonly used to characterize x-ray beams: the average photon energy ($\overline{E}$) and the HVL (mm Al). For the case of the clinical data, we compared the percentage absorbed depth-dose (PDD) and the off-axis dose profiles (DP).

4.2.3.1 Spectral comparison

Garcia-Martinez *et al.* (2014) determined $\overline{E}$ through the measurement of six tubes with a germanium crystal spectrometer located at 100 cm from the x-ray tube. The beam was collimated by two Pb pinholes collimators of 4mm (in the applicator) and 0.7 mm (in the detector) in diameter. As the attenuation of the flattening filter is not uniform due to its shape (see Fig. 3.1), $\overline{E}$ depends on

the distance from the beam axis to the detection volume. For that reason, comparing measured and simulated $\overline{E}$ requires considering only the photons within the same solid angle as in the experimental setup.

Such tight collimation drastically worsens the uncertainty of the simulation due to the reduced number of photons reaching the detector. To overcome this issue, we implemented a set of conditions that mimic the main characteristics of the experimental setup. These conditions are based on the constraints imposed by the filter geometry and the photon physics to extrapolate $\overline{E}$ from the data obtained with detectors of larger diameters (i.e., with better statistics).

We replicate the air attenuation locating the plane of detection at 1 mm distance from the applicator exit (6.1 cm from the source), filling the space between with an air volume of increased density (1.20479 g/cm^3), which maintains the photon path constant. In this condition, 0.7 mm diameter at 106 cm from the source is equivalent to 4×10^{-2} mm diameter ($r_0 = 2 \times 10^{-2}$ mm) at 6.1 cm.

If the simulated detector of radius r is centered with respect to the beam axis, the measured average energy $\overline{E}(r)_{IS}$ (we use here the IS configuration as example) will be defined as the average energy due to all photons scored at a distance smaller than r. As the photon path length (z) in the filter is not uniform, $\overline{E}_{IS}$ will change with a rate $d\overline{E}_{IS}/dz$. As we know that $dz/dr = 0$ at the beam axis ($r = 0$), the rate $d\overline{E}_{IS}/dr$ must increase monotonically to 0 when

r goes to 0. Therefore, there exists a convergence value $\overline{E}(0)_{IS}$. As r_0 is small enough with respect to the system dimensions, one can assume $\overline{E}(0)_{IS} \approx \overline{E}(r_0)_{IS}$. In these conditions, we can obtain an extrapolated value $\overline{E}(r_0)'_{IS}$ from its last two neighbors, $\overline{E}(r)_{IS}$ and $\overline{E}(r + \Delta r)_{IS}$. As $\overline{E}(r_0)_{IS}$ must comply with the following property: $\overline{E}(r)_{IS} < \overline{E}(r_0)_{IS} < \overline{E}(r_0)'_{IS}$, the estimation of $\overline{E}(r_0)_{IS}$ only requires the knowledge of the two last neighbors.

We should expect a monotonic increase in the slope $\Delta\overline{E}_{IS}/\Delta r$. However, this may not be the case in practice due to statistical fluctuations when r diminishes. For this reason, $\overline{E}(r)_{IS}$ (the last neighbor) will be the last point for which its slope maintains the expected behavior.

The HVL was determined analytically through a method similar to that used by Watson *et al.* (2017). The air-kerma ratio is calculated from the energy photon spectrum obtained from the PSF of the detailed setup:

$$K_{ratio} = \frac{\sum \Psi_i \left(\frac{\mu_{en}}{\rho}\right)_{i,air} exp(-\mu_{i,air}\ x_{air} - \mu_{i,Al}\ x_{Al})}{\sum \Psi_i \left(\frac{\mu_{en}}{\rho}\right)_{i,air} exp(-\mu_{i,air}\ x_{air})} \tag{4.1}$$

where Ψ_i and $(\mu_{en}/\rho)_{i,air}$ are the energy fluence and mass energy-absorption coefficient of each energy bin i, respectively. Additionally, $\mu_{i,air}$ and $\mu_{i,Al}$ are the attenuation coefficients of the air and the attenuator (i.e., aluminum), respectively. Finally, x_{air} and x_{Al}

are the source-to-detector distance in air (100 cm) and the thickness of the aluminum attenuator. The attenuation coefficients (total attenuation including the coherent scattering) were obtained consistently from PEN14.

The HVL is defined as the value of x_{Al} for which $K_{ratio} = 0.5$. To evaluate the effect of the detector radius (i.e., the dependence of $\overline{E}$ from r) in the determination of the HVL, several photon spectra (with a bin width of 0.1 keV) were generated for both applicators from the corresponding PSF, taking into account the lateral distance from the beam axis for the photons in the PSF. The fluences and the coefficients uncertainties were propagated across the Eq. 4.1. Following the analysis by Andreo *et al.* (2012), a Type B uncertainty (BIPM, 2010) of 2.2% ($k = 2$) in the $(\mu_{en}/\rho)_{air}$ was considered. The HVL was obtained for the IS and GES models.

4.2.3.2 Clinical comparison

The final PSFs were applied over a cylindrical water phantom (10 cm radius and 20 cm depth) with the water mass density (0.998 g/cm^3) recommended by the TG-43U1 (Rivard *et al.*, 2004). We used the VRPS technique, with splitting factors of 10^5 ($\text{APP}_{10\text{mm}}$) and 10^4 ($\text{APP}_{30\text{mm}}$). Collisional kerma was used as an absorbed dose estimator by scoring the absorbed energy using cylindrical symmetry with *EABS* = 1 keV for photons, disabling the electrons transport in the water phantom.

The absorbed depth dose (DD) was scored in central discs of

1 mm radius and a height $h = 0.25$ mm. The DP were tallied in concentric rings with r in the range $0 \leq r \leq$ applicator radius – Δr, Δr being the DP bin width, and the height $h = 1$ mm for all depths. The number of events collected in the rings increases with an increment of r. That condition makes possible to improve the spatial resolution by reducing Δr, keeping the uncertainty roughly constant. The bin widths were $\Delta r = 1$ mm for $r \leq 80\%$ of the applicator radius and $\Delta r = 0.1$ mm for $r > 80\%$ of the applicator radius. The PDD was normalized at 3 mm depth and the DP was normalized at the central bin.

We compared the results obtained with all source models. As an example, we will use the IS and GES. DPs are compared according to 100 x [1 - $(\mathrm{DD}_{GES})_i$ / $(\mathrm{IS}_{IS})_i$], where i is the index of the corresponding bin. PDD was compared according to $(\mathrm{PDD}_{GES})_i$ - $(\mathrm{PDD}_{IS})_i$. The penumbra was calculated as the difference between the radii corresponding to the 80% ($r_{80}\%$) and 20% ($r_{20}\%$) of the absorbed dose at the central axis, obtained through linear interpolations.

Garcia-Martinez *et al.* (2014) associated the existence of a systematic asymmetry of 1.5% in the DPs with a heel effect caused by the cathode. This would break the cylindrical symmetry used to tally the dosimetric scores. To evaluate the effect of such deviation from the cylindrical symmetry, we performed a simulation using Cartesian coordinates to score DPs in the x and y axes at 5 mm depth. The dose on the x axis was scored in voxels of 0.5 x 1.0 x 1.0 mm^3 and 1.13 x 1.0 x 1.0 mm^3, for $r > 80\%$ and $r \leq 80\%$

of the applicator radius, respectively (changing the coordinates accordingly to the y axis). The symmetry was evaluated as 100 x [1 - DP(-12 mm)/DP(+12 mm)]. Where DP(-12 mm) and DP(+12 mm) are the DP values at -12 mm and +12 mm, respectively.

The MC details are summarized in Table 4.1 following the recommendations of the RECORDS AAPM TG-268 report (Sechopoulos *et al.*, 2018).

4.2.4 Uncertainties analysis

All uncertainties will be expressed with a coverage factor $k = 2$, as recommended by the AAPM (DeWerd *et al.*, 2011). In the following subsections (4.3.1 - 4.3.3) only Type A (estimated by the history-by-history method) uncertainties will be shown. Type B uncertainties will be analyzed in a separate section, 4.3.4. In all cases the evaluation of the uncertainties followed BIPM recommendations (BIPM, 2010). We assumed all probabilities as normal distributions, except for the geometrical uncertainty introduced by the bin width in the DP. In this case, the probability considered having a rectangular distribution with bounds equal to the half of the bin width (0.05 mm).

Table 4.1: Summary of the main characteristics of the Monte Carlo method used in this chapter.

Item	Description	References
Code	1) PEN14, 2) penEasy (v. 2015-05-30) compiled with GNU Fortran 5.3.1 using the -O flag	1) Salvat *et al.* (2015) 2) Sempau *et al.* (2011)
Validation	Previously validated	Ye *et al.* (2004) Chica *et al.* (2009) Croce *et al.* (2012)
Timing	Time required to obtain the final PSF was 430 hrs. (CPU time). 8 processors, name: Intel(R) Core(TM) i7-3770k CPU @ 3.5 GHz	
Source description	Four electron sources models: 1) Ideal source IS: mono-energetic (69.5 keV) homogeneous distribution. 2) Gaussian energy source GES: Gaussian energy spectrum (FWHM 6.95 keV centered at 69.5 keV), homogeneous electron distribution. 3) Gaussian intensity source GIS: mono-energetic (69.5 keV) Gaussian electron distribution (FWHM = focal spot size of 1.8x1.3 mm^2). 4) Spread source SpS: Gaussian energy spectrum (FWHM = 6.95 keV, centered at 69.5 keV, Gaussian electron distribution (FWHM = focal spot size of 1.8x1.3 mm^2).	
Cross-Sections	1) Photoelectric: calculated with PHOTACS. 2) Rayleigh: non-relativistic perturbation theory. 3) Compton: relativistic impulse approximation.	1) (Sabbatucci *et al.*, 2016) 2) Sakurai (1967), Born (1969); Baym (1974), Cullen *et al.* (1997). 3) Ribberfors (1983)
Transport Parameters	Photon cutoff = 10 keV. Electron cutoff = 10 keV in the target, disabled otherwise. $C1$=$C2$=0.	
VRTs	Interaction forcing (hard bremsstrahlung emission) and particle splitting.	Salvat *et al.* (2015)
Scored quantity	Absorbed dose in water (collision kerma approximation)	
N hist./ uncertainties	10^9 primary particles / $< 2\%$ (Type A, $k = 2$)	
Statistical method	History-by-history	Salvat *et al.* (2015) Walters *et al.* (2002)

4.3 Results

4.3.1 Efficiency enhancing strategy

Fig. 4.1 shows the results of the simulations described in section 4.4.1. Unless otherwise stated, the results of the test simulations were obtained with 10^7 primary particles. The efficiency reaches a plateau at a VRIF factor near 150, improving the efficiency by a factor ~ 20. Modification of $C1$ and $C2$, in combination with $F = 150$, did not produce any further improvement. It has been observed that τ stabilizes for values around $N = 10^6$.

The control PSFs were obtained with *EABS* = 1 keV, F = 150, and N = 10^8. The energy bin in the control energy spectrum with 1% of its maximum intensity was 11 keV and 12 keV for the $\mathrm{APP}_{10\mathrm{mm}}$ and $\mathrm{APP}_{30\mathrm{mm}}$, respectively. Hence, an *EABS* = 10 keV was considered in the following simulations for both applicators. The energy scored by electrons at the applicator exit was 0.005% of that scored by photons. Hence the electron contamination was neglected.

In the control PSF, less than 1% of the photons have originated outside of the target. Their influence on the energy spectra is negligible, modifying the average energy from 35.43 ± 0.19 keV to 35.48 ± 0.13 keV if those photons were discarded.

The simulation in the detailed setup was carried out with $N = 10^8$. The corresponding parameters are summarized in Table 4.2.

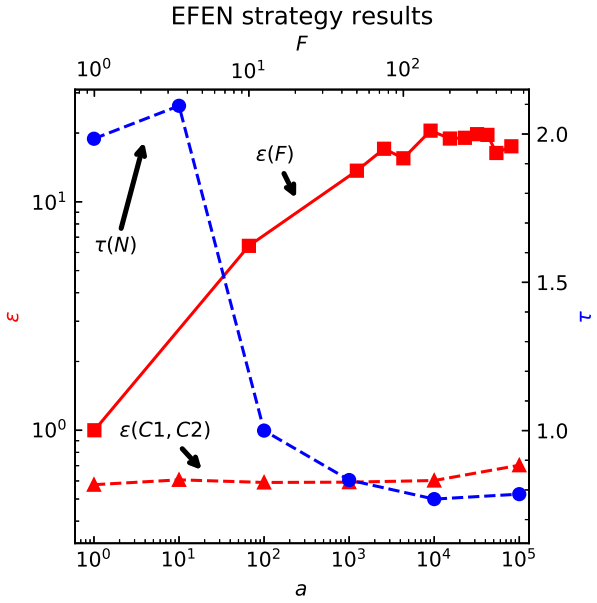

Figure 4.1: MC simulation efficiencies (ϵ and τ) of photon energy deposition in the beryllium window. The red lines (left axis) correspond to the efficiency ϵ calculated from Eq. 2.4 while the blue line (right axis) - to the intrinsic efficiency τ as defined in Eq. 2.5. The solid red line corresponds to the value of efficiency (F-axis), when F (VRIF enhancement factor) is modified, normalized to $F = 1$. Dashed lines correspond to the a-axis: red dashed line, $C1 = C2 = 10^{-6}a$ (log scale, normalized to the efficiency obtained with $C1 = C2 = 0$); blue dashed line, $N = 10^3 a$ (log scale normalized to $N = 10^5$).

Figure 4.2 compares the energy spectra of the control (*EABS* = 1keV) and test (*EABS* = 10 keV) PSFs obtained with $\text{APP}_{30\text{mm}}$. The 67%, 83%, 88% and 93% of the bins show an absolute difference below 2%, 3%, 5% and 10% (average equal to -0.8%, total range within -37.4% and 12.7%), respectively. All differences in

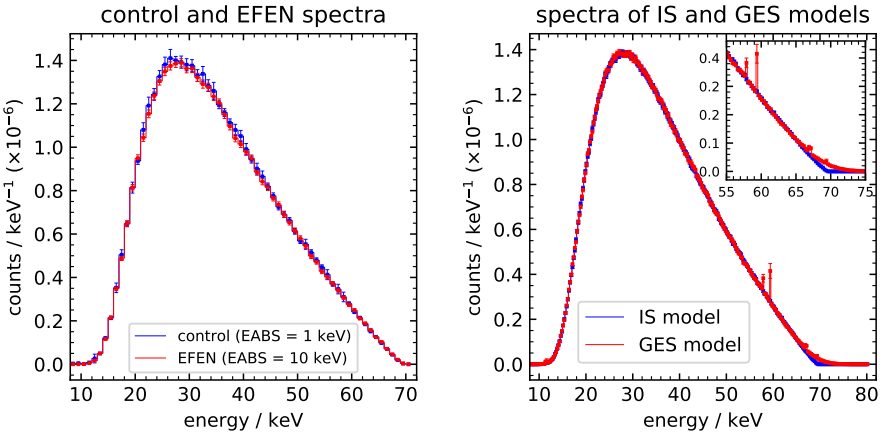

Figure 4.2: Energy spectra comparisons in the detailed setup. Left: Test simulations (APP_{30mm}, $N = 10^8$, bin width 1 keV). The blue line corresponds to the control PSF obtained with $EABS_{ph} = EABS_e = 1$ keV, the red line corresponds to the PSF obtained with $EABS_{ph} = 10$ keV for all materials, $EABS_e = 10$ keV for the target and the electron transport disabled for all other materials. Right: Final PSFs (APP_{30mm}, $N = 10^9$, bin width = 0.25 keV). The blue line corresponds to the simulation using the ideal source model, the red line corresponds to the simulation using the Gaussian energy source model. The inset corresponds to the zone where the difference between both spectra becomes noticeable, with the tungsten $K_{\alpha 1}$, $K_{\alpha 2}$, $K_{\beta 1}$ characteristic lines, which are well over the associated statistical uncertainties.

the range 14 keV $\leq$ bin $\leq$ 64 keV are below 5% (average equal to 0.2%, range within -2.9% and 4.3%). The use of these parameters allows a reduction of 92% to the CPU time.

Table 4.2: Monte Carlo efficiency enhancing strategy. Summary of the variance reduction techniques and transport parameters used to obtain the final PSFs.

Item	Value	Material
VRIF	150 ($ICOL = 4$, $WGMIN = 1$)	target
$C1$, $C2$, W_{cc}, and W_{cr}	0	all
$EABS_{ph}$	10 keV	all
$EABS_e$	10 keV 10^6 keV	- target - elsewhere

4.3.2 Final phase-space file

The final PSFs were obtained with $N = 10^9$ and the EFEN summarized in Table 4.2. Fig. 4.2 shows the differences in the energy spectra between IS and GES models in the case of $\text{APP}_{30\text{mm}}$. Differences are noticeable for energies higher than 56 keV due to the presence in the GES simulation of the tungsten characteristic lines $K\alpha 1$, $K\alpha 2$ and $K\beta 1$ (59.321 keV, 57.984 keV and 67.244 keV, respectively).

4.3.2.1 Average photon energy

If all photons were taken into account in the PSF, $\overline{E}_{IS} = 35.97 \pm 0.09$ keV and $\overline{E}_{GES} = 36.06 \pm 0.10$ keV were obtained for the $\text{APP}_{10\text{mm}}$ while $\overline{E}_{IS} = 35.47 \pm 0.03$ keV and $\overline{E}_{GES} = 35.57 \pm 0.03$

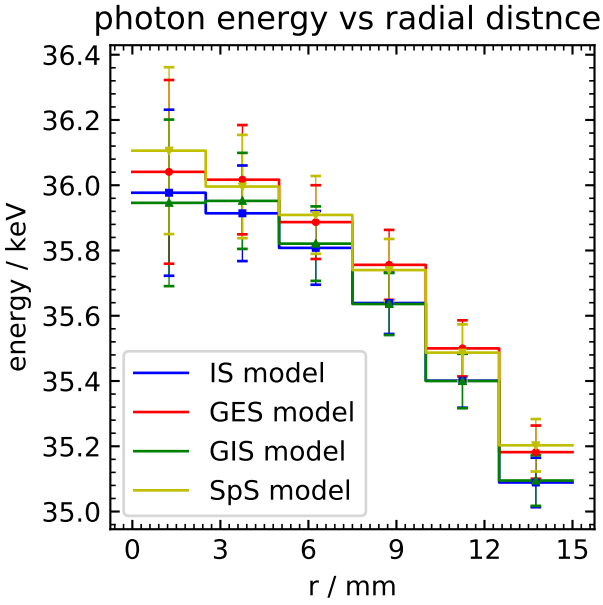

Figure 4.3: Average photon energy vs. distance from the beam axis, for the ideal (IS), Gaussian energy (GES), Gaussian intensity (GIS), and spread (SpS) source simulations. The bin width is 2.5 mm.

keV for the APP_{30mm}. Considering only photons with an off-axis position $r \leq 2.5$ mm (see Fig. 4.3), $\overline{E}_{IS} = 35.98 \pm 0.18$ keV for both applicators, while $\overline{E}_{GES} = 36.06 \pm 0.20$ keV and 36.04 ± 0.21 keV for the APP_{10mm} and APP_{30mm}, respectively.

Fig. 4.4 shows the average energy $\overline{E}$ detected through an air column of 1 mm (using a VRPS factor of 20), as a function of the detector radius for the IS simulation. The slope (i.e., $\Delta\overline{E}_{IS}/\Delta r$) increases monotonically when r goes to zero, as expected, but only until $r = 2.5$ mm. Using this value as threshold, $\overline{E}(r_0)_{IS}$ should be

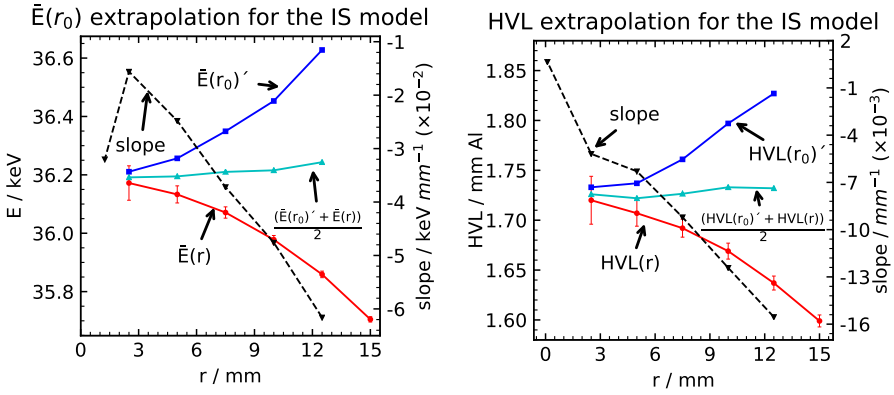

Figure 4.4: Extrapolation of the average photon energy $\overline{E}$ (left) and the HVL (right) for a 2×10^{-2} mm radius (r_0) detector, calculated using the ideal source model. Left: The red line corresponds to the average energy of all photons within the beam radius r. The black dashed line corresponds to the slope of the two neighbors. It is evident that at $r = 2.5$ mm the slope function breaks its expected behavior. The blue line corresponds to the extrapolation of $\overline{E}$ in $r = 2\times10^{-2}$ mm, calculated with the plotted slope and placed over its closer neighbor only for visual help. The cyan line corresponds to the average value between $\overline{E}$ for the actual detector radius, and the extrapolation made with the plotted slope. Right: The red line corresponds to the HVL, calculated with photon energy spectra generated considering only the photons within the beam radius r. The black dashed line corresponds to the slope of the last two neighbors, the slope function breaks its expected behavior at $r = 2.5$ mm. The blue line corresponds to the extrapolation of HVL in $r = 2 \times 10^{-2}$ mm, calculated with the plotted slope. The cyan line corresponds to the average value between the HVL for the actual detector radius and the extrapolation.

at some point between 36.17 keV (last neighbor $\overline{E}(r)$) and 36.21 keV (extrapolation $\overline{E}(r_0)'$). If we take the average of these two

limits as the expected $\overline{E}(r_0)$, then, $\overline{E}(r_0)_{IS} = 36.19 \pm 0.09$ keV and $\overline{E}(r_0)_{GES} = 36.25 \pm 0.10$ keV. These values agree with the 36.2 ± 0.2 keV ($k = 2$) measured by Garcia-Martinez *et al.* (2014).

4.3.2.2 HVL determination

The HVL for the APP_{30mm} shows the same dependence on r as $\overline{E}$ (see Fig. 4.4). The HVL value calculated using the IS model is 1.72 ± 0.04 mm of Al for both applicators. Differences between the IS and GES models are below 0.5%. Candela-Juan *et al.* (2015b) reported three HVL values depending on the chamber and setup used: 2.09 mm, 1.88 mm, and 1.69 mm. All values with an uncertainty of 0.10 mm ($k = 2$). Garcia-Martinez *et al.* (2014) reported two values: 1.86 ± 0.40 mm, obtained using oRTIgo (QA software for Barracuda detector, Version 6.4C), and 1.82 ± 0.32 mm, obtained by fitting the measurements (coverage factor $k = 2$ for both values). The HVL value, obtained in our study, agrees with the previously published values within the range of uncertainties.

4.3.3 Dosimetric data

4.3.3.1 Depth dose

For APP_{10mm}, the average differences in absorbed dose between DD_{IS} and DD_{GES} are 1.1% (from 0.4% to 2.2%, $\sigma = 0.4\%$) and 1.0% (from 0.5% to 1.4%, $\sigma = 0.2\%$) for the total depth range and the first centimeter, respectively. For APP_{30mm}, the corresponding

Table 4.3: Depth dose uncertainties (%) for the total depth range and for the first centimeter (with approximately 50% of the maximum absorbed dose at 0 mm depth). The average value is given first, followed by the minimum and the maximum values in parentheses.

Applicator	Ideal Source		Gaussian Energy Source	
	1 cm	Total	1 cm	Total
10 mm	1.3 (1.3-1.4)	1.7 (1.3-2.3)	1.4 (1.4-1.5)	1.8 (1.4-2.5)
30 mm	1.2 (1.1-1.3)	1.4 (1.1-2.1)	1.3 (1.2-1.4)	1.5 (1.2-3.5)

differences are 0.7% (from 1.35% to 3.4%, $\sigma = 0.7\%$) and 0.5% (from 0.02% to 1.2%, $\sigma = 0.2\%$). The uncertainties of the calculated DD values for both applicators are shown in Table 4.3.

For the APP_{10mm}, the average differences between PDD_{IS} and PDD_{GES} were -0.02% (from 0.33% to 0.24%, $\sigma = 0.06\%$) and -0.04% (from 0.33% to 0.24%, $\sigma = 0.12\%$) for the depth total range and the first centimeter, respectively. For APP_{30mm}, the average differences are -0.01% (from 0.47% to 0.90%, $\sigma = 0.15\%$) and 0.12% (from 0.37% to 0.90%, $\sigma = 0.26\%$) for the depth total range and the first centimeter, respectively.

Table 4.4 compares the PDD_{IS} with the data published by Garcia-Martinez *et al.* (2014), the data supplied by the manufacturer (Candela-Juan *et al.*, 2015a), and from a personal communication from Yury Niatsetski (Elekta) regarding a commissioning process from a Dutch center (Niatsetski, 2018). Fig. 4.5 shows a comparison of the PDD_{IS} for APP_{10mm} and APP_{30mm}, Fig. 4.5 compares between the PDD_{IS} and the PDD published by Garcia-

Table 4.4: PDD data for APP_{10mm} and APP_{30mm} (IS model), compared with Garcia-Martinez *et al.* (2014), Ref. 1, and the manufacturer's data, Ref. 2 (Candela-Juan *et al.*, 2015a), and from a personal communication, Ref. 3 (Niatsetski, 2018). The uncertainties are expressed with the coverage factor $k = 2$.

App	Depth (mm)					
	0.0	1.0	2.0	3.0	4.0	5.0
10 mm	122.8 (1.5)	115.3 (1.6)	107.4 (1.4)	100.0 (1.3)	93.2 (1.2)	86.9 (1.1)
Ref. 1	124.8	115.7	109.4	100.0	91.3	85.6
Ref. 2	124.5	115.8	107.7	100.0	92.9	86.3
Ref. 3	124.7	116.1	107.7	100.0	92.9	86.4
30 mm	119.0 (1.6)	112.7 (1.4)	106.3 (1.3)	100.0 (1.2)	94.3 (1.1)	88.8 (1.1)
Ref. 1	123.5	114.2	106.8	100.0	93.6	88.5
Ref. 2	122.5	114.6	107.1	100.0	93.5	87.4
Ref. 3	122.5	114.6	107.1	100.0	93.8	88.1
	Depth (mm)					
	6.0	7.0	8.0	9.0	10.0	–
10 mm	81.0 (1.1)	75.5 (0.9)	70.4 (0.9)	65.7 (0.9)	61.4 (0.8)	–
Ref. 1	79.7	73.8	69.8	64.5	60.5	–
Ref. 2	–	–	–	–	–	–
Ref. 3	80.2	–	69.7	–	59.9	–
30 mm	83.5 (1.0)	78.6 (0.9)	74.1 (0.9)	69.9 (0 8)	65.8 (0.7)	–
Ref. 1	83.2	77.7	72.8	68.3	65.1	–
Ref. 2	–	–	–	–	–	–
Ref. 3	82.6	–	72.7	–	64.6	–

Martinez *et al.* (2014) for the APP_{30mm}. The maximum differences between the simulated and the experimental PDDs are 2.0% for APP_{10mm} and 4.5% for APP_{30mm}. The maximum differences with the manufacturer's data for these applicators are 1.7% and 3.5%. It should be noted that the maximum differences are located at the phantom surface. Deeper than 1 mm, all the differences are within 2%.

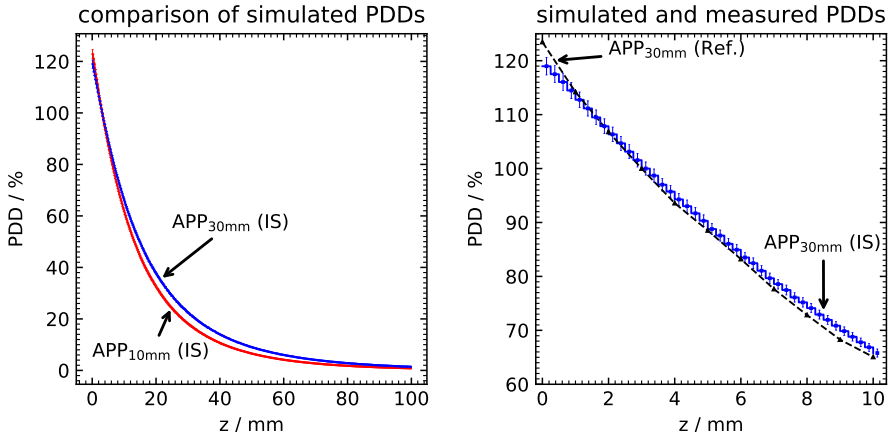

Figure 4.5: Left: Comparison between the simulated PDDs (IS model) for APP_{10mm} and APP_{30mm}. Right: Comparison between the PDD published by Garcia-Martinez *et al.* (2014), Ref., and simulated (IS model) for APP_{30mm}.

4.3.3.2 Dose profiles

Figure 4.6 shows the DP_{GIS} for APP_{30mm} at 0 mm, 3 mm, 5 mm, and 10 mm depths. Shallow profiles have clear horns, reaching 107% for the surface one. The profile at 5 mm depth, which is specified by the manufacturer as the reference depth (Garcia-Martinez *et al.*, 2014) has no horn. All dose profiles are obtained with an uncertainty below 2%.

Table 4.5 compares the penumbras obtained in this work with those reported by Garcia-Martinez *et al.* (2014). Variation of the electron energy spectrum did not produce any noticeable differences between DP_{GES} and DP_{GIS}, which were below 2% for both applicators. The differences between the dose profiles DP_{IS} and

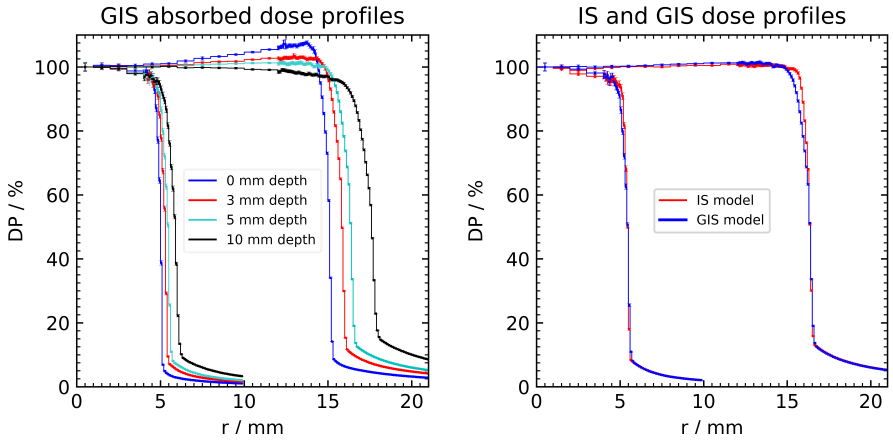

Figure 4.6: Simulated absorbed dose profiles for APP_{10mm} and APP_{30mm}. Left: using the Gaussian intensity source (GIS) model at 0 mm, 3 mm, 5 mm, and 10 mm depth. Right: comparison between the ideal source (IS) and GIS models at 5 mm depth.

DP_{GIS} at 5 mm depth, shown on the Figure 4.6, are below 1.5% for $r \leq 80\%$ of the $r_{50\%}$, and up to 12% for $r > 80\%$ of the $r_{50\%}$.

Fig. 4.7 compares the obtained DP_{GIS} with the measured profile from Garcia-Martinez *et al.* (2014) for APP_{30mm}. The differences are noticeable from $r \geq 7$ mm, being equal to 2%, 5% and 10% at $r = 11$ mm, 14 mm and 16 mm, respectively. In the range 16 mm$< r \leq 17$ mm the differences are below 15% and the distance to agreement is better than 0.4 mm.

The DP, simulated using the GIS model in Cartesian coordinate system, presents an average uncertainty of 1.7% (max 3.5%) in the plateau for both X and Y directions. An asymmetry of $2.2 \pm 1.4\%$ ($k = 2$) is observed along the x (cathode) axis. Along

Table 4.5: Penumbra values (mm) for different combinations between applicators and simulated electron sources and the average values from Garcia-Martinez *et al.* (2014), Ref. 1. All uncertainties are expressed with the coverage factor $k = 2$.

App	Depth (mm)			
	Ideal	Energy Gaussian	Intensity Gaussian	Spread
10 mm	0.28 (7)	0.29 (8)	0.44 (7)	0.45 (7)
Ref. 1		1.0 (1)		
30 mm	0.42 (7)	0.43 (7)	0.63 (7)	0.63 (7)
Ref. 1		1.0 (1)		

the y axis the asymmetry was below 1% and therefore within uncertainty. The average absolute differences between the cylindrical and the Cartesian profiles on the plateau were 0.8% (max 3.1%, $\sigma = 0.8\%$) and 0.6% (max 1.9%, $\sigma = 0.5\%$) for the x and y axes, respectively. Figure 4.7 compares DP_{GIS} obtained with cylindrical and Cartesian (x axis) tallies.

4.3.4 Uncertainties

There are three main sources of Type B uncertainties: manufacturing tolerances, cross-section libraries and electron source manufacturing uncertainties.

The flattening filter is the predominant structure determining the beam properties. According to the manufacturer's data, the maximum tolerance of the filter thickness is ± 0.035 mm, which implies a difference of $\pm 0.5\%$ in the energy absorption ($\mu_{en} = 1.531$ cm^{-1} for 36 keV). Based on the flattening filter geometry, the pho-

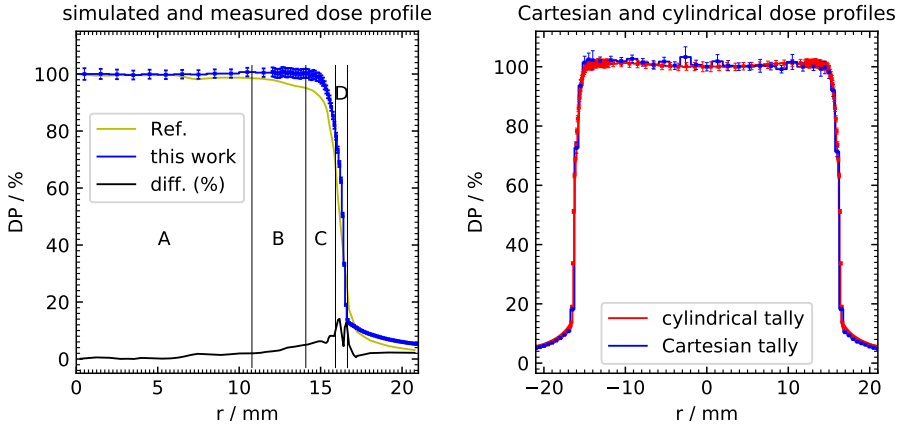

Figure 4.7: Simulated and measured absorbed dose profiles for APP_{30mm} at 5 mm depth. Left: Comparison between the simulated DP_{GIS} and the dose profile published by Garcia-Martinez *et al.* (2014) (Ref 1). The black curve represents the differences (%) between them. The differences in the indicated zones A, B, C and D are below the 2%, 5%, 10% and 15%, respectively. Distance to agreement in zone D is below 0.4 mm. Right: Simulated DP_{GIS} with the Cartesian and cylindrical tallies. Cylindrical tally profile was mirrored for negative r values for visual purposes.

ton path, and the data presented in Fig. 4.3, the average photon energy of the beam changes with a rate of 5.6% per millimeter thickness of the filter. That implies a change of the average photon energy of ±0.2% within the filter thickness tolerance. As discussed in chapter 6, the variation of the filter thickness by 0.035 mm leads to an HVL change of 1.4%. Therefore, the flattening-filter manufacturing adds 0.5% to the Type B uncertainty of the absorbed dose in water (DD and PDD) and in the average photon energy, while the uncertainty introduced in the HVL determination is 1.4%.

Andreo *et al.* (2012) analyzed Type B uncertainty of the cross-section libraries and proposed the value of 2.2% for a photon beam with the average energy of 34.1 keV in water (group μ_B (II) in that work, $k = 2$). This component adds 2.2% uncertainty to PDD, DD, DP and $\overline{E}(r_0)$.

The electron beam model has two major sources of uncertainties: the electron energy and focal spot distributions, and the impingement angle of the electrons on the target. We estimated an additional uncertainty of 1.1% due to the lack of knowledge of the electron energy spectrum and spatial distribution, based on the average difference between DD_{IS} and DD_{GES} for APP_{10mm}. Our simulation showed a difference of 1.5% in the radiation yield with the change of the impingement angle of the electrons over the range reported by the manufacturer. This component adds 1.9% Type B uncertainty to the absorbed depth dose and 1.5% to the dose profiles (see section 4.4.2, profile asymmetry discussion).

Table 4.6 shows the summary of all uncertainties for the investigated quantities.

4.4 Discussion

4.4.1 Efficiency enhancing strategy

The saturation of the simulation efficiency, observed in Fig. 4.1, is achieved when the electrons that impinge the target begin to

Table 4.6: Estimated uncertainties ($k = 2$) of the different beam characteristics, calculated during simulation. For the DD, the maximum values for the first 10 mm and for the entire range are showed. For the PDD and the DP, only the maximum value is shown, which is within the first 10 mm and the 80% of the applicator diameter, respectively.

Items	Uncertainties (%)		
	Type A	Type B	Combined, u_c
DD	1.5/3.5	2.9	3.2/4.5
PDD	2	2.2	3
DP	2	2.7	3.3
HVL	2.5	1.4	2.9
$\overline{E}(r_0)$	0.3	2.2	2.2

produce more than one photon (correlated photons) due to the use of high enhancement factors (F) of VRIF *ICOL* = 4. As the history-by-history statistical estimator considers the correlation between the particles, the correlated photons decrease their contribution to the variance reduction, while still consuming computation time (Chetty *et al.*, 2007; Ali and Rogers, 2007).

Ali and Rogers (2007) implemented the bremsstrahlung cross-section enhancement (BCSE) VRT in the EGSnrc code, the numerical technique which is equivalent to the VRIF *ICOL* = 4 implemented in PENELOPE. They analyzed the BCSE performance in the targets of equipments similar to the Esteya system, using detector array of different sizes (from 1 x 1 cm^2 to 4 x 4 cm^2) at a detector-to-target distance of 100 cm. In contrast to that, in our work we considered a single detector with a diameter in the order of the beryllium window size (1 cm), placed at 2 cm distance from

the target. The smaller solid angle of the individual detectors, used in the Ali and Rogers (2007) work, decreases the probability that the correlated photons arrive at a specific detector. For that reason, they obtained efficiency saturations at higher enhancement factors (over 1000) using only one VRT. Nevertheless, when they combined the BCSE and a splitting VRT (gaining a higher global efficiency), the optimum BCSE enhancement factor dropped to a range of 100 to 200, being in the same order as $F = 150$, found in our work.

Unlike other authors (Croce *et al.*, 2012; Pozuelo *et al.*, 2012) we found a deterioration in the simulation efficiency with the use of $C1$ and $C2$ parameters in combination with VRIF $F = 150$ (see Fig. 4.1). Sempau and Andreo (2006) showed that the use of a high value for $C1$ and $C2$ could lead to a relative decrement of the step length for the energy range of 30 keV and 80 keV in graphite (without VRT), hence increasing the computation time. As described in Section II, we have followed a two-step procedure. First, the optimum VRIF F factor was obtained; then, all the parameters controlling radiation transport were determined to achieve a more efficient simulation strategy. It has been pointed out in the literature that modifications of the transport parameters $C1$ and $C2$ for high energy electrons in the target, even with small nonzero values, may affect water dosimetry (Rodriguez *et al.*, 2015; Mayorga *et al.*, 2016). However, there is no evidence indicating that the use of VRIF may bias simulations in water (Rodriguez *et al.*, 2015; Mayorga *et al.*, 2016). In our opinion, the most efficient strategy is

to develop an EFEN by fixing the transport parameters only after the use of some VRT over the target.

The increase of *EABS* from 1 keV to 10 keV reduced the required computation time by 84%, causing the loss of 0.02% of the photons, detected at the applicator exit. By disabling electron transport in all materials except the target, an extra time reduction of 8% was achieved at the cost of losing an additional 1.2% of the photons. This measure modified the average photon energy by 0.14%. These differences might only play a role for prediction of the electron contamination at the patient surface. Nonetheless, it has been observed that the energy fluence of electrons is negligible compared to that of photons.

4.4.2 Phase-space and dosimetric outcomes

The analysis of the differences between the four source models used in this work shows that the main source of discrepancies comes from differences in the electron energy distribution. Electrons over 69.5 keV, present in the GES simulation, have enough energy to ionize the tungsten K shell (69.525 keV) generating the characteristic peaks observed in Fig. 4.2. These peaks are not observed in the experimental measurements reported by Garcia-Martinez *et al.* (2014).

The calculated HVL value (1.72 ± 0.02 mm) agrees, within the reported uncertainties, with previously published data (Candela-Juan *et al.*, 2015b; Garcia-Martinez *et al.*, 2014) depending on

the type of the detector used. The HVL measured (1.69 ± 0.1 mm) (Candela-Juan *et al.*, 2015b) using the Exradin A20 ionization chamber (Standard Imaging Inc., Middleton, WI) is closer to our result than the one obtained using a Barracuda (RTI Electronics AB, Mölndal, Sweden) solid-state detector (1.82 ± 0.3 mm published by Garcia-Martinez *et al.* (2014), and 1.88 ± 0.1 mm published by Candela-Juan *et al.* (2015b), both with a coverage factor $k = 2$).

The simulated PDDs show a good agreement (within 2%) with the experimental data beyond 1 mm depth. In a typical skin treatment, when a dose is prescribed at 3 mm depth, the discrepancies in the absorbed dose at the surface are in the range of 3.8%. Garcia-Martinez *et al.* (2014) used a plastic phantom with a PTW T34013 parallel-plate ionization chamber (PTW, Freiburg, Germany). To mimic these experimental conditions, we simulated the depth dose ($PDD_{plastic}$) in a plastic water phantom, using data published by Ramaseshan *et al.* (2008) the IS model for the APP_{30mm}, and the previously described setup for simulations in water. The comparison of the results shows that PDD_{water} was in average 0.4% (max 1.0%, $\sigma = 0.2\%$) higher than $PDD_{plastic}$ in the first centimeter. However, Watson *et al.* (2017) showed that the ratio of the absorbed dose in water and in the air cavity of the PTW 34013 chamber may not be depth independent for a beam of 50 kVp, which could make necessary the incorporation of correction factor up to 10% in the PDD determination. This dependence would be even more pronounced at shallow depths (Watson *et al.*, 2017), and

will be discussed in detail in Chapter 5.

Differences between simulated and measured PDDs may suggest a preference for less energetic photon beam, i.e. with the electron energy distribution shifted to the lower energies. Nevertheless, this option would move the values of $\overline{E}(r_0)$ and HVL away from the experimental results. In our opinion the mono-energetic source of 69.5 keV is the best option to reproduce the dosimetric characteristic of the Esteya system.

The most noticeable effect in the dosimetric outcomes was observed by varying the distribution of the electron beam over the focal spot area. Moving from the IS model to the GIS model increases the beam penumbra by 50%, which leads to a better agreement with the experimental data (see DP_{IS} and DP_{GIS} in Figure 4.6 and Table 4.5). However, the differences between DP_{GIS} and the reference dataset are not negligible (Garcia-Martinez *et al.*, 2014). Garcia-Martinez *et al.* (2014) measured the DP at 5 mm depth in plastic water, using the Gafchromic® EBT2 radiochromic film (Ashland Inc., Wayne, NJ). These differences could not be explained by the change in the energy spectrum (see Fig. 4.3) (Butson *et al.*, 2010), or by the angular dependence in the EBT2 (GafChromic, 2014). On the other hand, the uncertainties due to some common artifacts associated with the scan process of EBT2 films (e.g. Newton's rings and film curl) can reach 5% (Croce *et al.*, 2012; Kairn *et al.*, 2010; Lewis and Devic, 2015), and the errors in the system alignment can lead to non-negligible effects in the measurement results (Goubert and Parent, 2015), as it can be seen in

Chapter 5.

In our opinion, these differences agree within uncertainties with the values found in the literature. Fulkerson *et al.* (2014) simulated an Axxent eBT system with surface applicators (MCNP5 code) and found the differences up to 5% for the PDD, measured with an Exradin A20 ionization chamber. They also reported the differences in DP compared to EBT2 film dosimetry, associated with the alignment issues and inter-machine variations. Moradi *et al.* (2017) simulated an Intrabeam eBT system (MCNP5 code). The PDDs of two identical machines, measured with a PTW T34013 chamber in water, showed inter-machine variations within the first centimeter depth; over 20% for one of the machines and up to 5% for the other. Watson *et al.* (2017) simulated the PDD in water of an Intrabeam system (EGSnrc code), scoring the absorbed dose inside the air cavity of a PTW 34013 chamber, and found the differences up to 2.4% between the simulations and the measurements performed with the same ionization chamber. Croce *et al.* (2012) simulated (PENELOPE2006) a Papillon 50 system (Ariane Medical System, Nottinghamshire, UK), reporting a good agreement within the reported uncertainties with the PDDs (PTW T23342 chamber) and DPs (EBT2 film) measured in PMMA. Nevertheless, PDD differences at the phantom surface have not been reported.

Garcia-Martinez *et al.* (2014) found a systematic asymmetry of 1.5% that they associated to a heel effect produced by the cathode. We also found a similar asymmetry, determining however, that the cathode is away from the path of most of the photons reaching the

target. We concluded that the major reason of the asymmetry is due to the change of the differential bremsstrahlung cross-sections at different polar angles in the beam, which reach 10° at $r = 12$ mm for the APP_{30mm}. We found a similar difference in the radiative yield (1.5%) when the impingement angle of the electrons was modified by approximately the same range. Differences observed in Fig. 4.7 are within the uncertainties associated with the DP simulation (see Table 4.6). Furthermore, the DP_{GIS} in the y axis (Cartesian tally) does not show any asymmetry and is well reproduced by the cylindrical tally. For all these reasons, we consider that the cylindrical tally is a good and fast approximation to describe the Esteya beam, allowing the accurate determination of the beam characteristics (e.g., penumbra).

4.5 Chapter conclusions

We have obtained the phase-space of the Esteya system for the 10 mm and 30 mm applicators and used it to score the relevant dosimetric data in water. This was performed using an EFEN strategy that allowed us to reduce 90% of the computation time, compared to a simulation without the use of VRTs, with minimal impact on the simulated results. The comparison with experimental results showed good agreement with the findings published by other authors using similar equipment, within the reported uncertainties. In our Monte Carlo calculations we used four different options to model the electron beam of the Esteya source. We found that a

mono-energetic source combined with a Gaussian electron distribution over the focal spot was the most suitable choice to reproduce the experimental data. Further research is needed to study inter-machine variations and response of the most common ionization chambers used in clinical practice for this eBT beam.

Chapter 5

Depth-dose measurement corrections for the surface electronic brachytherapy beams of an Esteya unit: a Monte Carlo study

Most of the content of this chapter was published in the original research paper:

Valdes-Cortez, C., Ballester, F., Vijande, J., Gimenez, V., Gimenez-Alventosa, V., Perez-Calatayud, J., Niatsetski, Y., & Andreo, P.

(2020) Depth-dose measurement corrections for the surface electronic brachytherapy beams of an Esteya® unit: a Monte Carlo study. Physics in Medicine & Biology, (accepted).

Kind permission was granted by the journal to reprint this article as a chapter of this dissertation.

5.1 Introduction

The recommended dosimeter for low-energy kV x-rays is a special type of parallel-plate ionization chamber (Andreo *et al.*, 2000; Ma *et al.*, 2001), optimized either for in-air measurements or at the surface of a dedicated phantom. In the latter case, the chamber response needs to be corrected for the perturbations introduced by the insertion of the chamber in the phantom medium. It is usually assumed that perturbation correction factors are nearly depth-independent, which keeps the procedure simple in relative measurements (e.g., percentage depth-dose). However, some authors have suggested that this assumption could be unjustified, evidencing the introduction of errors up to 10% from 3 mm to 30 mm depth (Gimenez-Alventosa *et al.*, 2018; Watson *et al.*, 2017).

The election of a proper effective point of measurement (EPoM) of the chamber can minimize the effect of depth on the correction factors (see Kawrakow (2006) for MV photons). In this context, studies performed in a widely used parallel-plate ionization cham-

ber type, the PTW T34013 (PTW, Freiburg, Germany), using unfiltered 50 kV x-rays (Watson *et al.*, 2017) and ^{192}Ir gamma-rays (Gimenez-Alventosa *et al.*, 2018), showed that a modification of the EPoM, recommended by the chamber manufacturer, could describe the response of the chamber with depth.

At the time of writing, the PTW T34013 parallel-plate ionization chamber type (see Figure 5.1) is one of the few chambers designed for calibration measurements of low-energy x-ray beams in a plastic phantom. Therefore both Elekta and the AAPM TG-253 report recommend its use to perform depth-dose measurements of the Esteya unit (Fulkerson *et al.*, 2020; Candela-Juan *et al.*, 2015a). As was discussed in chapters 3 and 4, the nominal beam energy of the Esteya unit is 69.5 keV. This energy is between the 50 kV and an ^{192}Ir spectra, beams where the PTW T34013 chamber has been studied using MC methods (Watson *et al.*, 2017; Gimenez-Alventosa *et al.*, 2018; Fulkerson *et al.*, 2014).

This chapter aims at evaluating the dependence of the PTW T34013 chamber response on depth and applicator size, addressing their effect on the absorbed dose determination in an Esteya unit beam, and exploring strategies to minimize the effect of depth on the chamber response. The possible influence of chamber-to-chamber differences has also been explored.

Figure 5.1: PTW T34013 parallel-plate ionization chamber.

5.2 Material and method

5.2.1 Parallel-plate ionization chamber

The parallel-plate ionization chamber type studied in this work is the "soft x-ray" PTW T34013. The specifications and blueprints of the chamber have been provided by the manufacturer.

The chamber (see Figure 5.2) has a nominal sensitive volume of 0.005 cm^3 (1.45 mm radius and 0.9 mm height), surrounded by a guard ring at the same potential as the electrode. Reported manufacturing tolerances refer solely to the outer part of the chamber, i.e. distances between two external support structures and the external face of the entrance window. The chamber is not waterproof, being designed for use embedded in a solid phantom. This detector is calibrated by PTW (traceable to the Physikalisch-Technische

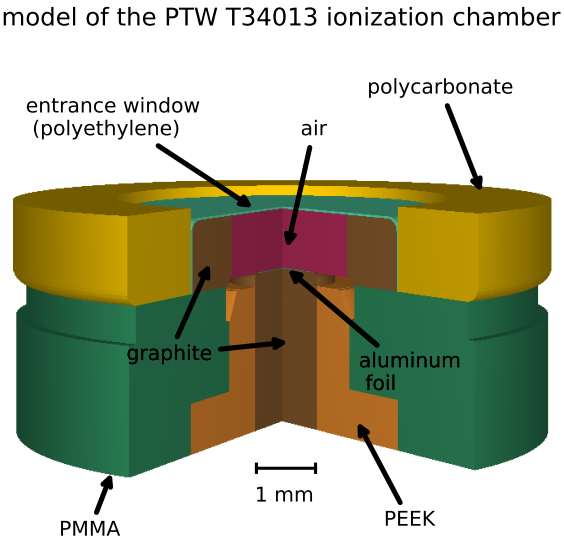

Figure 5.2: Geometry of the parallel-plate chamber used in PEN18.

Bundesanstalt laboratory) in a TW30 beam in a "plastic water" phantom (PW LR: CIRS, Norfolk, VA, USA). According to the manufacturer, the chamber EPoM is situated at the center of the inner surface of the entrance window ($EPoM_{man}$, top of the sensitive volume). The IAEA TRS-398 Code of Practice (Andreo *et al.*, 2000), however, specifies the reference point to be at the outside surface of the front window. It should be noted that there is a small air gap of about 0.15 mm between the entrance window of the chamber and the plastic cap of the applicator, being in contact with the top of the chamber body (see the step from the top surface of the polycarbonate outer ring and the entrance window in

figures 5.2 and 5.3). This air gap has been incorporated into our MC study to fully reproduce the experimental conditions. When the $EPoM_{man}$ is located at the phantom surface, a part of the chamber comes out of the phantom, preventing the contact between the applicator of the eBT with the phantom surface.

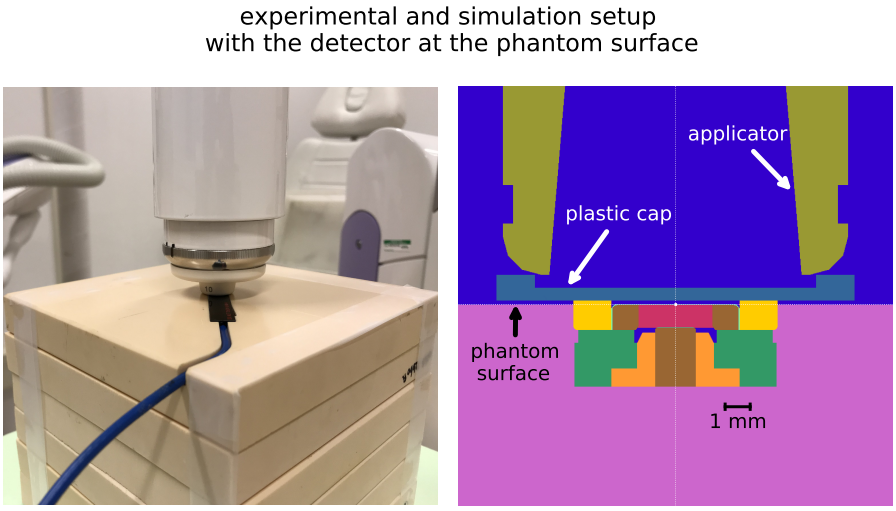

Figure 5.3: Experimental setup using the 10 mm applicator (left) and schematic geometry reproducing the experimental setup for the MC simulation (right). Dark blue and red zones (sensitive volume of the chamber) are filled with air.

5.2.2 Monte Carlo study

A full MC study of the Esteya unit has been performed in Chapter 4. There, the photon energy spectrum produced by bremsstrahlung

emission in the tungsten target and exiting the beryllium window of an Esteya unit was scored (see figure 3.1). To improve the calculation efficiency, in the present simulations this photon energy spectrum was used as a point-like source placed at the center of the lower surface of the tungsten target with a polar and azimuthal aperture of 18° (enough to fully cover the primary collimator) and 360°, respectively. Hence, the simulation ensemble includes the phantom, the chamber (when needed), and the full geometry of the Esteya eBT system.

Water has been recommended by the IAEA Code of Practice TRS-398 (Andreo *et al.*, 2000) and AAPM TG-253 (Fulkerson *et al.*, 2020) as the reference medium for the determination of the absorbed dose in kV photon beams. Therefore, in the present simulations the phantom considered was of liquid water with the composition recommended by ICRU Report 37 (Berger *et al.*, 1984) and the updated mean excitation energies and mass density given by ICRU Report 90 (Seltzer *et al.*, 2014).

The study of the chamber response with depth requires determining the perturbation correction factors at several depths along the beam axis in the water phantom. To accomplish that purpose, it is necessary to calculate the absorbed dose in water (D_w), the absorbed dose in the sensitive volume of the chamber (D_{cav}), and the ratios of the mean mass-energy absorption coefficients water to air $(\overline{\mu_{en}/\rho})_{w,air}$ at all the depths considered. Both D_w and D_{cav} have been scored directly by evaluating the energy imparted within the corresponding volume of interest, whereas the μ_{en}-ratios were

determined from the MC-calculated photon spectra (see below).

A desirable dosimetry condition is to perform measurements in regions with charge particle equilibrium (CPE) (Ma *et al.*, 2001). That condition should imply depths larger than the expected range of the secondary electrons in the water phantom (the continuous slowing down approximation range in water for electrons of 70 keV is 0.08 mm). Standard treatment conditions for the Esteya eBT system require the use of a polyfenilsulfone plastic cap (see figure 5.3) with a typical thickness of about 0.5 mm, which is intended to be in contact with the treatment surface. Hence, complete CPE is achieved at all depths.

All the results were obtained through parallelized MC simulations. The processes were kept uncorrelated through proper management of the initial seeds (Badal and Sempau, 2006). When electron transport was required (see below), it was simulated in detailed mode (PENELOPE transport parameters $C1 = C2 = 0$), i.e., without resorting to the mixed (Class II) algorithm option incorporated in PENELOPE. The VRTs used were VRPS and VRIF, with adequate use of the particle weight to maintain the simulation unbiased (see Section 2.2.3 and Salvat (2019)).

The selected energy cutoff for photons was 8 keV in all materials of the eBT device, and 1 keV in all structures embedded in the water phantom (i.e., ionization chamber and scoring volumes). The 8 keV threshold was selected because the amount of photons with energy lower than this value leaving the applicator (see figure 5.4) is negligible (Valdes-Cortez *et al.*, 2019). Due to the short range

of secondary electrons in water, electron transport can be ignored, and its energy assumed to be deposited on the spot, i.e., an infinite energy cutoff for electrons was considered for D_w. With respect to D_{cav}, the energy cutoff of 1 keV for electrons was chosen in all chamber materials and in a water envelope region of 0.1 mm thick around the chamber. When the chamber is in contact with the plastic cap (first depth voxel), the same electron cutoff was considered both in the plastic cap and in the air gap.

Table 5.1 summarizes the details concerning the MC simulations in this work following the recommendation of AAPM TG-268 (Sechopoulos *et al.*, 2018). Further information regarding the PENELOPE transport parameters and variance reduction tools can be found in chapters 2 and 4, and in Salvat (2019) and Sempau and Andreo (2006).

5.2.2.1 Absorbed depth-dose and mass-energy absorption coefficient

The absorbed dose in water, D_w, was scored between the water phantom surface (0 mm depth) and 20 mm depth, in cylinders of 1 mm radius and 0.1 mm height assuming CPE conditions. The absorbed dose in the sensitive volume of the chamber, D_{cav}, was scored with the chamber $\mathrm{EPoM_{man}}$ positioned at the same depth as the upper boundary of the corresponding D_w bin. The ratio of the mean mass-energy absorption coefficients water to air, $(\overline{\mu_{en}/\rho})_{w,air}$, averaged over the energy-fluence spectrum at each depth was cal-

Table 5.1: Summary of the main characteristics of the Monte Carlo simulations used in this work.

Item	Description	References
Code	1) PEN18 2) penEasy (v. 2019-09-21) Intel® Fortran compiler 18.0.3	1) Salvat (2019) 2) Sempau *et al.* (2011)
Validation	Previously validated	Ye *et al.* (2004), Croce *et al.* (2012), Valdes-Cortez *et al.* (2019), Chica *et al.* (2009)
Timing	Average values for APP_{10mm} (sum of parallel processes, Intel (R) Xeon(R) Gold 6154 CPU @3.00 GHz): - D_{cav} obtained in 28647 CPU hours and 7×10^{11} histories. - D_w obtained in 629 CPU hours and 10^{10} histories. - $(\overline{\mu_{en}/\rho})_{w,air}$ obtained in 1330 CPU hours and 5×10^{10} histories.	Parallel processes as of Badal and Sempau (2006)
Source description	Photon point collimated source. Spectrum from detailed modelling of the Esteya x-ray tube (GIS model, see reference)	Valdes-Cortez *et al.* (2019)
Cross-sections	1) Photoelectric from PHOTACS; 2) Rayleigh scattering using non-relativistic perturbation theory; 3) Compton from relativistic impulse approximation; 4) Atomic relaxation with EADL transition probabilities.	1) Sabbatucci *et al.* (2016); 2) Sakurai (1967), Born (1969), Baym (1974), Cullen *et al.* (1997); 3) Ribberfors (1983); 4) Perkins *et al.* (1991), Deslattes *et al.* (2003), Bearden (1967).
Transport parameters	Photon cut-off = 8 keV in all materials in eBT device, 1 keV elsewhere; Electron cut-off = 1 keV in all materials surrounding sensitive chamber volume and water envelope (PENELOPE parameters C1 = C2 = 0); Electron transport disabled elsewhere.	Valdes-Cortez *et al.* (2019), Sempau and Andreo (2006), Salvat (2019).
VRTs	1) Interaction forcing: D_w scoring bins and sensitive chamber volume; 2) Splitting particles (penEasy rotational option at the flattening filter).	1) Salvat (2019); 2) Sempau *et al.* (2011).
Scored quantities	Absorbed dose in water and chamber cavity; photon fluence.	
Statistical uncert.	$\leq 0.1\%$ ($k = 2$)	

culated as (Ma *et al.*, 2001):

$$\left(\overline{\frac{\mu_{\text{en}}}{\rho}}(z)\right)_{\text{w,air}} = \frac{\int_0^{E_{\max}} E\,\Phi_{E,\text{w}}\left[\left(\frac{\mu_{\text{en}}(E)}{\rho}\right)_{\text{w}}\right]\,dE}{\int_0^{E_{\max}} E\,\Phi_{E,\text{w}}\left[\left(\frac{\mu_{\text{en}}(E)}{\rho}\right)_{\text{air}}\right]\,dE}, \tag{5.1}$$

where $\Phi_{E,\text{w}}$ is the photon fluence differential in energy in water at a given depth z, and $[(\mu_{\text{en}}(E)/\rho)_{\text{w}}]$ and $[(\mu_{\text{en}}(E)/\rho)_{\text{air}}]$ are the mass energy-absorption coefficients for water and air, respectively. The photon fluence corresponds to spectra with a bin width of 0.1 keV scored in a cylinder of 1 mm height and 1 mm radius, with its upper surface positioned at the same depth in water as the EPoM_{man}. All the above-mentioned factors were consistently evaluated with PEN18.

5.2.2.2 Determination of the EPoM and correction factors

The absorbed dose to water at depth z, $D_{\text{w}}(z)$, can be calculated from the mean absorbed dose in the sensitive volume assigned to a point at depth z', $D_{\text{cav}}(z')$, through the ratio

$$\frac{D_{\text{w}}(z)}{D_{\text{cav}}(z')} = \left[\left(\overline{\frac{\mu_{\text{en}}}{\rho}}(z')\right)_{\text{w,air}}\right]\,p, \tag{5.2}$$

where $(\overline{\mu_{en}/\rho})_{w,air}$ is calculated in a volume centered at depth z', and p is an overall factor to correct for the perturbations created

by the presence of the chamber in the water phantom.

To determine the dependence of the chamber response on depth and evaluate p, three scenarios have been analyzed following the methodology proposed by Gimenez-Alventosa *et al.* (2018):

1. A surface correction factor ($p = p_{\text{surf}}$) obtained through equation 5.2 at the water phantom surface using the EPoM_{man} provided by the manufacturer, i.e., the chamber is located with the EPoM_{man} positioned at the phantom surface:

$$p_{\text{surf}} = \frac{D_{\text{w}}(z=0)}{D_{\text{cav}}(z'=0)\left[\left(\overline{\frac{\mu_{\text{en}}}{\rho}}(z'=0)\right)_{\text{w,air}}\right]}. \tag{5.3}$$

   This approach will indicate that a single measurement performed at the water phantom surface would suffice to correlate satisfactorily D_{cav} and D_w for all depths. Such procedure will resemble the methodology normally applied in kV beams.

2. A global correction factor ($p = p_{\text{glob}}$), calculated using the EPoM_{man}. Such method will require measuring and/or simulating the chamber response at all depths. To do so one evaluates the ratio:

$$f_i = \frac{D_{\text{w}}(z_i)}{D_{\text{cav}}(z_i)\left[\left(\overline{\frac{\mu_{\text{en}}}{\rho}}(z_i)\right)_{\text{w,air}}\right]} \tag{5.4}$$

   for all depths z_i. The correction factor p_{glob} is then obtained by minimizing the differences between D_w and D_{cav} using a

1D chi-square distribution

$$\chi^2\left(p_{\mathrm{glob}}\right) = \sum_{i=1}^{N} \frac{\left(f_i - p_{\mathrm{glob}}\right)^2}{\Delta f_i{}^2}, \tag{5.5}$$

where N is the number of the chamber positions, and Δf_i is the Type A uncertainty of the ratio f_i given in equation 5.4.

3. A shift correction factor ($p = p_{\mathrm{shift}}$) including a modification on the EPoM. We have used the approach proposed by Kawrakow (2006) to find the EPoM that minimizes the effect of depth in the correction factors. This consists on a refinement of case (ii) considering the EPoM as a free parameter to be specified within the ionization chamber sensitive volume.

   Starting from a depth $z = \mathrm{EPoM}_{\mathrm{man}}$, we found the Δz value for which the ratio

$$f_i = \frac{D_{\mathrm{w}}(z_i + \Delta z)}{D_{\mathrm{cav}}(z_i)\left[\left(\overline{\frac{\mu_{\mathrm{en}}}{\rho}}(z_i)\right)_{\mathrm{w,air}}\right]}, \tag{5.6}$$

   is as independent of depth as possible. Hence, Δz will provide an improved EPoM value. To accomplish that condition, it is necessary to minimize a 2D chi-square distribution

$$\chi^2\left(p_{\mathrm{shift}}, \Delta z\right) = \sum_{i=1}^{N} \frac{\left(f_i - p_{\mathrm{shift}}\right)^2}{\Delta f_i{}^2}, \tag{5.7}$$

   where N is the number of chamber positions, and Δf_i is

the Type A uncertainty of the ratio f_i given in equation 5.6. Further details of the minimization process can be found in e.g. Kawrakow (2006) and Gimenez-Alventosa *et al.* (2018).

5.2.3 Absorbed dose measurements

As mentioned earlier, the vendor does not report manufacturing tolerances in the chamber sensitive volume. The possible role played by such tolerances on the absorbed-dose determination has been evaluated by performing a set of depth-dose measurements, using three different PTW T34013 chambers (SN 000810, 000311, and 000146). These measurements were performed by a single person, using a single eBT Esteya unit and a Plastic Water Low Range (PW LR: CIRS, Norfolk, VA, USA) phantom. For the Esteya unit, the water equivalence of plastic phantoms was studied by Garcia-Martinez *et al.* (2014) and Candela-Juan *et al.* (2015b), reporting differences between the absorbed dose to a water voxel located at the surface of a water-equivalent plastic phantom and the absorbed dose to a water voxel located at the surface of a water phantom to be less than 0.2%, which agrees with the findings reported in Section 4.4.2.

Plastic Water LR phantom consists out of slabs with different thickness from 1 mm up to 20 mm. One 20 mm slab has a groove for inserting the T34013 chamber and its cable (see figure 5.3, left), so that the top surfaces of the chamber and the slab are aligned. Five 20 mm slabs were placed under the cham-

ber to provide full backscatter conditions. Two kinds of measurements were carried out: reference absorbed dose (D_{ref}) at 3 mm depth (typical reference depth used in clinical practice) to establish the output and relative depth-dose curves (PDD), normalized at 3 mm depth Ouhib *et al.* (2015); Guinot *et al.* (2018). D_{ref} was calculated according to the TRS-398 Code of Practice, using the method described in Candela-Juan *et al.* (2015b) and EPoM_{man}. All measurements were done for the two applicator diameters, $\text{APP}_{10\text{mm}}$ and $\text{APP}_{30\text{mm}}$, used throughout this work. The differences between the three chambers were evaluated through $\{[\text{PDD}(z)_a \times D_{\text{ref},a}] / [\text{PDD}(z)_b \times D_{\text{ref},b}] - 1\} \times 100$, where the subscripts a and b denote different chambers.

5.2.4 Estimation of uncertainties

The uncertainties of MC-derived quantities were evaluated according to the GUM recommendations BIPM (2010), assuming normal distributions. Uncertainties are expressed with a coverage factor $k = 2$ as recommended by the AAPM TG-138 DeWerd *et al.* (2011). Type A uncertainties were smaller than 0.1% for D_w, D_{cav}, $(\mu_{\text{en}}/\rho)_{\text{w}}$, and $(\mu_{\text{en}}/\rho)_{\text{air}}$. Type B and combined uncertainties were estimated as follows:

1. For $(\overline{\mu_{en}/\rho})_{w,air}$, Andreo *et al.* (2012) reported a combined uncertainty of 0.2% (group II for an x-ray beam with an average energy of 34.1 keV).

2. Ratio $D_{\mathrm{w}}/D_{\mathrm{cav}}$: Photoelectric cross-section uncertainties (predominant interaction for photons of 30 keV, considering all materials along their path) have been estimated between 2% and 3% for photons below 100 keV, mostly due to the implementation of the Pratt's Renormalization Screening Correction (PRSC) in the different MC codes Seltzer *et al.* (2014). $D_{\mathrm{w}}/D_{\mathrm{cav}}$ was evaluated at selected depths (0 mm, 3 mm, and 10 mm) with and without PRSC to estimate the Type B uncertainty associated, obtaining a value of about 0.2%.

3. The impact on the uncertainty estimation arising from the simplified source model describing the Esteya unit (see Section 5.2.2) was estimated by performing additional MC simulations at selected depths using the complete description given in Valdes-Cortez *et al.* (2019). Differences between the two source types were less than 0.02% for $(\overline{\mu_{en}/\rho})_{w,air}$ and less than 0.2% for $D_{\mathrm{w}}/D_{\mathrm{cav}}$ at all depths.

4. p_{surf}, p_{glob} and p_{shift}: Their combined Type B uncertainties were obtained by adding in quadrature the uncertainty values estimated in (i), (ii), and (iii).

5.3 Results and discussion

5.3.1 Mass-energy absorption coefficients

Figure 5.4 shows the fluence spectra of the $\mathrm{APP}_{10\mathrm{mm}}$ and $\mathrm{APP}_{30\mathrm{mm}}$ applicators at different depths. The maximum variation of $(\overline{\mu_{en}/\rho})_{w,air}$ from 0 to 20 mm depth was 0.06%. In addition, the largest difference between the $\mathrm{APP}_{10\mathrm{mm}}$ and $\mathrm{APP}_{30\mathrm{mm}}$ cases, for the entire range of depths, was 0.04%. Hence, $(\overline{\mu_{en}/\rho})_{w,air}$ was considered in the following a depth- and applicator-independent quantity, with a value of 1.018 and an uncertainty of 0.2% (see table 5.2). These values are in good agreement with the data and uncertainty estimates published by Ma *et al.* (2001); Andreo (2019), and with those found in Chapter 6.

5.3.2 Determination of the correction factors and the EPoM

Figure 5.5 shows the ratio $D_{\mathrm{w}}/D_{\mathrm{cav}}$ for both applicators, $\mathrm{APP}_{10\mathrm{mm}}$ and $\mathrm{APP}_{30\mathrm{mm}}$. These ratios were obtained with a Type A uncertainty of 0.1%. Type B uncertainties were evaluated incorporating the sources of uncertainty listed in Section 5.2.4 (ii) and (iii), leading to a combined uncertainty of about 0.3% (see table 5.2).

For $\mathrm{APP}_{10\mathrm{mm}}$, a variation in $D_{\mathrm{w}}/D_{\mathrm{cav}}$ of about 1% can be observed between the water phantom surface and at a depth of

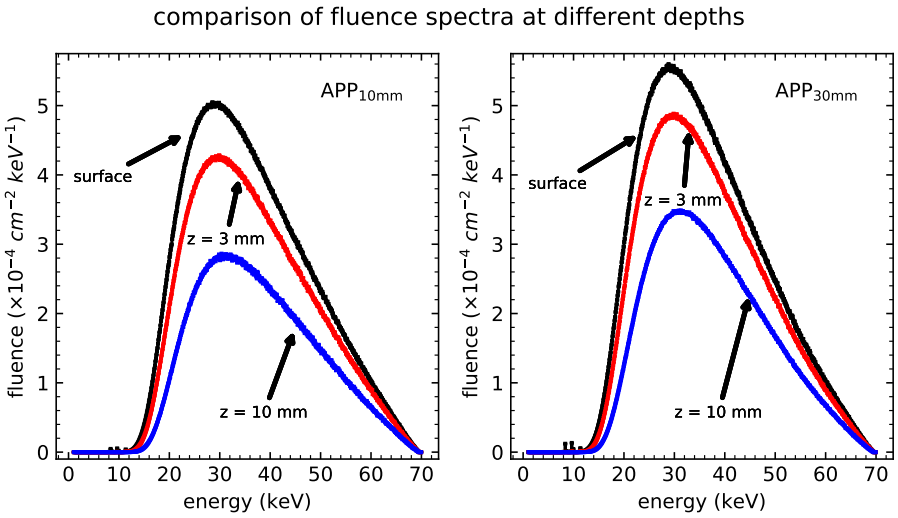

Figure 5.4: Fluence spectra for the 10 mm and 30 mm applicators, scored at different depths (z). The spectra were obtained with an energy resolution of 0.1 keV, tallied in cylindrical volumes of 1 mm radius and 1 mm height. The values are normalized to the number of primary particles.

10 mm, from 1.376 to 1.390. The corrections factors p_{surf} and p_{glob} obtained were 1.351 and 1.359, respectively.

With respect to the third proposed method, p_{shift}(EPoM), equation 5.7 reaches a minimum at $\Delta z = 0.4$ mm (see figure 5.6), with a value of $p_{\text{shift}} = 1.324$. Figure 5.7 shows the differences between D_w and the absorbed dose to water calculated using the three proposed methods, $p_{\text{shift}}(\text{EPoM}_{\text{man}})$, $p_{\text{glob}}(\text{EPoM}_{\text{man}})$, and p_{shift}(EPoM). It can be seen that the $p_{\text{glob}}(\text{EPoM}_{\text{man}})$ method reduces the differences to within [-0.4%, +0.6%], while p_{shift}(EPoM) (with an EPoM

at $\Delta z = 0.4$ mm) reduces the differences to within $\pm 0.4\%$ from 0 mm to 15 mm depth.

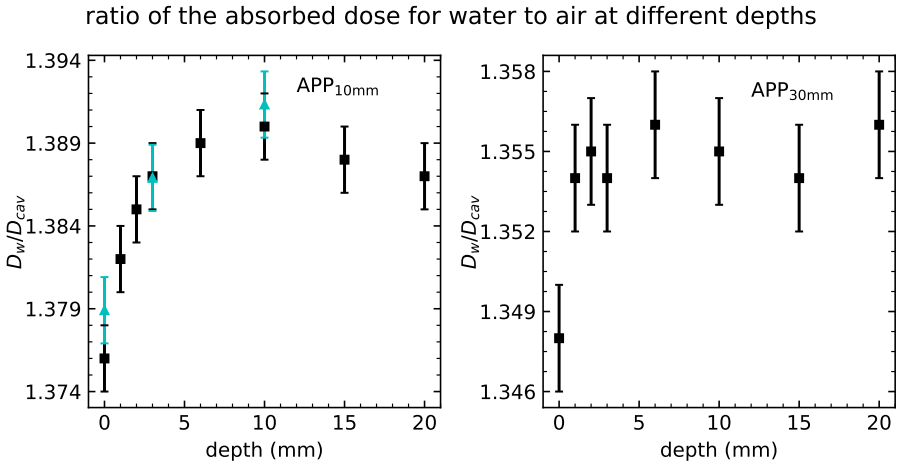

Figure 5.5: Ratios of absorbed doses ($D_{\mathrm{w}}/D_{\mathrm{cav}}$) (black squares) as a function of depth, calculated for applicators of 10 mm and 30 mm diameter. Cyan triangles (left image) represent $D_{\mathrm{w}}/D_{\mathrm{cav}}$ simulated without the Pratt's screening renormalization correction at 0 mm, 3 mm, and 10 mm depth. Only Type A uncertainties are shown.

In the case of the $\mathrm{APP}_{30\mathrm{mm}}$ applicator, the maximum variation of $D_{\mathrm{w}}/D_{\mathrm{cav}}$ was 0.6% at 6 mm depth, from 1.348 to 1.356. The values of p_{surf} and p_{glob} were 1.324 and 1.330, respectively.

With respect to p_{shift}(EPoM), the optimum EPoM value was also found at $\Delta z = 0.4$ mm below $\mathrm{EPoM}_{\mathrm{man}}$ (see figure 5.6 and table 5.3), with p_{shift} equal to 1.300. The use of p_{glob} ($\mathrm{EPoM}_{\mathrm{man}}$) reduces the differences between D_{cav} and D_w to within 0.5%, while p_{shift} (EPoM) (EPoM at $\Delta z = 0.4$ mm) reduces the differences to

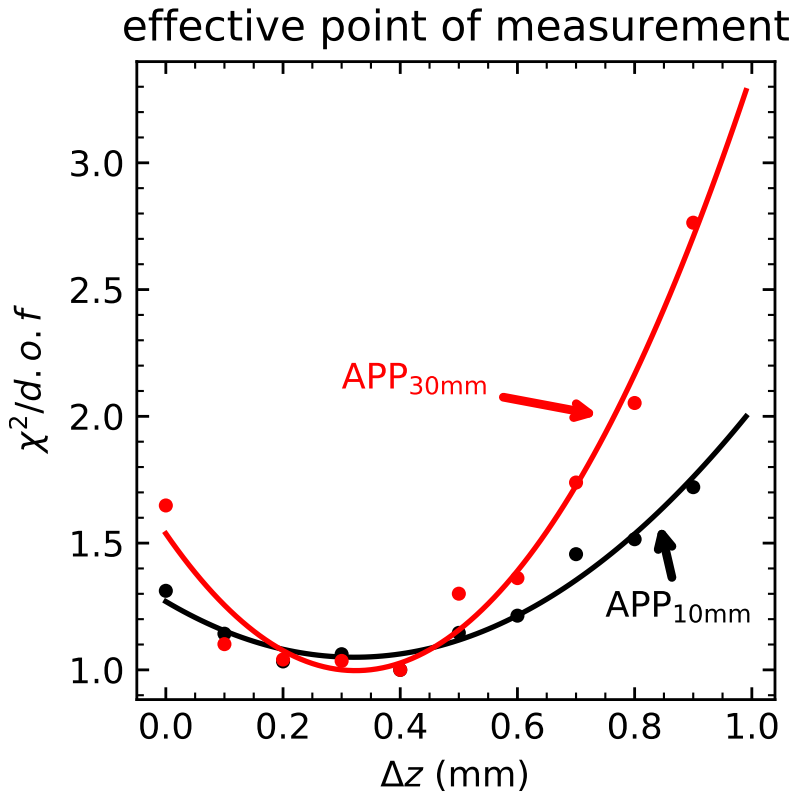

Figure 5.6: Values of χ^2 per degree of freedom (normalized to the minimum value of each applicator) vs EPoM shift, calculated for the 10 mm (APP_{10mm}) and 30 mm (APP_{30mm}) diameter applicators. The dots correspond to the values obtained with equation 5.7. The solid lines correspond to a second-degree polynomial fit. CPE is assumed at the water phantom surface. Δz runs toward the bottom of the sensitive volume of the chamber.

within 0.3%.

For both applicators, p_{surf} (EPoM_{man}), p_{glob} (EPoM_{man}), and

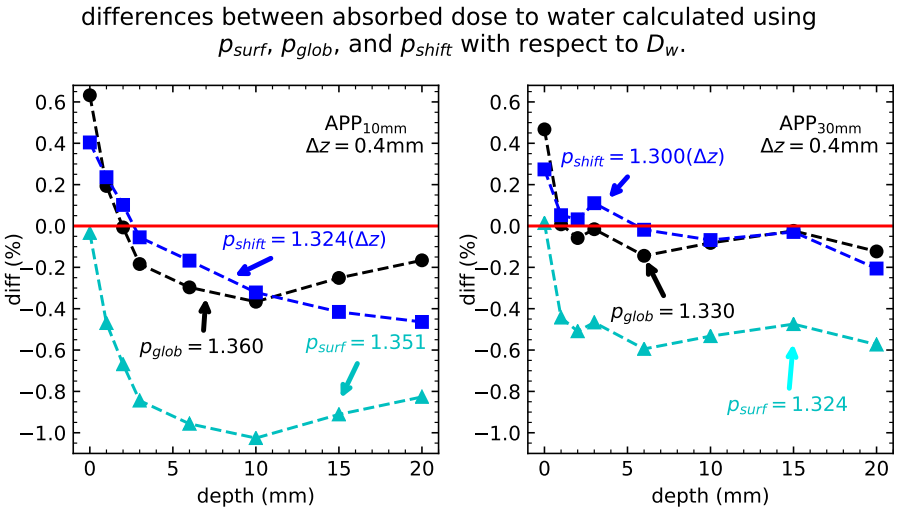

Figure 5.7: Differences between absorbed dose to water calculated using p_{glob} (black circles), p_{shift} (blue squares), and p_{surf} (cyan triangles) with respect to D_w (red line). Uncertainty bars have been removed for clarity.

p_{shift}(EPoM) were obtained with a combined uncertainty smaller than 0.4%. Table 5.2 shows the uncertainties estimated in the calculation of the various correction factors. Differences of about 2% were observed between the corresponding correction factors depending on the applicator considered, 10 mm or 30 mm in diameter. Hence, a conservative approach leads us to assume the same value for other applicators with diameters in-between 10 and 30 mm.

A summary of the correction factors and their estimated uncertainties is given in table 5.3.

Watson *et al.* (2017) explored the response of the T34013 cham-

Table 5.2: Estimated relative uncertainties ($k = 2$) for the correction factors and the quantities used in their calculation.

	Component	Uncertainty (%)	
		Type A	Type B
$(\overline{\mu_{\text{en}}/\rho})_{\text{w,air}}$	Grouping II (50 kV) in Andreo *et al.* (2012)[a]		0.2
	Effect of point vs full x-ray source		0.02
	MC statistics	0.1	
	u_{c}	0.2	
$D_{\text{w}}/D_{\text{cav}}$	Effect of photoelectric cross-section		0.2
	Effect of point vs full x-ray source		0.2
	MC statistics	0.1	
	u_{c}	0.3	
Correction factors	u_{c}	0.4	

[a]Effect of the photoelectric cross-section uncertainties is also considered.

ber with an unfiltered beam of 50 kV at the same depth intervals as in this work. They reported a modification with depth of about 2.5% in the value of $(\overline{\mu_{en}/\rho})_{w,air}$. When using EPoM_{man} and the nominal geometry provided by the chamber manufacturer, the ratio $D_{\text{w}}/D_{\text{cav}}$ was estimated to be 1.33 (approximated value) at 3 mm depth (first point of the published series), decreasing nearly by 5% at 15 mm depth. On the other hand, when the authors consider possible manufacturing tolerances in the height of the sensitive volume (using EPoM_{man}), they found differences in the ratio $D_{\text{w}}/D_{\text{cav}}$ with depth of about 12%. The authors conclude that changing the EPoM from the manufacturer's recommendation to the midpoint

Table 5.3: Summary of the values for the three correction factors proposed along with their combined estimated uncertainties ($k = 2$). The fifth column shows the differences [minimum, maximum] between the absorbed dose obtained from equation 5.2, using D_{cav} and the perturbation correction factors of the third column, and the simulated D_w. The *Uncorrected* row corresponds to the differences between D_{cav} and D_w before applying any of the proposed methods.

Applicator	Method	Perturbation correction factors (p)	Δz (mm)	Differences (%)
APP_{10mm}	*Uncorrected*	1	–	[-28.0, -27.3]
	p_{surf}	1.351 ± 0.005	–	[-1.0, 0.0]
	p_{glob}	1.360 ± 0.005	–	[-0.4, +0.6]
	p_{shift}	1.324 ± 0.005	0.4	[-0.5, +0.4]
APP_{30mm}	*Uncorrected*	1	–	[-26.3, -25.8]
	p_{surf}	1.324 ± 0.005	–	[-0.6, 0.0]
	p_{glob}	1.330 ± 0.005	–	[-0.1, +0.5]
	p_{shift}	1.300 ± 0.005	0.4	[-0.2, +0.3]

of the sensitive volume may reduce these variations in the chamber response. However, that change would increase the depth dependence of the correction factors of the chamber, from 5% to 15% at 15 mm depth.

Gimenez-Alventosa *et al.* (2018) simulated the response of the T34013 chamber for the case of the Valencia and Large Field Valencia applicators. Both surface applicators use a brachytherapy ^{192}Ir source. The authors found spectral variations due to differences in the design of the applicators (i.e., presence of a flattening filter in one of the applicators, different diameters, etc.). In that work, each applicator showed a constant $(\overline{\mu_{en}/\rho})_{w,air}$ value (within the statis-

tical uncertainties) for all depths investigated, with a variation of 0.4% in the value calculated between applicators, and 3% in p_{glob} (method I in that work). Furthermore, they found different Δz values for each model of applicator. The filtered beam produces a value $\Delta z = 0.57$ mm, while for the unfiltered beam the optimum Δz was found at $\mathrm{EPoM}_{\mathrm{man}}$ (i.e., $\Delta z = 0$).

5.3.3 Measurement results

The average absorbed dose rates at the clinical reference depth (3 mm) were 2.31 Gy min^{-1} and 2.64 Gy min^{-1} for the $\mathrm{APP}_{10\mathrm{mm}}$ and $\mathrm{APP}_{30\mathrm{mm}}$, respectively. The absorbed dose rates differences observed between the three chambers were within 1.5% for both applicators. Furthermore, for depth-dose measurements the differences in the relative measurements (up to 20 mm depth) were smaller than 2%, with an average difference within 1% for both applicators. Therefore, depth-dose measurements uncertainties associated with chamber-to-chamber differences can be estimated to be at most of 2%, a value that also includes the uncertainties related with the experimental setup (e.g., alignment and positioning, among others).

In Chapter 4, differences of 2% and 4.5% between the simulated and the measured PDDs were found for $\mathrm{APP}_{10\mathrm{mm}}$ and $\mathrm{APP}_{30\mathrm{mm}}$, respectively. Those disagreements decrease by nearly 1% when a correction of the depth dependence, showed in Figure 5.5, is applied to the measured PDDs (see Table 4.4). In this context,

the experimental uncertainty of 2% found here corresponds to an important component of such disagreements.

Watson *et al.* (2017) evaluated differences due to manufacturing tolerances for an unfiltered 50 kV eBT by performing different MC simulations. They reported that the effect of manufacturing tolerances on the T34013 chamber may generate differences in the absorbed dose of about 5% at 20 mm depth. It can be concluded that the effect of the manufacturer tolerances on the chamber response for an Esteya unit seems to be lower than estimations made in the literature for eBT 50 kV beams.

5.3.4 Limitations of this study and future research lines

This study relies on state-of-the-art MC simulations for a particular eBT system and an ionization chamber. Therefore, the obtained results depend strongly on the precise description of both the Esteya unit and the PTW34013 ionization chamber provided by the manufacturers. Any subsequent major structural modification implemented by any of the vendors will require repeating this study to rule out any unforeseen change in the correction factors and the effective point of measurement. Hence, the results reported here cannot be directly extrapolated to any other eBT system and/or ionization chamber, for which separate machine- and chamber-specific studies, including a faithful description of the systems involved, will be required.

5.4 Chapter conclusions

The response of the parallel-plate ionization chamber PTW T34013, recommended by TG-253 for depth-dose measurements in the x-ray beam of 69.5 kVp generated by the Esteya eBT unit, has been evaluated. Three different correction factors have been explored to describe the dependence of the chamber response with respect to depth and applicator size. Of those possibilities, the use of a depth-dependent perturbation factor including a shift of the effective point of measurement, $p_{\text{shift}}(\text{EPoM})$, yields the best results. Using this approach, differences between the absorbed dose in water and the corrected absorbed dose in the sensitive volume of the chamber are smaller than $\pm 0.5\%$ and $\pm 0.3\%$ at all depths for the 10 mm and 30 mm applicator respectively. The optimal effective point of measurement was found to be shifted from the one established by the manufacturer by 0.4 mm, being closer to the center of the sensitive volume of the chamber. Uncertainties due to chamber-to-chamber differences have been explored by performing measurements using three different T34013 chambers. Differences were found to be below 2%. The depth dependence of the chamber response and the experimental uncertainties reported here correspond to an important component of the differences between the measured and the simulated PDDs exposed in Chapter 4. The magnitude of these effects is much lower than those reported for other eBT devices using unfiltered beams of 50 kVp. The present results emphasize the importance of carrying out detailed Monte

Carlo studies for each electronic brachytherapy device and ionization chamber used for its dosimetry.

Chapter 6

Calibration of the eBT beam

Most of the content of this chapter was published in the original research paper:

Valdes-Cortez, C., Niatsetski, Y., Ballester, F., Vijande, J., Candela-Juan, C. & Perez-Calatayud, J. (2019). On the use of the absorbed depth-dose measurements in the beam calibration of a surface electronic high-dose-rate brachytherapy unit, a Monte Carlo-based study. Medical Physics, 47(2), 693-702.

Kind permission was granted by the journal to reprint this article as a chapter of this dissertation.

6.1 Introduction

The evaluation and verification of the absorbed depth-dose and the corresponding beam calibration represent an essential part of the quality assurance program for an eBT system (Thomadsen *et al.*, 2009; Candela-Juan *et al.*, 2015a; Eaton, 2015). Currently, there exist two well-known calibration protocols for low-energy photons, the TRS-398 of the IAEA (Andreo *et al.*, 2000) and the TG-61 of the AAPM (Ma *et al.*, 2001), both based on the measurement of different quantities. While the IAEA bases its protocol in dose to water standards ($N_{D,w}$ calibration factor), the AAPM protocol does it in-air kerma measurements (through N_K calibration factor).

The community recognizes the benefits of a dose to water protocol in the reduction of the uncertainties (Andreo *et al.*, 2000; Almond *et al.*, 1999). However, at the time of writing the TRS-398, there was a lack of dose to water standards for low-energy x-ray beams. For that reason, the IAEA included the in-air method as an intermediate step to obtain $N_{D,w}$ from N_K. This condition remains to this day, which is why the forthcoming update of the TRS-398 will recommend the TG-61 protocol for calibrations of eBT beams (Andreo, 2019).

Unlike the calibration protocols for high-energy photon beams in EBRT, which use the measured depth-dose to obtain the beam quality index (BQI) (Andreo *et al.*, 2000; Almond *et al.*, 1999), the calibration protocols for low-energy x-ray beams make use of

the experimentally measured HVL. This measurement requires the availability of aluminum slabs of high-purity (99.9%) with a thickness accuracy better than 0.05 mm and the acquisition of x-ray images for the system alignment, a cumbersome and time-consuming procedure. Furthermore, signal-to-noise ratio issues can appear when the measurement is performed far from the source, at 100 cm (distance where HVL is defined), due to the inverse square law. As the eBT user needs to measure the depth-dose as a part of the quality assurance program, the use of such measurements is the next logical step in the determination of the beam quality index (Andreo *et al.*, 2000; Ma *et al.*, 2001).

Nevertheless, the measurement of depth-dose is not a straightforward procedure either. The high dose gradient with the depth of the low-energy photons beams makes the procedure highly sensible to misalignments in the experimental setup (Fulkerson *et al.*, 2014; Goubert and Parent, 2015). Furthermore, detectors can show non-negligible changes in their performance with depth (Watson *et al.*, 2017; Gimenez-Alventosa *et al.*, 2018); effect corroborated in Chapter 5 for the T34013 parallel-plate ionization chamber with the 70 kV beam of the Esteya system. Such conditions may increase the uncertainties in the calibration procedure by using a beam quality index based on depth-dose measurements. This chapter aims to evaluate the use of the absorbed depth-dose in a water phantom either, as a BQI to obtain all factors required to a in-air beam calibration, or as an intermediate step to determine the HVL, addressing the effect of the manufacturing tolerances of the eBT device

and the uncertainties over the whole process.

6.2 Material and method

6.2.1 Monte Carlo model of the Esteya system

The flattening filter (FF) is the most relevant structure in determining the beam properties (see Fig. 3.1). According to the eBT vendor, the manufacturing tolerance of the FF thickness is ± 0.035 mm. Regarding the x-ray source, in Chapter 4, we studied the configuration that best mimics the experimental measurements published so far. However, this chapter requires a different approach to investigate the effect of changes in the tube potential in the use of absorbed depth-dose in a beam calibration. This approach must allow us to cover the manufacturing tolerances in the voltage generation (69.5 kV ± 0.5%, according to the manufacturer) and test the ability of this method to obtain the calibration factors under broader changes of the beam characteristics. With that purpose, we have modified the Ee^- from the nominal value of 69.5 kV to 60 kV and 80 kV.

We considered four possible geometries to model the investigated eBT system. The ideal geometry (IG), corresponds to the model with the nominal dimensions specified by the manufacturer. The negative (NG) and the positive (PG) geometries are used to considering the negative and the positive range of the manu-

facturing tolerances. The flattening filter-free (FFF) geometry is conceived to obtain the spectrum used in the HVLs calculations, speeding up the simulations through removing the FF. For the IG, we use the "detailed setup" (Fig. 3.1) of the APP_{10mm} with the GIS model, fully described in Section 4.2.1. Briefly, the Esteya x-ray source model, GIS, consists in a mono-energetic electron beam of 69.5 keV, with a Gaussian electron distribution centered on the rectangular foil with an FWHM equal to the focal spot size (1.8 x 1.3 mm^2).

MC simulations with different FF thicknesses (x_{FF}) were performed. The x_{FF} symbol denotes the thickness measured at the center of the FF (thickest section) in the direction of the beam axis. The minimum (x_{FFmin}) and maximum (x_{FFmax}) values were chosen to divide or multiply by a factor 2 the HVL from its nominal value (x_{FF} corresponding to IG and 69.5 keV).

6.2.2 Calibration protocols

The in-air TG-61 method requires the determination of three quantities: the N_K, $(\overline{\mu_{en}/\rho})_{w,air}$ and the backscatter factor (B_w). Usually, the calibration certificate of any ionization chamber comes with two or more values of N_K for different beam qualities. Additionally, the user can obtain the $(\overline{\mu_{en}/\rho})_{w,air}$ and B_w factors directly from the TG-61. The proper factors for a particular beam are obtained through interpolation from the calibration certificate and the TG-61 tables.

The in-water IAEA method is based mainly on two factors: the absorbed $N_{D,w}$ and the beam quality correction factor (k_{Q,Q_0}), which are specified in terms of the HVL of a reference beam quality. The chamber calibration certificate comes with one $N_{D,w}$ and two or more k_{Q,Q_0}. The user needs to find the proper k_{Q,Q_0} for the beam to be calibrated through an interpolation.

In this chapter, we divide the dosimetric parameters used in both calibration protocols into machine-dependent (i.e., HVL, B_w, and $(\overline{\mu_{en}/\rho})_{w,air}$) and detector-dependent (i.e., N_K and k_{Q,Q_0}) parameters. We will evaluate the feasibility of obtaining all the machine-dependent parameters from the absorbed depth-dose data and the effect of this method on the final uncertainty of the calibration.

6.2.3 Machine-dependent parameters

6.2.3.1 HVL

The HVL is defined as the aluminum thickness x_{Al} (in mm) at which the air-kerma rate is reduced to one-half of its original value. It can be calculated analytically through

$$K_{ratio} = \frac{\sum (\Psi_{FFF})_i^{free-space} \left(\frac{\mu_{en}}{\rho}\right)_{i,air} exp(-\mu_{i,air}x_{air} - \mu_{i,FF}x_{FF} - \mu_{i,Al}x_{Al})}{\sum (\Psi_{FFF})_i^{free-space} \left(\frac{\mu_{en}}{\rho}\right)_{i,air} exp(-\mu_{i,air}x_{air} - \mu_{i,FF}x_{FF})}, \tag{6.1}$$

where $(\mu_{en}/\rho)_{air}$ is the mass energy-absorption coefficient for air in each energy bin i; μ_{air}, μ_{FF}, and μ_{Al} are the linear attenuation coefficients for air, FF and aluminum, respectively; x_{FF} running from x_{FFmin} to x_{FFmax} for each evaluation of K_{ratio}; x_{air} is equal to 1000 mm minus the distance between the source and the applicator exit (approximately 60 mm, see Fig. 3.1). Therefore, the HVL is the aluminum thickness where $K_{ratio} = 0.5$. Both the attenuation and the mass energy-absorption coefficients were calculated with PEN14 using an energy resolution of 0.1 keV, the same as the bin width used in Eq. 6.1.

The $(\Psi_{FFF})^{free-space}$ is the energy fluence (for each energy bin i) obtained in a FFF geometry with a detector of 5 mm radius located at the applicator exit in vacuum. As the HVL is defined in a narrow beam geometry at a source-to-detector distance equal to 1000 mm (Ma *et al.*, 2001), the validity of using this spectrum is based on its independence with respect to the detector radius and distance from the source. To evaluate that condition, several spectra (test FFF spectra) were obtained with different detector radii (1 mm, 2.5 mm and 5 mm located at the applicator exit) and distances from the source (60 mm, 500 mm and 1000 mm for a detector of 5 mm radius).

Additionally, the HVL using $x_{FF} = x_{FF\_IG}$ (x_{FF} corresponding to IG) and the average energy of this setup was compared to those obtained in chapter 4 (using a different approach) and with the experimental data published by Garcia-Martinez *et al.* (2014). The proper calculation of the average energy from $(\Psi_{FFF})^{free-space}$

was performed considering its attenuation by x_{FF_IG} and an air column of approximately 940 mm. To evaluate the HVL in those configurations where we have modified the x-ray tube potential, two additional $(\Psi_{FFF})^{free-space}$ were simulated by changing Ee^- to 60 keV and 80 keV. $x_{FF} = x_{FF\_IG}$ was fixed in both cases.

The procedure for obtaining the spectra has been extensively described in Chapter 4. However, here we use a lower energy cutoff (8 keV) to take into account the characteristics x-ray lines appearing in the NG with x_{FFmin}.

All the spectra were obtained through 100 parallelized MC calculation processes following the principles (including the proper use of the initial seeds to keep the simulation uncorrelated) published by Badal and Sempau (2006). The MC details are summarized in Table 6.1 following the recommendations of the RECORDS AAPM TG-268 report (Sechopoulos *et al.*, 2018). Further information about the transport parameters, variance reduction tools, etc. is described in Chapter 2 and elsewhere (Valdes-Cortez *et al.*, 2019; Salvat *et al.*, 2015; Sempau and Andreo, 2006).

Table 6.1: Summary of the main characteristics of the Monte Carlo method used in this chapter.

Item	Description	References
Code	1) PEN14, 2) penEasy (v. 2015-05-30) compiled with INTEL(R) Fortran compiler (IFORT) 18.0.3.	1) Salvat (2019) 2) Sempau *et al.* (2011)
Validation	Previously validated	Ye *et al.* (2004) Chica *et al.* (2009) Croce *et al.* (2012) Valdes-Cortez *et al.* (2019)
Timing	Sum of 100 parallel processes: $(\Psi_{FFF})^{free-space}$ and $(\Psi_{x_{FFmin}})^{free-air}$ were obtained in 3362 and 4789 hrs., respectively (CPU time). All simulations were performed with N between 10^9 and 10^{10}.	
Source description	Electron beam model: mono-energetic (60, 69.5, and 80 kV), Gaussian electron distribution with FWHM = focal spot size of 1.8 x 1.3 mm^2 (see the GIS model in section 4.2.1).	Valdes-Cortez *et al.* (2019)
Cross-Sections	1) Photoelectric: calculated with PHOTACS. 2) Rayleigh: non-relativistic perturbation theory. 3) Compton: relativistic impulse approximation. 4) Atomic relaxation: using the EADL transition probabilities.	1) Sabbatucci *et al.* (2016) 2) Sakurai (1967), Born (1969); Baym (1974), Cullen *et al.* (1997). 3) Ribberfors (1983) 4) Perkins *et al.* (1991), Deslattes *et al.* (2003) Bearden (1967)
Transport parameters	Photon cutoff = 8 keV in all materials. Electron cutoff = 8 keV in the target, electron transport disabled elsewhere (PENELOPE transport parameters $C1 = C2 = 0$).	
VRTs	VRIF: hard bremsstrahlung emission (target) VRPS: rotational option (flattening filter).	Salvat (2019) Sempau *et al.* (2011)
Scored quantity	Absorbed dose in water (collision kerma approximation)	
Statistical uncert.	<1.4% ($k = 2$, maximum uncertainty reached of all calculated quantities)	
Statistical method	History-by-history	Salvat (2019) Walters *et al.* (2002)

6.2.3.2 Mass energy-absorption coefficient for air to water

The ratios (in free air) of mass energy-absorption coefficients of water to air were calculated from

$$\left(\overline{\frac{\mu_{en}}{\rho}}\right)_{w,air} = \frac{\sum \left(\Psi_{x_{FFmin}}\right)_i^{free-air} \left(\frac{\mu_{en}}{\rho}\right)_{i,w} exp(-\mu_{i,FF} x_{FFextra})}{\sum \left(\Psi_{x_{FFmin}}\right)_i^{free-air} \left(\frac{\mu_{en}}{\rho}\right)_{i,air} exp(-\mu_{i,FF} x_{FFextra})}. \quad (6.2)$$

Where $(\Psi_{x_{FFmin}})^{free-air}$ is the energy fluence in a small volume (cylinder of 1 mm radius 0.1 mm height) inserted in a free-air space (at the applicator exit) for each energy bin i, $x_{FFextra}$ is the thickness of the additional material added to x_{FFmin} ($0 \leq x_{FFextra} \leq x_{FFmax} - x_{FFmin}$), and $(\mu_{en}/\rho)_w$ is the mass energy-absorption coefficient for water.

Considering the $(\mu_{en}/\rho)_{i,medium}$ as tabulated parameters, the $(\overline{\mu_{en}/\rho})_{w,air}$ depends only on two variables, i.e., $(\overline{\mu_{en}/\rho})_{w,air}$ (Ψ, $x_{FFextra}$). In order to validate this procedure, two extra spectra were simulated; one using the IG, $(\Psi_{x_{FF\_IG}})^{free-air}$; and another using the PG, $(\Psi_{x_{FF\,\max}})^{free-air}$. Then, a comparison was made between the $(\overline{\mu_{en}/\rho})_{w,air}$ calculated with the following pairs of parameters:

- ($\Psi = (\Psi_{x_{FFmin}})^{free-air}$, $x_{FFextra} = x_{FF\_IG}$ - x_{FFmin}) with ($\Psi = (\Psi_{x_{FF\_IG}})^{free-air}$, $x_{FFextra} = 0$)

and

- ($\Psi = (\Psi_{x_{FFmin}})^{free-air}$, $x_{FFextra} = x_{FFmax}$ - x_{FFmin}) with ($\Psi = (\Psi_{x_{FF\,\max}})^{free-air}$, $x_{FFextra} = 0$).

Additionally, two extra spectra were simulated using the IG and a $x_{FFextra} = 0$ with Ee^- at 60 keV and 80 keV.

A comparison was made with the published data: from table IV in the AAPM TG-61 report (Ma *et al.*, 2001) and Table C1 in the study published by Andreo (2019). Values from both sources were obtained through linear interpolations using the simulated HVLs (see section 6.2.3.1).

6.2.3.3 Backscatter factor

The backscatter factors were calculated using the linear track-length estimator (Williamson, 1987) according to

$$B_w = \frac{\sum E_i \left(\frac{\mu_{en}}{\rho}\right)_{i,w} (l_i)_w^w}{\sum E_i \left(\frac{\mu_{en}}{\rho}\right)_{i,w} (l_i)_w^{air}}, \tag{6.3}$$

where $(l)_w^w$ and $(l)_w^{air}$ are the distances traveled by photons (tallied in each energy bin i) in a small volume of water (cylinder of 1 mm radius and 0.1 mm height) placed at the surface of a water phantom (cylinder of 100 mm radius 200 mm height) and in-air, respectively. Each quantity l_i was obtained through one simulation

for each value of x_{FF}. Two extra simulations were carried out using the IG conditions with Ee^- of 60 keV and 80 keV. To follow strictly its formal definition, one should use the mass energy-transfer coefficient for water, $(\mu_{tr}/\rho)_w$, instead of $(\mu_{en}/\rho)_w$. However, the difference between those two factors is negligible, less than 0.02% when considering photons up to 80 keV in water (Ma *et al.*, 2001; Andreo, 2019; Grosswendt, 1984).

A comparison was made with the data published in the TG-61 (Ma *et al.*, 2001) and by Andreo (2019). The B_w factors from the TG-61 were obtained through 2D linear interpolations of the data corresponding to SSDs of 5 cm and 7 cm, with a collimator of 10 mm diameter (TG-61 Table V). The B_w factors from the Andreo's study were obtained through linear interpolations using the Table C2 of that work (70 kV, SSD = 100 mm and 10 mm diameter).

6.2.4 Absorbed depth-dose calculation

The absorbed depth-dose (kerma approximation) was scored in a cylindrical mesh with cells of 1 mm radius and 0.1 mm height, running from 2.95 mm to 50.05 mm depth. The applicator exit was positioned at the surface of a cylindrical water phantom (ρ = 0.998 g/cm^3) (Rivard *et al.*, 2004) of 100 mm radius and 200 mm height. The water phantom is in turn, located at the center of a cylinder of 250 mm radius and 500 mm height filled with dry air ($\rho = 1.20479 \times 10^{-3}$ g/cm^3). Absorbed depth-dose curves were recorded for each FF thickness with Ee^- of 69.5 keV. Two

additional absorbed depth-dose curves were obtained using Ee^- of 60 keV and 80 keV with the IG.

In this chapter, we define $D_{z,3}$ as the absorbed dose ratio calculated from the absorbed dose obtained at z and 3 mm depth. The machine-dependent parameters, i.e., HVL_{fit}, $[\overline{(\mu_{en}/\rho)}_{w,air}]_{fit}$, and $(B_w)_{fit}$ (see Table 6.3), were fitted against $D_{10,3}$, $D_{20,3}$, and $D_{50,3}$. We used 3 mm depth as a fixed measurement point because this is the typical prescription depth for surface treatments (Ouhib *et al.*, 2015). The fitting functions were optimized taking into account only the data obtained with Ee^- of 69.5 keV. The uncertainty of the fitting functions was estimated through the quadrature sum of the maximum difference between the simulated and fitted values and the maximum internal uncertainty of each simulated value.

6.2.5 Effects of the measurement uncertainties on the calibration processes

We based our analysis on the data published by Candela-Juan *et al.* (2015b), for the calibration of an Esteya beam using the PTW T34013 (S/N 000146 in that work) parallel-plate ionization chamber (PTW, Freiburg, Germany). The chamber was calibrated in terms of N_K and $N_{D,w}$ for the beam qualities TW50 (50 kV, filtered by 1 mm Al, HVL = 1.13 mm Al) and TW70 (70 kV, filtered by 4 mm Al, HVL = 3.15 mm Al), henceforth called reference beams. The uncertainties estimated in that work were 4.8% and 5.4% (reference uncertainties) for the in-water and in-air methods,

respectively.

In Chapter 5, we establish the experimental uncertainty in depth-dose measurements by 2%. However, in this chapter, we used a broader uncertainty scenario of up to 10% to test the feasibility of using depth-dose ratios in the beam calibration. Hence, the effect of measuring $D_{z,3}$ with 0%, 2%, 5%, and 10% uncertainty ($k = 2$) was evaluated. With this information, the uncertainty of the machine-dependent parameters (i.e., HVL_{fit}, $[\overline{(\mu_{en}/\rho)}_{w,air}]_{fit}$ and $(B_w)_{fit}$) was divided into two components: the dataset uncertainty (i.e., only due to the use of the fitting functions, see section 6.2.4) and the uncertainty added exclusively by the absorbed dose ratios determination. To obtain the last component separately, we propagated the four scenarios over the fitting functions (see Table 6.3) assuming a dataset without uncertainty.

Those two components were added in quadrature to the reference uncertainties with the exception of the HVL_{fit}, whose uncertainty was propagated over the interpolations calculated to obtain the machine-dependent and detector-dependent parameters. Then, the interpolation uncertainty was added in quadrature to the reference uncertainties.

According to Candela-Juan *et al.* (2015b), the energy response of the ionization chamber for the reference beams is 0.1% for the k_{Q,Q_0} and 0.7% for the N_K. However, in order to explore the worst-case scenario, we raised that value up to 2%, matching our analysis with the maximum value recommended by the TG-61 and TRS-398 (Ma *et al.*, 2001; Andreo *et al.*, 2000).

6.2.6 Uncertainties

All uncertainties will be expressed with a coverage factor $k = 2$, as recommended by the AAPM (DeWerd *et al.*, 2011). The Type B uncertainties of the attenuation and absorption factors were propagated over Eqs. 6.1, 6.2, and 6.3, according to the BIPM recommendations assuming normal distribution (BIPM, 2010). The Type B uncertainty was obtained from Andreo *et al.* (2012), considering the 2.5% ($k = 2$) value given for the grouping II corresponding to a beam with an average photon energy equal to 34.1 keV (Table 1 in that work).

6.3 Results

6.3.1 HVL

HVLs were calculated with uncertainties below 0.7% (see Table 6.2). The HVL for the IG configuration (1.738 ± 0.009 mm Al) agrees within the associated uncertainties with the value reported in section 4.3.2.2 (Valdes-Cortez *et al.*, 2019). Such value was obtained using a different methodology and it is in the experimental range measured by other authors (Garcia-Martinez *et al.*, 2014; Candela-Juan *et al.*, 2015b). The calculated average photon energy (IG, $Ee^{-} = 69.5$ keV) is 36.3 ± 0.2 keV, also consistent with the one obtained in section 4.3.2.1 (36.19 ± 0.09 keV, $k = 2$) (Valdes-Cortez *et al.*, 2019) and with experimental measurements (36.2 ± 0.2 keV,

$k = 2$). The HVLs calculated from the test FFF spectra have an uncertainty below 1.4%, and differ from each other by no more than 0.3% (for all values of x_{FF} used in this work) without any systematic trend in their differences.

A variation of ±0.035 mm from x_{FF_IG} generates a change of ±1.4% of the HVL, while a modification of ±0.35 keV (0.5% of the nominal value) in Ee^- modifies the HVL by ±0.4% (see Figs. 6.1 and 6.2).

6.3.2 Free-in-air ratios of mass energy-absorption coefficient of water to air and backscatter factors

The $(\overline{\mu_{en}/\rho})_{w,air}$ were calculated with uncertainties below 0.4% (see Table 6.2). The differences with respect to the values reported by TG-61 (Ma *et al.*, 2001) and Andreo 2019 (Andreo, 2019) (see Fig. 6.3 and Table 6.2) are in all cases below the associated uncertainties. Differences between the $(\overline{\mu_{en}/\rho})_{w,air}$ obtained using $(\Psi_{x_{FFmin}})^{free-air}$, $(\Psi_{x_{FF\_IG}})^{free-air}$, and $(\Psi_{x_{FF\,\max}})^{free-air}$ were negligible ($\leq 0.1\%$).

The B_w factors were obtained with an uncertainty below 0.4%. The factors differ approximately 1% from the TG-61 data (see Table 6.2 and Fig. 6.4), within the 3% ($k = 2$) maximum tolerance reported by the AAPM (Ma *et al.*, 2001). The agreement with the data published by Andreo (2019) is, in general, within the

Table 6.2: Summary of simulation results compared against reported values (IG). In parentheses the uncertainty of the last significant figure. The TG-61 dataset is reported with 3% uncertainty ($k = 2$) (Ma *et al.*, 2001).

Items	Values								
Geometry		NG			IG			PG	
Ee^-		69.5 keV		60 keV	69.5 keV	80 keV		69.5 keV	
x_{FF} (mm)	0.590	0.790	1.190		1.590		2.199	3.310	4.980
HVL	0.859(6)	1.080(6)	1.435(8)	1.57(1)	1.738(9)	1.94(1)	2.14(1)	2.76(1)	3.49(2)
$D_{10,3}$	0.518(4)	0.551(5)	0.588(5)	0.601(5)	0.614(6)	0.623(4)	0.635(6)	0.658(6)	0.674(6)
$D_{20,3}$	0.241(2)	0.265(3)	0.298(3)	0.308(3)	0.323(4)	0.334(2)	0.346(3)	0.373(4)	0.396(4)
$D_{50,3}$	0.0410(5)	0.0477(6)	0.0570(7)	0.0585(7)	0.0645(8)	0.0711(5)	0.0742(9)	0.086(1)	0.097(1)
B_w	1.058(4)	1.064(4)	1.067(4)	1.068(3)	1.065(4)	1.067(4)	1.069(4)	1.073(4)	1.072(4)
Fit	1.059(5)	1.062(5)	1.066(5)	1.067(5)	1.068(5)	1.068(5)	1.069(5)	1.071(5)	1.072(5)
TG-61	1.044	1.047	1.050	1.052	1.053	1.054	1.057	1.059	1.060
Andreo	1.050(6)	1.053(6)	1.057(6)	1.060(6)	1.060(6)	1.060(6)	1.063(6)	1.067(6)	1.069(6)
$(\overline{\mu_{en}/\rho})_{w,air}$	1.023(3)	1.021(3)	1.019(3)	1.018(4)	1.018(3)	1.020(4)	1.018(4)	1.019(4)	1.020(4)
Fit	1.023(4)	1.021(4)	1.019(4)	1.018(4)	1.018(4)	1.018(4)	1.018(4)	1.019(4)	1.020(4)
TG-61	1.021	1.019	1.017	1.017	1.017	1.018	1.018	1.020	1.023
Andreo	1.020(4)	1.018(4)	1.016(4)	1.016(4)	1.016(4)	1.016(4)	1.016(4)	1.019(4)	1.024(4)

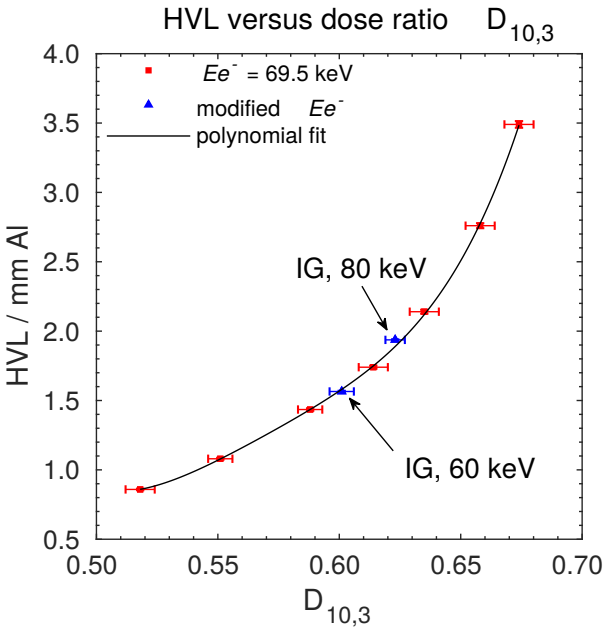

Figure 6.1: Correlation between HVL and the ratio of the doses at 10 mm to 3 mm depth. For the red squares, the different dose ratios were obtained varying the FF thickness maintaining Ee^- fixed. For the blue triangles, the different dose-ratios and HVLs were obtained using the ideal flattening filter thickness (x_{FF_IG}) varying the electron energy. The polynomial fit corresponds to a 4th order function optimized taking into account only the red squares.

uncertainties.

6.3.3 Absorbed depth-dose

Figs. 6.1 and 6.2 show the relation between the HVL and the dose ratios. The absorbed dose and the absorbed dose ratios were determined with uncertainties below 1.1% and 1.3%, respectively (see

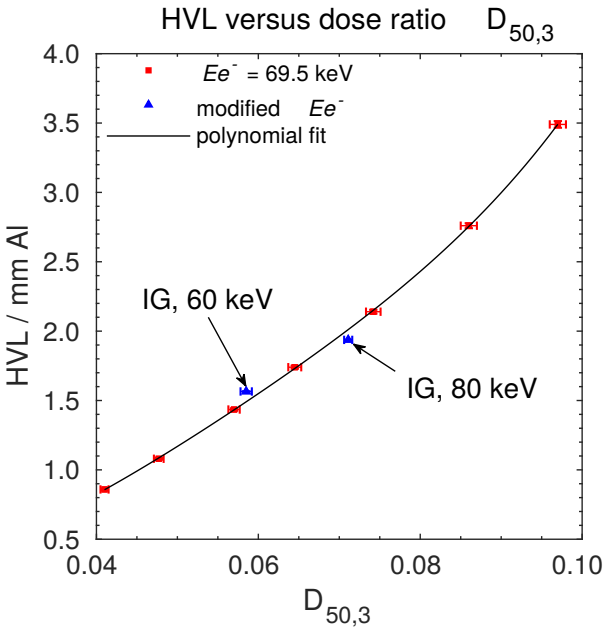

Figure 6.2: Correlation between HVL and the ratio of the doses at 50 mm to 3 mm depth. For the red squares, the different dose ratios were obtained varying the FF thickness maintaining Ee^- fixed. For the blue triangles, the different dose-ratios and HVLs were obtained using the ideal flattening filter thickness (x_{FF_IG}) varying the electron energy. The polynomial fit corresponds to a 4th order function optimized taking into account only the red squares.

Table 6.2). A variation of the FF by ± 0.035 mm generates changes of 0.3%, 0.5% and 0.9% in $D_{10,3}$, $D_{20,3}$, and $_{D50,3}$, respectively. A variation of $\pm 14\%$ in the Ee^- (for the IG configuration) generates a change of approximately 2%, 4% and 10% in $D_{10,3}$, $D_{20,3}$, and $D_{50,3}$, respectively. The HVL_{fit}, $[(\overline{\mu_{en}/\rho})_{w,air}]_{fit}$ and $(B_w)_{fit}$ (see Table 6.3) are in agreement within 1%, 0.02% and 0.3% as compared to the simulated HVL, $(\overline{\mu_{en}/\rho})_{w,air}$, and B_w. Considering

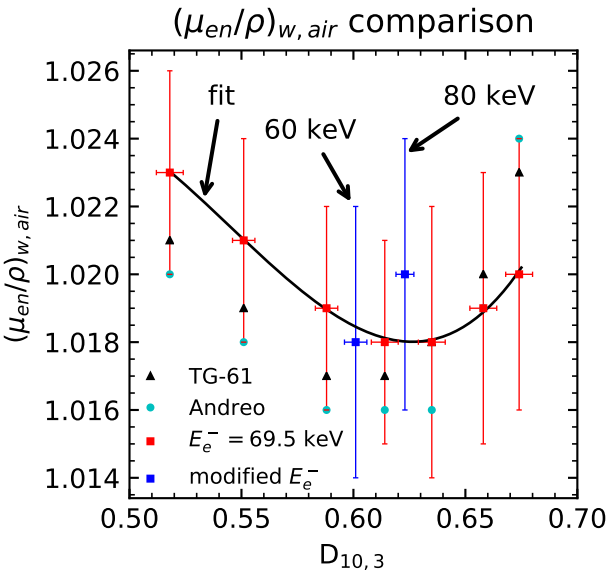

Figure 6.3: Relation between $(\overline{\mu_{en}/\rho})_{w,air}$ and the ratio between the doses at 10 mm to 3 mm depth. For the red squares, the different absorbed dose ratios were obtained varying the flattening filter thickness maintaining the electron energy fixed. For the blue circles, the different dose-ratios were obtained using the ideal flattening filter thickness (IG) varying Ee^-. Black triangles correspond to the values reported in the AAPM TG-61 report (Ma *et al.*, 2001). Cyan circles correspond to the values reported by Andreo (2019).The fit functions were optimized taking into account only the red squares.

the simulations with 60 keV and 80 keV, the HVL_{fit} agrees within 2.6%, 1.6% and 5.0%, $(\overline{\mu_{en}/\rho})_{w,air}$ agrees within 0.2% and the B_w factors agree within 0.1%, 0.2% and 0.3% of the simulated values for $D_{10,3}$, $D_{20,3}$ and $D_{50,3}$, respectively.

Table 6.4 shows the uncertainties calculated taking into consideration the four scenarios described in section 6.2.5. The dataset

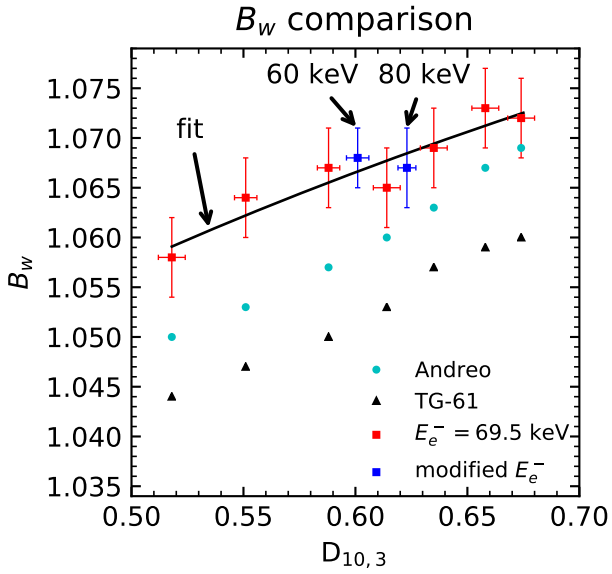

Figure 6.4: Relation between B_w and the ratio between the doses at 10 mm to 3 mm depth. For the red squares, the different absorbed dose ratios were obtained varying the flattening filter thickness maintaining the electron energy fixed. For the blue circles, the different dose-ratios were obtained using the ideal flattening filter thickness (IG) varying Ee^-. Black triangles correspond to the values reported in the AAPM TG-61 report (Ma *et al.*, 2001). Cyan circles correspond to the values reported by Andreo (2019). The fit functions were optimized taking into account only the red squares.

uncertainties are: 1.0%, 0.4% and 0.5% for HVL_{fit}, $[(\overline{\mu_{en}/\rho})_{w,air}]_{fit}$ and $(B_w)_{fit}$, respectively.

Table 6.3: Machine-dependent parameters fitted for the APP_{10mm} absorbed depth-doses, $HVL_{fit} = a_0 + a_1x + a_2x^2 + a_3x^3 + a_4x^4$, ($HVL_{fit}$ in mm) $[(\overline{\mu_{en}/\rho})_{w,air}]_{fit} = a_0 + a_1x + a_2x^2 + a_3x^3$, $(B_w)_{fit} = a_0 + a_1ln(x)$. These expressions take values from $D_{10,3}$, $D_{20,3}$ or $D_{50,3}$ ($Ee^- = 69.5$ keV). The uncertainties ($k = 2$) expected for datasets are 1.0%, 0.4% and 0.5%, respectively.

Parameter	$D_{z,3}$	a_0	a_1	a_2	a_3	a_4
HVL	$D_{10,3}$	8.30164×10^2	-5.845003×10^3	1.5425144×10^4	-1.8085974×10^4	7.962366×10^3
	$D_{20,3}$	2.216	-53.038	4.10327×10^2	-1.211388×10^3	1.34849×10^3
	$D_{50,3}$	1.28	-86.11	2.905427×10^3	-3.1169352×10^4	1.31920863×10^5
$(\overline{\mu_{en}/\rho})_{w,air}$	$D_{10,3}$	0.5408	2.7671	-5.1867	3.1693	–
	$D_{20,3}$	1.0613	-0.1851	-0.039	0.6156	–
	$D_{50,3}$	1.0562	-1.3142	14.2956	-47.2703	–
B_w	$D_{10,3}$	1.0925	0.0508	–	–	–
	$D_{20,3}$	1.0977	0.0268	–	–	–
	$D_{50,3}$	1.1096	0.0156	–	–	–

Table 6.4: Effect of the four absorbed dose-ratio uncertainty levels (d.r.u) over the machine-dependent and detector-dependent parameters. The column d.r.u. = 0% corresponds to the minimum possible uncertainty due to the use of a dataset. The other columns incorporate the additional d.r.u. The dataset uncertainty of the TG-61 machine-dependent and the detector-dependent parameters are already considered in the reference uncertainties. All values are presented with a coverage factor $k = 2$.

Type	Parameter	$D_{z,3}$	Dose ratio uncertainty (%)			
			10	5	2	0
Machine-dependent parameter (this work dataset)	HVL	$D_{10,3}$	51	25	10	1
		$D_{20,3}$	27	14	5	
		$D_{50,3}$	15	8	3	
	$(\overline{\mu_{en}/\rho})_{w,air}$	$D_{10,3}$	0.1	0.1	–	0.4
		$D_{20,3}$	0.1	–	–	
		$D_{50,3}$	–	–	–	
	B_w	$D_{10,3}$	0.5	0.2	0.1	0.5
		$D_{20,3}$	0.3	0.1	0.1	
		$D_{50,3}$	0.1	0.1	–	
Machine-dependent parameters (TG-61 dataset)	$(\overline{\mu_{en}/\rho})_{w,air}$	$D_{10,3}$	0.2	0.1	–	3
		$D_{20,3}$	0.1	–	–	
		$D_{50,3}$	0.1	–	–	
	B_w	$D_{10,3}$	0.8	0.4	0.2	
		$D_{20,3}$	0.4	0.2	0.1	
		$D_{50,3}$	0.2	0.1	–	
Chamber-dependend parameters	$N_K/k_{Q,Q_0}$	$D_{10,3}$	0.9	0.6	0.4	2/4
		$D_{20,3}$	0.6	0.5	0.3	
		$D_{50,3}$	0.5	0.4	0.2	

6.3.4 Effects of the measurement uncertainties on the calibration processes

The use of absorbed depth-dose to obtain the machine-dependent parameters adds as much as 0.2% to the calibration uncertainty

Table 6.5: Final uncertainties of the calibration methods for each dose ratio uncertainty (d.r.u.) scenario. The difference between the in-air "TG-61 dataset" and "this work dataset" for the d.r.u. = 0% is completely explained by the different dataset uncertainties considered for $(\overline{\mu_{en}/\rho})_{w,air}$ and B_w (see Table 6.4).

Method	$D_{z,3}$	Dose ratio uncertainty (%)			
		10	5	2	0
In-water	$D_{10,3}$	5.0	4.9	4.9	4.8
	$D_{20,3}$	4.9	4.9	4.9	
	$D_{50,3}$	4.9	4.9	4.9	
In-air "TG-61 dataset"	$D_{10,3}$	5.5	5.4	5.4	5.4
	$D_{20,3}$	5.4	5.4	5.4	
	$D_{50,3}$	5.4	5.4	5.4	
In-air "this work dataset"	$D_{10,3}$	3.5	3.4	3.3	3.3
	$D_{20,3}$	3.4	3.4	3.3	
	$D_{50,3}$	3.4	3.3	3.3	

(see Table 6.5) for an absorbed dose ratio with a 10% uncertainty. The use of $D_{50,3}$ instead of $D_{10,3}$ implies a maximum reduction of 0.1% over the final uncertainty budget. The use of the "this work dataset" instead of the "TG-61 dataset" would imply a reduction of nearly 40% in the overall uncertainty.

6.4 Discussion

By considering the HVL-to-dose-ratio fit given in Table 6.3 and Figs. 6.3 and 6.4 it is possible to determine the data required for a beam calibration using a simple and straightforward absorbed depth-dose measurement.

The limits proposed for the x_{FF} cover adequately the manufacturing tolerances reported by the vendor (±0.035 mm). As it was established in Chapter 4, the experimental measurements of the spectra from six Esteya x-ray tubes do not support an Ee^- value larger than 69.5 keV (Garcia-Martinez *et al.*, 2014). On the other hand, the average photon energy of the ($x_{FF} = x_{FF\_IG}$, Ee^- = 69.5 keV) agrees perfectly with the reported experimental value (36.2 ± 0.2 keV) (Garcia-Martinez *et al.*, 2014). As the average photon energy obtained with $Ee^- = 60$ keV ($x_{FF} = x_{FF\_IG}$) is considerably smaller (32.3 ± 0.2 keV), we can conclude that the ±14% variation of Ee^- also covers adequately both the manufacturing tolerance reported (±0.5%) and the experimental observations.

The uncertainties achieved in this work for the $(\overline{\mu_{en}/\rho})_{w,air}$ and B_w are similar to those reported by Andreo *et al.* (2012) and Andreo (2019). Both quantities are very robust, observing minor modifications, even when significant variations in the x_{FF} value are considered. This condition gives us confidence that any unreported source of uncertainty will not have a significant effect on the evaluated values in the proposed Dose-ratio-to-HVL formalism. In general, both factors agree within their uncertainties with the ones in the literature (Ma *et al.*, 2001; Andreo *et al.*, 2012; Andreo, 2019). The use of $D_{50,3}$ instead of $D_{10,3}$ reduces the HVL_{fit} uncertainty by a factor of three (see Table 6.4). However, deeper measurement points not only may bring challenges due to a smaller signal-to-noise ratio, but also could imply noticeable spectral changes that might affect the dosimeter performance (Watson

et al., 2017), as it was discussed in Chapter 5. Therefore, a trade-off exists between the measurement sensibility to its uncertainties and higher signals. A location between both extremes (e.g., $D_{20,3}$) could be an interesting option to explore in the clinical context.

Nevertheless, the effect of the dose ratio uncertainty on the overall uncertainty is less than 0.2%. This is true even in an extreme case of 10% dose ratio uncertainty, which was conceived to include any unknown effect of the chamber performance (Watson *et al.*, 2017; Gimenez-Alventosa *et al.*, 2018). However, and considering the findings showed in Chapter 5, it is more realistic to consider that the absorbed dose ratio can be determined with uncertainties lower than 5% (Valdes-Cortez *et al.*, 2019; Watson *et al.*, 2017). Furthermore, we have considered a large chamber energy response of 2%, when the particular chamber used in our evaluation presents values of 0.1% and 0.7% for the k_{Q,Q_0} and N_K, respectively. Hence, the additional uncertainty added by using the absorbed dose-ratios should be less than 0.1% when considering realistic chamber data in a clinical environment.

As all applicators of the Esteya system share the same flattening filter, they present the same narrow-beam spectrum (and HVL). With that condition, the HVL_{fit} obtained with the parameters of Table 6.3 (using the absorbed dose ratios of the $\mathrm{APP}_{10\mathrm{mm}}$) is representative of the whole set of applicators. However, the $D_{10,3}$ of the 30 mm diameter applicator is increased by 7% (from 0.614 to 0.658) compared to the 10 mm diameter applicator (see table 4.4). Such difference is due to changes in the scatter conditions,

which also increases the B_w nearly by the same amount (Ma *et al.*, 2001; Andreo, 2019). For that reason, Table 6.3 only can be used with the absorbed dose ratios of the APP_{10mm}. Furthermore, when the applicators do not share the same narrow-beam spectrum, as it could be the case for an eBT system whose flattening filters are not the same for the whole set, each applicator needs its HVL estimation.

Considering the data published by Candela-Juan *et al.* (2015b), the reduction of the $(\overline{\mu_{en}/\rho})_{w,air}$ and B_w uncertainties from 3% (TG-61 dataset) to 0.5% (this work dataset) generates a reduction of 40% in the overall calibration uncertainty for the APP_{10mm} of the Esteya system. As the largest part of the uncertainties reported in the TG-61 tables are accepted to keep them as general as possible (e.g., independent from kV), a reduction of 40% is worth the effort to include more details into consideration. Such reduction could even imply lower uncertainties for the in-air calibration than in-water calibration. In this context, the data generated under a machine-specific paradigm can complement the general tables published so far, which would be very helpful while the in-air calibration method is still in use.

This chapter is a proof-of-concept of the feasibility of using dose ratios in the calibration of a specific eBT system. In a first instance, this methodology could be applied to obtain the HVL as an intermediate step (e.g., as Dose-ratio-to-HVL formalism). The use of dose ratios directly as a beam quality index requires more research pointing to associate the energy response of a chamber with

the dose ratios of different beams. This work opens the possibility of applying our method for other devices using proper machine-specific data (i.e., HVL-to-dose-ratio fits). However, the high dose gradient of low-energy x-ray beams requires a better understanding of how some sources of uncertainties, such as alignment inaccuracies, can affect the final budget.

6.5 Chapter conclusions

The results of this work show the feasibility of using the absorbed depth-dose curve of the APP_{10mm} to obtain all the data required in the beam calibration of the Esteya eBT system, adding a minimal amount (generally negligible) of uncertainty to the entire process. The use of factors specifically obtained for each applicator and eBT system allow a considerable reduction in the in-air calibration uncertaity.

Chapter 7

Summary and general conclusions

Non-melanoma skin cancers (or keratinocyte carcinomas) are among the most common human malignancies (Madan *et al.*, 2010; Nehal and Bichakjian, 2018), presenting a continuous increase in their incidence around the world (Perera *et al.*, 2015; Rogers *et al.*, 2015; Rubió-Casadevall *et al.*, 2016; Leiter *et al.*, 2017). In this context, surface Electronic Brachytherapy (eBT) has become an effective treatment, achieving excellent control rates and good cosmetic results (Bhatnagar, 2013; Ouhib *et al.*, 2015; Ballester-Sánchez *et al.*, 2017; Guinot *et al.*, 2018).

Surface eBT systems consist basically of two components: an x-ray tube and an applicator attached. The x-ray tube accelerates

electrons in the energy range between 50 and 70 kV, producing flattened x-ray beams. The eBT applicator serves as a collimator positioned directly in contact with the skin, producing conical beams of 10 to 50 mm diameter. The Flattening Filter (FF) may or may not be included in the applicator, which depends on the eBT system design (Candela-Juan *et al.*, 2015b).

The eBT devices came to solve some problems related to radiation safety due to the use of radionuclides in high-dose-rate brachytherapy (Eaton, 2015). However, eBT is far from being a drawback-free technique. The use of low-energy photon beams introduces several challenges to the absorbed dose determination. All of them, translates into an increment of the associated uncertainties (Hill *et al.*, 2014), which is crucial in the correlation of the absorbed doses with biological responses (Aird *et al.*, 2016). Historically, Monte Carlo (MC) simulations have been used in solving some of those problems, increasing the knowledge about radiation therapy (Chetty *et al.*, 2007; Beaulieu *et al.*, 2012; Perez-Calatayud *et al.*, 2012). However, MC systems have their own issues with low-energy photons, mostly related to different implementations of some of their libraries (Andreo *et al.*, 2012; Seltzer *et al.*, 2014).

The problems above mentioned can be grouped in three main categories:

1. Increased uncertainties in the cross-section libraries used by MC codes.

2. Increased uncertainties in the detectors response.

3. Issues related to beam calibration procedures (beam quality indexes, correction factors, etc.).

This thesis aims to characterize a clinical surface eBT device of 69.5 kV, while attempting to ameliorate some of the drawbacks mentioned above. The energy beam of the treatment unit here studied is in the upper range of the eBT machines commercially available (Eaton, 2015), which presents a lack of published information.

The core of this project was divided into three main stages. First, a complete dosimetric characterization of the studied eBT system was performed (see Chapter 4). The methodologies and findings of this stage were used as the basis for the following sections. In the second part (see Chapter 5), a study of the performance of the recommended detector for in-water dosimetry of the eBT beams was performed. Specifically, we evaluated how its dependencies with depth and the applicator size can affect the absorbed dose determination, which, as far as we know, is the first time that this information is published at this range of energies. This data was used in the third part (see Chapter 6), where we studied the uncertainties arising in a beam calibration. In this final section, novel procedures were proposed to facilitate and reduce the calibration uncertainties of the eBT beams.

The MC system used in this work was PENELOPE, an open-source code, widely used in medical applications (Perez-Calatayud *et al.*, 2012; Rodriguez *et al.*, 2013), along with penEasy (Sempau *et al.*, 2011), the main steering program to handle all the func-

tionalities of the MC system. PENELOPE has been well benchmarked in high- (Sempau *et al.*, 2003; Herranz *et al.*, 2015) and low-energy photons (Ye *et al.*, 2004; Chica *et al.*, 2009). Also, PENELOPE has been successfully used in BT studies with electronic- (Croce *et al.*, 2012) and radionuclide-based sources (Ballester *et al.*, 2015; Vijande *et al.*, 2013; Almansa *et al.*, 2017). Two release versions of PENELOPE and penEasy were used through this work, PENELOPE-2014 (PEN14), PENELOPE-2018 (PEN18), penEasy-2015, and penEasy-2019, respectively (Salvat *et al.*, 2015; Salvat, 2019; Sempau, 2019). The reader can find a more detailed description of this MC system in Chapter 2. Also, a comparison of the results obtained with both release versions is shown in Appendix A.

The surface eBT device studied is the Esteya® system (Elekta Brachytherapy, Veenendaal, The Netherlands), showed in Figure 3.1, which is extensively described in Chapter 3. Its x-ray tube accelerates electrons at 69.5 kV toward a tungsten target, generating a bremsstrahlung beam flattened by a 1.6 mm thick (measured at the beam axis) aluminum filter (flattening filter), collimated by applicators from 10 mm to 30 mm diameter. A plastic cap covers the exit of the applicators in order to reduce the electronic contamination of the beam, leaving a constant Source to Sourface Distance (SSD) of 60 mm (Candela-Juan *et al.*, 2015b).

The dosimetric characterization of the Esteya eBT system was performed with PEN14 and penEasy-2015 (see Chapter 4). The applicators of 10 mm (APP_{10mm}) and 30 mm diameter (APP_{30mm})

were considered, which present the smallest and highest diameters available. The aim of this part of the work was threefold. Firstly, finding the most efficient ways to simulate the eBT system, without "or with a negligible bias" of the simulation results. Secondly, finding the most suitable models (e.g., x-ray source) to reproduce the experimental results published elsewhere. Finally, generating a Phase-Spase File (PSF) at the exit of both applicators to be used in future parts of this thesis. It is worth mentioning that all the information available of this eBT system was obtained experimentally; therefore, this is the first study that fully characterizes the Esteya system through MC methods.

From all the Efficiency-Enhancing Techniques (EFENs) tested, the Variance Reduction Interaction Forcing (VRIF) and the modification of the cutoff energy threshold, *EABS*, were the most useful (see table 4.2), both described in Chapter 2. A VRIF with a factor of 150 over the hard bremsstrahlung emission interactions (*ICOL* = 4, see table 2.1) in the target improves the efficiency of the simulation by 20 (see Figure 4.1). On the other hand, Figure 4.2 shows a negligible amount of photons with energies lower than 10 keV escaping the applicator exit, while the electrons reaching the plastic cap's exterior face contribute with the 0.005% of the photon energy scored at that place. For that reasons, applying *EABS* = 10 keV for photons in all materials, and electrons in the target (electron transport disabled elsewhere) allows reducing the simulation time by a 92% without any noticeable change in the PSF.

Modeling the x-rays source can be one of the most challeng-

ing and sensible procedures in the simulation of an eBT machine (Hiatt *et al.*, 2016). In this work, we tested four x-rays source models (see Section 4.2.1), comparing their results with experimental data. The comparison was divided into two categories: spectral and clinical. From those comparisons, it can be concluded that the Gaussian Intensity Source (GIS), corresponding to a monoenergetic electron beam of 69.5 keV with Gaussian electron distribution (FWHM equal to the focal spot size, see Section 4.2.1), delivers the best results. Hence, the GIS was selected to be used in the following sections.

The final PSFs were obtained with 10^9 histories for both applicators. The calculated average photon energy was 36.19 ± 0.09 keV, which is in an excellent agreement with the 36.2 ± 0.1 keV, experimentally obtained by Garcia-Martinez *et al.* (2014) (see Section 4.3.2.1). The calculated Half-Value Layer (HVL) (see Equation 4.1, and Section 4.3.2.2) was 1.72 ± 0.04 mm, which is within the experimental range measured by Garcia-Martinez *et al.* (2014) and Candela-Juan *et al.* (2015b).

The FF is the most important structure in the beam path. Figure 3.1 shows how the photons "see" different filter thicknesses in their path, depending on their radial position regarding the beam axis, which generates different attenuations. This characteristic affects the mean energy of the beam, as shown in Figure 4.3. This eBT device shares the same FF with all its applicators. Thus, it is expected that any dosimetric difference between applicators should be related mostly with changes in the scatter conditions.

However, the FF effect on the dosimetry should be considered when characterizing an eBT device with different FFs in each applicator.

The clinical data comparison shows reasonable differences between the simulated and the measured data (considering the uncertainties involved), which are in agreement with those found by other authors (Croce *et al.*, 2012; Fulkerson *et al.*, 2014; Moradi *et al.*, 2017; Watson *et al.*, 2017). The maximum difference between the simulated and measured Percentage absorbed Depth-Dose (PDD) is 4.5% (see Figure 4.5), which is located at the phantom surface. However, when depths deeper than 1 mm are considered, the differences decrease to 2%. Regarding the Off-axis Dose Profile (DP) comparison, differences of 15% at radius 16 mm $<$ r $<$ 17 mm were observed. However, those differences were obtained in a high dose gradient zone, presenting a submillimetric dose-to-agreement (0.4 mm, see Figure 4.7).

The verification of the absorbed dose represents an essential part of the quality assurance program in radiation therapy (Andreo *et al.*, 2000; Ma *et al.*, 2001; Venselaar *et al.*, 2004), including eBT (Thomadsen *et al.*, 2009; Candela-Juan *et al.*, 2015a; Eaton, 2015). In this regard, the recommended dosimeter in low-energy photon beams is the parallel-plate ionization chamber (Andreo *et al.*, 2000; Ma *et al.*, 2001). Due to the properties of the eBT beams discussed in Section 1.2, the detector expected response could be highly sensitive to changes in the beam characteristics (e.g., due to beam hardening with depth), or by detector-to-detector differences (e.g., due to manufacturing tolerances), as it was proved for 50 kV (Wat-

son *et al.*, 2017) and ^{192}Ir (Gimenez-Alventosa *et al.*, 2018) beam.

As far as we know, the T34013 (PTW, Freiburg, Germany) parallel-plate ionization chamber (see Figure 5.2) is the only dosimeter recommended for the in-water dosimetry of eBT beams (Candela-Juan *et al.*, 2015a; Fulkerson *et al.*, 2020). For that reason, this part of the work, which is fully described in Chapter 5, studied the dependence of this detector response with depth and the applicator size, proposing strategies to mitigate those effects, such as finding its optimum Effective Point of Measurement (EPoM). Additionally, the experimental uncertainties in a depth dose measurement have been assessed.

The study of the ionization chamber response required evaluating the changes of its perturbation correction factors with depth and the applicator size. From Equation 5.2, it is necessary the calculation of three different quantities at different depths and applicators ($\mathrm{APP}_{10\mathrm{mm}}$ and $\mathrm{APP}_{30\mathrm{mm}}$) to achieve that goal. Those quantities are the mass energy-absorption coefficient ratio water to air, $(\overline{\mu_{en}/\rho})_{w,air}$ (see Equation 5.1), and the ratio between the absorbed dose to water (D_w, without the presence of the ionization chamber) and the absorbed dose in the cavity of the ionization chamber (D_{cav}) in the water phantom. All those simulations were performed using PEN18 with penEasy-2019, which were extensively described in Section 5.2.

Obtaining those quantities requires a computationally intensive procedure, especially for D_{cav}. Thus, a modification of the GIS model was made to increase the simulation efficiency, avoiding the

electrons transport in the x-ray source model. Firstly, the GIS energy spectrum was scored at the beryllium window of the x-ray tube (see Figure 3.1), using the simplified setup described in Section 4.2.1. Then, this spectrum was used in a collimated photon point-like source, with enough aperture to cover the entire primary collimator (see Figure 3.1). The effect of this modification on the result was assessed through additional simulations with the GIS model, which were evaluated to be less than 0.2% (see Table 5.2).

Three methods were proposed to mitigate the effect of depth on the chamber response. The first one considers a surface correction factor, p_{surf} (see Equation 5.3), which relates D_{cav} with D_w at the surface of the water phantom (typical case in the clinical practice), maintaining the Effective Point of Measurement recommended by the manufacturer (EPoM_{man}) (center of the inner face of the entrance window, see figures 5.2 and 5.3). The next case uses a global correction factor, p_{glob} (see equations 5.4 and 5.5), considering all depths included in this work (up to 20 mm), also maintaining EPoM_{man}. The last method (see equations 5.6 and 5.7), also considers the entire depth range but, this time, shifting the EPoM_{man} to the point where the perturbation correction factor, p_{shift}, was as depth independent as possible.

The value of $(\overline{\mu_{en}/\rho})_{w,air}$ was 1.018±0.02, which is in agreement with the available data published for beams with similar kV and HVL (Ma *et al.*, 2001; Andreo, 2019). The variation of this ratio with depth and the applicator size was less than 0.06%. Therefore, this quantity was considered constant. The ratio D_w/D_{cav}

varies by 1% and 0.6% with depth for APP_{10mm} and APP_{30mm} (see Figure 5.5), respectively. The same variation is obtained when the absorbed dose is calculated with Equation 5.2 using p_{surf} (see Table 5.3 and Figure 5.7). The use of p_{glob} reduces the differences in the absorbed dose determination within 0.6% and 0.5% for APP_{10mm} and APP_{30mm}, respectively. When the absorbed dose is calculated using p_{shift} and an EPoM shifted by 0.4 mm toward the bottom of the sensitive volume (see Figure 5.6), the observed changes with depth reduce to 0.5% and 0.3% for APP_{10mm} and APP_{30mm}, respectively. Regarding the dependence with the applicator size of the perturbation correction factors, a difference of 2% was observed between APP_{10mm} and APP_{30mm}.

The three quantities here calculated were obtained with uncertainties within 0.4%. A complete report of the uncertainties considered in their calculations can be found in Table 4.6. An especial emphasis was paid in the treatment of the photoelectric libraries, in particular, to the use of the Pratt's Renormalization Screening Correction (PRSC, see Section 2.2.2), which has been extensively discussed elsewhere (Andreo *et al.*, 2012; Seltzer *et al.*, 2014; Sabbatucci and Salvat, 2016; Pratt, 2014). The differences found due to its implementation (or not) are within 0.2%.

The experimental uncertainties were estimated though several depth-dose measurements, performed with three different T34013 ionization chambers (see Figure 5.3 and Section 5.2.3 for more details). The procedures were performed by a single person, with one Esteya unit, in a plastic phantom. The differences in the ab-

sorbed dose between measurements were under 2%. This result included the structural detector differences and the experimental uncertainties in alignment, chamber positioning, among others.

Watson *et al.* (2017) studied the T34013 ionization chamber with an unfiltered eBT beam of 50 kV. They found a change of $(\overline{\mu_{en}/\rho})_{w,air}$ of 2.5% in the same range of depths used in this thesis. Furthermore, this research group found differences in the chamber response with depth up to 5% at 15 mm, using the detector geometry intended by the manufacturer (without considering the manufacturing tolerances). When the authors considered possible differences in the chamber structures due to manufacturing tolerances, changes with depth of 12% on the chamber response were reported. Regarding the EPoM, they suggested that the chamber response dependency with the manufacturing tolerances can be mitigated by shifting the EPoM_{man} to the midpoint of its sensitive volume. Nevertheless, according to the data presented, that change increases the differences in depth.

The results here exposed allow concluding that the T34013 is significantly less prone to suffer changes in its response with the Esteya beam than those obtained with a 50 kV beam. Furthermore, the dependencies with depth can be reduced from 1% to less than 0.6% by using p_{glob} or p_{shift} methods. The field size dependency (2%) was obtained in the limit of the field sizes offered by the manufacturer. Considering that all the applicators share the same FF, 2% can be considered as a conservative value for the entire set of applicators. The optimum EPoM was found to be at 0.4 mm

from $EPoM_{man}$. This finding agrees with the TG-61 (Ma *et al.*, 2001), which recommends placing the EPoM at the midpoint of the sensitive volume. However, the position of the optimum EPoM can be very dependent on the characteristics of the beam, as it was reported by Gimenez-Alventosa *et al.* (2018), which found significant differences in its position for two surface HDR BT applicators, using an ^{192}Ir source. Hence, this is a topic that requires further research.

The beam calibration is a critical procedure in the absorbed dose verification. There exist two recommended methods for calibrations of the eBT beams. The in-air method, proposed in the TG-61 (Ma *et al.*, 2001), which is based on the measurement of air kerma, using the in-air calibration factor, N_K. While, the in-water method of the TRS-398 (Andreo *et al.*, 2000), is based in the absorbed dose to water, through the use of $N_{D,w}$. From the point of view of the calibration factors (see Section 6.2.2), we can divide them into two categories depending on their dependencies with the detector or with the beam. Among the detector-dependent factors, one can mention the $N_{D,w}$, N_K, or k_{Q,Q_0} (factor that corrects by the differences between the reference and the user beam qualities). While the machine-dependent factors considered in this work are $(\overline{\mu_{en}/\rho})_{w,air}$ and the backscatter factor (B_w).

Whichever the chosen method, eBT beam calibrations present two important drawbacks regarding the same procedure in External Beam Radiation Therapy (EBRT). First, eBT beam calibrations present higher uncertainties, estimated between 5% and 7%

(Ma *et al.*, 2001; Candela-Juan *et al.*, 2015b), compared to EBRT, whose uncertainties have been estimated in less than 4% ($k = 2$ in both cases) (Andreo *et al.*, 2000; Castro *et al.*, 2008). An important part of this increment is due to the contribution of some machine-dependent correction factors such as $(\overline{\mu_{en}/\rho})_{w,air}$ and B_w, which, with the currently available dataset (i.e., the TG-61), add nearly 40% of the combined value (Candela-Juan *et al.*, 2015b). It is recognized that the use of the in-water method should deliver lower uncertainties due to the spare of the correction factors mentioned above. However, when writing the TRS-398, there was a lack of standards for low-energy photons. That situation encouraged the International Atomic Energy Agency (IAEA) to implement a procedure to obtain the $N_{D,w}$ from N_K, a procedure that seems to be needed up today. For this reason, the future updated version of the TRS-398 will recommend the TG-61 as an intermediary step to obtain $N_{D,w}$ (Andreo, 2019).

The second important drawback corresponds to the use of the HVL as part of the Beam Quality Index (BQI) of the eBT beams. The BQI in EBRT is obtained from the PDDs (e.g., $\%dd(10)$ or $TPR_{20,10}$), which are intensively used in the clinic (Podgorsak, 2005). However, the HVL has no other practical use. Furthermore, its measurement is a cumbersome procedure, requiring the obtaining of alignment images in a trial and error iteration, and absorbent slabs of with a well-known thickness and high purity. Finally, its definition requires measurements at large source-to-detector distances, which can generate problems with the signal-to-noise ratio.

For those reasons, both the IAEA and the AAPM agree that additional studies regarding the use of BQIs obtained from depth-dose measurements are required.

Chapter 6 discuss both issues, proposing novel methods to solve them. Here, the impact of using depth-dose measurements to calculate the eBT beam BQI (or at least as an intermediary step to obtain the HVL), on the calibration uncertainties was assessed. In this regard, the information collected in chapters 4 and 5, and the data published by Candela-Juan *et al.* (2015b) regarding the uncertainties in calibrations of the Esteya system, were essential in this evaluation.

Using depth-dose as BQI requires to consider the effect of two main sources of uncertainty on its measurement: experimental and those related to the manufacturing tolerances of the eBT system. The experimental uncertainties are mainly due alignment issues and the dosimeter response (see Chapter 5). Regarding the changes in the eBT device, as previously discussed, the main structure responsible for the beam characteristics is the FF, whose tolerances in its manufacturing process are crucial. However, changes in the x-rays tube potential can also affect the beam properties in a non-negligible way.

Also, to be able to use depth-dose measurements to obtain the different factors used in the calibration, it is necessary to establish the relationship between the involved factors and the index obtained from the PDDs. To do that, we used the APP_{10mm} as a proof-of-concept, performing several simulations with PEN14 and

penEasy-2015, using the full GIS model described in Chapter 4. The simulations correlated different beam qualities, which are traduced in different PDDs, with $(\overline{\mu_{en}/\rho})_{w,air}$, B_w, and HVL (see figures 6.1, 6.2, 6.3, and 6.4). The different beam qualities were obtained by changing the thickness of the FF and the energy of the electrons in the x-rays source (Ee^-), sampling a range covering all the manufacturing tolerances provided by the vendor.

The depth-dose ratio $D_{z,3}$, which denotes the ratio of the absorbed dose measured at z mm to 3 mm depth, was used. The depths, z, explored were 10, 20, and 50 mm. From Chapter 5, the experimental uncertainties, combining the changes in the chamber response and alignment issues, can be estimated by 3%. However, to test the sensitivity of those three $D_{z,3}$, four scenarios of experimental uncertainty (0, 2, 5, and 10%) were evaluated (see tables 6.4 and 6.5). Additionally, this analysis also includes the effect of using the correction factors here reported, following a machine-specific paradigm, versus those obtained from the TG-61 dataset.

A detailed report of the results can be found in Section 6.3. The $(\overline{\mu_{en}/\rho})_{w,air}$ and B_w were calculated with uncertainties within 0.4% ($k = 2$). Both factors are in agreement, within the associated uncertainties, with the data published elsewhere for beams with similar characteristics (Ma *et al.*, 2001; Andreo, 2019). Furthermore, their values agree with those reported in chapters 4 and 5, obtained from different approaches and different release versions of PENELOPE. Figures 6.3 and 6.4 show the stability of $(\overline{\mu_{en}/\rho})_{w,air}$ and B_w, even when significant variations of the beam properties

were applied. This condition gives confidence regarding the small effect on the results that any other source of uncertainty, not considered here, may have.

The manufacturing tolerances of the FF thickness and x-rays tube potential are 0.035 mm and 0.35 kV, respectively. Those ranges change the HVL by 1.4% and 0.4%. As shown in Table 6.4, these changes produce a negligible effect on the final budget of uncertainties.

From Table 6.4, it can be appreciated that $D_{10,3}$ is the most sensitive to uncertainties in the depth-dose measurement, followed by $D_{20,3}$, and $D_{50,3}$. However, the use of deeper points to obtain $D_{z,3}$ may be traduced in signal-to-noise issues. From this point of view, an intermediate point, such as $D_{20,3}$, appears as a good compromise. However, even considering a 10% uncertainty (much higher than the value found in Chapter 5), with the most sensitive dose ratio, the effect of using depth-dose measurements as to obtain the eBT beam BQI, or as an intermediate step to find the HVL, adds only 0.2% top to the final calibration budget.

The TG-61, published in 2000 (Ma *et al.*, 2001), corresponds to the most widely used dataset for beam calibrations of low-energy photons (Andreo, 2019). However, the uncertainties estimated there are higher than those published recently by Andreo (2019), and those found here. In this regard, Table 6.5 shows that a reduction of 40% (from 5.4% to 3.4%, $k = 2$) in the combined uncertainty can be achieved, only by using the data reported in Chapter 6.

On the other hand, it is recognized that some differences in the design of the radiotherapy devices (e.g., use of open- or close-ended collimators) can significantly affect the machine-dependent factors (Ma *et al.*, 2001). In the case of the eBT, the situation is complex due to the existence of multiple applicators for the same device, with entirely different designs, intended to be used in different kind of treatments (e.g., surface, intracavitary, interstitial, etc.). For that reason, general-purpose tables with machine-dependent factors, as those published in the TG-61, may not be accounting for the specificities implicit in each applicator (e.g., different SSD, FF shapes, etc.). In this context, the generation of machine-specific datasets to obtain the machine-dependent factors could play a roll in complementing the general-purpose tables included in different protocols.

It is worth mentioning that a proper BQI should specify both the machine- and the detector-dependent factors of a determined protocol. That condition requires calibration certificates specified in terms of that quantity. Because that requirement is not meet, this work left open the possibility of using $D_{z,3}$ as an intermediate step to find the HVL, from which it is possible to obtain the detector-dependent factors, with a negligible impact in the process uncertainty. Figures 6.3 and 6.4 shown that a complete characterization of the machine-dependent factors (at least for that specific applicator size) can be obtained directly from depth-dose measurements, but further research is needed to apply this methodology directly on the detector-dependent factors.

The user obtains the detector-dependent factors from the calibration certificates. According to the certificate of the T34013 ionization chamber, the detector-dependent factors are obtained at distances $\geq$ 300 mm. However, the beam calibrations of the eBT devices are performed in configurations closer to the treatment setup (Fulkerson *et al.*, 2014; Candela-Juan *et al.*, 2015b), which can change the scatter conditions achieved in the laboratory. In the Esteya system case, the calibrations are made at a source-to-detector distance of 60 mm approximately.

Generally, the laboratories deliver calibration certificates with factors corresponding to two or more beam qualities near the user beam. Hence, the user needs to obtain the factors through interpolations. For this reason, the TG-61 recommends that the difference between the detector-dependent factors used in the interpolation should be less than 2%, normally obtaining differences lower than 1%. As an example, the ionization chamber used in Chapter 6 presents an energy dependence of 0.1% between k_{Q,Q_0} of 50 (HVL = 1.13 mm Al) and 70 kV (HVL = 3.15 mm Al) beams. Nevertheless, in Chapter 5, a difference in the correction factors of 2% was found, for the same T34013, between beams with the same Ee^- (69.5 kV) and filtration (same FF shared by all applicators) but different field size (i.e., $\text{APP}_{10\text{mm}}$ and $\text{APP}_{30\text{mm}}$). This results require more research regarding the effect of changes in the scatter conditions on the chamber response, and the role that the applicator design play in this phenomenon.

Summarizing, in this thesis, a complete dosimetric character-

ization of the Esteya system have been performed, which is the first time that this work is accomplished through MC methods in a eBT beam of 70 kV and, in particular, using PENELOPE. The data here obtained have been compared with experimental results, whose differences (generally $< 5\%$) are within those found by other authors simulating other eBT units with different MC systems.

The procedures here exposed show that some of the most relevant ratios used in radiation dosimetry of low-energy photons (e.g., $(\overline{\mu_{en}/\rho})_{w,air}$, B_w, D_w/D_{cav}, etc.) can be obtained with combined uncertainties within 0.5%. These results represent a significant improvement regarding the uncertainties reported in other dosimetric datasets such as the TG-61, whose uncertainties are considered on 3% ($k = 2$).

The experimental uncertainties in the depth-dose measurements, here defined as the combination of the system alignment, the manufacturing tolerances, and the detector response dependencies, have been obtained to be about 3%, when the recommended detector, the T34013 parallel-plate ionization chamber, is used. From this value, which is lower than those reported elsewhere for beams of 50 kV, 1% corresponds to the dependence with depth, while 2% corresponds to changes due to different applicator sizes. From all the indexes tested, the ratio of the doses measured at 20 mm to 3 mm depth ($D_{20,3}$) appears as a good candidate to be used.

Considering this information, the use of depth-doses measurements to obtain the machine- and detector-dependent factors improves the calibration procedure, avoiding the downsides of the

experimental HVL determination. This improvement is achieved with a negligible or nonexistent effect in the final calibration budget. Furthermore, the use of machine-specific datasets, together with allowing the extension of this formalism to other eBT units, makes it possible to reduce the uncertainties of absorbed dose measurements by a significant amount.

Chapter 8

Resumen en español

El cáncer de piel no melanoma (o carcinoma queratinocítico) es uno de las neoplasias más comunes en humanos (Madan *et al.*, 2010; Nehal and Bichakjian, 2018), cuya incidencia aumenta continuamente en todo el mundo (Perera *et al.*, 2015; Rogers *et al.*, 2015; Rubió-Casadevall *et al.*, 2016; Leiter *et al.*, 2017). En este contexto, la braquiterapia electrónica (eBT) de superficie se ha convertido en un tratamiento efectivo, logrando excelentes tasas de control y buenos resultados cosméticos (Bhatnagar, 2013; Ouhib *et al.*, 2015; Ballester-Sánchez *et al.*, 2017; Guinot *et al.*, 2018).

Los sistemas eBT de superficie consisten, básicamente, en dos componentes: un tubo de rayos X y un aplicador adosado. El tubo de rayos X acelera electrones en un rango de energías entre 50 keV y 70 keV, produciendo haces de rayos X aplanados. El aplicador

eBT sirve como colimador, el cual se coloca en contacto directo con la piel, posibilitando haces cónicos de 10 mm a 50 mm de diámetro. El filtro aplanador (FF) puede o no estar incluido en el aplicador, lo cual depende del diseño del sistema eBT (Candela-Juan *et al.*, 2015b).

Los dispositivos eBT resuelven algunos problemas relacionados con protección radiológica generados por el uso de radionucleidos en braquiterapia de alta tasa de dosis (Eaton, 2015). Sin embargo, el uso de fotones de baja energía dificulta la determinación de la dosis absorbida, lo que se traduce en un incremento de las incertidumbres asociadas (Hill *et al.*, 2014), cruciales para estudiar la correlación entre la dosis absorbida y la respuesta biológica (Aird *et al.*, 2016). Históricamente, las simulaciones Monte Carlo (MC) se han utilizado para resolver alguno de estos problemas, incrementando el conocimiento en relación con la terapia con radiaciones ionizantes (Chetty *et al.*, 2007; Beaulieu *et al.*, 2012; Perez-Calatayud *et al.*, 2012). Sin embargo, los métodos MC tienen sus propias limitaciones con respecto a los fotones de baja energía, en su mayoría relacionados con las diferentes implementaciones en sus librerías.

Los problemas mencionados anteriormente pueden agruparse en tres categorías:

1. Mayores incertidumbres de las secciones eficaces utilizadas en los códigos MC.

2. Mayores incertidumbres en la respuesta de los detectores.

3. Problemas relacionados con los procedimientos de calibración (índices de calidad de haz, factores de corrección, etc.).

El objetivo de esta tesis es caracterizar un dispositivo eBT de superficie de 69.5 kV, solucionando en parte alguno de los problemas mencionadas anteriormente. La energía del haz de la unidad de tratamiento aquí estudiada se encuentra en el rango superior de los dispositivos eBT comercialmente disponibles (Eaton, 2015), sobre el cual existe un déficit de información publicada.

Este proyecto se dividió en tres etapas principales. En la primera, se realizó una caracterización dosimétrica completa del sistema eBT estudiado (Capítulo 4). La metodología y resultados obtenidos en esta etapa fueron utilizados como base para las secciones siguientes. En la segunda etapa (Capítulo 5), se estudió la respuesta del detector recomendado para la dosimetría en agua de haces eBT. Específicamente, se evaluó cómo su dependencia con la profundidad y el tamaño del aplicador pueden afectar a la medida de la dosis absorbida, lo cual, hasta donde sabemos, es la primera vez que se publica esta información para este rango de energías. Estos datos fueron utilizados en la tercera etapa (Capítulo 6), donde se estudiaron las incertidumbres que emergen en una calibración de haz. En esta sección final, se propusieron nuevos procedimientos para facilitar y reducir las incertidumbres de calibración de haces eBT.

El sistema MC utilizado en este trabajo fue PENELOPE, ampliamente utilizado en aplicaciones médicas (Perez-Calatayud *et al.*,

2012; Rodriguez *et al.*, 2013), junto con penEasy (Sempau *et al.*, 2011), el programa principal que maneja todas las funcionalidades de este sistema MC. PENELOPE ha sido verificado en fotones de alta (Sempau *et al.*, 2003; Herranz *et al.*, 2015) y baja energía (Ye *et al.*, 2004; Chica *et al.*, 2009). Además, PENELOPE ha sido usado exitosamente en estudios de braquiterapia tanto con radionucleidos (Ballester *et al.*, 2015; Vijande *et al.*, 2013; Almansa *et al.*, 2017) como con fuentes electrónicas (Croce *et al.*, 2012). Se usaron dos versiones de PENELOPE y penEasy durante este trabajo, PENELOPE-2014 (PEN14), PENELOPE-2018 (PEN18), penEasy-2015 y penEasy-2019, respectivamente (Salvat *et al.*, 2015; Salvat, 2019; Sempau, 2019). El lector puede encontrar una descripción detallada de este sistema MC en el Capítulo 2. Además, una comparación de los resultados obtenidos con ambas versiones se encuentra en el Apéndice A.

El dispositivo de eBT de superficie estudiado es el sistema Esteya® (Elekta Brachytherapy, Veenendaal, Países Bajos), el cual se muestra en la Figura 3.1 y se describe extensamente en el Capítulo 3. Su tubo de rayos X acelera electrones a 69.5 keV hacia un blanco de tungsteno, generando un haz de radiación de frenado aplanado por un filtro de aluminio de 1.6 mm de grosor (medido en el eje del haz) y colimado por aplicadores desde 10 mm a 30 mm de diámetro. La salida de los aplicadores está cubierta con un plástico para reducir la contaminación electrónica del haz, dejando una distancia fuente superficie (SSD) de 60 mm (Candela-Juan *et al.*, 2015b).

La caracterización dosimétrica del sistema Esteya fue realizada con PEN14 y penEasy-2015 (ver Capítulo 4). Los aplicadores considerados fueron los de 10 mm (APP_{10mm}) y 30 mm (APP_{30mm}) de diámetro, los que presentan la menor y mayor dimensión disponible. El objetivo de esta parte del trabajo es triple. Primero, encontrar la manera más eficiente de simular el sistema eBT, sin sesgo o con un «sesgo despreciable» en los resultados de la simulación. Segundo, encontrar los modelos más apropiados (ej. fuente de rayos X) para reproducir los resultados experimentales publicados por otros autores. Finalmente, generar un archivo de espacio de fases (PSF) a la salida del aplicador para ser utilizado posteriormente en esta tesis. Vale la pena mencionar, que toda la información actualmente disponible para este sistema eBT fue obtenida experimentalmente; por lo tanto, este es el primer estudio que caracteriza por completo al sistema Esteya a través de métodos MC.

De todas las técnicas de mejora de eficiencia (EFEN) probadas, la reducción de varianza de interacción forzada (VRIF) y la modificación de las energías de corte, *EABS*, fueron las más útiles (ver Tabla 4.2), ambas descritas en el Capítulo 2. La VRIF con un factor de 150 sobre las interacciones de emisión Bremsstrahlung (*ICOL* = 4, ver Tabla 2.1) en el blanco mejora la eficiencia de la simulación en un factor de 20 (ver Figura 4.1). Por otro lado, el espectro enerégtico que aparece en la Figura 4.2 muestra una cantidad despreciable de fotones con energías menores a 10 keV saliendo del aplicador, mientras los electrones que alcanzan la cara exterior de la cubierta plástica contribuyen con un 0.005% de la energía que

registran los fotones en ese mismo lugar. Por esta razón, aplicar un *EABS* = 10 keV para fotones en todos los materiales, y para electrones en el blanco (transporte de electrones deshabilitado en cualquier otro material) permite reducir el tiempo de simulación en un 92% sin ningún cambio apreciable en el PSF.

Modelar la fuente de rayos X puede ser una de las tareas más desafiantes y sensibles en la simulación de un equipo eBT (Hiatt *et al.*, 2016). En este trabajo, hemos probado cuatro modelos de fuente de rayos X (ver Sección 4.2.1), comparando sus resultados con datos experimentales. La comparación se dividió en dos categorías: espectral y clínica. De esas comparaciones, se puede concluir que la Fuente de Intensidad Gaussiana (GIS), la cual presenta un haz monoenergético de electrones de 69.5 keV con una distribución de intensidad de electrones Gaussiana (ancho de media altura igual al tamaño de foco, ver sección 4.2.1), proporciona los mejores resultados. Así, la GIS fue elegida para usarse en las siguientes secciones.

El PSF final fue obtenido con 10^9 historias para los dos aplicadores. La energía promedio de los fotones fue 36.19 ± 0.09 keV, valor que concuerda con los 36.2 ± 0.2 keV obtenidos por Garcia-Martinez *et al.* (2014) (ver Sección 4.3.2.1). La capa hemireductora (HVL) calculada (ver Ecuación 4.1 y Sección 4.3.2.2) fue de 1.72 ± 0.04 mm, valor que se encuentra dentro del rango experimental medido por Garcia-Martinez *et al.* (2014) y Candela-Juan *et al.* (2015b).

El FF es la estructura más importante en el camino del haz

de radiación. La Figura 3.1 muestra como los fotones saliendo del tubo de rayos X «ven» diferentes espesores de filtro en su camino, dependiendo de la posición radial que estos presentan con respecto al eje del haz, lo cual genera diferentes atenuaciones. Esta característica afecta la energía promedio del haz, tal como se aprecia en la Figura 4.3. Este dispositivo eBT comparte el mismo FF con todos los aplicadores. Por esto, se espera que cualquier diferencia dosimétrica entre aplicadores esté relacionada, principalmente, con cambios en las condiciones de dispersión. Sin embargo, el efecto del FF sobre la dosimetría debe ser considerado al caracterizar un dispositivo eBT con diferentes FFs en cada aplicador.

La comparación de datos clínicos muestra diferencias esperables entre los datos simulados y medidos (considerando las incertidumbres asociadas), las cuales son comparables con aquellas encontradas por otros autores (Croce *et al.*, 2012; Fulkerson *et al.*, 2014; Moradi *et al.*, 2017; Watson *et al.*, 2017). Las diferencias máximas encontradas entre los porcentajes de dosis en profundidad (PDD) simulados y medidos es de un 4.5% (ver Figura 4.5), la cual se encuentra en la superficie del maniquí. No obstante, a profundidades mayores a 1 mm, las diferencias bajan a menos de un 2%. Respecto a la comparación de los perfiles de dosis fuera de eje (DP), diferencias de hasta un 15% en radios 16 mm $<$ r $<$ 17 mm fueron encontradas. Sin embargo, dichas diferencias fueron obtenidas en zonas de alto gradiente de dosis, donde son subsanadas con un corrimiento de 0.4 mm en el perfil (ver Figura 4.7).

La verificación de la dosis absorbida representa una parte esen-

cial del programa de garantía de calidad en radioterapia (Andreo *et al.*, 2000; Ma *et al.*, 2001; Venselaar *et al.*, 2004), incluyendo a la eBT (Thomadsen *et al.*, 2009; Candela-Juan *et al.*, 2015a; Eaton, 2015). En este sentido, el dosímetro recomendado en haces de fotones de bajas energías es la cámara de ionización plano paralela (Andreo *et al.*, 2000; Ma *et al.*, 2001). Debido a las propiedades de los haces eBT discutidas en la Sección 1.2, la respuesta esperada del detector puede ser muy sensible a cambios en las características del haz (ej., debido al endurecimiento del haz con la profundidad), o a diferencias detector a detector (ej., tolerancias de fabricación), tal como fue probado para haces de 50 kV (Watson *et al.*, 2017) e ^{192}Ir (Gimenez-Alventosa *et al.*, 2018).

Hasta donde sabemos, la cámara de ionización plano paralela PTW 34013 (PTW, Freiburg, Alemania) (ver Figura 5.2) es el único dosímetro recomendado para dosimetría en agua de haces eBT (Candela-Juan *et al.*, 2015a; Fulkerson *et al.*, 2020). Por esta razón, esta parte del trabajo, la cual está descrita completamente en el Capítulo 5, estudió la dependencia de la respuesta de este detector con la profundidad y el tamaño del aplicador, proponiendo estrategias para mitigar estos efectos, tales como encontrar el punto efectivo de medida (EPoM) óptimo. Adicionalmente, las incertidumbres experimentales en las medidas de dosis en profundidad fueron abordadas.

El estudio de la cámara de ionización requirió evaluar los cambios en los factores de corrección de perturbación con la profundidad y el tamaño del aplicador. En el caso de la ecuación 5.2, es

necesario calcular tres diferentes cantidades a diferentes profundidades y con diferentes aplicadores (APP_{10mm} y APP_{30mm}) para lograr ese objetivo. Esas cantidades son la razón de los coeficientes de absorción de energía másico agua a aire $(\overline{\mu_{en}/\rho})_{w,air}$ (ver Ecuación 5.1), la razón entre la dosis absorbidas en agua (D_w, sin la presencia de la cámara de ionización) y en la cavidad de la cámara (D_{cav}) en el maniquí de agua. Dichas simulaciones fueron realizadas utilizando PEN18 con penEasy-2019, ambos descritos extensamente en la Sección 5.2.

La obtención de las cantidades mencionadas anteriormente requieren un procedimiento intensivo en poder de cálculo, en especial para D_{cav}. Por este motivo, se realizó una modificación del modelo GIS para incrementar la eficiencia de la simulación, evitando el transporte de electrones en el modelo de la fuente de rayos X. Primero, el espectro de energía GIS fue registrado en la ventana de berilio del tubo de rayos X (ver Figura 3.1), utilizando la configuración simplificada descrita en la sección 4.2.1. Después, este espectro fue utilizado en una fuente puntual colimada, con una apertura suficiente como para cubrir completamente el colimador primario (ver Figura 3.1). El efecto de esta modificación en los resultados fue abordado a través de simulaciones adicionales con el modelo GIS, siendo evaluado en menos de un 0.2% (ver Tabla 5.2).

Tres métodos fueron propuestos para mitigar el efecto de la profundidad en la respuesta de la cámara. El primero, considera un factor de corrección de superficie, p_{surf}, (ver Ecuación 5.3), la

cual relaciona D_{cav} con D_w en la superficie del maniquí de agua (caso típico en la práctica clínica), manteniendo el EPoM recomendado por el fabricante ($\mathrm{EPoM_{man}}$) (centro de la cara interna de la ventana de entrada, ver figuras 5.2 y 5.3). El siguiente caso usa un factor de corrección global, p_{glob} (ver ecuaciones 5.4 y 5.5), considerando todas las profundidades simuladas en esta parte del trabajo (hasta 20 mm de profundidad), también utilizando $\mathrm{EPoM_{man}}$. El último método (ver ecuaciones 5.6 y 5.7), también considera el rango completo de profundidades pero, esta vez, cambiando el $\mathrm{EPoM_{man}}$ a un punto donde el factor de corrección de perturbación, p_{shift}, es lo más independiente de la profundidad posible.

El valor de $(\overline{\mu_{en}/\rho})_{w,air}$ fue 1.018 ± 0.02, lo cual concuerda con los datos publicados para haces con kV y HVL similares (Ma *et al.*, 2001; Andreo, 2019). La variación de esta razón con la profundidad y el tamaño del aplicador es menor a 0.06%. Por lo tanto, esta cantidad fue considerada constante. La razón D_w/D_{cav} varia en 1% y 0.6% con la profundidad para $\mathrm{APP_{10mm}}$ y $\mathrm{APP_{30mm}}$ (ver Figura 5.5), respectivamente. La misma variación fue obtenida cuando la dosis absorbida fue calculada con la Ecuación 5.2 utilizando p_{surf} (ver Tabla 5.3 y Figura 5.7). El uso de p_{glob} redujo las diferencias en la determinación de la dosis absorbida dentro del 0.6% y 0.5% para $\mathrm{APP_{10mm}}$ y $\mathrm{APP_{30mm}}$, respectivamente. Cuando la dosis absorbida fue calculada utilizando p_{shift} y un EPoM corrido por 0.4 mm hacia el fondo del volumen sensible (ver Figura 5.6), los cambios observados con la profundidad se redujeron a 0.5% y 0.3% para $\mathrm{APP_{10mm}}$ y $\mathrm{APP_{30mm}}$, respectivamente. Respecto a la depen-

dencia del factor de perturbación con el tamaño del aplicador, se observó una diferencia de un 2% entre APP_{10mm} y APP_{30mm}.

Las tres cantidades aquí calculadas fueron obtenidas con una incertidumbre de un 0.4%. Un reporte completo de las incertidumbres consideradas en sus cálculos puede ser encontrado en la Tabla 4.6. Un especial énfasis fue puesto en el tratamiento de las librerías fotoeléctricas, en particular, a la corrección de renormalización de Pratt (ver Sección 2.2.2), la cual ha sido extensamente discutida por otros autores (Andreo *et al.*, 2012; Seltzer *et al.*, 2014; Sabbatucci and Salvat, 2016; Pratt, 2014). Las diferencias debido a su inclusión (o no) son menores a 0.2%.

Las incertidumbres experimentales fueron estimadas a través de varias mediciones de dosis en profundidad, realizadas con tres cámaras de ionización PTW T34013 diferentes (ver Figura 5.3 y Sección 5.2.3 para más detalles). Las medidas fueron realizadas por una sola persona, con una unidad Esteya, en un maniquí plástico. Las diferencias en las dosis absorbidas entre las medidas fueron menores a 2%. Este resultado incluye las diferencias estructurales entre detectores y las incertidumbres experimentales en alineamiento, posicionamiento de la cámara, entre otros.

Watson *et al.* (2017) estudiaron la cámara PTW T34013 con un haz sin filtrar de 50 kV. Ellos encontraron un cambio de un 2.5% en el $(\overline{\mu_{en}/\rho})_{w,air}$, en el mismo rango de profundidades utilizados en esta tesis. Además, encontraron diferencias en la respuesta de la cámara hasta de un 5% a 15 mm de profundidad, utilizando la geometría del detector especificada por el fabricante (sin considerar

las tolerancias de fabricación). Cuando los autores incorporaron en el análisis las posibles diferencias en la estructura de la cámara debido a las tolerancias de fabricación, se reportaron cambios de un 12% en la respuesta de la cámara con la profundidad. Con respecto al EPoM, ellos sugirieron que el efecto de la tolerancia de fabricación sobre la respuesta de la cámara puede ser mitigada cambiando el $\mathrm{EPoM_{man}}$ al punto medio de su volumen sensible. Si embargo, de acuerdo con los datos presentados, este cambio incrementa la dependencia con la profundidad.

Los resultados aquí presentados permiten concluir que la T34014 es significativamente menos susceptible a sufrir cambios en su respuesta con el haz Esteya que aquellos obtenidos con un haz de 50 kV. Además, las dependencias con la profundidad pueden ser reducidas desde un 1% a menos de un 0.6% al utilizar los métodos p_{glob} o p_{shift}. La dependencia con el tamaño de campo (2%) fue obtenida en los tamaños de campo límite ofrecidos por el fabricante. Considerando que todos los aplicadores comparten el mismo FF, 2% puede ser considerado como un valor conservativo para el juego completo de aplicadores. El EPoM óptimo fue encontrado a 0.4 mm desde $\mathrm{EPoM_{man}}$. Este hallazgo concuerda con el TG-61, que recomienda posicionar el EPoM en el punto medio del volumen sensible de la cámara (Ma *et al.*, 2001). No obstante, la posición del EPoM óptimo puede ser muy dependiente de las características del haz, tal como fue reportado por Gimenez-Alventosa *et al.* (2018), quienes encontraron diferencias significativas en su posición para dos aplicadores de braquiterapia alta tasa de dosis utilizando

una fuente de ^{192}Ir. Por este motivo, este es un tema que requiere de más investigación.

La calibración de haz es un procedimiento crítico en la verificación de la dosis absorbida. Existen dos métodos recomendados para la calibración de haces eBT. El método en aire, propuesto en el TG-61 (Ma *et al.*, 2001), está basado en medidas de kerma en aire, utilizando el factor N_K. Mientras que el método en agua del TRS-398 (Andreo *et al.*, 2000), está basado en dosis absorbida en agua, a través del $N_{D,w}$. Desde el punto de vista de los factores de calibración (ver Sección 6.2.2), podemos dividirlos en dos clases, dependiendo de si dependen del detector o del equipo de tratamiento. Dentro de los factores detector dependiente, podemos mencionar al $N_{D,w}$, N_K, o al k_{Q,Q_0} (factor que corrige por las diferencias entre la calidad del haz de referencia y la calidad del haz del usuario). Mientras que los factores equipo dependiente considerados en este trabajo son $(\overline{\mu_{en}/\rho})_{w,air}$ y el factor de retrodispersión (B_w).

Sin importar el método elegido, las calibraciones de haces eBT presentan dos importantes desventajas con respecto al mismo procedimiento en radioterapia de haces externos (EBRT). Primero, las calibraciones de haces eBT presentan incertidumbres más altas, estimadas entre un 5% y un 7% (Ma *et al.*, 2001; Candela-Juan *et al.*, 2015b), comparado con EBRT, cuyas incertidumbres han sido estimadas en menos de un 4%, con un $k = 2$ en ambos casos (Ma *et al.*, 2001; Castro *et al.*, 2008). Una parte importante en este incremento se debe a la contribución de algunos factores de corrección equipo dependiente, como el $(\overline{\mu_{en}/\rho})_{w,air}$ y el B_w, los cuales,

con el juego de datos actualmente disponibles (ej., TG-61), agregan cerca de un 40% al valor combinado (Candela-Juan *et al.*, 2015b). Es reconocido que el uso del método en agua debería entregar calibraciones con incertidumbres menores debido que prescinde de los factores de corrección mencionados anteriormente. Sin embargo, al momento de escribir el TRS-398 no habían estándares para fotones de baja energía. Esta situación hizo que la Organización Internacional de Energía Atómica (OIEA) implementara un procedimiento para la obtención del $N_{D,w}$ a partir del N_K; procedimiento que, al parecer, continúa siendo necesario hasta el día de hoy. Por este motivo, la futura versión actualizada del TRS-398 recomendará la utilización del TG-61 como un paso intermedio para la obtención del $N_{D,w}$ (Andreo, 2019).

La segunda desventaja corresponde al uso de la HVL como parte del índice de calidad de haz (BQI). En EBRT, el BQI es obtenido desde los PDDs (ej., $\%dd(10)$ o $\mathrm{TPR}_{20,10}$), los cuales son intensamente utilizados en la clínica (Podgorsak, 2005). No obstante, la HVL no tiene otro uso práctico. Además, su medida es un procedimiento engorroso, requiriendo la obtención de imágenes de alineamiento en un proceso iterativo de ensayo y error, y de láminas absorbentes con espesores de alta precisión y pureza. Finalmente, su definición requiere medidas a una larga distancia fuente detector, lo que genera problemas con el índice señal ruido. Por estas razones, tanto la OIEA como la AAPM concuerdan en que se requieren más estudios con respecto al uso de BQIs obtenidos desde medidas de dosis en profundidad (Ma *et al.*, 2001; Andreo *et al.*,

2000).

El Capítulo 6 discute ambos problemas, proponiendo nuevos métodos para solucionarlos. Aquí, se abordó el impacto de utilizar medidas de dosis en profundidad para el calculo del BQI de un haz eBT (o como un paso intermedio para la obtención de la HVL) sobre las incertidumbres de calibración. En este sentido, la información obtenida en los capítulos 4 y 5, y los datos publicados por Candela-Juan *et al.* (2015b) en relación a las incertidumbres de calibración del sistema eBT Esteya, fueron esenciales en esta evaluación.

La utilización de la dosis en profundidad para el cálculo del BQI requiere considerar el efecto de dos fuentes principales de incertidumbre en su medida: la experimental y aquellas relacionadas con las tolerancias de fabricación en el sistema eBT. Las incertidumbres experimentales se deben principalmente a problemas de alineación y a la respuesta de la cámara de ionización (ver Capitulo 5). Con respecto a los cambios en el dispositivo eBT, como ya fue discutido, la estructura más importante responsable por las características del haz es el FF, cuya tolerancia en su fabricación son cruciales. Sin embargo, también hay que considerar el potencial del tubo de rayos X, cuyos cambios pueden afectar las propiedades del haz de manera no despreciable.

Además, para ser capaz de utilizar medidas de dosis en profundidad para la obtención de los diferentes factores utilizados en la calibración, es necesario establecer la relación entre dichos factores y los índices obtenidos a partir de los PDDs. Para hacer esto,

hemos utilizado el $\mathrm{APP}_{10\mathrm{mm}}$ como prueba de concepto, a través de varias simulaciones con PEN14 y penEasy-2015, utilizando el modelo GIS descrito en el Capítulo 4. Las simulaciones correlacionaron diferentes calidades de haz, las cuales se traducen en diferentes PDDs, con el $(\overline{\mu_{en}/\rho})_{w,air}$, B_w, y la HVL (ver figuras 6.1, 6.2, 6.3, y 6.4). Las diferentes calidades de haz fueron obtenidas cambiando el grosor del FF y la energía de los electrones en la fuente de rayos X (Ee^-), recorriendo un rango que cubre todas las tolerancias de fabricación comunicadas por el vendedor.

La índice de dosis en profundidad utilizado fue $D_{z,3}$, el cual denota la razón entre las dosis absorbidas medidas a la profundidades z mm y 3 mm. Las profundidades z exploradas fueron 10, 20 y 50 mm. En el Capítulo 5, las incertidumbres experimentales, las cuales combinan los cambios en la respuesta de la cámara y diferencias en el alineamiento del sistema, pueden ser estimadas en un 3%. No obstante, para probar la sensibilidad de las tres $D_{z,3}$ cuatro escenarios de incertidumbre experimental (0, 2, 5 y 10%) fueron evaluados (ver tablas 6.4 y 6.5). Adicionalmente, este análisis también incluye el efecto de usar los factores de calibración aquí reportados, siguiendo un paradigma equipo específico, comparados con aquellos obtenidos del juego de datos TG-61.

En la Sección 6.3 se incluye una descripción detallada de los resultados obtenidos. Los $(\overline{\mu_{en}/\rho})_{w,air}$ y B_w fueron calculados con incertidumbres dentro del 0.4% ($k = 2$). Ambos factores concuerdan, dentro de las incertidumbres asociadas, con los datos publicados por otros autores para haces de características similares

(Ma *et al.*, 2001; Andreo, 2019). Además, sus valores concuerdan con aquellos reportados en el Capítulo 5, obtenidos con diferentes aproximaciones y versiones de PENELOPE. Las figuras 6.3 y 6.4 muestran la estabilidad de los $(\overline{\mu_{en}/\rho})_{w,air}$ y B_w, inclusive cuando variaciones significativas de las propiedades del haz fueron aplicadas. Esta condición indica el pequeño efecto en los resultados que cualquier otra fuente de incertidumbre, no considerada aquí, pueda tener.

Las tolerancias de fabricación en el grosor del FF y el potencial de tubo de rayos X son 0.035 mm y 0.35 kV, respectivamente. Estos rangos cambian la HVL en 1.4% y 0.4%. Como se muestra en la Tabla 6.4, esos cambios generan un efecto despreciable en las incertidumbre final de calibración.

De la Tabla 6.4, puede ser apreciado que $D_{10,3}$ es el más sensible a las incertidumbres en la medida de dosis en profundidad, seguido por $D_{20,3}$ y $D_{50,3}$. Sin embargo, el uso de puntos a mayor profundidad para la obtención de $D_{z,3}$ puede generar problemas en la razón señal ruido. Desde este punto de vista, un punto intermedio, como el $D_{20,3}$, aparece como una buena opción. Sin perjuicio de lo anterior, incluso considerando una incertidumbre de un 10% (superando con creces el valor establecido en el Capítulo 5), con la razón de dosis más sensible, el efecto de utilizar las medidas de dosis en profundidad para la obtención del BQI de haces eBT, o como un paso intermedio para encontrar la HVL, agrega un 0.2% como máximo a la incertidumbre combinada de calibración.

El TG-61, publicado en el año 2000 (Ma *et al.*, 2001), corres-

ponde al conjunto de datos más utilizado para la calibración de haces de fotones de baja energía (Andreo, 2019). Sin embargo, las incertidumbres estimadas en ese documento son mayores a las publicadas por Andreo (2019) y a las reportadas aquí. En este sentido, la Tabla 6.5 muestra que una reducción del 40% (desde un 5.4% a un 3.4% con un $k = 2$) en la incertidumbre combinada puede ser alcanzada, solo por utilizar los datos ofrecidos en el Capitulo 6.

Por otro lado, es sabido que algunas diferencias en el diseño de los equipos de radioterapia (ej., el uso de colimadores con salida abierta o cerrada) puede afectar significativamente los factores equipo dependiente (Ma *et al.*, 2001). En el caso de la eBT, la situación es compleja debido a la existencia de múltiples aplicadores para el mismo equipo, con diseños completamente diferentes, ideados para ser usados en diferentes tipos de tratamiento (ej., superficial, intracavitario, intersticial, etc.). Por esta razón, tablas con datos generales con factores equipo dependiente, como aquellos publicados en el TG-61, pueden no estar tomando en cuenta las especificaciones implícitas en cada aplicador (ej., diferentes SSD, formas de FF, etc.). En este contexto, la obtención de conjuntos de datos equipo específico para al obtención de factores equipo dependiente puede jugar un papel en complementar las tablas generales incluidas en distintos protocolos.

Es necesario mencionar que un BQI debería especificar tanto los factores detector y equipo dependiente en un protocolo determinado. Esta condición requiere certificados de calibración especificados en términos de esa cantidad. Debido a que este requerimiento

no está siendo cumplido, este trabajo deja abierta la posibilidad de utilizar $D_{z,3}$ como un paso intermedio para encontrar la HVL, desde la cual es posible obtener los factores detector dependiente, con un impacto despreciable en la incertidumbre del proceso. Las figuras 6.3 y 6.4 muestran que una completa caracterización de dichos factores (al menos para ese tamaño de aplicador concreto) puede ser obtenida completamente a partir de medidas de dosis en profundidad, pero se requiere más investigación para aplicar esta metodología directamente en los factores detector dependiente.

El usuario obtiene los factores detector dependiente de los datos incluidos en el certificado de calibración. De acuerdo con el certificado de la cámara T34013, estos fueron obtenidos a distancias mayores a 300 mm. Sin embargo, la calibración de los haces eBT son realizadas en configuraciones cercanas a las de tratamiento (Fulkerson *et al.*, 2014; Candela-Juan *et al.*, 2015b), lo cual puede cambiar las condiciones de dispersión logradas en el laboratorio. En el caso del sistema Esteya, la calibración de haz se realiza a una distancia fuente detector de 60 mm, aproximadamente.

Generalmente, los laboratorios entregan certificados con factores correspondientes a dos o más calidades de haz cercanos al del usuario, por lo que este debe realizar interpolaciones para obtener los datos específicos para su haz de tratamiento. Por este motivo, el TG-61 recomienda que la diferencia entre los factores usados en la interpolación deben ser menores que 2%, donde es normal obtener diferencias menores a un 1%. Como ejemplo, la cámara de ionización utilizada en el Capítulo 6 presenta una dependencia en

energía de un 0.1% entre el k_{Q,Q_0} de los haces de 50 (HVL = 1.13 mm Al) y 70 kV (HVL = 3.15 mm Al). No obstante, en el Capítulo 5 fue encontrada una diferencia en el factor de corrección de un 2%, para la misma T34013, con la misma filtración (mismo FF compartido por todos los aplicadores) y Ee^- (69.5 kV), pero con distintos tamaños de campo (es decir, $\mathrm{APP}_{10\mathrm{mm}}$ y $\mathrm{APP}_{30\mathrm{mm}}$). Estos resultados requieren mayor investigación con respecto al efecto que los cambios en las condiciones de dispersión puedan tener sobre la respuesta de la cámara, y el papel que el diseño del aplicador puede tener en este fenómeno.

En resumen, en esta tesis se ha realizado una completa caracterización del sistema Esteya, lo cual es la primera vez que esto es logrado a través de métodos MC en un equipo eBT de 70 kV y, en particular, utilizando PENELOPE. Los resultados aquí obtenidos han sido comparados con datos experimentales cuyas diferencias (generalmente $< 5\%$) están dentro de las encontradas por otros autores, simulando otros equipos eBT con diferentes sistemas MC.

Los procedimientos aquí expuestos muestran que algunos de las cantidades más relevantes en dosimetría de radiaciones de fotones de baja energía (ej., $(\overline{\mu_{en}/\rho})_{w,air}$, B_w, D_w/D_{cav}, etc.) pueden ser obtenidos con incertidumbres combinadas dentro del 0.5%. Estos resultados representan una mejora considerable con respecto a las incertidumbres reportadas en otros juegos de datos como el TG-61, cuyas incertidumbres son consideradas en un 3% ($k = 2$).

La incertidumbre experimental, aquí definida como la combinación del alineamiento del sistema, las tolerancias de fabricación

y las dependencias de la respuesta del detector, han sido calculadas en un 3%, cuando el detector recomendado, la cámara de ionización plano paralela T34013, es utilizado. De este 3%, el cual es menor que aquel reportado por otros autores para haces de 50 kV, un 1% corresponde a dependencias con la profundidad y un 2% corresponde a diferencias en los tamaños de aplicador. De todos los índices probados, la razón de las dosis medidas a 20 mm y 3 mm de profundidad ($D_{20,3}$) aparece como un buen candidato para ser usado como BQI en calibraciones de haces eBT.

Considerando esta información, se puede concluir que el uso de medidas de dosis en profundidad para obtener los factores equipo y detector dependiente mejora el procedimiento de calibración, evitando las desventajas de la determinación experimental de la HVL. Esta mejora es lograda con un efecto despreciable o no existente en la incertidumbre final de calibración. Además, el uso un juego de datos equipo específico, junto con permitir la extensión de este formalismo a otras unidades eBT, hace posible reducir las incertidumbres de las medidas de dosis absorbida en una proporción significativa.

References

Aird, E., Bentzen, S., Coffey, M., Gomola, I., Hamilton, C., Healy, B., *et al.* (2016). *Accuracy Requirements and Uncertainties in Radiotherapy*. INTERNATIONAL ATOMIC ENERGY AGENCY, Vienna. URL https://www.iaea.org/publications/10668/accuracy-requirements-and-uncertainties-in-radiotherapy.

Ali, E. S. M. and Rogers, D. W. O. (2007). Efficiency improvements of x-ray simulations in EGSnrc user-codes using bremsstrahlung cross-section enhancement (BCSE). *Med. Phys.*, 34:2143–2154. URL http://doi.wiley.com/10.1118/1.2736778.

Almansa, J. F., Guerrero, R., Torres, J., and Lallena, A. M. (2017). Monte Carlo dosimetric characterization of the Flexisource Co-60 high-dose-rate brachytherapy source using PENELOPE. *Brachytherapy*, 16(5):1073–1080. URL http://dx.doi.org/10.1016/j.brachy.2017.04.245.

Almond, P. R., Biggs, P. J., Coursey, B. M., Hanson, W. F., Huq,

M. S., Nath, R., *et al.* (1999). AAPM's TG-51 protocol for clinical reference dosimetry of high-energy photon and electron beams. *Med. Phys.*, 26(9):1847–1870. URL http://doi.wiley.com/10.1118/1.598691.

Andreo, P. (2019). Data for the dosimetry of low- and medium-energy kV x rays. *Phys. Med. Biol.*, 64(20):205019. URL http://iopscience.iop.org/article/10.1088/1361-6560/ab421d.

Andreo, P., Burns, D. T., Hohlfeld, K., Huq, M. S., Kanai, T., Laitano, F., *et al.* (2000). *Absorbed Dose Determination in External Beam Radiotherapy.* INTERNATIONAL ATOMIC ENERGY AGENCY, Vienna. URL https://www.iaea.org/publications/5954/absorbed-dose-determination-in-external-beam-radiotherapy.

Andreo, P., Burns, D. T., and Salvat, F. (2012). On the uncertainties of photon mass energy-absorption coefficients and their ratios for radiation dosimetry. *Phys. Med. Biol.*, 57(8):2117–2136. URL http://stacks.iop.org/0031-9155/57/i=8/a=2117?key=crossref.687d36896c52f5d4b8e20093c96baf0d.

Badal, A. and Sempau, J. (2006). A package of Linux scripts for the parallelization of Monte Carlo simulations. *Comput. Phys. Commun.*, 175(6):440–450. URL https://linkinghub.elsevier.com/retrieve/pii/S001046550600230X.

Ballester, F., Carlsson Tedgren, Å., Granero, D., Haworth, A., Mourtada, F., Fonseca, G. P., *et al.* (2015). A generic high-dose

rate 192 Ir brachytherapy source for evaluation of model-based dose calculations beyond the TG-43 formalism. *Med. Phys.*, 42:3048–3062. URL http://doi.wiley.com/10.1118/1.4921020.

Ballester-Sánchez, R., Pons-Llanas, O., Candela-Juan, C., de Unamuno-Bustos, B., Celada-Alvarez, F. J., Tormo-Mico, A., *et al.* (2017). Two years results of electronic brachytherapy for basal cell carcinoma. *J. Contemp. Brachytherapy*, 3(3):251–255. URL https://www.termedia.pl/doi/10.5114/jcb.2017.68191.

Basaglia, T., Pia, M. G., and Saracco, P. (2020). Evolutions in Photoelectric Cross Section Calculations and Their Validation. *IEEE Trans. Nucl. Sci.*, 67(3):492–501. URL https://ieeexplore.ieee.org/document/8978746/.

Baym, G. (1974). *Lectures in Quantum Mechanics*. Westview Press, Boulder, Colorado.

Bearden, J. A. (1967). X-Ray Wavelengths. *Rev. Mod. Phys.*, 39(1):78–124. URL https://link.aps.org/doi/10.1103/RevModPhys.39.78.

Beaulieu, L., Carlsson Tedgren, Å., Carrier, J.-F., Davis, S. D., Mourtada, F., Rivard, M. J., *et al.* (2012). Report of the Task Group 186 on model-based dose calculation methods in brachytherapy beyond the TG-43 formalism: Current status and recommendations for clinical implementation. *Med. Phys.*,

39(10):6208–6236. URL http://doi.wiley.com/10.1118/1.4747264.

Berger, M. J., Inokuti, M., Anderson, H. H., Bichsel, H., Dennis, J. A., Powers, D., *et al.* (1984). Report 37: Stopping Powers for Elecctrons and Positrons. *J. Int. Comm. Radiat. Units Meas.*, os19(2):NP–NP. URL https://academic.oup.com/jicru/article/2923758/Report.

Bhatnagar, A. (2013). Nonmelanoma skin cancer treated with electronic brachytherapy: Results at 1 year. *Brachytherapy*, 12(2):134–140. URL https://linkinghub.elsevier.com/retrieve/pii/S153847211200236X.

BIPM (2010). Evaluation of measurement data — Guide to the expression of uncertainty in measurement. Technical report, BIPM.

Born, M. (1969). *Atomic Physics*. Blackie and Son, London.

Butson, M. J., Yu, P. K., Cheung, T., and Alnawaf, H. (2010). Energy response of the new EBT2 radiochromic film to x-ray radiation. *Radiat. Meas.*, 45(7):836–839. URL http://dx.doi.org/10.1016/j.radmeas.2010.02.016.

Candela-Juan, C., Niatsetski, Y., Ouhib, Z., Ballester, F., Vijande, J., and Perez-Calatayud, J. (2015a). Commissioning and periodic tests of the Esteya® electronic brachytherapy system. *J. Contemp. Brachytherapy*, 2(2):189–195. URL http://www.termedia.pl/doi/10.5114/jcb.2015.51523.

Candela-Juan, C., Vijande, J., García-Martínez, T., Niatsetski, Y., Nauta, G., Schuurman, J., *et al.* (2015b). Comparison and uncertainty evaluation of different calibration protocols and ionization chambers for low-energy surface brachytherapy dosimetry. *Med. Phys.*, 42(8):4954–4964. URL `http://doi.wiley.com/10.1118/1.4927059`.

Castro, P., García-Vicente, F., Mínguez, C., Floriano, A., Sevillano, D., Pérez, L., *et al.* (2008). Study of the uncertainty in the determination of the absorbed dose to water during external beam radiotherapy calibration. *J. Appl. Clin. Med. Phys.*, 9(1):70–86. URL `http://doi.wiley.com/10.1120/jacmp.v9i1.2676`.

Chassagne, D., Dutreix, A., Almond, P., Burgers, J. M. V., Busch, M., and Joslin, C. A. (1985). Report 38: Dose and Volume Specification for Reporting Intracavitary Therapy in Gynecology. *J. Int. Comm. Radiat. Units Meas.*, os20(1):NP–NP. URL `https://academic.oup.com/jicru/article/2923724/Report`.

Chetty, I. J., Curran, B., Cygler, J. E., DeMarco, J. J., Ezzell, G., Faddegon, B. A., *et al.* (2007). Report of the AAPM Task Group No. 105: Issues associated with clinical implementation of Monte Carlo-based photon and electron external beam treatment planning. *Med. Phys.*, 34(12):4818–4853. URL `http://doi.wiley.com/10.1118/1.2795842`.

Chica, U., Anguiano, M., and Lallena, A. (2009). Benchmark of PENELOPE for low and medium energy X-rays. *Phys. Medica*,

25(2):51–57. URL http://dx.doi.org/10.1016/j.ejmp.2008.04.001.

Clausen, S., Schneider, F., Jahnke, L., Fleckenstein, J., Hesser, J., Glatting, G., *et al.* (2012). A Monte Carlo based source model for dose calculation of endovaginal TARGIT brachytherapy with INTRABEAM and a cylindrical applicator. *Z. Med. Phys.*, 22(3):197–204. URL http://linkinghub.elsevier.com/retrieve/pii/S0939388912000645.

Croce, O., Hachem, S., Franchisseur, E., Marcié, S., Gérard, J.-P., and Bordy, J.-M. (2012). Contact radiotherapy using a 50kV X-ray system: Evaluation of relative dose distribution with the Monte Carlo code PENELOPE and comparison with measurements. *Radiat. Phys. Chem.*, 81(6):609–617. URL http://linkinghub.elsevier.com/retrieve/pii/S0969806X12000515.

Cullen, D., Hubbell, J., and Kissel, L. (1997). EPDL97: the evaluated photo data library '97 version. Technical report, Lawrence Livermore National Laboratory (LLNL), Livermore, CA. URL http://www.osti.gov/servlets/purl/295438-uZu33l/webviewable/.

Deslattes, R. D., Kessler, E. G., Indelicato, P., de Billy, L., Lindroth, E., and Anton, J. (2003). X-ray transition energies: new approach to a comprehensive evaluation. *Rev. Mod. Phys.*, 75(1):35–99. URL https://link.aps.org/doi/10.1103/RevModPhys.75.35.

DeWerd, L. A., Ibbott, G. S., Meigooni, A. S., Mitch, M. G., Rivard, M. J., Stump, K. E., *et al.* (2011). A dosimetric uncertainty analysis for photon-emitting brachytherapy sources: Report of AAPM Task Group No. 138 and GEC-ESTRO. *Med. Phys.*, 38(2):782–801. URL http://doi.wiley.com/10.1118/1.3533720.

Eaton, D. J. (2015). Electronic brachytherapy—current status and future directions. *Br. J. Radiol.*, 88(1049):20150002. URL http://www.birpublications.org/doi/10.1259/bjr.20150002.

Famulari, G., Renaud, M.-A., Poole, C. M., Evans, M. D. C., Seuntjens, J., and Enger, S. A. (2018). RapidBrachyMCTPS: a Monte Carlo-based treatment planning system for brachytherapy applications. *Phys. Med. Biol.*, 63(17):175007. URL https://iopscience.iop.org/article/10.1088/1361-6560/aad97a.

Fulkerson, R. K., Micka, J. A., and DeWerd, L. A. (2014). Dosimetric characterization and output verification for conical brachytherapy surface applicators. Part I. Electronic brachytherapy source. *Med. Phys.*, 41(2):022103. URL http://doi.wiley.com/10.1118/1.4862505.

Fulkerson, R. K., Perez-Calatayud, J., Ballester, F., Buzurovic, I., Kim, Y., Niatsetski, Y., *et al.* (2020). Surface brachytherapy: Joint report of the AAPM and the GEC-ESTRO Task Group No. 253. *Med. Phys.* URL https://doi.org/10.1002/mp.14436.

GafChromic (2014). White Paper: GafChromic ® EBT2 and

EBT3 films for Ball Cube II Phantom. Technical report. URL http://www.gafchromic.com/documents/BallCube_II_EBT2_3_box_insert_201404.pdf.

Garcia-Martinez, T., Chan, J.-P., Perez-Calatayud, J., and Ballester, F. (2014). Dosimetric characteristics of a new unit for electronic skin brachytherapy. *J. Contemp. Brachytherapy*, 1(1):45–53. URL http://www.termedia.pl/doi/10.5114/jcb.2014.40770.

Gerbaulet, A., Pötter, R., Mazeron, J.-J., Meertens, H., and Van Limbergen, E. (2002). *The GEC ESTRO Handbook of Brachytherapy*. ESTRO, Brussels, 1 edition.

Gimenez-Alventosa, V., Gimenez, V., Ballester, F., Vijande, J., and Andreo, P. (2018). Correction factors for ionization chamber measurements with the 'Valencia' and 'large field Valencia' brachytherapy applicators. *Phys. Med. Biol.*, 63(12):125004. URL http://stacks.iop.org/0031-9155/63/i=12/a=125004?key=crossref.a8fa2669d6d0d57086590b19df9c5c47.

Goubert, M. and Parent, L. (2015). Dosimetric characterization of INTRABEAM® miniature accelerator flat and surface applicators for dermatologic applications. *Phys. Medica*, 31(3):224–232. URL http://dx.doi.org/10.1016/j.ejmp.2015.01.009.

Grosswendt, B. (1984). Backscatter factors for x-rays generated at voltages between 10 and 100 kV. *Phys. Med. Biol.*, 29(5):579–

591. URL http://stacks.iop.org/0031-9155/29/i=5/a=010?key=crossref.f297dfcc438c548565432f2c46ac499c.

Guedea, F. (2014). Perspectives of brachytherapy: Patterns of care, new technologies, and "new biology". *Cancer/Radiothérapie*, 18(5-6):434–436. URL http://dx.doi.org/10.1016/j.canrad.2014.07.143.

Guinot, J. L., Rembielak, A., Perez-Calatayud, J., Rodríguez-Villalba, S., Skowronek, J., Tagliaferri, L., *et al.* (2018). GEC-ESTRO ACROP recommendations in skin brachytherapy. *Radiother. Oncol.*, 126(3):377–385. URL https://linkinghub.elsevier.com/retrieve/pii/S0167814018300355.

Herranz, E., Herraiz, J. L., Ibáñez, P., Pérez-Liva, M., Puebla, R., Cal-González, J., *et al.* (2015). Phase space determination from measured dose data for intraoperative electron radiation therapy. *Phys. Med. Biol.*, 60(1):375–401. URL http://stacks.iop.org/0031-9155/60/i=1/a=375?key=crossref.24bc8b20fd78075c8bfb38d8f2583993.

Hiatt, J. R., Davis, S. D., and Rivard, M. J. (2015). A revised dosimetric characterization of the model S700 electronic brachytherapy source containing an anode-centering plastic insert and other components not included in the 2006 model. *Med. Phys.*, 42:2764–2776. URL http://doi.wiley.com/10.1118/1.4919280.

Hiatt, J. R., Rivard, M. J., and Hughes, H. G. (2016). Simula-

tion evaluation of NIST air-kerma rate calibration standard for electronic brachytherapy. *Med. Phys.*, 43(3):1119–1129. URL http://doi.wiley.com/10.1118/1.4940791.

Hill, R., Healy, B., Holloway, L., Kuncic, Z., Thwaites, D., and Baldock, C. (2014). Advances in kilovoltage x-ray beam dosimetry. *Phys. Med. Biol.*, 59(6):R183–R231. URL http://stacks.iop.org/0031-9155/59/i=6/a=R183?key=crossref.ce53fed329f640c23f1508026c0112d3.

IAEA (2003). *Security of Radioactive Sources - Interim Guidance for Comment*. INTERNATIONAL ATOMIC ENERGY AGENCY, Vienna. URL https://www.iaea.org/publications/6861/security-of-radioactive-sources-interim-guidance-for-comment.

Ibanez-Rosello, B., Bautista-Ballesteros, J. A., Candela-Juan, C., Villaescusa, J. I., Ballester, F., Vijande, J., *et al.* (2017). Evaluation of the shielding in a treatment room with an electronic brachytherapy unit. *J. Radiol. Prot.*, 37(2):N5–N12. URL http://stacks.iop.org/0952-4746/37/i=2/a=N5?key=crossref.7d35c1cbaf948988490e21ab2ca2cbf4.

Joiner, M. C. and van der Kogel, A. (2009). *Basic Clinical Radiobiology*. CRC Press, London. URL https://www.taylorfrancis.com/books/9781444109610.

Kairn, T., Aland, T., and Kenny, J. (2010). Local heterogeneities in early batches of EBT2 film: a suggested solution. *Phys. Med.*

Biol., 55(15):L37–L42. URL http://stacks.iop.org/0031-9155/55/i=15/a=L02?key=crossref.189f3ce1d13f3c93550b84d509029122.

Kawrakow, I. (2006). On the effective point of measurement in megavoltage photon beams. *Med. Phys.*, 33:1829–1839. URL http://doi.wiley.com/10.1118/1.2201147.

Kubo, H. D., Glasgow, G. P., Pethel, T. D., Thomadsen, B. R., and Williamson, J. F. (1998). High dose-rate brachytherapy treatment delivery: Report of the AAPM Radiation Therapy Committee Task Group No. 59. *Med. Phys.*, 25(4):375–403. URL http://doi.wiley.com/10.1118/1.598232.

Leiter, U., Keim, U., Eigentler, T., Katalinic, A., Holleczek, B., Martus, P., *et al.* (2017). Incidence, Mortality, and Trends of Nonmelanoma Skin Cancer in Germany. *J. Invest. Dermatol.*, 137(9):1860–1867. URL http://dx.doi.org/10.1016/j.jid.2017.04.020.

Lewis, D. and Devic, S. (2015). Correcting scan-to-scan response variability for a radiochromic film-based reference dosimetry system. *Med. Phys.*, 42(10):5692–5701. URL http://doi.wiley.com/10.1118/1.4929563.

Ma, C.-M., Coffey, C. W., DeWerd, L. A., Liu, C., Nath, R., Seltzer, S. M., *et al.* (2001). AAPM protocol for 40-300 kV x-ray beam dosimetry in radiotherapy and radiobiology. *Med. Phys.*,

28(6):868–893. URL http://doi.wiley.com/10.1118/1.1374247.

Ma, C. M. C., Chetty, I. J., Deng, J., Faddegon, B., Jiang, S. B., Li, J., *et al.* (2019). Beam modeling and beam model commissioning for Monte Carlo dose calculation-based radiation therapy treatment planning: Report of AAPM Task Group 157. *Med. Phys.*

Madan, V., Lear, J. T., and Szeimies, R. M. (2010). Non-melanoma skin cancer. *Lancet*, 375(9715):673–685. URL https://linkinghub.elsevier.com/retrieve/pii/S014067360961196X.

Mayorga, P. A., Brualla, L., Flühs, A., Sauerwein, W., and Lallena, A. M. (2016). Testing Monte Carlo absolute dosimetry formalisms for a small field 'D'-shaped collimator used in retinoblastoma external beam radiotherapy. *Biomed. Phys. Eng. Express*, 2(6):065008. URL http://stacks.iop.org/2057-1976/2/i=6/a=065008?key=crossref.76b0bf3b204f1134493774d9d8add425.

Moradi, F., Ung, N. M., Khandaker, M. U., Mahdiraji, G. A., Saad, M., Abdul Malik, R., *et al.* (2017). Monte Carlo skin dose simulation in intraoperative radiotherapy of breast cancer using spherical applicators. *Phys. Med. Biol.*, 62(16):6550–6566. URL http://stacks.iop.org/0031-9155/62/i=16/a=6550?key=crossref.19566b95c08ce9f5951c4799230232e1.

Nath, R., Anderson, L. L., Luxton, G., Weaver, K. A., Williamson,

J. F., and Meigooni, A. S. (1995). Dosimetry of interstitial brachytherapy sources: Recommendations of the AAPM Radiation Therapy Committee Task Group No. 43. *Med. Phys.*, 22(2):209–234. URL http://doi.wiley.com/10.1118/1.597458.

Nath, R., Rivard, M. J., DeWerd, L. A., Dezarn, W. A., Thompson Heaton, H., Ibbott, G. S., *et al.* (2016). Guidelines by the AAPM and GEC-ESTRO on the use of innovative brachytherapy devices and applications: Report of Task Group 167. *Med. Phys.*, 43:3178–3205. URL http://doi.wiley.com/10.1118/1.4951734.

Nehal, K. S. and Bichakjian, C. K. (2018). Update on keratinocyte carcinomas. *N. Engl. J. Med.*, 379(4):363–374.

Niatsetski, Y. (2018). Personal comunication.

NUDAT 2.8 (2020). National Nuclear Data Center, Brookhaven National Laboratory. URL https://www.nndc.bnl.gov/nudat2/.

Ouhib, Z., Kasper, M., Perez Calatayud, J., Rodriguez, S., Bhatnagar, A., Pai, S., *et al.* (2015). Aspects of dosimetry and clinical practice of skin brachytherapy: The American Brachytherapy Society working group report. *Brachytherapy*, 14(6):840–858. URL https://linkinghub.elsevier.com/retrieve/pii/S1538472115005048.

Perera, E., Gnaneswaran, N., Staines, C., Win, A. K., and Sinclair, R. (2015). Incidence and prevalence of non-melanoma skin cancer in Australia: A systematic review. *Australas. J. Dermatol.*, 56(4):258–267. URL `http://doi.wiley.com/10.1111/ajd.12282`.

Perez-Calatayud, J., Ballester, F., Das, R. K., DeWerd, L. A., Ibbott, G. S., Meigooni, A. S., *et al.* (2012). Dose calculation for photon-emitting brachytherapy sources with average energy higher than 50 keV: Report of the AAPM and ESTRO. *Med. Phys.*, 39(5):2904–2929. URL `http://doi.wiley.com/10.1118/1.3703892`.

Perkins, S. T., Cullen, D. E., Chen, M. H., Hubbell, J. H., Rathkopf, J., and Scofield, J. H. (1991). Tables and Graphs of Atomic Subshell and Relaxation Data Derived from the LLNL Evaluated Atomic Data Library (EADL), Z = 1-100, Technical Report UCRL-ID-50400. Technical report, Lawrence Livermore National Laboratory, Livermore, CA.

Podgorsak, E. (2005). *Radiation Oncology Physics: A Handbook for Teachers and Students*. IAEA, Vienna. URL `https://www.iaea.org/publications/7086/radiation-oncology-physics`.

Pozuelo, F., Gallardo, S., Querol, A., Verdu, G., and Rodenas, J. (2012). X-ray simulation with the Monte Carlo code PENELOPE. Application to Quality Control. In *2012 Annu. Int.*

Conf. IEEE Eng. Med. Biol. Soc., volume 2012, pages 5777–5780. IEEE. URL http://ieeexplore.ieee.org/document/6347307/.

Pratt, R. (2014). Photon absorption and photon scattering—What we do not know and why it matters. *Radiat. Phys. Chem.*, 95:4–13. URL http://dx.doi.org/10.1016/j.radphyschem.2013.10.018.

Ramaseshan, R., Kohli, K., Cao, F., and Heaton, R. (2008). Dosimetric evaluation of Plastic Water Diagnostic Therapy. *J. Appl. Clin. Med. Phys.*, 9(2):98–111. URL http://doi.wiley.com/10.1120/jacmp.v9i2.2761.

Ribberfors, R. (1983). X-ray incoherent scattering total cross sections and energy-absorption cross sections by means ofsimple calculation routines R. *Phys. Rev. A*, 27(6):3061–3070. URL https://link.aps.org/doi/10.1103/PhysRevA.27.3061.

Rivard, M. J., Coursey, B. M., DeWerd, L. A., Hanson, W. F., Saiful Huq, M., Ibbott, G. S., *et al.* (2004). Update of AAPM Task Group No. 43 Report: A revised AAPM protocol for brachytherapy dose calculations. *Med. Phys.*, 31(3):633–674. URL http://doi.wiley.com/10.1118/1.1646040.

Rivard, M. J., Davis, S. D., DeWerd, L. A., Rusch, T. W., and Axelrod, S. (2006). Calculated and measured brachytherapy dosimetry parameters in water for the Xoft Axxent X-Ray Source: An electronic brachytherapy source. *Med. Phys.*,

33(11):4020–4032. URL http://doi.wiley.com/10.1118/1.2357021.

Rodriguez, M., Sempau, J., and Brualla, L. (2013). PRIMO: A graphical environment for the Monte Carlo simulation of Varian and Elekta linacs. *Strahlentherapie und Onkol.*, 189(10):881–886. URL http://link.springer.com/10.1007/s00066-013-0415-1.

Rodriguez, M., Sempau, J., and Brualla, L. (2015). Technical Note: Study of the electron transport parameters used in PENELOPE for the Monte Carlo simulation of Linac targets. *Med. Phys.*, 42:2877–2881. URL http://doi.wiley.com/10.1118/1.4916686.

Rogers, H. W., Weinstock, M. A., Feldman, S. R., and Coldiron, B. M. (2015). Incidence Estimate of Nonmelanoma Skin Cancer (Keratinocyte Carcinomas) in the US Population, 2012. *JAMA Dermatology*, 151(10):1081. URL http://archderm.jamanetwork.com/article.aspx?doi=10.1001/jamadermatol.2015.1187.

Rubió-Casadevall, J., Hernandez-Pujol, A., Ferreira-Santos, M., Morey-Esteve, G., Vilardell, L., Osca-Gelis, G., *et al.* (2016). Trends in incidence and survival analysis in non-melanoma skin cancer from 1994 to 2012 in Girona, Spain: A population-based study. *Cancer Epidemiol.*, 45:6–10. URL https://linkinghub.elsevier.com/retrieve/pii/S1877782116301473.

Sabbatucci, L. and Salvat, F. (2016). Theory and calculation of the atomic photoeffect. *Radiat. Phys. Chem.*, 121:122–140. URL `https://linkinghub.elsevier.com/retrieve/pii/S0969806X15300815`.

Safigholi, H., Faghihi, R., Jashni, S. K., and Meigooni, A. S. (2012). Characteristics of miniature electronic brachytherapy x-ray sources based on TG-43U1 formalism using Monte Carlo simulation techniques. *Med. Phys.*, 39(4):1971–1979. URL `http://doi.wiley.com/10.1118/1.3693046`.

Sakurai, J. J. (1967). *Advanced Quantum Mechanics*. Addison and Wesley, New York, 1 edition.

Salvat, F. (2019). PENELOPE-2018: A Code System for Monte Carlo Simulation of Electron and Photon Transport.

Salvat, F., Fernández-Varea, J., and Sempau, J. (2015). PENELOPE-2014: A Code System for Monte Carlo Simulation of Electron and Photon Transport.

Sechopoulos, I., Rogers, D. W., Bazalova-Carter, M., Bolch, W. E., Heath, E. C., McNitt-Gray, M. F., *et al.* (2018). RECORDS: Improved Reporting of montE CarlO RaDiation transport Studies: Report of the AAPM Research Committee Task Group 268. *Med. Phys.*, 45(1):e1–e5.

Seltzer, S. M., Fernandez-Varea, J. M., Andreo, P., Bergstrom, P. M., Burns, D. T., Krajcar-Bronic, I., *et al.* (2014). Report

90: Key Data for Ionizing-Radiation Dosimetry: Measurement Standards and Applications. *J. ICRU*, 14(1):NP.2–NP. URL https://academic.oup.com/jicru/article-lookup/doi/10.1093/jicru/ndw043.

Sempau, J. (2019). PENELOPE / penEasy User Manual. Technical report, Barcelona, Spain. URL https://inte.upc.edu/en/downloads/peneasy/usermanual.pdf/view.

Sempau, J. and Andreo, P. (2006). Configuration of the electron transport algorithm of PENELOPE to simulate ion chambers. *Phys. Med. Biol.*, 51(14):3533–3548. URL http://stacks.iop.org/0031-9155/51/i=14/a=017?key=crossref.35055128a4c1e9d57145e29aa0c6bcb9.

Sempau, J., Badal, A., and Brualla, L. (2011). A PENELOPE -based system for the automated Monte Carlo simulation of clinacs and voxelized geometries-application to far-from-axis fields. *Med. Phys.*, 38(11):5887–5895. URL http://doi.wiley.com/10.1118/1.3643029.

Sempau, J., Fernández-Varea, J., Acosta, E., and Salvat, F. (2003). Experimental benchmarks of the Monte Carlo code penelope. *Nucl. Instruments Methods Phys. Res. Sect. B Beam Interact. with Mater. Atoms*, 207(2):107–123. URL http://linkinghub.elsevier.com/retrieve/pii/S0168583X03004531.

Sempau, J., Sánchez-Reyes, A., Salvat, F., ben Tahar, H. O., Jiang, S. B., and Fernández-Varea, J. M. (2001). Monte Carlo

simulation of electron beams from an accelerator head using PENELOPE. *Phys. Med. Biol.*, 46(4):1163–1186. URL http://stacks.iop.org/0031-9155/46/i=4/a=318?key=crossref.3d0c8bae90d54ddfcffcf90654093646.

Thomadsen, B. R., Biggs, P. J., Cardarelli, G. A., Chu, J. C., Cormack, R. A., Feng, W., *et al.* (2019). Electronic Intracavitary Brachytherapy Quality Management based on Risk Analysis: The Report of AAPM TG 182. *Med. Phys.*, 53(9):mp.13910. URL https://onlinelibrary.wiley.com/doi/abs/10.1002/mp.13910.

Thomadsen, B. R., Biggs, P. J., DeWerd, L. A., II, C. C. W., Chiu-Tsao, S.-T., Gossman, M. S., *et al.* (2009). The 2007 AAPM response to the CRCPD request for recommendations for the CRCPD's model regulations for electronic brachytherapy. Technical report. URL https://www.aapm.org/pubs/reports/detail.asp?docid=157.

Tom, M. C., Hepel, J. T., Patel, R., Kamrava, M., Badiyan, S. N., Cohen, G. N., *et al.* (2018). The American Brachytherapy Society consensus statement for electronic brachytherapy. *Brachytherapy*. URL https://linkinghub.elsevier.com/retrieve/pii/S1538472118306731.

Valdes-Cortez, C., Niatsetski, Y., Perez-Calatayud, J., Ballester, F., and Vijande, J. (2019). A Monte Carlo-based dosimetric characterization of Esteya ® , an electronic surface brachyther-

apy unit. *Med. Phys.*, 46(1):356–369. URL http://doi.wiley.com/10.1002/mp.13275.

Venselaar, J., Pérez-Calatayud, J., Bidmead, M., Briot, E., Burgers, J., Ferreira, I., *et al.* (2004). A practical guide to quality control of brachytherapy equipment. *Eur. Guidel. Qual. Assur. Radiother.*, 8(January 2001).

Vidal, M., Ibáñez, P., Guerra, P., Valdivieso-Casique, M. F., Rodríguez, R., Illana, C., *et al.* (2019). Fast optimized Monte Carlo phase-space generation and dose prediction for low energy x-ray intra-operative radiation therapy. *Phys. Med. Biol.*, 64(7):075002. URL http://stacks.iop.org/0031-9155/64/i=7/a=075002?key=crossref.be99cfec49e5be32bd045ea5221ddb9f.

Vijande, J., Granero, D., Perez-Calatayud, J., and Ballester, F. (2012). Monte Carlo dosimetric study of the Flexisource Co-60 high dose rate source. *J. Contemp. Brachytherapy*, 1(1):34–44. URL http://www.termedia.pl/doi/10.5114/jcb.2012.27950.

Vijande, J., Granero, D., Perez-Calatayud, J., and Ballester, F. (2013). Monte Carlo dosimetric study of the medium dose rate CSM40 source. *Appl. Radiat. Isot.*, 82:283–288. URL http://linkinghub.elsevier.com/retrieve/pii/S0969804313003722.

Walters, B. R. B., Kawrakow, I., and Rogers, D. W. O. (2002). History by history statistical estimators in the BEAM code sys-

tem. *Med. Phys.*, 29(12):2745–2752. URL http://doi.wiley.com/10.1118/1.1517611.

Watson, P. G. F., Popovic, M., and Seuntjens, J. (2017). Determination of absorbed dose to water from a miniature kilovoltage x-ray source using a parallel-plate ionization chamber. *Phys. Med. Biol.*, 63(1):015016. URL http://stacks.iop.org/0031-9155/63/i=1/a=015016?key=crossref.b81eabc95f663370c3829152692055eb.

Williamson, J. F. (1987). Monte Carlo evaluation of kerma at a point for photon transport problems. *Med. Phys.*, 14(4):567–576. URL http://doi.wiley.com/10.1118/1.596069.

Ye, S.-J., Brezovich, I. A., Pareek, P., and Naqvi, S. A. (2004). Benchmark of PENELOPE code for low-energy photon transport: dose comparisons with MCNP4 and EGS4. *Phys. Med. Biol.*, 49(3):387–397. URL http://stacks.iop.org/0031-9155/49/i=3/a=003?key=crossref.23d3c7488c85bf3929192c2e4f9ab7b5.

Appendix A

Comparison between PENELOPE versions

A.1 Introduction

This work mainly required the calculation of four quantities: kerma in water, photon energy fluence (Ψ), mass energy-absorption coefficient ratio water to air ($(\overline{\mu_{en}/\rho})_{w,air}$), and absorbed dose in a volume of air. All those quantities were calculated up to a maximum depth of 50 mm. As it was already mentioned, two versions of PENELOPE (PEN14 and PEN18) were used through this thesis. Hence, a comparison of the four quantities above described, calculated with both release versions, is required to ensure the consistency of the data. The simulation setup used in the comparisons of

Ψ and $(\overline{\mu_{en}/\rho})_{w,air}$, was extensively described in Chapter 6. While the configuration used in the comparison of the absorbed dose in a volume of air, was fully described in Chapter 5. For the case of the kerma in water comparison, the simulation setup is described in this chapter.

A.2 Kerma in water comparison

The comparison of the kerma in water was made in a water sphere of 15 cm radius. Monoenergetic photon beams were emitted, with initial energies (E_0) of 5, 10, 15, 35, 45, 55, and 75 keV, from a point-like isotropic source at the center of the sphere. Photons were tracked with a cutoff energy of 1 keV, while the electrons transport was disabled (infinite cutoff energy). To take advantage of the spherical symmetry, the energy transferred by photons to the medium was scored in spherical shells of 1 mm thick, from 1 mm to 50 mm distance from the source (49 bins in total). The maximum distance from the source was chosen to include the entire depths range considered in this thesis. Each simulation was made with at least 1×10^{11} primary particles, which allow keeping the Type A uncertainties below 0.1% up to 10 mean free paths (MFP). To generalize the results, a comparison of the data was made taking the MFP of the photons with energy equal to E_0 as a distance unit (see table A.1).

A.3 Mass energy-absorption coefficient ratio comparisons

The comparisons of the photon energy fluence and $(\overline{\mu_{en}/\rho})_{w,air}$ were performed using the geometry of the Esteya eBT system (see Figure 3.1). The Ψ spectrum corresponds to an x-ray beam generated with an electron beam that impinges the tungsten target of the Esteya x-ray tube that mimics the conditions of the real eBT machine. The Ψ spectrum was scored at the exit of the 10 mm diameter applicator (APP_{10mm}) of the Esteya system, in a cylindrical air volume of 1 mm radius and 0.1 mm height, embedded in free air, with an energy resolution of 0.1 keV. The mass energy-absorption coefficient ratio of water to air was calculated through equation 5.1. Both $(\mu_{en}/\rho)_w$ and $(\mu_{en}/\rho)_{air}$ were calculated with the *mutren* code, available in each PENELOPE release.

A.4 Comparison of absorbed dose in a volume of air

The absorbed dose comparison requires the use of two complex geometries, corresponding to the Esteya eBT unit and the parallel-plate ionization chamber PTW T34013. The absorbed dose was scored in the sensitive volume of the T34013 chamber (see Figure 5.2), which is filled with air. The ionization chamber was placed

with the inner center of its entrance foil at the surface of a water phantom. The Esteya APP_{10mm} was placed in contact with the upper surface of the chamber (see figure 5.3). The x-ray source of the Esteya system (called GIS in sections 4 and 5) was replaced by a point-like photon source placed at the lower center of the target (called "simplified source" or SSo in Section 5). SSo used the energy spectrum of the GIS x-ray beam scored in the beryllium window of the Esteya x-ray tube (see Figure 3.1). In this comparison, the photons were tracked with a cutoff energy of 8 keV in the structures within the eBT system and 1 keV elsewhere. The electron transport was disabled in all materials but those closer than 0.1 mm from the sensitive volume of the ionization chamber, and in the sensitive volume itself. In the materials where the electron transport was enabled, they were tracked with an energy cutoff of 1 keV.

A.5 Results

A.5.1 Kerma in water comparison

A summary of the results can be observed in table A.1 and figure A.1. For 5 and 10 keV, differences within 0.1% and 0.4% were found for 5 and 15 MFP, respectively. The differences found in the 15 keV comparison were lower than 0.2 % up to 50 mm depth. For all the other energies, the differences were within 0.1% in the entire depth range. Weighting the differences by energy over the Esteya unit spectra results in a global difference lower than 0.1%

Table A.1: Summary of the kerma in water comparison between PEN14 and PEN18. Energies above 35 keV present the same results.

energy (keV)	Item	MFP			
		1	5	10	15
5	depth (mm)	0.2	1.2	2.4	3.6
	max. uncert. (%)	–	< 0.1	< 0.1	2.3
	dif. max. (%)	–	0.1	0.2	0.4
10	depth (mm)	1.9	9.6	19.2	28.8
	max. uncert. (%)	< 0.1	< 0.1	< 0.1	1.5
	dif. max. (%)	0.02	0.1	0.2	0.4
15	depth (mm)	6.1	30.4	50.0	
	max. uncert. (%)	< 0.1	< 0.1	< 0.1	
	dif. max. (%)	0.02	0.1	0.2	
35	depth (mm)		50.0		
	max. uncert. (%)		< 0.1		
	dif. max. (%)		< 0.1		

between both codes for all depths.

A.5.2 Mass energy-absorption coefficients ratio

The calculated $(\overline{\mu_{en}/\rho})_{w,air}$ were 1.01865 (4) and 1.01861 (3) for PEN14 and PEN18, respectively. The difference obtained is within the statistical uncertainties.

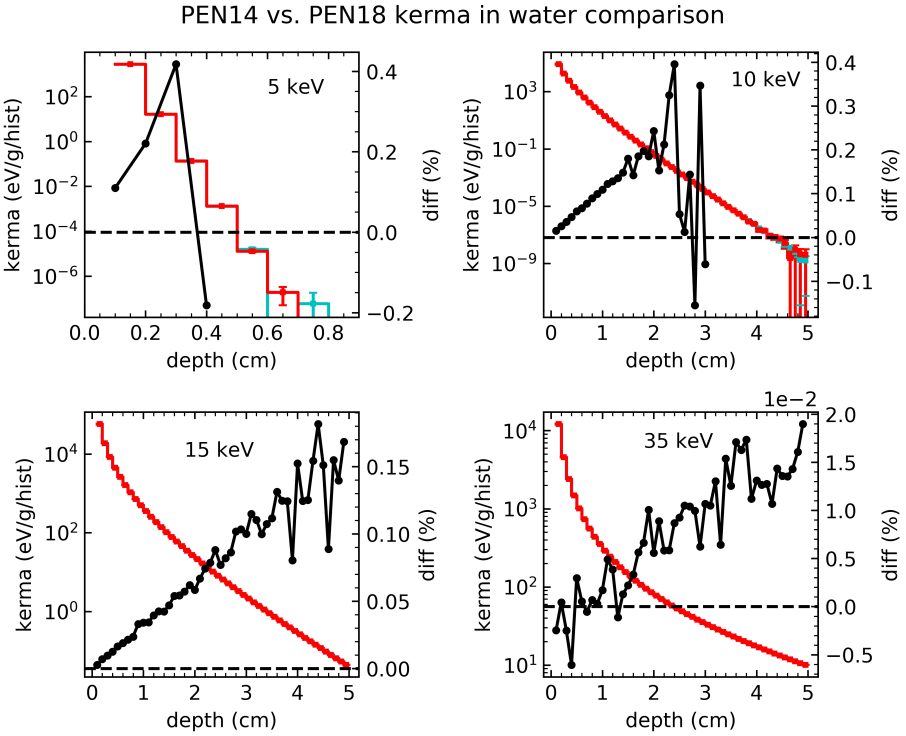

Figure A.1: Comparison between the kerma in water calculated with PEN14 and PEN18 for 5, 10, 15, and 35 keV. Cyan and red curves correspond to PEN14 and PEN18, respectively (left axes). The black curve corresponds to the difference (%) between codes (right axes). The differences are showed up to 15 mean free paths (5 and 10 keV) or up to 50 mm depth (from 15 to 75 keV) as appropriate.

A.5.3 Absorbed dose in a volume of air

The doses calculated inside the sensitive volume of the chamber were 3.590×10^{-4} eV/g for both code releases. The statistical

uncertainties were kept within 0.1%.

A.6 Conclusions

The findings presented in this chapter show that PEN14 and PEN18 deliver equivalent results, allowing using the data obtained with the oldest version as a base of the simulations ran with the newest one. Thus, without losing internal coherence in the performed calculations.

Appendix B

Publications

B.1 Published articles

Valdes-Cortez, C., Niatsetski, Y., Perez-Calatayud, J., Ballester, F., & Vijande, J. (2019). A Monte Carlo-based dosimetric characterization of Esteya, an electronic surface brachytherapy unit. Medical Physics, 46(1), 356–369.

Valdes-Cortez, C., Niatsetski, Y., Ballester, F., Vijande, J., Candela-Juan, C. & Perez-Calatayud, J. (2020). On the use of the absorbed depth-dose measurements in the beam calibration of a surface electronic high-dose-rate brachytherapy unit, a Monte Carlo-based study. Medical Physics, 47(2), 693-702.

Valdes-Cortez, C., Ballester, F., Vijande,J., Gimenez, V., Gimenez-

Alventosa, V., & Andreo, P. (2020) Corrections for the T34013 parallel-plate ionization chamber in depth-dose measurements of surface electronic brachytherapy beam, a Monte Carlo study on the Esteya® eBT system. Physics in Medicine & Biology (Accepted).

B.2 Conference proceeding

Valdes, C., Niatsetski, Y., Perez-Calatayud, J., Ballester, F., & Vijande, J. (2018). SU-I-GPD-T-36 Obtaining the Phase Space of An Electronic Brachytherapy Equipment for Surfaces Treatments Through Monte Carlo Simulations. Medical Physics, 45(6), e246–e246.

C. Valdés, F. Ballester, J. Vijande & J. Perez-Calatayud (2019). EP-1749 Relation between depth dose and HVL for electronic brachytherapy systems: a Monte Carlo study. Radiotherapy and Oncology, 133, S943-S944.

Valdes-Cortez, C., Niatsetski, Y., Vijande, J., Ballester, F., Candela-Juan, C., & Perez-Calatayud, J. (2020). PO-GeP-T-38 A New HVL-Free Method to Calibrate Surface Electronic Brachytherapy Devices Using Depth-Dose Ratios. Medical Physics, (accepted).

Appendix C

Published original papers

A Monte Carlo-based dosimetric characterization of Esteya®, an electronic surface brachytherapy unit

Christian Valdes-Cortez
Department of Atomic, Molecular and Nuclear Physics, University of Valencia, Burjassot 46100, Spain
Radiotherapy Department, Centro Oncológico de Antofagasta, Los Pumas, 10255 Antofagasta, Chile

Yury Niatsetski
R&D Elekta Brachytherapy, Waardgelder 1, 3905 TH Veenendaal, The Netherlands

Jose Perez-Calatayud
Unidad Mixta de Investigación en Radiofísica e Instrumentación Nuclear en Medicina (IRIMED) Instituto de Investigación Sanitaria La Fe (IIS-La Fe)-Universitat de Valencia (UV), E-46026 Valencia, Spain
Radiotherapy Department, La Fe Hospital, E-46026 Valencia, Spain

Facundo Ballester[a)] and Javier Vijande
Department of Atomic, Molecular and Nuclear Physics, University of Valencia, Burjassot 46100, Spain
Unidad Mixta de Investigación en Radiofísica e Instrumentación Nuclear en Medicina (IRIMED), Instituto de Investigación Sanitaria La Fe (IIS-La Fe)-Universitat de Valencia (UV), Burjassot 46100, Spain

(Received 14 June 2018; revised 7 October 2018; accepted for publication 23 October 2018; published 28 November 2018)

Purpose: The purpose of this work is threefold: First, to obtain the phase space of an electronic brachytherapy (eBT) system designed for surface skin treatments. Second, to explore the use of some efficiency enhancing (EFEN) strategies in the determination of the phase space. Third, to use the phase space previously obtained to perform a dosimetric characterization of the Esteya eBT system.
Methods: The Monte Carlo study of the 69.5 kVp x-ray beam of the Esteya® unit (Elekta Brachytherapy, Veenendaal, The Netherlands) was performed with PENELOPE2014. The EFEN strategies included the use of variance reduction techniques and mixed Class II simulations, where transport parameters were fine-tuned. Four source models were studied varying the most relevant parameters characterizing the electron beam impinging the target: the energy spectrum (mono-energetic or Gaussian shaped), and the electron distribution over the focal spot (uniform or Gaussian shaped). Phase spaces obtained were analyzed to detect differences in the calculated data due to the EFEN strategy or the source configuration. Depth dose curves and absorbed dose profiles were obtained for each source model and compared to experimental data previously published.
Results: In our EFEN strategy, the interaction forcing variance reduction (VRIF) technique increases efficiency by a factor ~20. Tailoring the transport parameters values (C1 and C2) does not increase the efficiency in a significant way. Applying a universal cutoff energy EABS of 10 keV saves 84% of CPU time while showing negligible impact on the calculated results. Disabling the electron transport by imposing an electron energy cutoff of 70 keV (except for the target) saves an extra 8% (losing in the process 1.2% of the photons). The Gaussian energy source (FWHM = 10%, centered at the nominal kVp, homogeneous electron distribution) shows characteristic K-lines in its energy spectrum, not observed experimentally. The average photon energy using an ideal source (mono-energetic, homogeneous electron distribution) was 36.19 ± 0.09 keV, in agreement with the published measured data of 36.2 ± 0.2 keV. The use of a Gaussian-distributed electron source (mono-energetic) increases the penumbra by 50%, which is closer to the measurement results. The maximum discrepancy of the calculated percent depth dose with the corresponding measured values is 4.5% (at the phantom surface, less than 2% beyond 1 mm depth) and 5% (for the 80% of the field) in the dose profile. Our results agree with the findings published by other authors and are consistent within the expected Type A and B uncertainties.
Conclusions: Our results agree with the published measurement results within the reported uncertainties. The observed differences in PDD, dose profiles, and photon spectrum come from three main sources of uncertainty: intermachine variations, measurements, and Monte Carlo calculations. It has been observed that a mono-energetic source with a Gaussian electron distribution over the focal spot is a suitable choice to reproduce the experimental data. [https://doi.org/10.1002/mp.13275]

Key words: dosimetry, electronic brachytherapy, Monte Carlo simulation, simulation efficiency, surface treatment, x-ray source

1. INTRODUCTION

High-dose-rate (HDR) brachytherapy has been widely used in surface skin treatments. This technique normally uses a radioisotope in combination with different applicators, all extensively detailed in the literature.[1–4] The HDR radioisotopes used are the ^{192}Ir, with an average photon energy of 350.0 keV, and the ^{60}Co, with an average photon energy of 1252.9 keV.[5] In recent years, a new kind of skin electronic HDR brachytherapy (eBT) units has been introduced, generating great interest in the medical community due to their clinical properties.[3] That has encouraged the AAPM/ESTRO Task Group No. 253 on Surface Brachytherapy to undergo a review of surface eBT devices.

The surface eBT systems consist mainly of an x-ray tube, which accelerates electrons in the energy range between 50 and 70 kVp, and an applicator (sizes between 10 and 50 mm), which may serve as collimator and flattening filter.[6] Following other brachytherapy treatments, the surface HDR eBT treatments are delivered with the applicator positioned directly in contact with the skin. Currently, there are three HDR eBT systems specially designed for surface treatments, the Xoft Axxent® (iCad, San Jose, CA), the Zeiss INTRABEAM® (Carl Zeiss Surgical Gmbh, Oberkochen, Germany), and the Esteya® (Elekta Brachytherapy, Veenendaal, The Netherlands).[6]

Some of the practical advantages of the eBT systems are the reduction of the shielding requirements and the avoidance to replace the radiation source.[7] However, the low energy of the generated x rays, far below the energy range of the HDR radionuclides, results in some drawbacks. The steep absorbed dose fall-off with depth increases the volume-averaging effect of the dosimeters, affecting absorbed dose measurement accuracy.[6] Furthermore, at these energies the mass energy absorption coefficients differ substantially for different body tissues, which could lead to large errors in the dose estimation whenever the dose determination is performed based on a single reference tissue (e.g., water). This encourages the use of more sophisticated treatment planning systems (TPS), capable of taking into account tissue heterogeneities.[8] Thus, it is imperative to obtain a better understanding of the dosimetric characteristics of the eBT systems.

To accomplish that purpose, it is necessary to acquire relevant data, often by experimental and theoretical means, both complementary to each other. The Monte Carlo (MC) calculation is the theoretical gold standard. However, the computation time required to achieve results with an acceptable uncertainty is a major concern. To manage this situation, the MC calculation is often performed in two stages. In a first step, the beam phase space is obtained through the simulation of a detailed model of the equipment under study. In the second step, the machine phase space, stored as a manageable file (PSF), is used to reproduce the beam and simulate its interaction with different materials.[9] This approach is very useful when studying clinical cases, allowing variation in specific patient anatomy and body composition; or in the study of dosimetric equipment for a particular energy spectrum (e.g., effective point of measurement, correction factors, etc.).[10]

The MC efficiency relates Type A uncertainties with the computational time required to achieve it. Therefore, to tackle complex and time-consuming simulations, all MC codes incorporate some kind of efficiency enhancing (EFEN) techniques.[9] However, the use of these tools often increases the time required to simulate a single history. Therefore, they are only useful if the overall efficiency is improved. That implies an extra effort of trial-and-error iterations until the appropriate parameters are found on a case-by-case basis. Moreover, there is evidence that the inappropriate manipulation of some user-defined transport model parameters could result in biasing outcomes.[5,8,9,11,12] For these reasons, the EFEN strategies need to be used carefully.

The Esteya eBT system has been studied by other authors, mainly experimentally.[6,7,13–15] The aim of this work is divided into three main objectives: obtaining the phase space at the applicator exit of the Esteya system, exploring some EFEN strategies to achieve a good compromise between reliability and efficiency, and performing a dosimetric characterization of the Esteya system using the obtained phase space.

2. MATERIAL AND METHODS

2.A. The Esteya high-dose-rate electronic brachytherapy system

The Esteya system was fully described elsewhere.[6,13] For that reason, we will only make a brief description here. The x-ray tube accelerates electrons at 69.5 kVp toward a tungsten target. Its maximum absorbed dose rate is 198 Gy/h, measured at the phantom surface. This dose rate is above the lower limit (12 Gy/h) of the HDR classification.[16]

This unit has a set of conical applicators of 10, 15, 20, 25, and 30 mm diameter, which provide a circular radiation shape of the corresponding size. Each applicator has a plastic cap, especially designed to reduce the electron contamination and to keep the source to surface distance (SSD) approximately equal to 6 cm.[6,13] In this work, we will explore the characteristics of the smallest and largest applicators, 10 mm (APP_{10mm}) and 30 mm (APP_{30mm}) diameter, respectively.

2.B. Monte Carlo Esteya model

Two types of setups were implemented: the detailed setup, used to obtain the final PSF; and the simplified setup, used in the determination of the EFEN strategy. Figure 1 shows a schematic drawing of the detailed machine modeled with PENELOPE2014 using the data provided by the manufacturer. The simplified setup only includes the target and the beryllium window, both surrounded by vacuum. The rationale for this choice is that EFEN strategies will only be applied over the target material and the window will be used as a detector.

The cathode and the anode are protected by a stainless-steel housing (Fig. 1). The photon beam generated in the tungsten target is filtered by: a 0.3-mm-thick beryllium window, a 1.6-mm-thick (measured in the thickest part) flattening filter (mostly composed of aluminum), and the plastic cap at

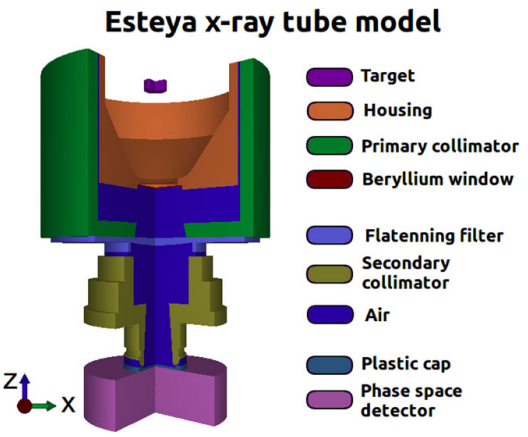

FIG. 1. Model of the Esteya unit in PENELOPE2014 using the data provided by the manufacturer. The elements have the following materials: Tungsten (target), lead (primary collimator), aluminum (flattening filter), Densimet® (secondary collimator of the surface applicator), Polyfenilsulfone (plastic cap). [Color figure can be viewed at wileyonlinelibrary.com]

the surface applicator exit [made of Polyfenilsulfone (PPSU)]. The photon beam is collimated by two structures: the primary lead collimator and the secondary collimator, which is part of the surface applicator, made of Densimet® D176. All the parts below the beryllium window (in the beam path) are surrounded by standard dry air (1.20479 × 10^{-3} g/cm^3). The geometry file of the Esteya model is included as Supporting Information (geometry input file for PENELOPE2014 and the corresponding phase space files.).

We have performed MC calculations for four electron source models commonly used in the literature:[17–21]

(a) The ideal source (IS): A mono-energetic electron beam of 69.5 keV with a homogeneous electron distribution over the focal spot.
(b) The Gaussian energy source (GES): Having its energy centered at 69.5 keV with a FWHM = 6.95 keV and a homogeneous electron distribution over the focal spot.
(c) The Gaussian intensity source (GIS): A mono-energetic electron beam of 69.5 keV, with a Gaussian electron distribution centered on the rectangular foil with a FWHM equal to the focal spot size of 1.8 × 1.3 mm^2.
(d) The spread source (SpS): A combination of GES and GIS.

Additionally, for the case of the simplified setup, we have looked for variations in the radiative yield due to the changes in the impingement angle of the electrons on the target. This allowed us to explore beam tolerances as reported by the manufacturer.

2.C. Monte Carlo code

The MC calculations were performed using penEasy (v. 2015-05-30),[22] a modular program for PENELOPE2014.[23] PENELOPE2014 allows simulating the transport of particles from 50 eV to 1 GeV through matter and has been successfully used to study both radioisotope[24–26] and electronic[13,19] sources and extensively benchmarked.[27–30]

The PENELOPE2014 transport algorithm is determined by six user-defined parameters (henceforth called transport parameters): the energy absorption (EABS), which determines the energy at which particles are assumed to be stopped and absorbed in the medium; the mean free path (C1) and the maximum average fractional energy loss between hard elastic events (C2); the cutoff energies for the production of hard inelastic (WCR) and bremsstrahlung (WCC) events; and the upper limit to the allowed step length (DSMAX).[11,23] These parameters allow to go from a detailed simulation of the electron transport (C1 = C2 = WCR = WCC = 0), that is, interaction by interaction, to a mixed Class II simulation (C1, C2, WCR, WCC > 0), where the events below the user-defined thresholds are simulated only as a mean effect between two hard events.[11,12,23]

PENELOPE2014 uses photoelectric cross sections, calculated by the Fortran program PHOTACS,[31] using the elementary theory of the atomic photoelectric effect (independent electron model),[32,33] to calculate the tables of excitation and ionization cross sections.[31] The Rayleigh scattering cross sections are calculated using the nonrelativistic perturbation theory[34–36] obtaining the atomic form factors from EPDL97.[37] Compton interactions use the relativistic impulse approximation,[38] which take into account the binding effects and Doppler broadening. Furthermore, PENELOPE2014 simulates the emission of characteristic x rays, Auger and Coster–Kronig electrons that result from vacancies produced in K, L, M, and N shells.[23] The MC details are summarized in Table I following the recommendations of the RECORDS AAPM TG-268 report.[39]

2.D. Efficiency enhancing

In this work, we have considered two of the variance reduction tools (VRT) implemented in penEasy: Interaction Forcing (VRIF) and Particle Splitting (VRPS). The VRIF increases the probability of a given interaction (e.g., hard bremsstrahlung emission), reducing its mean free path (λ) by an enhancement factor F (i.e., λ/F), producing daughter particles with weights w_0/F, where w_0 is the weight of the father particle. The VRPS transforms one particle into a number S ($S > 1$) of identical particles with weights w_0/S.[23] The VRTs keep the simulation unbiased through the assignation of the above-mentioned weights to the resultant particles and their scores (e.g., absorbed dose).[9,23,40]

The MC efficiency ε is defined as

$$\varepsilon = \frac{1}{\sigma^2 t} \tag{1}$$

where σ^2 is the variance of the evaluated specific score and t is the CPU time required to simulate the number of particles N.[9] Because N is proportional to t and σ^2 is inversely proportional to N, the MC efficiency ε is independent of N.

TABLE I. Summary of the main characteristics of the Monte Carlo method used to obtain the final PSFs.

Item	Description	References
Code	(1) PENELOPE2014 (2) penEasy (v. 2015-05-30) compiled with GNU Fortran (GCC) 5.3.1. using the -0 optimization flag.	(1) Salvat et al.[23] (2) Sempau et al.[22]
Validation	Previously validated	Ye et al.[28], Chica et al. [29], Croce et al.[19]
Timing	Time required to obtain the final PSFs was 430 h (CPU time). Eight processors, model name: Intel(R) Core(TM) i7-3770K CPU @ 3.50 GHz	
Source description	Four electron beam models: (1) Ideal source (IS): mono-energetic (65.5 keV), homogeneous electron distribution. (2) Gaussian energy source (GES): Gaussian energy spectrum (FWHM = 6.95 keV, centered at 69.5 keV), homogeneous electron distribution. (3) Gaussian source (GIS): mono-energetic (65.5 keV), Gaussian electron distribution (FWHM = focal spot size of 1.8 × 1.3 mm^2). (4) Spread source (SpS): Gaussian energy spectrum (FWHM = 6.95 keV, centered at 69.5 keV), Gaussian electron distribution (FWHM = focal spot size of 1.8 × 1.3 mm^2).	
Cross sections	(1) Photoelectric: calculated with PHOTACS (2) Rayleigh scattering: using nonrelativistic perturbation theory (3) Compton: relativistic impulse approximation	(1) Sabbatucci et al.[31] (2) Sakurai[34], Born[35], Baym[36], Cullen et al.[37] (3) Ribberfors[38]
Transport parameters	Photon cutoff = 10 keV. Electron cutoff = 10 keV in the target, electron transport disabled otherwise. C1 = C2 = 0	
Variance reduction tools	Interaction forcing: hard bremsstrahlung emission. Splitting particles.	
Scored quantities	Absorbed dose in water (collision kerma approximation)	
History/statistical uncertainties	10^9 primary particles/<2% (k = 2)	
Statistical method	History-by-history	Salvat et al.[23]
Post processing	None	

However, that is not the case in practice due to statistical fluctuation at small values of N.[23] Thus, N is required to be high enough to minimize the statistical fluctuations, but small enough to keep a reasonable t to handle several test simulations. To evaluate the stability of ε with respect to N, we used another index incorporated into penEasy, the so-called "intrinsic efficiency"

$$\varepsilon_{intr} = \frac{1}{\sigma^2 N} \tag{2}$$

In a first instance, we have searched the optimum value for the VRIF factor F for the hard bremsstrahlung emission (ICOL = 4) and inner shell interactions (ICOL = 5) using the simplified setup. These simulations were performed using a cutoff of 1 keV for both electrons and photons. The remaining transport parameters (except for DSMAX, which follow its own rule) were set equal to 0 to generate a detailed simulation. The PSF obtained here was stored and used as control. In a second step, we have evaluated the dependence of the efficiency with respect to C1 and C2, using the previously found F factor while keeping all the other parameters constant. For the sake of simplicity, we kept C1 equal to C2 and WCC and WCR were set to match EABS for electrons and photons, respectively. DSMAX was chosen to be equal to one tenth of the target thickness to assure a minimum of ten interactions within the target.[23]

To determine the proper choice of EABS, a control simulation was performed in the detailed setup using the parameters found in the previous two steps. In this occasion, the phase space was stored at the applicator exit window. A photon spectrum analysis was made to find the minimum energy bin detected, defined as the first bin with less than 1% of the peak counting. Additionally, the electron contamination, defined as the ratio between the electron and photon energy fluences, were recorded. Then, a new simulation was performed with an EABS (applied to all materials) just lower than the previously found minimum bin, obtaining a new phase space. This process was finalized with a comparison between both PSFs obtained in the detailed setup, showing the photon energy spectrum and the electron contamination.

2.E. Phase space file

We have compared the energy spectra of the final PSFs with the data published by Candela-Juan et al.[6] and García-Martínez et al.[13] using two different metrics normally used to characterize x-ray beams: the average photon energy ($\bar{E}$) and the half-value layer (HVL) of Al.

2.E.1 Average photon energy

García-Martínez et al.[13] determined $\bar{E}$ through the measurement of six x-ray tubes with a germanium crystal spectrometer located at 100 cm from the x-ray tube. The beam was collimated by two lead pinholes of 4 mm (in the applicator) and 0.7 mm (in the detector) in diameter. As the attenuation of the flattening filter is not uniform due to its shape (see Fig. 1), $\bar{E}$ depends on the distance from the beam axis to the detection volume (see Fig. 4). For that reason, comparing measured and simulated $\bar{E}$ requires considering only the photons within the same solid angle as in the experimental setup. Such tight collimation drastically worsens the uncertainty of the simulation due to the reduced number of photons reaching the detector. To overcome this issue, a set of conditions that mimic the main characteristics of the experimental setup has been implemented. These conditions are based on the constraints imposed by the filter geometry and the photon physics to extrapolate $\bar{E}$ from the data obtained with detectors of larger diameters (i.e., with better statistics).

To replicate the air attenuation, the plane of detection was located at 1 mm distance from the PSF plane (6.1 cm from the source), and the space was filled with air of an increased density (1.20479 g/cm^3), which maintains the photon path constant. In this condition, 0.7 mm diameter at 106 cm from the source is equivalent to 4×10^{-2} mm diameter ($r_0 = 2 \times 10^{-2}$ mm) at 6.1 cm. If the simulated detector of radius r is centered with respect to the beam axis, the measured average energy $\bar{E}(r)_{IS}$ (we use here the "ideal source" configuration) will be defined as the average energy due to all photons scored at a distance smaller than r. As the photon path length (z) in the filter is not uniform, $\bar{E}_{IS}$ change with a rate $d\bar{E}_{IS}/dz$. As we know that $dz/dr = 0$ at the beam axis ($r = 0$), the rate $d\bar{E}_{IS}/dr$ must increase monotonically to 0 when r goes to 0. Therefore, there exists a convergence value $\bar{E}(0)_{IS}$. As r_0 is small enough with respect to the system dimensions, one can assume $\bar{E}(0)_{IS} \approx \bar{E}(r_0)_{IS}$. In these conditions, we are able to obtain an extrapolated value $\bar{E}(r_0)_{IS}$' from its last two neighbors, $\bar{E}(r)_{IS}$ and $\bar{E}(r + \Delta r)_{IS}$. As $\bar{E}(r_0)_{IS}$ must comply with the following property: $\bar{E}(r)_{IS} < \bar{E}(r_0)_{IS} < \bar{E}(r_0)_{IS}$', the estimation of $\bar{E}(r_0)_{IS}$ only requires the knowledge of the two last neighbors.

We should expect a monotonic increase in the slope $\Delta\bar{E}_{IS}/\Delta r$. However, this may not be the case in practice due to statistical fluctuations when r diminishes. For this reason, $\bar{E}(r)_{IS}$ (the last neighbor) will be the last point for which its slope maintains the expected behavior.

2.E.2 HVL estimation

The HVL was determined analytically through a method similar to that used by Watson et al.[41] The air-kerma ratio is calculated from the energy photon spectrum, obtained from the PSF:

$$K_{ratio} = \frac{\sum E_i \phi_i \left(\frac{\mu_{en}}{\rho}\right)_{i,air} exp(-\mu_{i,air} x_{air} - \mu_{i,atte} x_{atte})}{\sum E_i \phi_i \left(\frac{\mu_{en}}{\rho}\right)_{i,air} exp(-\mu_{i,air} x_{air})}, \quad (3)$$

where E_i, ϕ_i, and $(\mu_{en}/\rho)_{i,air}$ are the energy, fluence and mass energy absorption coefficient of each energy bin i, respectively. Additionally, $\mu_{i,air}$ and $\mu_{i,atte}$ are the attenuation coefficients of the air and the attenuator (i.e., aluminum), respectively. Finally, x_{air} and x_{atte} are the source-to-detector distance in air (100 cm) and the thickness of the attenuator. The attenuation coefficients (total attenuation including the coherent scattering) were obtained consistently from PENELOPE2014.

The HVL is defined as the value of x_{atte} for which $K_{ratio} = 0.5$. To evaluate the effect of the detector radius (i.e., the dependence of $\bar{E}$ from r) in the determination of the HVL, several photon spectra (with a bin width of 0.1 keV) were generated for both applicators from the corresponding PSF, taking into account the lateral distance from the beam axis for the photons in the PSF. The fluences and the coefficients uncertainties were propagated across the Eq. (3). Following the analysis by Andreo et al.[42], a Type B uncertainty of 2.2% ($k = 2$) was considered. The HVL was obtained for the IS and GES models.

2.F. Clinical data

The final PSFs were applied over a cylindrical water phantom (10 cm radius and 20 cm depth) with the water mass density (0.998 g/cm^3) recommended by the TG-43U1.[43] We used the VRPS variance reduction technique, with the splitting factors of 10^5 (APP_{10mm}) and 10^4 (APP_{30mm}). The collisional kerma was used as absorbed dose estimator with $EABS_{ph}$ = 1 keV, which was tallied using cylindrical symmetry.

The absorbed depth dose (DD) was scored in central disks of 1 mm radius and a height h = 0.25 mm. The absorbed dose profiles (DP) were tallied in concentric rings with r in the range $0 \leq r \leq$ applicator radius — Δr, Δr being the DP bin width, and the height h = 1 mm in all depths. The number of events collected in the rings increases with an increment of r. That condition makes possible to improve the spatial resolution through reducing Δr, keeping the uncertainty roughly constant. The bin widths were Δr = 1 mm for $r \leq 80\%$ of the applicator radius and Δr = 0.1 mm for $r > 80\%$ of the applicator radius. The percentage depth dose (PDD) was normalized at 3 mm depth and the DP was normalized at the central bin.

We compared the results obtained with all source models. As an example, we will use the ideal (IS) and the Gaussian

energy (GES) sources. DPs are compared according to $100 \times [1 - (DD_{GES})_i/(DD_{IS})_i]$, where i is the index of the corresponding bin. PDD was compared according to $(PDD_{GES})_i - (PDD_{IS})_i$. The penumbra was calculated as the difference between the radii corresponding to the 80% ($r_{80\%}$) and 20% ($r_{20\%}$) of the absorbed dose at the central axis, obtained through linear interpolations.

García-Martínez et al.[13] associated the existence of a systematic asymmetry of 1.5% in the DPs with a heel effect caused by the cathode. This would break the cylindrical symmetry used to tally the dosimetric scores. To evaluate the effect of such deviation from the cylindrical symmetry, we performed a simulation using Cartesian coordinates to score DPs in the x and y axes at 5 mm depth. The dose on the x axis was scored in voxels of $0.5 \times 1.0 \times 1.0$ mm^3 and $1.13 \times 1.0 \times 1.0$ mm^3, for $r > 80\%$ and $r \leq 80\%$ of the applicator radius, respectively (changing the coordinates accordingly to the y axis). The symmetry was evaluated as $100 \times [1 - \text{DP}(-12\text{ mm})/\text{DP}(+12\text{ mm})]$ Where DP(−12 mm) and DP (+12 mm) are the DP values at −12 mm and +12 mm, respectively.

2.G. Uncertainties analysis

All uncertainties will be expressed with a coverage factor $k = 2$. In the following subsections (Sections 3.a–3.c) only Type A (estimated by the history-by-history method) uncertainties will be shown. Type B uncertainties will be analyzed in a separate Section 3.D. In all cases the evaluation of the uncertainties followed BIMP recommendations.[44] We assumed all probabilities as normal distributions, except for the geometrical uncertainty introduced by the bin width in the DP. In this case, the probability considered having a rectangular distribution with bounds equal to the half of the bin width (0.05 mm).

3. RESULTS

3.A. Efficiency enhancing strategy

Figure 2 shows the results of the test simulations. Unless otherwise stated, the test results were obtained with 10^7 primary particles. The efficiency reaches a plateau at a VRIF factor near 150, improving the efficiency by a factor ~20. Modification of C1 and C2, in combination with $F = 150$, did not produce any further improvement. It has been observed that ε_{intr} stabilizes for values around $N = 10^6$.

The minimum energy bin detected at the applicator exit of the detailed setup (EABS = 1 keV, $F = 150$ and $N = 10^8$) was 12 keV (0.4 ± 0.3% of the maximum counting bin) and 11 keV (0.6 ± 0.1% of the maximum counting bin) for APP_{10mm} and APP_{30mm}, respectively. The average electron contamination represents 0.005 ± 0.005% of the photon energy fluence.

In the control PSF, less than 1% of the photons have originated outside of the target. Their influence on the energy spectra is negligible, modifying the average energy from 35.43 ± 0.19 keV to 35.48 ± 0.13 keV if those photons were discarded.

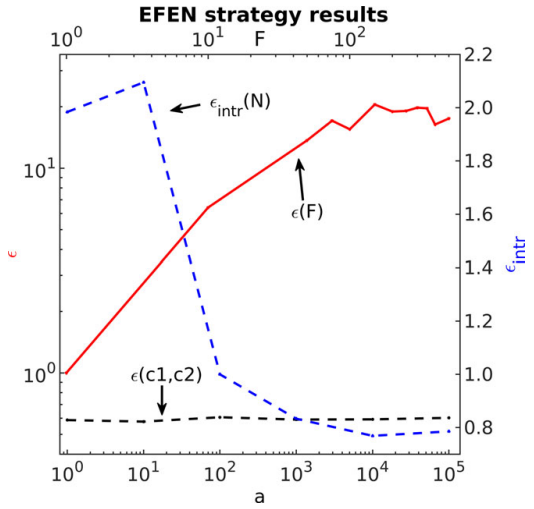

FIG. 2. MC simulation efficiencies (ε and ε_{intr}) of photon energy deposition in the beryllium window. The red lines (left axis) correspond to the efficiency ε calculated from Eq. (1) while the blue line (right axis) corresponds to the intrinsic efficiency ε_{intr} as defined in Eq. (2). The solid red line corresponds to the value of efficiency (F-axis), when F (VRIF enhancement factor) is modified, normalized to F = 1. Dashed lines correspond to the a-axis: red dashed line, C1 = C2 = 1×10^{-6}a (log scale, normalized to the efficiency obtained with C1 = C2 = 0); blue dashed line, N = 1×10^3a (log scale normalized to N = 1×10^5). [Color figure can be viewed at wileyonlinelibrary.com]

TABLE II. Monte Carlo efficiency enhancing strategy. Summary of the variance reduction techniques and transport parameters used to obtain the final PSFs.

Item	Value	Material
VRIF	150 (ICOL = 4, WMIN = 1)	Target
C1, C2, WCC, and WCR	0	All
$EABS_{ph}$	10 keV	All
$EABS_e$	10 keV	Target
	10^6 keV	All other

The simulation in the detailed setup was carried out with $N = 10^8$. The corresponding parameters are summarized in Table II. Figure 3 shows the comparison with the energy spectrum of the control PSF for APP_{30mm}. The 67%, 83%, 88%, and 93% of the bins show an absolute difference below 2%, 3%, 5%, and 10% (average equal to −0.8%, total range within −37.4% and 12.7%), respectively. All differences in the range 14 keV ≤ bin ≤ 64 keV are below 5% (average equal to 0.2%, range within −2.9% and 4.3%). The use of these parameters allows a reduction of 92% to the CPU time.

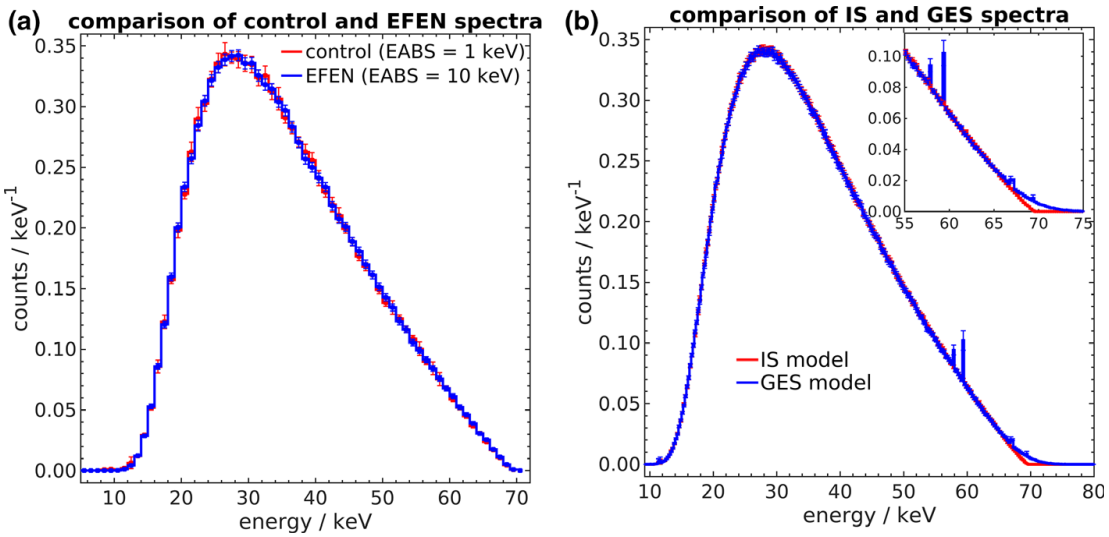

FIG. 3. Energy spectra comparisons in the detailed setup. (a): Test simulations (APP_{30mm}, N = 10^8, bin width 1 keV). The red line corresponds to the control PSF obtained with $EABS_{ph}$ = $EABS_e$ = 1 keV, the blue line corresponds to the PSF obtained with EABSph = 10 keV for all materials, $EABS_e$ = 10 keV for the target and the electron transport disabled for all other materials. (b): Final PSFs (APP_{30mm}, N = 10^9, bin width 0.25 keV). The red line corresponds to the simulation using the ideal source model, the blue line corresponds to the simulation using the Gaussian energy source model. The inset corresponds to the zone where the difference between both spectra becomes noticeable, with the tungsten Kα1, Kα2, and Kβ1 characteristic lines, which are well over the associated statistical uncertainties. [Color figure can be viewed at wileyonlinelibrary.com]

3.B. Final phase space file

The final PSFs were obtained with $N = 10^9$ and the EFEN strategy summarized in Table II (see the Supporting Information link for the geometry input file for PENELOPE2014 and the corresponding phase space files.). Figure 3 shows the differences in the energy spectra between IS and GES models in the case of APP_{30mm}. Differences are noticeable for energies higher than 56 keV due to the presence in the GES simulation of the tungsten characteristic lines Kα1, Kα2, and Kβ1 (59.321, 57.984, and 67.244 keV, respectively).

3.B.1. Average photon energy

If all photons were taken into account in the PSF, $\bar{E}_{IS}$ = 35.97 ± 0.09 keV and $\bar{E}_{GES}$ = 36.06 ± 0.10 keV were obtained for the APP_{10mm} as well as $\bar{E}_{IS}$ = 35.47 ± 0.03 keV and $\bar{E}_{GES}$ = 35.57 ± 0.03 keV for the APP_{30mm}. Considering only photons with an off-axis position $r \leq 2.5$ mm (see Fig. 4), $\bar{E}_{IS}$ = 35.98 ± 0.18 keV for both applicators, while $\bar{E}_{GES}$ = 36.06 ± 0.20 keV and 36.04 ± 0.21 keV for the APP_{10mm} and APP_{30mm}, respectively.

Figure 5 shows the average energy $\bar{E}$ detected through an air column of 1 mm (using a VRPS factor of 20), as a function of the detector radius for the IS simulation. The slope (i.e., $\Delta\bar{E}_{IS}/\Delta r$) increases monotonically when r goes to zero, as expected, but only until r = 2.5 mm. Using this value as threshold, $\bar{E}(r_0)_{IS}$ should be at some point between

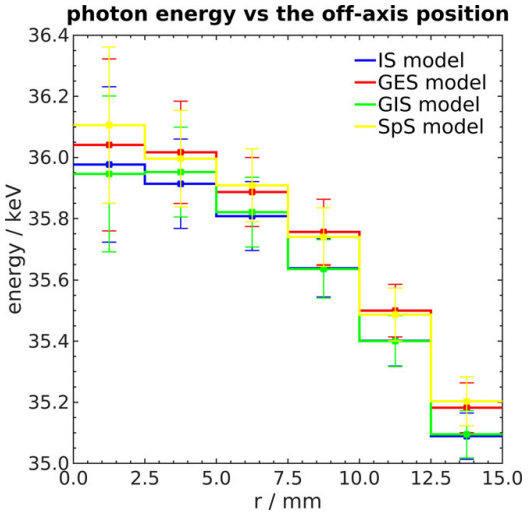

FIG. 4. Average photon energy vs distance from the beam axis, for the ideal (IS), Gaussian energy (GES), Gaussian intensity (GIS), and spread (SpS) source simulations. The bin width is 2.5 mm. [Color figure can be viewed at wileyonlinelibrary.com]

36.17 keV (last neighbor $\bar{E}$(r)) and 36.21 keV (extrapolation $\bar{E}(r_0)$'). If we take the average of these two limits as the expected $\bar{E}(r_0)$, then, $\bar{E}(r_0)_{IS}$ = 36.19 ± 0.09 keV and $\bar{E}(r_0)_{GES}$ = 36.25 ± 0.10 keV. These values agree with the

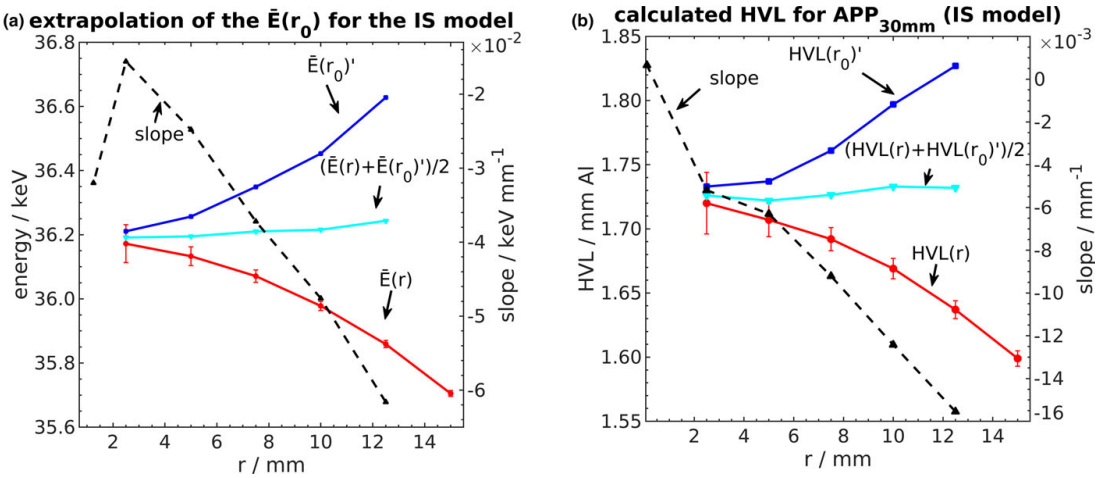

FIG. 5. Extrapolation of the average photon energy Ē (a) and the HVL (b) for a 2×10^{-2} mm radius (r_0) detector, calculated using the ideal source model. (a): The red line corresponds to the average energy of all photons within the beam radius r. The black dashed line corresponds to the slope of the two neighbors. It is evident that at r = 2.5 mm the slope function breaks its expected behavior. The blue line corresponds to the extrapolation of Ē in $r = 2 \times 10^{-2}$ mm, calculated with the plotted slope and placed over its closer neighbor only for visual help. The cyan line corresponds to the average value between Ē for the actual detector radius, and the extrapolation made with the plotted slope. (b): The red line corresponds to the HVL, calculated with photon energy spectra generated considering only the photons within the beam radius r. The black dashed line corresponds to the slope of the last two neighbors, the slope function breaks its expected behavior at r = 2.5 mm. The blue line corresponds to the extrapolation of HVL in $r = 2 \times 10^{-2}$ mm, calculated with the plotted slope. The cyan line corresponds to the average value between the HVL for the actual detector radius, and the extrapolation using the ideal source model. [Color figure can be viewed at wileyonlinelibrary.com]

36.2 ± 0.2 keV (k = 2) measured by García-Martínez et al.[13]

3.B.2. HVL determination

The HVL for the APP_{30mm} shows the same dependence on *r* as $\bar{E}$ (see Fig. 5). The HVL value calculated using the IS model is 1.72 ± 0.04 mm of Al for both applicators. Differences between the IS and GES models are below 0.5%. Candela-Juan et al.[6] reported three HVL values depending on the chamber and setup used: 2.09, 1.88, and 1.69 mm. All values with an uncertainty of 0.10 mm (*k* = 2). García-Martínez et al.[13] reported two values: 1.86 ± 0.40 mm, obtained using oRTIgo (QA software for Barracuda detector, Version 6.4C), and 1.82 ± 0.32 mm, obtained by fitting the measurements (coverage factor *k* = 2 for both values). The HVL value, obtained in our study, agrees with the previously published values within the range of uncertainties.

3.C. Dosimetric data

3.C.1. Depth dose

For APP_{10mm}, the average differences in absorbed dose between DD_{IS} and DD_{GES} are 1.1% (−0.4% − 2.2%, σ = 0.4%) and 1.0% (0.5% − 1.4%, σ = 0.2%) for the total depth range and the first centimeter, respectively. For APP_{30mm}, the corresponding differences are 0.7% (−1.35% − 3.4%, σ = 0.7%) and 0.5% (−0.02% − 1.2%, σ = 0.2%). The uncertainties of the calculated DD values for both applicators are shown in Table III.

TABLE III. Depth dose uncertainties for the total depth range and for the first centimeter (with approximately 50% of the maximum absorbed dose at 0 mm depth). The average value is given first, followed by the minimum and the maximum values in parentheses.

	Ideal source		Gaussian energy source	
Applicator	1 cm (%)	Total (%)	1 cm (%)	Total (%)
10 mm	1.3 (1.3–1.4)	1.7 (1.3–2.3)	1.4 (1.4–1.5)	1.8 (1.4–2.5)
30 mm	1.2 (1.1–1.3)	1.4 (1.1–2.1)	1.3 (1.2–1.4)	1.5 (1.2–3.5)

For the APP_{10mm}, the average differences between PDD_{IS} and PDD_{GES} were −0.02% (−0.33% − 0.24%, σ = 0.06%) and −0.04% (−0.33% − 0.24%, σ = 0.12%) for the depth total range and the first centimeter, respectively. For APP_{30mm}, the average differences are −0.01% (−0.47% − 0.90%, σ = 0.15%) and 0.12% (−0.37% − 0.90%, σ = 0.26%) for the depth total range and the first centimeter, respectively.

Table IV compares the PDD_{IS} with the data published by García-Martínez et al.[13] and the data supplied by the manufacturer.[45] Figure 6 shows a comparison of the PDD_{IS} for APP_{10mm} and APP_{30mm} (left) and a comparison between the PDD_{IS} and the PDD published by García-Martínez et al.[13] for the APP_{30mm} (right). The maximum differences between the simulated and the experimental

TABLE IV. PDD data for APP_{10mm} and APP_{30mm} (IS model), compared with Garcia-Martinez et al.[13] and the manufacturer's data.[45] The uncertainties are expressed with the coverage factor $k = 2$.

	Depth (mm)									
Applicator	0.0	1.0	2.0	3.0	4.0	5.0	6.0	7.0	8.0	9.0	10.0
APP_{10mm}	122.8 ± 1.7	115.3 ± 1.6	107.4 ± 1.4	100.0 ± 1.3	93.2 ± 1.2	86.9 ± 1.1	81.0 ± 1.1	75.5 ± 1.0	70.4 ± 0.9	65.7 ± 0.9	61.4 ± 0.8
Ref. [13]	124.8	115.7	109.4	100.0	91.3	85.6	79.7	73.8	69.8	64.5	60.5
Ref. [45]	124.5	115.8	107.7	100.0	92.9	86.3					
APP_{30mm}	119.0 ± 1.6	112.7 ± 1.4	106.3 ± 1.3	100.0 ± 1.2	94.3 ± 1.1	88.8 ± 1.1	83.5 ± 1.0	78.6 ± 0.9	74.1 ± 0.9	69.9 ± 0.8	65.8 ± 0.7
Ref. [13]	123.5	114.2	106.8	100.0	93.6	88.5	83.2	77.7	72.8	68.3	65.1
Ref. [45]	122.5	114.6	107.1	100.0	93.5	87.4					

PDDs are 2.0% for APP_{10mm} and 4.5% for APP_{30mm}. The maximum differences with the manufacturer's data for these applicators are 1.7% and 3.5%. It should be noted that the maximum differences are located at the phantom surface. Deeper than 1 mm, all the differences are within 2%.

3.C.2. Dose profiles

Figure 7 shows the DP_{GIS} for APP_{30mm} at 0, 3, 5, and 10 mm depths. Shallow profiles have clear horns, reaching 107% for the surface one. The profile at 5 mm depth, which is specified by the manufacturer as the reference depth,[13] has no horn. All dose profiles are obtained with an uncertainty below 2%.

Table V compares the penumbras obtained in this work with those reported by García-Martínez et al.[13] Variation in the electron energy spectrum did not produce any noticeable differences between DP_{GES} and DP_{IS}, which were below 2% for both applicators. The differences between the dose profiles DP_{IS} and DP_{GIS} at 5 mm depth, shown on the Fig. 7, are below 1.5% for $r \leq 80\%$ of the $r_{50\%}$, and up to 12% for $r > 80\%$ of the $r_{50\%}$.

Figure 8 (left) compares the obtained DP_{GIS} with the measured profile from García-Martinez et al.[13] for APP_{30mm}. The differences are noticeable from $r \geq 7$ mm, being equal to 2%, 5%, and 10% at $r = 11$, 14, and 16 mm, respectively. In the range 16 mm $< r \leq 17$ mm the differences are below 15% and the distance to agreement is better than 0.4 mm.

The DP, simulated using the GIS model in Cartesian coordinate system, presents an average uncertainty of 1.7% (max 3.5%) in the plateau for both X and Y directions. The asymmetry of 2.2 × 1.4% ($k = 2$) observed along the x (cathode) axis. Along the y axis the asymmetry was below 1% and therefore within uncertainty. The average absolute differences between the cylindrical and the Cartesian profiles on the plateau were 0.8% (max 3.1%, $\sigma = 0.8\%$) and 0.6% (max 1.9%, $\sigma = 0.5\%$) for the x and y axes, respectively. The right-side image of the Fig. 8 shows a comparison of the DP_{GIS} obtained with cylindrical and Cartesian (x axis) tallies.

3.D. Uncertainties

There are three main sources of Type B uncertainties: manufacturing tolerances, cross-section libraries, and electron source manufacturing uncertainties.

The flattening filter is the predominant structure determining the beam properties. According to the manufacturer's data, a maximum tolerance of the filter thickness is ±0.01 mm, which implies a difference of ±0.08% in the energy absorption ($\mu_{en} = 1.531\ cm^{-1}$ for 36 keV). Based on the flattening filter geometry, the photon path, and the Fig. 4 data, the photon average energy of the beam changes with a rate of 5.6% per millimeter thickness of the filter. That implies a change in the photon average energy of ±0.06% within the filter thickness

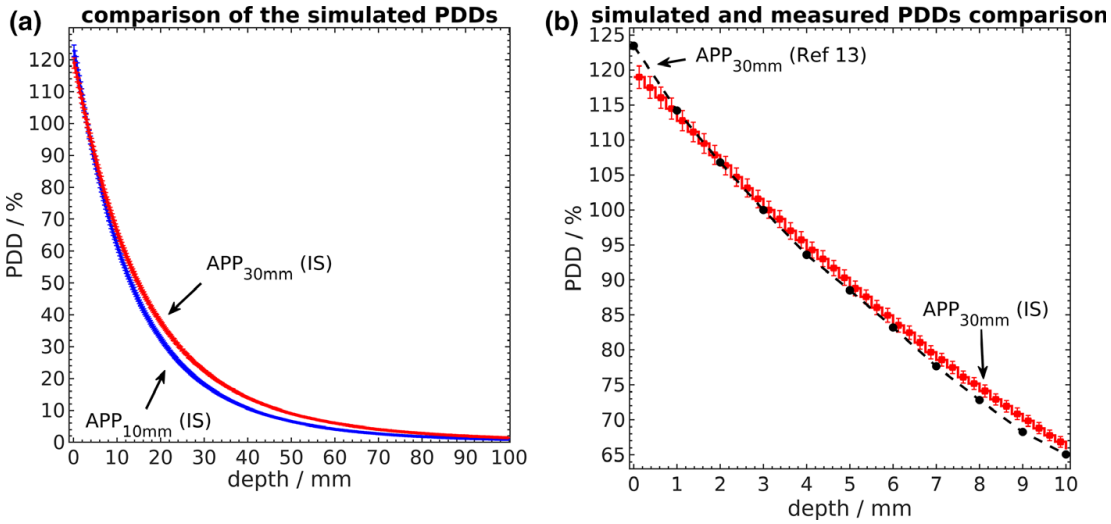

FIG. 6. Simulated and measured PDDs. (a): Comparison between the simulated (IS model) PDDs, for APP_{10mm} and APP_{30mm}. (b): Comparison between the PDD published by García-Martínez et al.[13] and simulated PDD_{IS}, for APP_{30mm}. [Color figure can be viewed at wileyonlinelibrary.com]

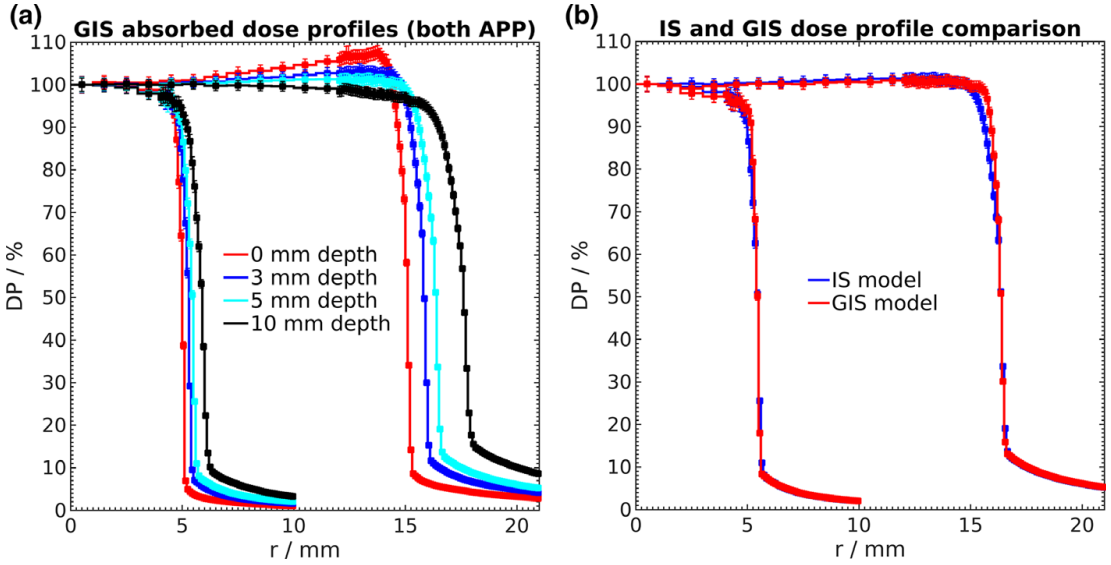

FIG. 7. Absorbed dose profiles for APP_{10mm} and APP_{30mm}: simulated using Gaussian intensity source model at 0, 3, 5, and 10 mm depth (a), and using Ideal and Gaussian intensity source models at 5 mm depth (b). [Color figure can be viewed at wileyonlinelibrary.com]

tolerance. Finally, the variation in the filter thickness by 0.01 mm leads to the HVL change by 0.4%. Therefore, we consider a 0.1% value as an estimate of the uncertainty introduced in the absorbed dose in water (DD and PDD) and in the average photon energy; while the uncertainty introduced in the HVL determination is 0.4%.

Andreo et al.[42] analyzed Type B uncertainty of the cross-section libraries and proposed the value of 2.2% for a photon beam with the average energy of 34.1 keV in water (group μ_B(II) in that work, $k = 2$). This component adds 2.2% uncertainty to PDD, DD, DP, and $\bar{E}(r_0)$.

The electron beam model has two major sources of uncertainties: the electron energy and focal spot distributions, and the impingement angle of the electrons on the target. We estimated an additional uncertainty of 1.1% due to the lack of knowledge of the electron energy spectrum and spatial

TABLE V. Penumbra values (mm) for different combinations between applicators and simulated electron sources and the average values from García-Martínez et al.[13] All uncertainties are expressed with the coverage factor $k = 2$.

	Source models			
Applicators	Ideal	Energy Gaussian	Intensity Gaussian	Spread
APP_{10mm}	0.28 ± 0.07	0.29 ± 0.08	0.44 ± 0.07	0.45 ± 0.07
Ref. [13]		0.95 ± 0.13		
APP_{30mm}	0.42 ± 0.07	0.43 ± 0.07	0.63 ± 0.07	0.63 ± 0.07
Ref. [13]		1.03 ± 0.12		

TABLE VI. Estimated uncertainties ($k = 2$) of the different beam characteristics, calculated during simulation. For the DD, the maximum values for the first 10 mm and for the entire range are showed. For the PDD and the DP, only the maximum value is shown, which is within the first 10 mm and the 80% of the applicator diameter, respectively.

	Uncertainties		
Items	Type A (%)	Type B (%)	Combined, u_c (%)
DD	1.5/3.5	2.9	3.2/4.5
PDD	2	2.2	3
DP	2	2.7	3.3
HVL	2.5	0.4	2.5
$\bar{E}(r_0)$	0.3	2.2	2.2

distribution, based on the average difference between DD_{IS} and DD_{GES} for APP_{10mm}. Our simulation showed a difference of 1.5% in the radiation yield with the change in the impingement angle of the electrons over the range reported by the manufacturer. This component adds 1.9% Type B uncertainty to the absorbed depth dose and 1.5% to the dose profiles (see section IV.b, profile asymmetry discussion).

Table VI shows the summary of all uncertainties for the investigated quantities.

4. DISCUSSION

4.A. Efficiency enhancing strategy

The saturation of the simulation efficiency, observed in Fig. 2, is achieved when the electrons that impinge the target begin to produce more than one photon (correlated photons) due to the use of high enhancement factors (F) of VRIF ICOL = 4. As the history-by-history statistical estimator considers the correlation between the particles, the correlated photons decrease their contribution to the variance reduction, while still consuming computation time.[9,40]

Ali et al.[40] described and implemented the bremsstrahlung cross-section enhancement (BCSE) VRT in the EGSnrc code, the numerical technique which is equivalent to the VRIF ICOL = 4 implemented in PENELOPE. They analyzed the BCSE performance in the targets of equipments similar to the Esteya system, using detector array of different sizes (from 1 × 1 cm^2 to 4 × 4 cm^2) at a detector-to-target distance of 100 cm. In contrast to that, in our work we considered a single detector with a diameter in

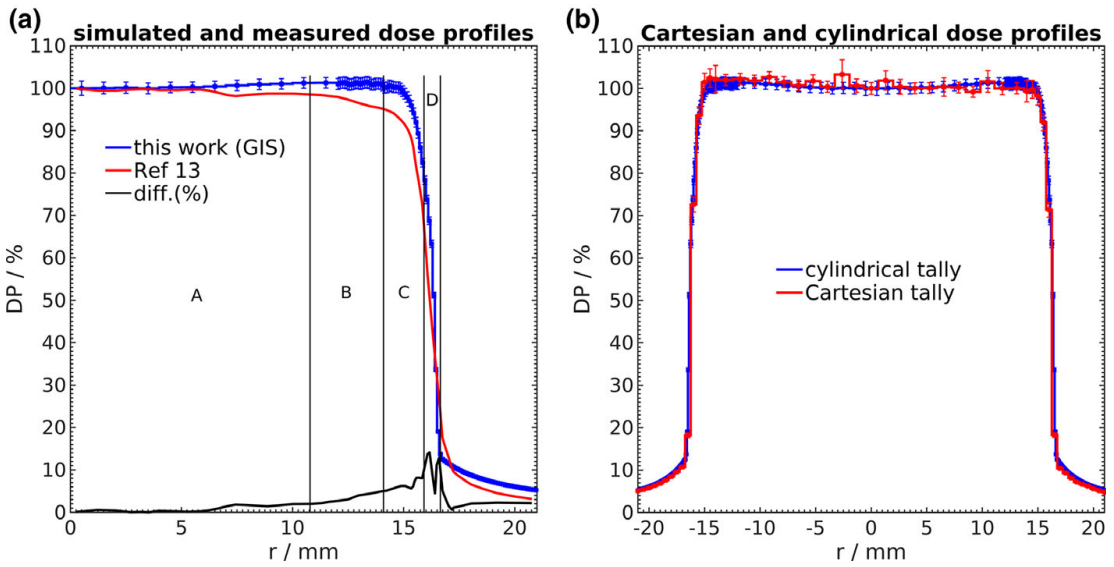

FIG. 8. Absorbed dose profiles of APP_{30mm} at 5 mm depth. (a): Simulated DP_{GIS}, published[13] profile and the absolute difference between them on the same scale. The differences in the indicated zones A, B, C, and D are below the 2%, 5%, 10%, and 15%, respectively. Distance to agreement in zone D is below 0.4 mm. (b): Simulated DP_{GIS} with the Cartesian and cylindrical tallies. Cylindrical tally profile was mirrored for negative r values for visual purposes. [Color figure can be viewed at wileyonlinelibrary.com]

the order of the beryllium window size (1 cm), placed at 2 cm distance from the target. The smaller solid angle of the individual detectors, used in the Ali et al.[40] work, decreases the probability that the correlated photons arrive at a specific detector. For that reason, they obtained efficiency saturations at higher enhancement factors (over 1000) using only one VRT. Nevertheless, when they combined the BCSE and a splitting VRT (gaining a higher global efficiency), the optimum BCSE enhancement factor dropped to a range of 100–200, being in the same order as $F = 150$, found in our work.

Unlike other authors,[19,46] we found a deterioration in the simulation efficiency with the use of C1 and C2 parameters in combination with VRIF $F = 150$ (see Fig. 2). Sempau et al.[11] showed that the use of a high value for C1 and C2 could lead to a relative decrement of the step length for the energy range of 30 and 80 keV in graphite (without VRT), hence increasing the computation time. As described in Section 2, we have followed a two-step procedure. First, the optimum VRIF F factor was obtained; then, all the parameters controlling radiation transport were determined to achieve a more efficient simulation strategy. It has been pointed out in the literature that modifications of the transport parameters C1 and C2 for high-energy electrons in the target, even with small nonzero values, may affect water dosimetry.[12,47] However, there is no evidence indicating that the use of VRIF may bias simulations in water.[12,46] In our opinion, the most efficient strategy is to develop an EFEN by fixing the transport parameters only after the use of some VRT over the target.

The increase in EABS from 1 to 10 keV reduced the required computation time by 84%, causing the loss of 0.02% of the photons, detected at the applicator exit. By disabling electron transport in all materials except the target, an extra time reduction of 8% was achieved at the cost of losing an additional 1.2% of the photons. This measure modified the average photon energy by 0.14%. These differences might only play a role for prediction of the electron contamination at the patient surface. Nonetheless, it has been observed that the energy fluence of electrons is negligible compared to that of photons.

4.B. Phase space and dosimetric outcomes

The accurate description of eBT sources may be one of the most challenging Monte Carlo calculations in radiation dosimetry.[48] The analysis of the differences between the four source models used in this work shows that the main source of discrepancies comes from differences in the electron energy distribution. Electrons over 69.5 keV, present in the GES simulation, have enough energy to ionize the tungsten K shell (69.525 keV) generating the characteristic peaks observed in Fig. 3. These peaks are not observed in the experimental measurements reported by García-Martínez et al.[13]

The calculated HVL value (1.72 ± 0.02 mm) agrees, within the reported uncertainties, with previously published data,[6,13] depending on the type of the detector used. The HVL measured (1.69 ± 0.1 mm)[6] using the Exradin A20 ionization chamber (Standard Imaging Inc., Middleton, WI) is closer to our result than the one obtained using a Barracuda (RTI Electronics AB, Mölndal, Sweden) solid-state detector (1.82 mm[13] and 1.88 mm[6]).

The simulated PDDs show a good agreement (within 2%) with the experimental data beyond 1 mm depth. In a typical skin treatment, when a dose is prescribed at 3 mm depth, the discrepancies in the absorbed dose at the surface are in the range of 3.8%. García-Martínez et al.[13] used a plastic phantom with a PTW T34013 parallel-plate ionization chamber (PTW, Freiburg, Germany). To mimic these experimental conditions, we simulated the depth dose ($PDD_{plastic}$) in a plastic water phantom, using data published by Ramaseshan et al.,[49] the IS model for the APP_{30mm}, and the previously described setup for simulations in water. The comparison of the results shows that PDD_{water} was in average 0.4% (max 1.0%, $\sigma = 0.2\%$) higher than $PDD_{plastic}$ in the first centimeter. However, Watson et al.[10] showed that the ratio of the absorbed dose in water and in the air cavity of the PTW 34013 chamber may not be depth independent for a beam of 50 kVp, which could make necessary the incorporation of correction factor up to 10% in the PDD determination. This dependence would be even more pronounced at shallow depths.[10]

Differences between simulated and measured PDDs may suggest a preference for less energetic photon beam, that is, with the electron energy distribution shifted to the lower energies. Nevertheless, this option would move the values of $\bar{E}(r_0)$ and HVL away from the experimental results. In our opinion the mono-energetic source of 69.5 keV is the best option to reproduce the dosimetric characteristic of the Esteya system.

The most noticeable effect in the dosimetric outcomes was observed by varying the distribution of the electron beam over the focal spot area. Moving from the IS model to the GIS model increases the beam penumbra by 50%, which leads to a better agreement with the experimental data (see DP_{IS} and DP_{GIS} in Fig. 7 and Table V). However, the differences between DP_{GIS} and the reference dataset are not negligible.[13] García-Martínez et al. measured the DP at 5 mm depth in plastic water, using the Gafchromic® EBT2 radiochromic film (Ashland Inc., Wayne, NJ). These differences could not be explained by the change in the energy spectrum (see Fig. 4),[50] or by the angular dependence in the EBT2.[51] On the other hand, the uncertainties due to some common artifacts associated with the scan process of EBT2 films (e.g., Newton's rings and film curls) can reach 5%,[19,52,53] and the errors in the system alignment can lead to non-negligible effects in the measurement results.[54]

In our opinion, these differences agree within uncertainties with the values found in the literature. Fulkerson et al. simulated an Axxent eBT system with surface applicators (MCNP5 code) and found the differences up to 5% for the PDD, measured with an Exradin A20 ionization chamber. They also reported the differences in DP compared to EBT2 film dosimetry, associated with the alignment issues and

intermachine variations.[21] Moradi et al. simulated an Intrabeam eBT system (MCNP5 code). The PDDs of two identical machines, measured with a PTW T34013 chamber in water, showed intermachine variations within the first centimeter depth; over the 20% for one of the machines and up to 5% for the other.[55] Watson et al. simulated the PDD in water of an Intrabeam system (EGSnrc code), scoring the absorbed dose inside the air cavity of a PTW 34013 chamber, and found the differences up to 2.4% between the simulations and the measurements performed with the same ionization chamber.[10] Croce et al. simulated (PENELOPE2006) a Papillon 50 system (Ariane Medical System, Nottinghamshire, UK), reporting a good agreement within the reported uncertainties with the PDDs (PTW T23342 chamber) and DPs (EBT2 film) measured in PMMA.[19] Nevertheless, PDD differences at the phantom surface have not been reported. Therefore, the dosimetric response of some ionization chambers to the eBT beams[10] and the intermachine variability[21,55] are topics that require further investigation.

García-Martínez et al.[13] found a systematic asymmetry of 1.5% that they associated with a heel effect produced by the cathode. However, we also found a similar asymmetry, determining that the cathode is away from the path of most of the photons reaching the target. We concluded that the major reason of the asymmetry is due to the change in the differential bremsstrahlung cross sections at different polar angles in the beam, which reach 10° at r = 12 mm for the APP_{30mm}. We found a similar difference in the radiative yield (1.5%) when the impingement angle of the electrons was modified by approximately the same range. Differences observed in Fig. 8 are within the uncertainties associated with the DP simulation (see Table VI). Furthermore, the DP_{GIS} in the y axis (Cartesian tally) does not show any asymmetry and is well reproduced by the cylindrical tally. For all these reasons, we consider that the cylindrical tally is a good and fast approximation to describe the Esteya beam, allowing the accurate determination of the beam characteristics (e.g., penumbra).

5. CONCLUSIONS

We have obtained the phase space of the Esteya system for the 10 and 30 mm applicators and used it to score the relevant dosimetric data in water. This was performed using an EFEN strategy that allowed us to reduce 90% of the computation time, compared to a simulation without the use of VRTs, with minimal impact on the simulated results. The comparison with experimental results showed good agreement with the findings published by other authors using similar equipment, within the reported uncertainties. In our Monte Carlo calculations we used four different options to model the electron beam of the Esteya source. We found that a mono-energetic source combined with a Gaussian electron distribution over the focal spot was the most suitable choice to reproduce the experimental data. Further research is needed to study intermachine variations and response of the most common ionization chambers used in clinical practice for this eBT beam.

ACKNOWLEDGMENT

F. Ballester; Jose Perez-Calatayud, and J. Vijande acknowledge financial support from the Universitat de València under project UV-INV-AE17-707705.

[a)]Author to whom correspondence should be addressed. Electronic mail: facundo.ballester@uv.es; Telephone +34 963543883.

REFERENCES

1. Guix B, Finestres F, Tello J-I, et al. Treatment of skin carcinomas of the face by high-dose-rate brachytherapy and custom-made surface molds. *Int J Radiat Oncol*. 2000;47:95–102.
2. Pérez-Calatayud J, Granero D, Ballester F, et al. A dosimetric study of Leipzig applicators. *Int J Radiat Oncol*. 2005;62:579–584.
3. Ouhib Z, Kasper M, Perez Calatayud J, et al. Aspects of dosimetry and clinical practice of skin brachytherapy: the American Brachytherapy Society working group report. *Brachytherapy*. 2015;14:840–858.
4. Candela-Juan C, Niatsetski Y, van der Laarse R, et al. Design and characterization of a new high-dose-rate brachytherapy Valencia applicator for larger skin lesions. *Med Phys*. 2016;43:1639–1648.
5. Perez-Calatayud J, Ballester F, Das RK, et al. Dose calculation for photon-emitting brachytherapy sources with average energy higher than 50 keV: report of the AAPM and ESTRO. *Med Phys*. 2012;39:2904–2929.
6. Candela-Juan C, Vijande J, García-Martínez T, et al. Comparison and uncertainty evaluation of different calibration protocols and ionization chambers for low-energy surface brachytherapy dosimetry. *Med Phys*. 2015;42:4954–4964.
7. Ibanez-Rosello B, Bautista-Ballesteros JA, Candela-Juan C, et al. Evaluation of the shielding in a treatment room with an electronic brachytherapy unit. *J Radiol Prot*. 2017;37:N5–N12.
8. Beaulieu L, Carlsson Tedgren Å, Carrier J-F, et al. Report of the Task Group 186 on model-based dose calculation methods in brachytherapy beyond the TG-43 formalism: current status and recommendations for clinical implementation. *Med Phys*. 2012;39:6208–6236.
9. Chetty IJ, Curran B, Cygler JE, et al. Report of the AAPM Task Group No. 105: issues associated with clinical implementation of Monte Carlo-based photon and electron external beam treatment planning. *Med Phys*. 2007;34:4818–4853.
10. Watson PGF, Popovic M, Seuntjens J. Determination of absorbed dose to water from a miniature kilovoltage x-ray source using a parallel-plate ionization chamber. *Phys Med Biol*. 2017;63:015016.
11. Sempau J, Andreo P. Configuration of the electron transport algorithm of PENELOPE to simulate ion chambers. *Phys Med Biol*. 2006;51:3533–3548.
12. Rodriguez M, Sempau J, Brualla L. Technical note: study of the electron transport parameters used in penelope for the Monte Carlo simulation of Linac targets. *Med Phys*. 2015;42:2877–2881.
13. Garcia-Martinez T, Chan J-P, Perez-Calatayud J, Ballester F. Dosimetric characteristics of a new unit for electronic skin brachytherapy. *J Contemp Brachytherapy*. 2014;1:45–53.
14. Pai S, Patel RR, Quhib Z, Perez-Calatayud J. Comparative dosimetry of two electronic brachytherapy systems: Xoft Axxent electronic brachytherapy system (50 Kvp) and Esteya (EleKta) electronic brachytherapy system (69.5 Kvp) for skin application. *Brachytherapy*. 2014;13:S49–S50.
15. Perez-Calatayud J, Candela-Juan C, Vijande J, et al. PD-0186: dosimetric evaluation of the electronic brachytherapy system Esteya. *Radiother Oncol*. 2015;115:S93.
16. Venselaar J, Pérez-Calatayud J. A practical guide to quality control of brachytherapy equipment. Eur Guidel Qual Assur Radiother. 2004: 8 (January 2001).
17. Rivard MJ, Davis SD, DeWerd LA, Rusch TW, Axelrod S. Calculated and measured brachytherapy dosimetry parameters in water for the Xoft

Axxent x-ray source: an electronic brachytherapy sourcea). *Med Phys*. 2006;33:4020–4032.
18. Clausen S, Schneider F, Jahnke L, et al. A Monte Carlo based source model for dose calculation of endovaginal TARGIT brachytherapy with INTRABEAM and a cylindrical applicator. *Z Med Phys*. 2012;22:197–204.
19. Croce O, Hachem S, Franchisseur E, Marcié S, Gérard J-P, Bordy J-M. Contact radiotherapy using a 50kV X-ray system: evaluation of relative dose distribution with the Monte Carlo code PENELOPE and comparison with measurements. *Radiat Phys Chem*. 2012;81:609–617.
20. Safigholi H, Faghihi R, Jashni SK, Meigooni AS. Characteristics of miniature electronic brachytherapy x-ray sources based on TG-43U1 formalism using Monte Carlo simulation techniques. *Med Phys*. 2012;39:1971–1979.
21. Fulkerson RK, Micka JA, DeWerd LA. Dosimetric characterization and output verification for conical brachytherapy surface applicators. Part I. Electronic brachytherapy source. *Med Phys*. 2014;41:022103.
22. Sempau J, Badal A, Brualla L. A PENELOPE -based system for the automated Monte Carlo simulation of clinacs and voxelized geometries-application to far-from-axis fields. *Med Phys*. 2011;38:5887–5895.
23. Salvat F, Fernández-Varea J, Sempau J. PENELOPE-2014: A Code System for Monte Carlo Simulation of Electron and Photon Transport; 2015, (July):408.
24. Almansa JF, Guerrero R, Torres J, Lallena AM. Monte Carlo dosimetric characterization of the flexisource Co-60 high-dose-rate brachytherapy source using PENELOPE. *Brachytherapy*. 2017;16:1073–1080.
25. Vijande J, Granero D, Perez-Calatayud J, Ballester F. Monte Carlo dosimetric study of the medium dose rate CSM40 source. *Appl Radiat Isot*. 2013;82:283–288.
26. Ballester F, Carlsson Tedgren Å, Granero D, et al. A generic high-dose rate 192 Ir brachytherapy source for evaluation of model-based dose calculations beyond the TG-43 formalism. *Med Phys*. 2015;42:3048–3062.
27. Sempau J, Fernández-Varea JM, Acosta E, Salvat F. Experimental benchmarks of the Monte Carlo code penelope. *Nucl Instruments Methods Phys Res Sect B*. 2003;207:107–123.
28. Ye S-J, Brezovich IA, Pareek P, Naqvi SA. Benchmark of PENELOPE code for low-energy photon transport: dose comparisons with MCNP4 and EGS4. *Phys Med Biol*. 2004;49:387–397.
29. Chica U, Anguiano M, Lallena AM. Benchmark of PENELOPE for low and medium energy X-rays. *Phys Med*. 2009;25:51–57.
30. Herranz E, Herraiz JL, Ibáñez P, et al. Phase space determination from measured dose data for intraoperative electron radiation therapy. *Phys Med Biol*. 2015;60:375–401.
31. Sabbatucci L, Salvat F. Theory and calculation of the atomic photoeffect. *Radiat Phys Chem*. 2016;121:122–140.
32. Pratt RH, Ron A, Tseng HK. Atomic photoelectric effect above 10 keV. *Rev Mod Phys*. 1973;45:273–325.
33. Scofield JH. *Theoretical Photoionization Cross Sections from 1 to 1500 KeV*. Livermore, CA: Lawrence Livermore Laboratory; 1973. https://www.osti.gov/servlets/purl/4545040.
34. Sakurai JJ. *Advanced Quantum Mechanics*, 1st ed. New York, NY: Addison and Wesley; 1967.
35. Born M. *Atomic Physics*. London: Blackie and Son; 1969.
36. Baym G. *Lectures in Quantum Mechanics*. Boulder, Colorado: Westview Press; 1974.
37. Cullen DE, Hubbell JH, Kissel L. *EPDL97: The Evaluated Photo Data Library `97 Version*, Vol. 6. Livermore, CA: Lawrence Livermore Laboratory; 1997.
38. Ribberfors R. X-ray incoherent scattering total cross sections and energy-absorption cross sections by means of simple calculation routines. *Phys Rev A*. 1983;27:3061–3070.
39. Sechopoulos I, Rogers DWO, Bazalova-Carter M, et al. RECORDS: improved Reporting of montE CarlO RaDiation transport Studies: report of the AAPM Research Committee Task Group 268. *Med Phys*. 2018;45:e1–e5.
40. Ali ESM, Rogers DWO. Efficiency improvements of x-ray simulations in EGSnrc user-codes using bremsstrahlung cross-section enhancement (BCSE). *Med Phys*. 2007;34:2143–2154.
41. Watson PGF, Seuntjens J. Technical note: effect of explicit M and N - shell atomic transitions on a low-energy x-ray source. *Med Phys*. 2016;43:1760–1763.
42. Andreo P, Burns DT, Salvat F. On the uncertainties of photon mass energy-absorption coefficients and their ratios for radiation dosimetry. *Phys Med Biol*. 2012;57:2117–2136.
43. Rivard MJ, Coursey BM, DeWerd LA, et al. Update of AAPM Task Group No. 43 Report: a revised AAPM protocol for brachytherapy dose calculations. *Med Phys*. 2004;31:633–674.
44. BIMP. *Evaluation of Measurement Data — Guide to the Expression of Uncertainty in Measurement*; 2010.
45. Candela-Juan C, Niatsetski Y, Ouhib Z, Ballester F, Vijande J, Perez-Calatayud J. Commissioning and periodic tests of the Esteya® electronic brachytherapy system. *J Contemp Brachytherapy*. 2015;2:189–195.
46. Pozuelo F, Gallardo S, Querol A, Verdu G, Rodenas J. X-ray simulation with the Monte Carlo code PENELOPE. Application to Quality Control. In: 2012 Annual International Conference of the IEEE Engineering in Medicine and Biology Society. Vol 2012. IEEE; 2012:5777-5780. https://doi.org/10.1109/embc.2012.6347307
47. Mayorga PA, Brualla L, Flühs A, Sauerwein W, Lallena AM. Testing Monte Carlo absolute dosimetry formalisms for a small field 'D'-shaped collimator used in retinoblastoma external beam radiotherapy. *Biomed Phys Eng Express*. 2016;2:065008.
48. Hiatt JR, Rivard MJ, Hughes HG. Simulation evaluation of NIST air-kerma rate calibration standard for electronic brachytherapy. *Med Phys*. 2016;43:1119–1129.
49. Ramaseshan R, Kohli K, Cao F, Heaton R. Dosimetric evaluation of plastic water diagnostic therapy. *J Appl Clin Med Phys*. 2008;9:98–111.
50. Butson MJ, Yu PKN, Cheung T, Alnawaf H. Energy response of the new EBT2 radiochromic film to x-ray radiation. *Radiat Meas*. 2010;45:836–839.
51. White Paper: GafChromic ® EBT2 and EBT3 Films for Ball Cube II Phantom. http://www.gafchromic.com/documents/BallCube_II_EBT2_3_box_insert_201404.pdf.
52. Kairn T, Aland T, Kenny J. Local heterogeneities in early batches of EBT2 film: a suggested solution. *Phys Med Biol*. 2010;55:L37–L42.
53. Lewis D, Devic S. Correcting scan-to-scan response variability for a radiochromic film-based reference dosimetry system. *Med Phys*. 2015;42:5692–5701.
54. Goubert M, Parent L. Dosimetric characterization of INTRABEAM® miniature accelerator flat and surface applicators for dermatologic applications. *Phys Med*. 2015;31:224–232.
55. Moradi F, Ung NM, Khandaker MU, et al. Monte Carlo skin dose simulation in intraoperative radiotherapy of breast cancer using spherical applicators. *Phys Med Biol*. 2017;62:6550–6566.

SUPPORTING INFORMATION

Additional supporting information may be found online in the Supporting Information section at the end of the article.

Data S1: General information.
Data S2: 10 mm Esteya applicator geometry file for PENELOPE2014.
Data S3: 10 mm Esteya applicator PSF.
Data S4: 30 mm Esteya applicator geometry file.
Data S5: 30 mm Esteya applicator PSF.

On the use of the absorbed depth-dose measurements in the beam calibration of a surface electronic high-dose-rate brachytherapy unit, a Monte Carlo-based study

Christian Valdes-Cortez[a)]
Departamento de Física Atómica, Molecular y Nuclear, Universidad de Valencia (UV), Valencia 46100, Spain
Radiotherapy Department, Centro Oncológico del Norte, Antofagasta 1240000, Chile

Yury Niatsetski
R&D Elekta Brachytherapy, Waardgelder 1,3905 TH, Veenendaal, The Netherlands

Facundo Ballester and Javier Vijande
Departamento de Física Atómica, Molecular y Nuclear, Universidad de Valencia (UV), Valencia 46100, Spain
IRIMED Joint Research Unit (IIS La Fe - UV), Valencia, Spain

Cristian Candela-Juan
Centro Nacional de Dosimetría (CND), Instituto Nacional de Gestión Sanitaria, Valencia 46009, Spain

Jose Perez-Calatayud
Radiotherapy Department, La Fe Hospital, Valencia 46026, Spain
IRIMED Joint Research Unit (IIS La Fe - UV), Valencia, Spain

(Received 24 June 2019; revised 6 November 2019; accepted for publication 6 November 2019; published 4 December 2019)

Purpose: To evaluate the use of the absorbed depth-dose as a surrogate of the half-value layer in the calibration of a high-dose-rate electronic brachytherapy (eBT) equipment. The effect of the manufacturing tolerances and the absorbed depth-dose measurement uncertainties in the calibration process are also addressed.

Methods: The eBT system Esteya® (Elekta Brachytherapy, Veenendaal, The Netherlands) has been chosen as a proof-of-concept to illustrate the feasibility of the proposed method, using its 10 mm diameter applicator. Two calibration protocols recommended by the AAPM (TG-61) and the IAEA (TRS-398) for low-energy photon beams were evaluated. The required Monte Carlo (MC) simulations were carried out using PENELOPE2014. Several MC simulations were performed modifying the flattening filter thickness and the x-ray tube potential, generating one absorbed depth-dose curve and a complete set of parameters required in the beam calibration (i.e., HVL, backscatter factor (B_w), and mass energy-absorption coefficient ratios $(\mu_{en}/\rho)_{water,air}$), for each configuration. Fits between each parameter and some absorbed dose-ratios calculated from the absorbed depth-dose curves were established. The effect of the manufacturing tolerances and the absorbed dose-ratio uncertainties over the calibration process were evaluated by propagating their values over the fitting function, comparing the overall calibration uncertainties against reference values. We proposed four scenarios of uncertainty (from 0% to 10%) in the dose-ratio determination to evaluate its effect in the calibration process.

Results: The manufacturing tolerance of the flattening filter (±0.035 mm) produces a change of 1.4% in the calculated HVL and a negligible effect over the B_w, $(\mu_{en}/\rho)_{water,air}$, and the overall calibration uncertainty. A potential variation of 14% of the electron energies due to manufacturing tolerances in the x-ray tube (69.5 ± ~10 keV) generates a variation of 10% in the HVL. However, this change has a negligible effect over the B_w and $(\mu_{en}/\rho)_{water,air}$, adding 0.1% to the overall calibration uncertainty. The fitting functions reproduce the data with an uncertainty ($k = 2$) below 1%, 0.5%, and 0.4% for the HVL, B_w, and $(\mu_{en}/\rho)_{water,air}$, respectively. The four studied absorbed dose-ratio uncertainty scenarios add, in the worst-case scenario, 0.2% to the overall uncertainty of the calibration process.

Conclusions: This work shows the feasibility of using the absorbed depth-dose curve in the calibration of an eBT system with minimal loss of precision. [https://doi.org/10.1002/mp.13920]

Key words: beam calibration, dosimetry, electronic brachytherapy, Monte Carlo simulation

1. INTRODUCTION

Surface high-dose-rate electronic brachytherapy (eBT) has become an effective treatment option for the non-melanoma skin cancer, achieving excellent control rates and good cosmetic results.[1–7] A surface eBT system consists mainly of two components: an x-ray tube, which accelerates electrons in the energy range between 50 and 70 kVp and a surface applicator (between 10 and 50 mm diameters) positioned directly in contact with the skin. The applicator may serve as collimator and flattening filter (depending on the eBT system), producing conical irradiation beams.[8]

Evaluation and verification of the absorbed depth-dose and the corresponding beam calibration represent an essential part of the quality control procedure for an eBT system.[9–11] Currently, the most common calibration protocols make use of the experimentally measured half-value layer (HVL) as the beam quality index.[12,13] Performing such measurement requires the availability of aluminum slabs of high purity (99.9%) with a thickness accuracy better than 0.05 mm.[12,13] The HVL measurement requires the acquisition of x-ray images for the system alignment,[12] a cumbersome and time-consuming procedure to achieve the proper geometry. Furthermore, noise-to-signal ratio issues are expected to appear when the measurement is performed far from the source, at 100 cm (distance where HVL is defined), due to the inverse square law. Those characteristics are a drawback compared to the external beam radiation therapy (EBRT), where the beam quality index is obtained directly from absorbed depth-dose measurements.[13,14] Although it is true that some EBRT machines would benefit from imaging to align the dosimeters, this is not a widespread practice in clinical routine.

The low-energy range of the eBT devices makes the entire system (source, detector, and propagation medium) very sensitive even to minimal deviations from their intended designs. A few publications are reporting on noticeable disagreements between the measured and expected values, mostly due to machine-to-machine differences of some of its components (tolerances in the manufacturing of the target, flattening filter, etc.) or inaccuracies in the system alignment.[15,16] Other studies show that dosimeters, typically used in the absorbed depth-dose determination for brachytherapy systems, would require the incorporation of additional (depth-dependent) correction factors and modification of the effective point of measurement recommended by the manufacturer.[17,18] Those are the issues that need to be considered in the uncertainty evaluation.

The aim of this work was to evaluate the use of the absorbed depth-dose in a water phantom to determine the HVL and other dosimetric factors used in the calibration of a specific eBT system, the effect of the manufacturer tolerances, and the uncertainties over the whole process.

2. MATERIALS AND METHODS

2.A. High-dose-rate electronic brachytherapy systems

The Esteya® eBT system (Elekta Brachytherapy, Veenendaal, The Netherlands) accelerates electrons in its x-ray tube at 69.5 kV toward a tungsten target, delivering an x-ray beam with maximum absorbed dose-rate of 198 Gy/h at the phantom surface. This system comes with a set of conical applicators of 10, 15, 20, 25, and 30 mm diameter, closed by a plastic cap. The applicators share the same flattening filter (attached to the primary collimator) and a source-to-surface distance (SSD) of approximately 60 mm (see Fig. 1).[8,10,19,20]

2.B. Monte Carlo code

The simulations were performed using penEasy (v. 2015-05-30),[21] a modular program for PENELOPE2014, which simulates electrons and photons transport from 50 eV to 1 GeV.[22] PENELOPE has been successfully used in the study of both electronic[8,23] and radioisotope-based[18,24–26] brachytherapy sources.

The photoelectric cross sections are calculated with the code PHOTACS,[27] using the elementary theory of the atomic photoelectric effect (independent electron model)[28,29] to calculate the tables of excitation and ionization cross sections.[27] The Rayleigh scattering cross sections are calculated using nonrelativistic perturbation theory,[30–32] obtaining the atomic form factors from EPDL97.[33] Compton interactions use the relativistic impulse approximation, which takes into account both binding effects and Doppler broadening.[34] Furthermore, PENELOPE2014 simulates explicitly[35] the emission of characteristic x rays, Auger and Coster-Kronig electrons that result from vacancies produced in K, L, M and N shells,[22]

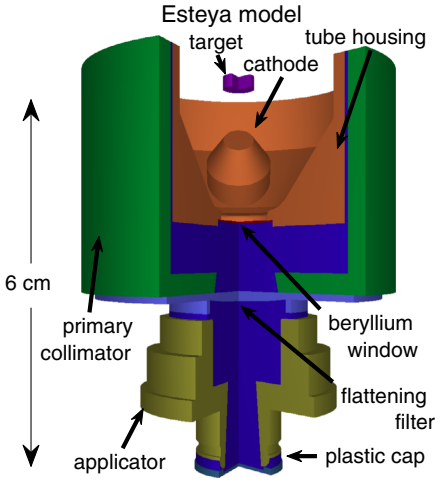

FIG. 1. Ideal geometry for the APP10 mm of the Esteya unit. SSD is 6 cm as indicated. [Color figure can be viewed at wileyonlinelibrary.com]

using transition probabilities extracted from the evaluated atomic data library (EADL).[36] The energy of the x rays published in the EADL was updated, when available, being the K and L shell transitions from Deslattes et al.[37] and the M lines from Bearden.[38] Other transition energies are calculated from the energy eigenvalues of the Dirac-Hartree-Fock-Slater equations for neutral atoms.[36]

2.C. Monte Carlo model of the Esteya system

The flattening filter (*FF*) is the most relevant structure in determining the beam properties (see Fig. 1). According to the eBT vendor, the manufacturing tolerance of the *FF* thickness is ±0.035 mm. We do not have information regarding the tolerance of the tube potential. Therefore, to study the effect of unintended modifications in the x-ray tube potential (Ee^-) on the beam properties, we have modified the Ee^- from the nominal value of 69.5 kV to 60 kV and 80 kV.

We considered four possible geometries to model the investigated eBT system. The ideal geometry (IG) corresponds to the model with the nominal dimensions specified by the manufacturer. The negative (NG) and the positive (PG) geometries are used to consider the negative and positive ranges of the manufacturing tolerances. The flattening filter-free (*FFF*) geometry is conceived to obtain the spectrum used in the HVL calculations, speeding up the simulations through removing the *FF*. For the IG, we use the "detailed setup" (Fig. 1) of the 10 mm diameter applicator (APP_{10mm}) with the Gaussian intensity electron source model, fully described in a previous publication.[8] Briefly, the Esteya electron source model is a mono-energetic electron beam of 69.5 keV, with a Gaussian electron distribution centered on the rectangular foil with an FWHM equal to the focal spot size (1.8 × 1.3 mm^2).

2.D. Calibration protocols

There are two well-known calibration protocols — the in-air method (based on air kerma), recommended by the AAPM in the TG-61[12] and the in-water method (based on absorbed dose-to-water), recommended by the IAEA in the TRS-398.[13]

The in-air TG-61 method requires the determination of the following three quantities: the air-kerma calibration factor (N_k), the air-to-water mass energy-absorption coefficient ratio ($(\mu_{en}/\rho)_{water,air}$), and the backscatter factor (B_w). Usually, the calibration certificate of any ionization chamber comes with two or more values of N_k for different beam qualities. Additionally, the user can obtain the ($(\mu_{en}/\rho)_{water,air}$) and B_w factors directly from the TG-61. The proper factors for a particular beam are obtained through interpolation from the calibration certificate and the TG-61 tables.

The in-water IAEA method is based mainly on the following two factors: the absorbed dose-to-water calibration factor ($N_{D,w}$) and the beam quality correction factor ($k_{Q,Q0}$), which are specified in terms of the HVL of a reference beam quality. The chamber calibration certificate comes with one $N_{D,w}$ and two or more $k_{Q,Q0}$. The user needs to find the proper $k_{Q,Q0}$ for the beam to be calibrated through an interpolation.

In this work, we divide the dosimetric parameters used in both calibration protocols into machine-dependent (i.e., HVL, $(\mu_{en}/\rho)_{water,air}$ and B_w) and chamber-dependent (i.e., N_k and $k_{Q,Q0}$) parameters. We will evaluate the feasibility of obtaining all the machine-dependent parameters from the absorbed depth-dose data and the effect of this method on the final uncertainty of the calibration.

2.E. Machine-dependent parameters

2.E.1. HVL

The HVL is defined as the aluminum thickness x_{Al} (in mm) at which the air-kerma rate is reduced to one-half of its original value. It can be calculated analytically through

$$K_{ratio} = \frac{\sum(\Psi_{FFF})_i^{free-space}\left(\frac{\mu_{en}}{\rho}\right)_{i,air} exp\left(-\mu_{i,air}x_{air} - \mu_{i,FF}x_{FF} - \mu_{i,Al}x_{Al}\right)}{\sum(\Psi_{FFF})_i^{free-space}\left(\frac{\mu_{en}}{\rho}\right)_{i,air} exp\left(-\mu_{i,air}x_{air} - \mu_{i,FF}x_{FF}\right)}, \quad (1)$$

MC simulations with different *FF* thicknesses (x_{FF}) were performed. The x_{FF} symbol denotes the thickness measured at the center of the *FF* (thickest section) in the direction of the beam axis. The minimum (x_{FFmin}) and maximum (x_{FFmax}) values of x_{FF} were chosen to achieve 2 HVL and 1/2 HVL, respectively, where HVL is the value obtained with IG and Ee^- = 69.5 keV.

where $(\mu_{en}/\rho)_{i,air}$ is the mass energy-absorption coefficient for air in each energy bin *i*; $\mu_{i,air}$, $\mu_{i,FF}$, and $\mu_{i,Al}$ are the linear attenuation coefficients for air, *FF*, and aluminum, respectively; x_{FF} running from x_{FFmin} to x_{FFmax} for each evaluation of K_{ratio}; x_{air} is equal to 1000 mm minus the distance between the source and the applicator exit (approximately 60 mm, see Fig. 1). Therefore, the HVL is the aluminum thickness where K_{ratio} = 0.5. Both the attenuation and the mass energy-absorption coefficients were calculated with PENELOPE2014 using an energy resolution of 0.1 keV, the same as the bin width used in the Eq. (1).

The $(\Psi_{FFF})_i^{free-space}$ is the energy fluence (for each energy bin *i*) obtained in a *FFF* geometry with a detector of 5 mm

TABLE I. Summary of the main characteristics of the Monte Carlo method used in this work.

Item	Description	References
Code	(a) PENELOPE2014, (b) penEasy (v. 2015-05-30) compiled with GNU Fortran (GCC) 5.3.1 using the −0 optimization flag	(1) Salvat et al.[22](2) Sempau et al.[21]
Validation	Previously validated	Valdes-Cortez et al.[8] Ye et al.,[42] Chica et al.,[43] Croce et al.[23]
Timing	$(\Psi_{FFF})^{free-space}$ and $(\Psi_{xCOlmin})^{free-air}$ were obtained in 3362 and 4789 h, respectively (CPU time, total sum of 100 parallel processes). All simulations were performed with a number of histories between 10^9 and 10^{10}	Parallel process treatment from Badal and Sempau.[39]
Source description	Electron beam model: Mono-energetic (60, 69.5, and 80 keV), Gaussian electron distribution (FWHM = focal spot size of 1.8 × 1.3 mm^2)	Valdes-Cortez et al.[8]
Cross sections	(a) Photoelectric calculated with PHOTACS, (b) Rayleigh scattering using nonrelativistic perturbation theory, (c) Compton uses a relativistic impulse approximation, (d) Atomic relaxation using the EADL transition probabilities.	(a) Sabbatucci et al.[27]; (b) Sakurai,[30] Born,[31] Baym,[32] Cullen et al.[33]; (c) Ribberfors[34]; (d) Perkins et al.,[36] Deslattes et al.,[37] Bearden.[38]
Transport parameters	Photon cutoff = 8 keV; Electron cutoff = 8 keV in the target, electron transport disabled otherwise, with PENELOPE transport parameters C1 = C2 = 0	Valdes-Cortez et al.,[8] Sempau et al.,[41] Salvat et al.[22]
Variance reduction tools	(a) Interaction forcing: hard bremsstrahlung emission (target). (b) Splitting particles (penEasy rotational option at the flattening filter)	(a) Salvat et al.[22] (b) Sempau et al.[21]
Scored quantities	Absorbed dose in water (kerma approximation)	
Statistical uncertainties	≤1.4% (k = 2, maximum uncertainty of all calculated quantities)	
Statistical method	History-by-history	Salvat et al.[22]
Post-processing	None	

radius located at the applicator exit in vacuum. As the HVL is defined in a narrow beam geometry at a source-to-detector distance equal to 1000 mm,[12] the validity of using this spectrum is based on its independence with respect to the detector radius and distance from the source. To evaluate that condition, several spectra (test *FFF* spectra) were obtained with different detector radii (1, 2.5, and 5 mm located at the applicator exit) and distances from the source (60, 500, and 1000 mm for a detector of 5 mm radius).

Additionally, the HVL using $x_{FF} = x_{FF\_IG}$ (x_{FF} corresponding to IG) and the average energy of this setup was compared to those obtained in a previous work (using a different approach)[8] and with the experimental data published by Garcia-Martinez et al.[19] The proper calculation of the average energy from $(\Psi_{FFF})^{free-space}$ was performed considering its attenuation by x_{FF_IG} and an air column of approximately 940 mm. To evaluate the HVL in those configurations where we have modified the Ee^-, two additional $(\Psi_{FFF})^{free-space}$ were simulated by changing Ee^- to 60, and 80 keV. $x_{FF} = x_{FF\_IG}$ was fixed in both cases.

The procedure for obtaining the spectra has been extensively described in a previous work.[8] However, here we use a lower energy cutoff (8 keV) to take into account the characteristics x-ray lines appearing in the NG with x_{FFmin}.

All the spectra were obtained through 100 parallelized MC calculation processes following the principles (including the proper use of the initial seeds to keep the simulation uncorrelated) published by Badal and Sempau.[39] The MC details are summarized in Table I following the recommendations of the RECORDS AAPM TG-268 report.[40] Further information about the transport parameters, variance reduction tools, etc. is described elsewhere.[8,22,41]

2.E.2. Mass energy-absorption coefficient for air to water

The ratios (in free-air) of mass energy-absorption coefficients of water to air were calculated from

$$\left(\frac{\mu_{en}}{\rho}\right)_{water,air} = \frac{\sum(\Psi_{xFFmin})_i^{free-air}\left(\frac{\mu_{en}}{\rho}\right)_{i,water} exp\left(-\mu_{i,FF}x_{FFextra}\right)}{\sum(\Psi_{xFFmin})_i^{free-air}\left(\frac{\mu_{en}}{\rho}\right)_{i,air} exp\left(-\mu_{i,FF}x_{FFextra}\right)}, \quad (2)$$

where $(\Psi_{xFFmin})_i^{free-air}$ is the energy fluence in a small volume (cylinder of 1 mm radius 0.1 mm height) inserted in a free-air space (at the applicator exit) for each energy bin i. $x_{FFextra}$ is the thickness of the additional material added to x_{FFmin} ($0 \le x_{FFextra} \le x_{FFmax} - x_{FFmin}$). $(\mu_{en}/\rho)_{i,water}$ is the mass energy-absorption coefficient for water.

Considering the $(\mu_{en}/\rho)_{i,medium}$ as tabulated parameters, the $(\mu_{en}/\rho)_{water,air}$ ratio depends only on two variables, that is, $[(\mu_{en}/\rho)_{water,air}](\Psi, x_{FFextra})$. In order to validate this procedure, two extra spectra were simulated with IG (Ψx_{FF_IG}) and PG (Ψx_{FFmax}), comparing the values of $(\mu_{en}/\rho)_{water,air}$ calculated with the following pairs of parameters: ($\Psi = \Psi x_{FFmin}$, $x_{FFextra} = x_{FF\_IG} - x_{FFmin}$) with ($\Psi = \Psi x_{FF\_IG}$, $x_{FFextra} = 0$) and ($\Psi = \Psi x_{FFmin}$, $x_{FFextra} = x_{FFmax} - x_{FFmin}$) with ($\Psi = \Psi x_{FFmax}$, $x_{FFextra} = 0$). Additionally, two extra spectra were simulated using the IG and a $x_{FFextra} = 0$ with Ee^- at 60 and 80 keV.

A comparison was made with the published data: from Table IV in the AAPM TG-61 report[12] and Table C1 in the recent study by Andreo.[42] Values from both sources were obtained through linear interpolations using the simulated HVLs (see Section 2.E.1). [Correction added on January 08, 2020, after first Online publication: Table 1 has been changed to Table C1 in this paragraph.]

2.E.3. Backscatter factor

The backscatter factors were calculated using the linear track-length estimator[43] according to

$$B_w = \frac{\sum \mathrm{E}_i \left(\frac{\mu_{en}}{\rho}\right)_{i,water} (l_i)^{water}_{water}}{\sum \mathrm{E}_i \left(\frac{\mu_{en}}{\rho}\right)_{i,water} (l_i)^{in-air}_{water}}, \quad (3)$$

where $(l_i)^{water}_{water}$ and $(l_i)^{in-air}_{water}$ are the distances traveled by photons (tallied in each energy bin i) in a small volume of water (cylinder of 1 mm radius and 0.1 mm height) placed at the surface of a water phantom (cylinder of 100 mm radius 200 mm height) and in-air, respectively. Each quantity l_i was obtained through one simulation for each value of x_{FF}. Two extra simulations were carried out using the IG conditions with Ee^- of 60 and 80 keV. To follow strictly its formal definition, one should use $(\mu_{tr}/\rho)_{i,water}$ mass energy-transfer coefficient, instead of $(\mu_{en}/\rho)_{i,medium}$. However, the difference between those two factors is negligible, less than 0.02% when considering photons up to 80 keV in water.[12,42,44]

A comparison was made with the data published by the AAPM (TG-61)[12] and by Andreo.[42] The B_w factors from the TG-61 were obtained through 2D linear interpolations of the data corresponding to SSDs of 5 and 7 cm, with a collimator of 10 mm diameter (TG-61 Table V).[12] The B_w factors from the study of Andreo were obtained through linear interpolations using the Table C2 of that work (70 kV, SSD = 100 mm and 10 mm diameter).[42] [Correction added on January 08, 2020, after first Online publication: Table 2 has been changed to Table C2 in this paragraph.]

2.F. Absorbed depth-dose calculation

The absorbed depth-dose (kerma approximation) was scored in a cylindrical mesh with cells of 1 mm radius and 0.1 mm height, running from 2.95 to 50.05 mm depth. The applicator exit was positioned at the surface of a cylindrical water phantom (ρ = 0.998 g/cm^3)[45] of 100 mm radius and 200 mm height. The water phantom is in turn located at the center of a cylinder of 250 mm radius and 500 mm height filled with dry air ($\rho = 1.20479 \times 10^{-3}$ g/cm^3). Absorbed depth-dose curves were recorded for each *FF* thickness with Ee^- of 69.5 keV. Two additional absorbed depth-dose curves were obtained using Ee^- of 60 and 80 keV with the IG.

In this work, we define $D_{z,3}$ as the absorbed dose-ratio calculated from the absorbed dose obtained at z and 3 mm

TABLE II. Summary of simulation results compared against reported values (IG). In parentheses: the uncertainty of the last significant figure. The TG-61 dataset is reported with 3% uncertainty (k = 2).[12]

Items	Values								
Geometry	NG			IG			PG		
Ee^-	69.5 keV			60 keV	69.5 keV	80 keV	69.5 keV		
x_{FF} (mm)[a]	0.590	0.790	1.190	1.590	1.590	1.590	2.199	3.310	4.980
HVL[b]	0.859(6)	1.080(6)	1.435(8)	1.57(1)	1.738(9)	1.94(1)	2.14(1)	2.76(1)	3.49(2)
$D_{10,3}$	0.518(4)	0.551(5)	0.588(5)	0.601(5)	0.614(6)	0.623(4)	0.635(6)	0.658(6)	0.674(6)
$D_{20,3}$	0.241(2)	0.265(3)	0.298(3)	0.308(3)	0.323(4)	0.334(2)	0.346(3)	0.373(4)	0.396(4)
$D_{50,3}$	0.0410(5)	0.0477(6)	0.0570(7)	0.0585(7)	0.0645(8)	0.0711(5)	0.0742(9)	0.086(1)	0.097(1)
B_w	1.058(4)	1.064(4)	1.067(4)	1.068(3)	1.065 (4)	1.067(4)	1.069(4)	1.073(4)	1.072(4)
Fit	1.059(5)	1.062(5)	1.066(5)	1.067(5)	1.068(5)	1.068(5)	1.069(5)	1.071(5)	1.072(5)
TG-61.[12]	1.044	1.047	1.050	1.052	1.053	1.054	1.057	1.059	1.060
Andreo.[44]	1.050(6)	1.053(6)	1.057(6)	1.060(6)	1.060(6)	1.060(6)	1.063(6)	1.067(6)	1.069(6)
$(\mu_{en}/\rho)_{water,air}$	1.023(3)	1.021(3)	1.019(3)	1.018(4)	1.018(3)	1.020(4)	1.018(4)	1.019(4)	1.020(4)
Fit	1.023(4)	1.021(4)	1.019(4)	1.018(4)	1.018(4)	1.018(4)	1.018(4)	1.019(4)	1.020(4)
TG-61.[12]	1.021	1.019	1.017	1.017	1.017	1.018	1.018	1.020	1.023
Andreo.[44]	1.020(4)	1.018(4)	1.016(4)	1.016(4)	1.016(4)	1.016(4)	1.016(4)	1.019(4)	1.024(4)

[a]Measured at the center of the filter (thickest part).
[b]In mm Al.

depth. The machine-dependent parameters (i.e., HVL_{fit}, $[(\mu_{en}/\rho)_{water,air}]_{fit}$ and $(Bw)_{fit}$, see Table III) were fitted against $D_{10,3}$, $D_{20,3}$, and $D_{50,3}$. We used 3 mm depth as a fixed measurement point because this is the typical prescription depth for surface treatments.[7] The fitting functions were optimized taking into account only the data obtained with Ee^- of 69.5 keV. The uncertainty of the fitting functions was estimated through the quadrature sum of the maximum difference between the simulated and fitted values and the maximum internal uncertainty of each simulated value.

2.G. Effects of the measurement uncertainties on the calibration processes

We based our analysis on the data published by Candela-Juan et al.[20] for the calibration of an Esteya beam using the PTW T34013 (S/N 000146 in that work) parallel-plate ionization chamber (PTW, Freiburg, Germany). The chamber was calibrated in terms of N_k and $N_{D,w}$ for the beam qualities TW50 (50 kV, filtered by 1 mm Al, HVL = 1.13 mm Al) and TW70 (70 kV, filtered by 4 mm Al, HVL = 3.15 mm Al), henceforth called reference beams. The uncertainties estimated in that work were 4.8% and 5.4% (reference uncertainties) for the in-water and in-air methods, respectively.

We have defined four different levels for the uncertainty of the measured absorbed dose-ratios: 0%, 2%, 5%, and 10% uncertainty ($k = 2$). With this information, the uncertainty of the machine-dependent parameters (i.e., HVL_{fit}, $[(\mu_{en}/\rho)_{water,air}]_{fit}$ and $(B_w)_{fit}$) was divided into two components: the dataset uncertainty (i.e., only due to the use of the fitting functions, see Section 2.F.) and the uncertainty added exclusively by the absorbed dose-ratios determination. To obtain the last component separately, we propagated the four scenarios over the fitting functions (see Table III) assuming a dataset without uncertainty.

Those two components were added in quadrature to the reference uncertainties with the exception of the HVL_{fit}, whose uncertainty was propagated over the interpolations calculated to obtain the machine-dependent and chamber-dependent parameters. Then, the interpolation uncertainty was added in quadrature to the reference uncertainties.

According to Candela-Juan et al.,[20] the energy response of the ionization chamber for the reference beams is 0.1% for the $k_{Q,Q0}$ and 0.7% for the N_k. However, in order to explore the worst-case scenario, we raised that value up to 2%, matching our analysis with the maximum value recommended by the TG-61 and TRS-398.[12,13]

2.H. Uncertainties

All uncertainties will be expressed with a coverage factor $k = 2$. The Type B uncertainties of the attenuation and absorption factors were propagated over Eqs. (1), (2), and (3), according to the BIMP recommendations assuming normal distribution.[46] The Type B uncertainty was obtained from Andreo et al.,[47] considering the 2.5% ($k = 2$) value given for the grouping II corresponding to a beam with an average photon energy equal to 34.1 keV (Table I in that work).

3. RESULTS

3.A. HVL

HVLs were calculated with uncertainties below 0.7% (see Table II). The HVL for the IG configuration (1.738 ± 0.009 mm Al) agrees within the associated uncertainties with the value reported in a previous work.[8] Such value was obtained using a different methodology and it is in the experimental range measured by other authors.[8,19,20] The calculated average photon energy (IG, $Ee^- = 69.5$ keV) is 36.3 ± 0.2 keV, also consistent with the one obtained in a previous work (36.19 ± 0.09 keV, $k = 2$)[8] and with experimental measurements (36.2 ± 0.2 keV, $k = 2$).[19] The HVLs calculated from the test *FFF* spectra have an uncertainty below 1.4%, and differ from each other by not more than 0.3% (for all values of x_{FF} used in this work) without any systematic trend in their differences.

A variation of ±0.035 mm from x_{FF_IG} generates a change of ±1.4% of the HVL, while a modification of ±10 keV in the nominal Ee^- (69.5 keV) modifies the HVL by ±10% (see Fig. 2).

3.B. Free-in-air ratios of mass energy-absorption coefficient of water to air and backscatter factors

The $(\mu_{en}/\rho)_{water,air}$ ratios were calculated with uncertainties below 0.4% (see Table II). The differences with respect to the values reported by TG-61[10] and Andreo[39] (see Fig. 3 and Table II) are in all cases below the associated uncertainties. Differences between the $(\mu_{en}/\rho)_{water,air}$ obtained using $(\Psi_{xFFmin})^{free-air}$, $(\Psi_{xFF\_IG})^{free-air}$ and $(\Psi_{xFFmax})^{free-air}$ were negligible (≤0.1%).

The B_w factors were obtained with an uncertainty below 0.4%. The factors differ approximately 1% from the TG-61 data (see Table II and Fig. 3), within the 3% ($k = 2$) maximum tolerance reported by the AAPM.[12] The agreement with the data published by Andreo is, in general, within the uncertainties.[42]

3.C. Absorbed depth-dose

Figure 2 shows the relation between the HVL and the absorbed dose-ratios. The absorbed dose and the absorbed dose-ratios were determined with uncertainties below 1.1% and 1.3%, respectively (see Table II). A variation of the *FF* by ±0.035 mm generates changes of 0.3%, 0.5%, and 0.9% in $D_{10,3}$, $D_{20,3}$, and $D_{50,3}$, respectively. A variation of ±14% in the Ee^- (for the IG configuration) generates a change of approximately 2%, 4%, and 10% in $D_{10,3}$, $D_{20,3}$, and $D_{50,3}$, respectively. The HVL_{fit}, $[(\mu_{en}/\rho)_{water,air}]_{fit}$, and $(B_w)_{fit}$ (see Table III) are in agreement within 1%, 0.02%, and 0.3% as compared to the simulated HVL, $(\mu_{en}/\rho)_{water,air}$, and B_w. Considering the simulations with 60 and 80 keV, the HVL_{fit}

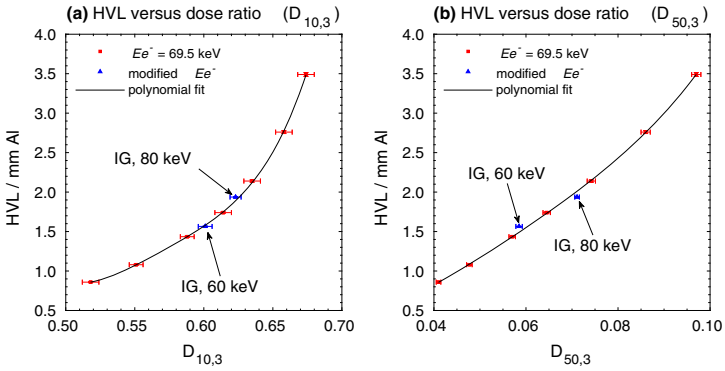

FIG. 2. (a) Correlation between HVL and the ratio of the doses at 10 to 3 mm depth. (b) Same for the ratio of the doses at 50 to 3 mm depth. For the red squares, the different dose-ratios were obtained varying the FF thickness maintaining *Ee-* fixed. For the blue triangles, the different dose-ratios and HVLs were obtained using the ideal flattening filter thickness (x_{FF_IG}) by varying the electron energy. The polynomial fit corresponds to a fourth order function optimized taking into account only the red squares. [Color figure can be viewed at wileyonlinelibrary.com]

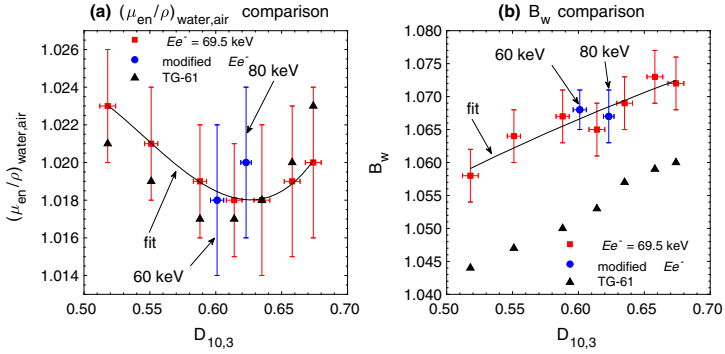

FIG. 3. (a) Relation between $(\mu_{en}/\rho)_{water,air}$ and the ratio between the absorbed doses at 10 to 3 mm depth. (b) Relation between B_w and the ratio between the absorbed doses at 10 to 3 mm depth. For the red squares, the different absorbed dose-ratios were obtained varying the flattening filter thickness maintaining the electron energy fixed. For the blue circles, the different dose-ratios were obtained using the ideal flattening filter thickness (IG) by varying *Ee-*. Black triangles correspond to the values reported in the AAPM TG-61 report.[12] The fit functions were optimized taking into account only the red squares. [Color figure can be viewed at wileyonlinelibrary.com]

TABLE III. Machine-dependent parameters fitted for the APP_{10mm} absorbed depth-doses, $HVL_{fit} = a_0 + a_1 x + a_2 x^2 + a_3 x^3 + a_4 x^4$ (HVL_{fit} in mm) $[(\mu_{en}/\rho)_{water,air}]_{fit} = a_0 + a_1 x + a_2 x^2 + a_3 x^3$, and $(B_w)_{fit} = a_0 + a_1 \ln(x)$. These expressions take values from $D_{10,3}$, $D_{20,3}$, or $D_{50,3}$ (Ee^- = 69.5 keV). The uncertainties (k = 2) expected for datasets are 1.0%, 0.4%, and 0.5%, respectively.

Parameter	Absorbed dose-ratio	a_0	a_1	a_2	a_3	a_4
HVL	$D_{10,3}$	8.30164×10^2	-5.845003×10^3	1.5425144×10^4	-1.8085974×10^4	7.962366×10^3
	$D_{20,3}$	2.216	−53.038	4.10327×10^2	-1.211388×10^3	1.34849×10^3
	$D_{50,3}$	1.28	−86.11	2.905427×10^3	-3.1169352×10^4	1.31920863×10^5
$(\mu_{en}/\rho)_{water,air}$	$D_{10,3}$	0.5408	2.7671	−5.1867	3.1693	–
	$D_{20,3}$	1.0613	−0.1851	−0.039	0.6156	–
	$D_{50,3}$	1.0562	−1.3142	14.2956	−47.2703	–
B_w	$D_{10,3}$	1.0925	0.0508	–	–	–
	$D_{20,3}$	1.0977	0.0268	–	–	–
	$D_{50,3}$	1.1096	0.0156	–	–	–

TABLE IV. Effect of the four absorbed dose-ratio uncertainty levels (d.r.u) over the machine-dependent and chamber-dependent parameters. The column d.r.u. = 0% corresponds to the minimum possible uncertainty due to the use of a dataset. The other columns incorporate the additional d.r.u. The dataset uncertainty of the TG-61 machine-dependent and the chamber-dependent parameters are already considered in the reference uncertainties. All values are presented with a coverage factor $k = 2$.

			Dose-ratio uncertainty			
Parameter type	Parameter	Absorbed dose-ratio	10%	5%	2%	0%
Machine-dependent parameters (this work dataset)	HVL	$D_{10,3}$	51%	25%	10%	1%
		$D_{20,3}$	27%	14%	5%	
		$D_{50,3}$	15%	8%	3%	
	$(\mu_{en}/\rho)_{water,air}$	$D_{10,3}$	0.1%	0.1%	–	0.4%
		$D_{20,3}$	0.1%	–	–	
		$D_{50,3}$	–	–	–	
	B_w	$D_{10,3}$	0.5%	0.2%	0.1%	0.5%
		$D_{20,3}$	0.3%	0.1%	0.1%	
		$D_{50,3}$	0.1%	0.1%	–	
Machine-dependent parameters (TG-61 dataset)	$(\mu_{en}/\rho)_{water,air}$	$D_{10,3}$	0.2%	0.1%	–	3%
		$D_{20,3}$	0.1%	–	–	
		$D_{50,3}$	0.1%	–	–	
	B_w	$D_{10,3}$	0.8%	0.4%	0.2%	
		$D_{20,3}$	0.4%	0.2%	0.1%	
		$D_{50,3}$	0.2%	0.1%	–	
Chamber-dependent parameters	$N_k/k_{Q,Q0}$	$D_{10,3}$	0.9%	0.6%	0.4%	2%/4%
		$D_{20,3}$	0.6%	0.5%	0.3%	
		$D_{50,3}$	0.5%	0.4%	0.2%	

agrees within 2.6%, 1.6%, and 5.0%; $(\mu_{en}/\rho)_{water,air}$ agrees within 0.2%; and the B_w factors agree within 0.1%, 0.2%, and 0.3% of the simulated values for $D_{10,3}$, $D_{20,3}$, and $D_{50,3}$, respectively.

Table IV shows the uncertainties calculated taking into consideration the four scenarios described in Section 2.7. The dataset uncertainties ($k = 2$) are: 1.0%, 0.4%, and 0.5% for HVL_{fit}, $[(\mu_{en}/\rho)_{water,air}]_{fit}$, and $(B_w)_{fit}$, respectively.

TABLE V. Final uncertainties of the calibration methods for each dose-ratio uncertainty (d.r.u.) scenario. The difference between the in-air "TG-61 dataset" and "this work dataset" for the d.r.u. = 0% is completely explained by the different dataset uncertainties considered for $(\mu_{en}/\rho)_{water,air}$ and B_w (see Table IV).

		Dose-ratio uncertainty			
Calibration method	Dose-ratio	10%	5%	2%	0%
In-water	$D_{10,3}$	5.0%	4.9%	4.9%	4.8%[a]
	$D_{20,3}$	4.9%	4.9%	4.9%	
	$D_{50,3}$	4.9%	4.9%	4.9%	
In-air "TG-61 dataset"	$D_{10,3}$	5.5%	5.4%	5.4%	5.4%[a]
	$D_{20,3}$	5.4%	5.4%	5.4%	
	$D_{50,3}$	5.4%	5.4%	5.4%	
In-air "this work dataset"	$D_{10,3}$	3.5%	3.4%	3.3%	3.3%
	$D_{20,3}$	3.4%	3.4%	3.3%	
	$D_{50,3}$	3.4%	3.3%	3.3%	

[a]Reference uncertainties from Candela-Juan et al.[20]

3.D. Effects of the measurement uncertainties on the calibration processes

The use of absorbed depth-dose to obtain the machine-dependent parameters adds as much as 0.2% to the calibration uncertainty (see Table V) for an absorbed dose-ratio with a 10% uncertainty. The use of $D_{50,3}$ instead of $D_{10,3}$ implies a maximum reduction of 0.1% over the final uncertainty budget. The use of the "this work dataset" instead of the "TG-61 dataset" would imply a reduction of nearly 40% in the overall uncertainty.

4. DISCUSSION

By considering the HVL-to-dose-ratio fit given in Table III and Fig. 2 it is possible to determine the data required for a beam calibration using a simple and straightforward absorbed depth-dose measurement.

The limits proposed for the x_{FF} cover adequately the manufacturing tolerances reported by the vendor (±0.035 mm). As it was established in a previous work,[8] the experimental measurements of the spectra from six Esteya x-ray tubes do not support an Ee^- value larger than 69.5 keV.[19] On the other hand, the average photon energy of the $(\Psi_{FFF})^{free-space}$ ($x_{FF} = x_{FF\_IG}$, $Ee^- = 69.5$ keV) agrees perfectly with the reported experimental value (36.2 ± 0.2 keV).[19] As the average photon energy obtained with $Ee^- = 60$ keV ($x_{FF} = x_{FF\_IG}$) is considerably smaller (32.3 ± 0.2 keV), we can conclude that

the ±14% variation of Ee^{-} also covers adequately the manufacturing tolerance of the tube potential.

The uncertainties achieved in this work for the $(\mu_{en}/\rho)_{water,air}$ and B_w are similar to those reported by Andreo et al.[42,47] Both quantities are very robust, observing minor modifications, even when significant variations in the x_{FF} value are considered. This condition gives us the confidence that any unreported source of uncertainty will not have a significant effect on the evaluated values in the proposed Dose-ratio-to-HVL formalism. In general, both factors agree within their uncertainties with the ones in the literature.[12,42,47] The use of $D_{50,3}$ instead of $D_{10,3}$ reduces the HVL_{fit} uncertainty by a factor of 3 (see Table IV). However, deeper measurement points not only may bring challenges due to a smaller signal-to-noise ratio, but also could imply noticeable spectral changes that might affect the dosimeter performance.[17] Therefore, a trade-off exists between the measurement sensibility to its uncertainties and higher signals. A location between both extremes (e.g., $D_{20,3}$) could be an interesting option to explore in the clinical context.

Nevertheless, the effect of the dose-ratio uncertainty on the overall uncertainty is less than 0.2%. This is true even in an extreme case of 10% dose-ratio uncertainty, which was conceived to include any unknown effect of the chamber performance.[17,18] However, it is more realistic to consider that the absorbed dose-ratio can be determined with uncertainties lower than 5%.[8,17] Furthermore, we have considered a large chamber energy response of 2%, when the particular chamber used in our evaluation presents values of 0.1% and 0.7% for the $k_{Q,Q0}$ and N_k, respectively. Hence, the additional uncertainty added by the absorbed dose-ratios should be <0.1% when considering realistic chamber data in a clinical environment.

As all applicators of the Esteya system share the same flattening filter, they present the same narrow-beam spectrum (and HVL).[8] With that condition, the HVL_{fit} obtained with the parameters of Table III (using the absorbed dose-ratios of the APP_{10mm}) is representative of the whole set of applicators. However, the $D_{10,3}$ of the 30 mm diameter applicator is increased by 7% (from 0.614 to 0.658) compared to the 10 mm diameter applicator.[8] Such difference is due to the changes in the scatter conditions, which also increases the B_w nearly by the same amount.[12,42] For that reason, Table III only can be used with the absorbed dose-ratios of the APP_{10mm}. Furthermore, when the applicators do not share the same narrow-beam spectrum, as it could be the case for an eBT system whose flattening filters are not the same for the whole set, each applicator needs its HVL estimation.

Considering the data published by Candela-Juan et al.,[20] the reduction of the $(\mu_{en}/\rho)_{water,air}$ and B_w uncertainties from 3% (TG-61 dataset) to 0.5% (this work dataset) generates a reduction of 40% in the overall calibration uncertainty for the APP_{10mm} of the Esteya system. As the largest part of the uncertainties reported in the TG-61 tables are accepted to keep them as general as possible (e.g., independent from kV), a reduction of 40% is worth the effort to include more details into consideration. Such reduction could even imply lower uncertainties for the in-air calibration than the in-water calibration. In this context, the data generated under a machine-specific paradigm can complement the general tables published so far, which would be very helpful while the in-air calibration method is still in use.

This work is a proof-of-concept of the feasibility of using dose-ratios in the calibration of a specific eBT system. In a first instance, this methodology could be applied to obtain the HVL as an intermediate step (e.g., as Dose-ratio-to-HVL formalism). The use of dose-ratios directly as a beam quality index requires more research pointing to associate the energy response of a chamber with the dose-ratios of different beams.

This work opens the possibility of applying our method for other devices using proper machine-specific data (i.e., HVL-to-dose-ratio fits). However, the high-dose gradient of low-energy x-ray beams requires a better understanding of how some sources of uncertainties, such as alignment inaccuracies, can affect the final budget.

5. CONCLUSIONS

The results of this work show the feasibility of using the absorbed depth-dose curve of the APP_{10mm} to obtain all the data required in the beam calibration of the Esteya eBT system, adding a minimal amount (generally negligible) of uncertainty to the entire process. The use of factors specifically obtained for each applicator and eBT system allows a considerable reduction in the in-air calibration uncertainty.

ACKNOWLEDGMENTS

This work has been partially funded by Ministerio de Economía, Industria y Competitividad (Spain) and EU FEDER under Contract PGC2018-101302, and by Generalitat Valenciana through the project AICO/2019/132.

CONFLICT OF INTEREST

The authors have no conflict to disclose.

[a]Author to whom correspondence should be addressed. Electronic mail: cvalcort@gmail.com; Telephone: +34 684166861.

REFERENCES

1. Bhatnagar A. Nonmelanoma skin cancer treated with electronic brachytherapy: results at 1 year. *Brachytherapy.* 2013;12:134–140.
2. Goyal U, Kim Y, Tiwari HA, Witte R, Stea B. A pilot study of ultrasound-guided electronic brachytherapy for skin cancer. *J Contemp Brachytherapy.* 2015;5:374–380.
3. Paravati AJ, Hawkins PG, Martin AN, et al. Clinical and cosmetic outcomes in patients treated with high-dose-rate electronic brachytherapy for nonmelanoma skin cancer. *Pract Radiat Oncol.* 2015;5:e659–e664.
4. Delishaj D, Rembielak A, Manfredi B, et al. Non-melanoma skin cancer treated with high-dose-rate brachytherapy: a review of literature. *J Contemp Brachytherapy.* 2016;6:533–540.
5. Ballester-Sánchez R, Pons-Llanas O, Candela-Juan C, et al. Two years results of electronic brachytherapy for basal cell carcinoma. *J Contemp Brachytherapy.* 2017;3:251–255.

6. Guinot JL, Rembielak A, Perez-Calatayud J, et al. GEC-ESTRO ACROP recommendations in skin brachytherapy. *Radiother Oncol*. 2018;126:377–385.
7. Ouhib Z, Kasper M, Perez Calatayud J, et al. Aspects of dosimetry and clinical practice of skin brachytherapy: the American Brachytherapy Society working group report. *Brachytherapy.* 2015;14: 840–858.
8. Valdes-Cortez C, Niatsetski Y, Perez-Calatayud J, Ballester F, Vijande J. A Monte Carlo-based dosimetric characterization of Esteya ®, an electronic surface brachytherapy unit. *Med Phys*. 2019;46:356–369.
9. Thomadsen BR, Biggs PJ, DeWerd LA, et al.The 2007 AAPM Response to the CRCPD Request for Recommendations for the CRCPD's Model Regulations for Electronic Brachytherapy; 2009. https://www.aapm.org/pubs/reports/detail.asp?docid=157
10. Candela-Juan C, Niatsetski Y, Ouhib Z, Ballester F, Vijande J, Perez-Calatayud J. Commissioning and periodic tests of the Esteya® electronic brachytherapy system. *J Contemp Brachytherapy.* 2015;2:189–195.
11. Eaton DJ. Electronic brachytherapy—current status and future directions. *Br J Radiol*. 2015;88:20150002.
12. Ma C-M, Coffey CW, DeWerd LA, et al. AAPM protocol for 40–300 kV x-ray beam dosimetry in radiotherapy and radiobiology. *Med Phys*. 2001;28:868–893.
13. IAEA. *Absorbed Dose Determination in External Beam Radiotherapy.* Vienna: International Atomic Energy Agency; 2000. https://www.iaea.org/publications/5954/absorbed-dose-determination-in-external-beam-radiotherapy
14. Almond PR, Biggs PJ, Coursey BM, et al. AAPM's TG-51 protocol for clinical reference dosimetry of high-energy photon and electron beams. *Med Phys*. 1999;26:1847–1870.
15. Fulkerson RK, Micka JA, DeWerd LA. Dosimetric characterization and output verification for conical brachytherapy surface applicators. Part I. Electronic brachytherapy source. *Med Phys*. 2014;41:022103.
16. Moradi F, Ung NM, Khandaker MU, et al. Monte Carlo skin dose simulation in intraoperative radiotherapy of breast cancer using spherical applicators. *Phys Med Biol*. 2017;62:6550–6566.
17. Watson PGF, Popovic M, Seuntjens J. Determination of absorbed dose to water from a miniature kilovoltage x-ray source using a parallel-plate ionization chamber. *Phys Med Biol*. 2017;63:015016.
18. Gimenez-Alventosa V, Gimenez V, Ballester F, Vijande J, Andreo P. Correction factors for ionization chamber measurements with the 'Valencia' and 'large field Valencia' brachytherapy applicators. *Phys Med Biol*. 2018;63:125004.
19. Garcia-Martinez T, Chan J-P, Perez-Calatayud J, Ballester F. Dosimetric characteristics of a new unit for electronic skin brachytherapy. *J Contemp Brachytherapy.* 2014;1:45–53.
20. Candela-Juan C, Vijande J, García-Martínez T, et al. Comparison and uncertainty evaluation of different calibration protocols and ionization chambers for low-energy surface brachytherapy dosimetry. *Med Phys*. 2015;42:4954–4964.
21. Sempau J, Badal A, Brualla L. A PENELOPE -based system for the automated Monte Carlo simulation of clinacs and voxelized geometries-application to far-from-axis fields. *Med Phys*. 2011;38:5887–5895.
22. Salvat F, Fernández-Varea J, Sempau J. PENELOPE-2014: A Code System for Monte Carlo Simulation of Electron and Photon Transport; 2015.
23. Croce O, Hachem S, Franchisseur E, Marcié S, Gérard J-P, Bordy J-M. Contact radiotherapy using a 50kV X-ray system: evaluation of relative dose distribution with the Monte Carlo code PENELOPE and comparison with measurements. *Radiat Phys Chem.* 2012; 81:609–617.
24. Ballester F, Carlsson Tedgren Å, Granero D, et al. A generic high-dose rate 192 Ir brachytherapy source for evaluation of model-based dose calculations beyond the TG-43 formalism. *Med Phys*. 2015;42:3048–3062.
25. Vijande J, Granero D, Perez-Calatayud J, Ballester F. Monte Carlo dosimetric study of the medium dose rate CSM40 source. *Appl Radiat Isot*. 2013;82:283–288.
26. Almansa JF, Guerrero R, Torres J, Lallena AM. Monte Carlo dosimetric characterization of the Flexisource Co-60 high-dose-rate brachytherapy source using PENELOPE. *Brachytherapy.* 2017;16:1073–1080.
27. Sabbatucci L, Salvat F. Theory and calculation of the atomic photoeffect. *Radiat Phys Chem*. 2016;121:122–140.
28. Pratt RH, Ron A, Tseng HK. Atomic photoelectric effect above 10 keV. *Rev Mod Phys*. 1973;45:273–325.
29. Scofield JH. Theoretical Photoionization Cross Sections from 1 to 1500 KeV. Livermore, CA; 1973. https://www.osti.gov/servlets/purl/4545040
30. Sakurai JJ. *Advanced Quantum Mechanics*, 1st ed. New York: Addison and Wesley; 1967.
31. Born M. *Atomic Physics*. London: Blackie and Son; 1969.
32. Baym G. *Lectures in Quantum Mechanics*. Boulder, Colorado: Westview Press; 1974.
33. Cullen DE, Hubbell JH, Kissel L. EPDL97: The Evaluated Photo Data Library '97 Version. Vol 6. Livermore, CA; 1997. https://doi.org/10.2172/295438
34. Ribberfors R. Erratum: X-ray incoherent scattering total cross sections and energy-absorption cross sections by means of simple calculation routines. *Phys Rev A*. 1983;27:3061–3070.
35. Watson PGF, Seuntjens J. Technical note: effect of explicit M and N - shell atomic transitions on a low-energy x-ray source. *Med Phys*. 2016;43:1760–1763.
36. Perkins ST, Cullen DE, Chen MH, Hubbell JH, Rathkopf J, Scofield JH. Tables and Graphs of Atomic Subshell and Relaxation Data Derived from the LLNL Evaluated Atomic Data Library (EADL), Z = 1-100, Technical Report UCRL-ID-50400. Livermore, CA; 1991.
37. Deslattes RD, Kessler EG, Indelicato P, de Billy L, Lindroth E, Anton J. X-ray transition energies: new approach to a comprehensive evaluation. *Rev Mod Phys*. 2003;75:35–99.
38. Bearden JA. X-ray wavelengths. *Rev Mod Phys*. 1967;39:78–124.
39. Badal A, Sempau J. A package of Linux scripts for the parallelization of Monte Carlo simulations. *Comput Phys Commun*. 2006;175:440–450.
40. Sechopoulos I, Rogers DWO, Bazalova-Carter M, et al. RECORDS: Improved Reporting of montE CarlO RaDiation transport Studies: Report of the AAPM Research Committee Task Group 268. *Med Phys*. 2018;45:e1–e5.
41. Sempau J, Andreo P. Configuration of the electron transport algorithm of PENELOPE to simulate ion chambers. *Phys Med Biol*. 2006;51:3533–3548.
42. Andreo P. Data for the dosimetry of low- and medium-energy kV x rays. *Phys Med Biol*. 2019;64:205019.
43. Williamson JF. Monte Carlo evaluation of kerma at a point for photon transport problems. *Med Phys*. 1987;14:567–576.
44. Grosswendt B. Backscatter factors for x-rays generated at voltages between 10 and 100 kV. *Phys Med Biol*. 1984;29:579–591.
45. Rivard MJ, Coursey BM, DeWerd LA, et al. Update of AAPM Task Group No. 43 Report: a revised AAPM protocol for brachytherapy dose calculations. *Med Phys*. 2004;31:633–674.
46. BIMP. Evaluation of Measurement Data — Guide to the Expression of Uncertainty in Measurement; 2010.
47. Andreo P, Burns DT, Salvat F. On the uncertainties of photon mass energy-absorption coefficients and their ratios for radiation dosimetry. *Phys Med Biol*. 2012;57:2117–2136.

Depth-dose measurement corrections for the surface electronic brachytherapy beams of an Esteya® unit: a Monte Carlo study

Depth-dose measurement corrections for the surface electronic brachytherapy beams of an Esteya® unit: a Monte Carlo study

Christian Valdes-Cortez[1,2]‡, Facundo Ballester[1,3], Javier Vijande[1,3,4], Vicente Gimenez[4,5], Vicente Gimenez-Alventosa[6], Jose Perez-Calatayud[3,7], Yury Niatsetski[8] and Pedro Andreo[9]

[1] Departamento de Física Atómica, Molecular y Nuclear, Universitat de Valencia (UV), Burjassot, Spain

[2] Radiotherapy Department, Centro Oncológico del Norte, Antofagasta, Chile

[3] Unidad Mixta de Investigación en Radiofísica e Instrumentación Nuclear en Medicina (IRIMED), Instituto de Investigación Sanitaria La Fe (IIS-La Fe)–Universitat de Valencia (UV), Valencia, Spain

[4] Instituto de Física Corpuscular, IFIC (UV-CSIC), Burjassot, Spain

[5] Department of Theoretical Physics, University of Valencia, Burjassot, Spain

[6] Instituto de Instrumentación para Imagen Molecular (I3M), Centro Mixto CSIC–Universitat Politècnica de València, Valencia, Spain

[7] Radiotherapy Department, La Fe Hospital, Valencia, Spain

[8] R&D Elekta Brachytherapy, Veenendaal, The Netherlands

[9] Department of Medical Radiation Physics and Nuclear Medicine, Karolinska University Hospital, Stockholm, Sweden

Abstract. Three different correction factors for measurements with the parallel-plate ionization chamber PTW T34013 on the Esteya electronic brachytherapy unit have been investigated. This chamber type is recommended by AAPM TG-253 for depth-dose measurements in the 69.5 kV x-ray beam generated by the Esteya unit.

Monte Carlo simulations using the PENELOPE-2018 system were performed to determine the absorbed dose deposited in water and in the chamber sensitive volume at different depths with a Type A uncertainty smaller than 0.1%. Chamber-to-chamber differences have been explored performing measurements using three different chambers. The range of conical applicators available, from 10 to 30 mm in diameter, has been explored.

Using a depth-independent global chamber perturbation correction factor without a shift of the effective point of measurement yielded differences between the absorbed dose to water and the corrected absorbed dose in the sensitive volume of the chamber of up to 1% and 0.6% for the 10 mm and 30 mm applicators, respectively. Calculations using a depth-dependent perturbation factor, including or excluding a shift of the effective point of measurement, resulted in depth-dose differences of about $\pm 0.5\%$ or less for both applicators. The smallest depth-dose differences were obtained when a shift of the effective point of measurement was implemented, being displaced 0.4 mm towards the center of the sensitive volume of the chamber. The correction factors were obtained with combined uncertainties of 0.4% ($k = 2$). Uncertainties due to chamber-to-chamber differences are found to be lower than 2%.

The results emphasize the relevance of carrying out detailed Monte Carlo studies for each electronic brachytherapy device and ionization chamber used for its dosimetry.

‡ Corresponding author, cvalcort@gmail.com

Keywords: electronic brachytherapy, eBT, dosimetry, ionization chambers, Monte Carlo
Submitted to: *Phys. Med. Biol.*

May 22, 2020

1. Introduction

Electronic high-dose-rate brachytherapy (eBT) replaces the low- and high-energy radionuclides typically used in brachytherapy (BT) by an x-ray generator of 50 kV to 70 kV (Eaton 2015). It is becoming widely used in gynecological, breast, and surface treatments (Tom *et al.* 2018). In particular, surface eBT has proven to be an effective therapy for non-melanoma skin cancer, achieving good therapeutic and cosmetic results (Ballester-Sánchez *et al.* 2017, Guinot *et al.* 2018, Ouhib *et al.* 2015). Typically, the dosimetrically relevant components for a surface eBT system are an x-ray tube with an attached applicator positioned in contact with the skin, which serves as collimator and (depending on the system) flattening filter, allowing conical and flattened beams from 10 mm to 50 mm in diameter (Eaton 2015).

The use of x-rays tubes instead of radionuclides in these type of treatments minimizes issues related to radiation protection, avoids radioactive material handling, and improves the treatment time due to the significantly higher dose rate (Ibanez-Rosello *et al.* 2017, Eaton 2015). However, eBT is far from being a complication-free technique as its low-energy photons pose a major challenge for dosimetric measurements. Their high dose gradient makes necessary the use of dosimeters with small sensitive volumes to minimize the loss of spatial resolution, and the dosimeter response becomes highly sensitive to the materials used in its construction (Hill *et al.* 2014, Ma *et al.* 2001). Furthermore, in Monte Carlo (MC) calculations, the simulation of low-energy photons implies the use of cross-sections with large uncertainties, especially for the photoelectric interaction (Andreo *et al.* 2012, Seltzer *et al.* 2014).

The recommended dosimeter for low-energy kV x-rays is a special type of parallel-plate ionization chamber (Andreo *et al.* 2000, Ma *et al.* 2001), optimized either for in-air measurements or at the surface of a dedicated phantom. In the latter case, the chamber response needs to be corrected for the perturbations introduced by the insertion of the chamber in the phantom medium. It is usually assumed that perturbation correction factors are nearly depth-independent, which keeps the procedure simple in relative measurements (e.g., percentage depth-dose). However, some authors have suggested that this assumption could be unjustified, evidencing the introduction of errors up to 10% from 3 mm to 30 mm depth (Gimenez-Alventosa *et al.* 2018, Watson *et al.* 2017).

The election of a proper effective point of measurement (EPoM) of the chamber can minimize the effect of depth on the correction factors (see Kawrakow 2006 work for MV photons). In this context, studies performed in a widely used parallel-plate ionization chamber type, the PTW T34013 (PTW, Freiburg, Germany), using unfiltered 50 kV x-rays (Watson *et al.* 2017) and ^{192}Ir gamma-rays (Gimenez-Alventosa *et al.* 2018), showed that a modification of the EPoM, recommended by the chamber manufacturer, could describe the response of the chamber with depth.

The Esteya unit (Elekta Brachytherapy, Veenendaal, The Netherlands) is an eBT device designed to treat skin lesions with a flattened x-ray beam of 69.5 kV. At the time of writing, the PTW T34013 parallel-plate ionization chamber type is one of the few chambers designed for calibration measurements of low-energy x-ray beams in a plastic phantom. Therefore both

Elekta and the AAPM TG-253 report recommend its use to perform depth-dose measurements (Fulkerson *et al.* 2020, Candela-Juan *et al.* 2015a). The beam energy of the Esteya unit is between 50 kV and an ^{192}Ir spectrum, beams where the PTW T34013 chamber has been studied using MC methods (Watson *et al.* 2017, Gimenez-Alventosa *et al.* 2018, Fulkerson *et al.* 2014).

This work aims at evaluating the dependence of the PTW T34013 chamber response on depth and applicator size, addressing their effect on the absorbed dose determination in an Esteya unit beam, and exploring strategies to minimize the effect of depth on the chamber response. The possible influence of chamber-to-chamber differences has also been explored.

2. Material and methods

2.1. High-dose-rate electronic brachytherapy systems

The Esteya eBT unit (see figure 1) accelerates electrons at 69.5 keV impinging on a tungsten target. This system includes a set of conical applicators, with diameters between 10 mm and 30 mm, closed by a polyfenilsulfone plastic cap (applicator exit), which allows a minimum source-to-surface distance (SSD) of 60 mm (Garcia-Martinez *et al.* 2014, Candela-Juan *et al.* 2015b, Valdes-Cortez *et al.* 2019). The applicators considered in this work were the smallest, 10 mm (APP_{10mm}), and the largest, 30 mm (APP_{30mm}), so that the full range of field sizes could be covered. The kV photon beam spectrum has an average energy of 36.3 keV (Valdes-Cortez *et al.* 2020).

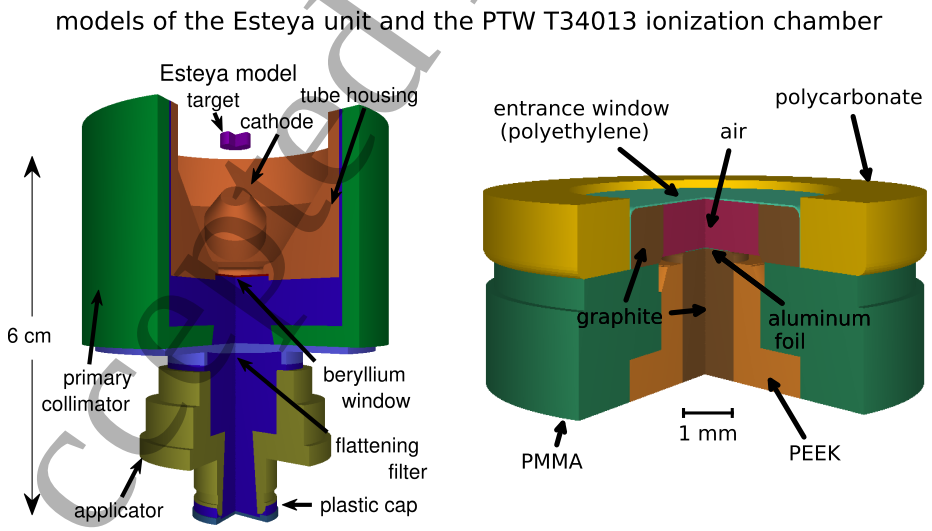

Figure 1: *Schematic geometry of the Esteya Unit (left) and the PTW T34013 parallel-plate chamber (right) implemented in PENELOPE-2018*

2.2. Parallel-plate ionization chamber

The parallel-plate ionization chamber type studied in this work is the "soft x-ray" PTW T34013. The specifications and blueprints of the chamber have been provided by the manufacturer.

The chamber (see figure 1) has a nominal sensitive volume of 0.005 cm^3 (1.45 mm radius and 0.9 mm height), surrounded by a guard ring at the same potential as the electrode. Reported manufacturing tolerances refer solely to the outer part of the chamber, i.e. distances between two external support structures and the external face of the entrance window. The chamber is not waterproof, being designed for use embedded in a solid phantom. The chamber is calibrated by PTW (traceable to PTB) in a TW30 beam in a "plastic water" phantom (PW LR: CIRS, Norfolk, VA, USA). According to the manufacturer, the chamber EPoM is situated at the center of the inner surface of the entrance window (EPoM$_{man}$, top of the sensitive volume). The IAEA TRS-398 Code of Practice (Andreo *et al.* 2000), however, specifies the reference point to be at the outside surface of the front window. It should be noted that there is a small air gap of about 0.15 mm between the entrance window of the chamber and the plastic cap of the applicator, being in contact with the top of the chamber body (see figures 1 and 2, the step from the top surface of the polycarbonate outer ring and the entrance window). This air gap has been incorporated into our MC study to fully reproduce the experimental conditions. When the EPoM$_{man}$ is located at the phantom surface, a part of the chamber comes out of the phantom, preventing the contact between the applicator of the eBT with the phantom surface.

2.3. Monte Carlo code

We have used the PENELOPE-2018 MC system (henceforth denoted PEN18) (Salvat 2019) together with the penEasy v. 2019-09-21 code (Sempau *et al.* 2011). PENELOPE simulates electron and photon transport from 50 eV to 1 GeV, used in the study of both electronic (Valdes-Cortez *et al.* 2020, Valdes-Cortez *et al.* 2019, Croce *et al.* 2012) and radionuclide-based (Ballester *et al.* 2015, Vijande *et al.* 2013, Almansa *et al.* 2017, Gimenez-Alventosa *et al.* 2018) brachytherapy sources.

PEN18 obtains the photoelectric cross-sections from the PHOTACS database (Sabbatucci and Salvat 2016), by using the elementary theory of the atomic photoelectric effect (independent electron model) (Pratt *et al.* 1973, Scofield 1973) to calculate tables of excitation and ionization cross-sections The user can choose to include or exclude the so-called "Pratt's renormalization screening" (PRS) (Seltzer *et al.* 2014, Andreo *et al.* 2012), which is enabled by default (Salvat 2019).

The Rayleigh scattering cross-sections are calculated using non-relativistic perturbation theory, obtaining the atomic form factors from EPDL97 (Cullen *et al.* 1997). Compton interactions use the relativistic impulse approximation, which takes into account both binding effects and Doppler broadening (Ribberfors 1983). Furthermore, PEN18 simulates explicitly the emission of characteristic x-rays, Auger and Coster-Kronig electrons that result from vacancies produced in K, L, M and N shells, using transition probabilities extracted from

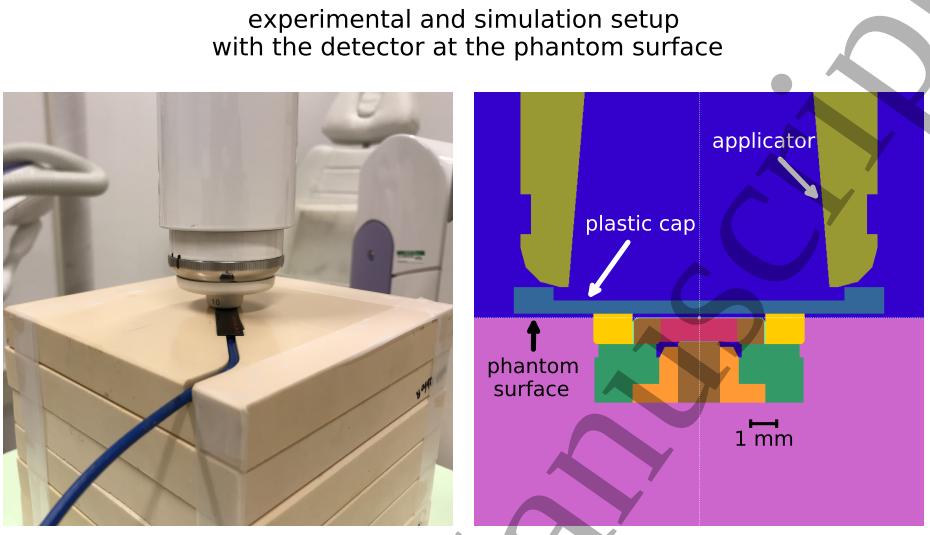

Figure 2: *Experimental setup using the 10 mm applicator (left) and schematic geometry reproducing the experimental setup for the MC simulation (right). Dark blue and red zones (sensitive volume of the chamber) are filled with air.*

the Evaluated Atomic Data Library (EADL) (Perkins *et al.* 1991). The energy of the x-rays published in the EADL was updated, when available, with the K and L shell transitions from Deslattes *et al.* (2003), and the M lines from Bearden (1967). Other transition energies are calculated from the energy eigenvalues of the Dirac-Hartree-Fock-Slater equations for neutral atoms (Perkins *et al.* 1991).

2.4. Monte Carlo study

A full MC study of the Esteya unit has been performed elsewhere (Valdes-Cortez *et al.* 2019). There, the photon energy spectrum produced by bremsstrahlung emission in the tungsten target and exiting the beryllium window of an Esteya unit was scored (see figure 1). To improve the calculation efficiency, in the present simulations this photon energy spectrum was used as a point-like source placed at the center of the lower surface of the tungsten target with a polar and azimuthal aperture of 18º (enough to fully cover the primary collimator) and 360º, respectively. Hence, the simulation ensemble includes the phantom, the chamber (when needed), and the full geometry of the Esteya eBT system.

Water has been recommended by the IAEA Code of Practice TRS-398 (Andreo *et al.* 2000) and AAPM TG-253 (Fulkerson *et al.* 2020) as the reference medium for the determination of the absorbed dose in kV photon beams. Therefore, in the present simulations the phantom considered was of liquid water with the composition recommended by ICRU Report 37 (Berger *et al.* 1984) and the updated mean excitation energies and mass density

given by ICRU Report 90 (Seltzer *et al.* 2014).

The study of the chamber response with depth requires determining the perturbation correction factors at several depths along the beam axis in the water phantom. To accomplish that purpose, it is necessary to calculate the absorbed dose in water (D_{w}), the absorbed dose in the sensitive volume of the chamber (D_{cav}), and the ratios of the mean mass-energy absorption coefficients water to air $(\overline{\mu_{\mathrm{en}}/\rho})_{\mathrm{w,air}}$ at all the depths considered. Both D_{w} and D_{cav} have been scored directly by evaluating the energy imparted within the corresponding volume of interest, whereas the μ_{en}-ratios were determined from the MC-calculated photon spectra (see below).

A desirable dosimetry condition is to perform measurements in regions with charge particle equilibrium (CPE) (Ma *et al.* 2001). That condition should imply obtaining at depths larger than the expected range of the secondary electrons in the water phantom (the continuous slowing down approximation range in water for electrons of 70 keV is 0.08 mm). Standard treatment conditions for the Esteya eBT system require the use of a polyfenilsulfone plastic cap (see figure 2) with a typical thickness of about 0.5 mm, which is intended to be in contact with the treatment surface. Hence, complete CPE is achieved at all depths.

All the results were obtained through parallelized MC simulations. The processes were kept uncorrelated through proper management of the initial seeds (Badal and Sempau 2006). When electron transport was required (see below), it was simulated in detailed mode (PENELOPE transport parameters C1 = C2 = 0), i.e., without resorting to the mixed (Class II) algorithm option incorporated in PENELOPE. The variance reduction tools used were particle splitting and interaction forcing, with adequate use of the particle weight to maintain the simulation unbiased (Salvat 2019).

The selected energy cutoff for photons was 8 keV in all materials of the eBT device, and 1 keV in all structures embedded in the water phantom (i.e., ionization chamber and scoring volumes). The 8 keV threshold was selected because the amount of photons with energy lower than this value leaving the applicator (see figure 3) is negligible (Valdes-Cortez *et al.* 2019). Due to the short range of secondary electrons in water, electron transport can be ignored, and its energy assumed to be deposited on the spot, i.e., an infinite energy cutoff for electrons was considered for D_{w}. With respect to D_{cav}, the energy cutoff of 1 keV for electrons was chosen in all chamber materials and in a water envelope region of 0.1 mm thick around the chamber. When the chamber is in contact with the plastic cap (first depth voxel), the same electron cutoff was considered both in the plastic cap and in the air gap.

Table 1 summarizes the details concerning the MC simulations in this work following the recommendation of AAPM TG-268 (Sechopoulos *et al.* 2018). Further information regarding the PENELOPE transport parameters and variance reduction tools can be found in its manual (Valdes-Cortez *et al.* 2019, Salvat 2019, Sempau and Andreo 2006).

2.4.1. Absorbed depth-dose and mass-energy absorption coefficient The absorbed dose in water, D_{w}, was scored between the water phantom surface (0 mm depth) and 20 mm depth, in cylinders of 1 mm radius and 0.1 mm height assuming CPE conditions. The absorbed dose in the sensitive volume of the chamber, D_{cav}, was scored with the chamber $\mathrm{EPoM_{man}}$ positioned at the same depth as the upper boundary of the corresponding D_{w} bin. The ratio

Table 1: *Summary of the main characteristics of the Monte Carlo simulations used in this work.*

Item	Description	References
Code	1) PENELOPE-2018 2) penEasy (v. 2019-09-21) Intel® Fortran compiler 18.0.3	1) Salvat (2019) 2) Sempau *et al.* (2011)
Validation	Previously validated	Ye *et al.* (2004), Croce *et al.* (2012), Valdes-Cortez *et al.* (2019), Chica *et al.* (2009)
Timing	Average values for APP_{10mm} (sum of parallel processes, Intel (R) Xeon(R) Gold 6154 CPU @3.00 GHz): - D_{cav} obtained in 28647 CPU hours and 7×10^{11} histories. - D_w obtained in 629 CPU hours and 10^{10} histories. - $(\overline{\mu_{en}/\rho})_{w,air}$ obtained in 1330 CPU hours and 5×10^{10} histories.	Parallel processes as of Badal and Sempau (2006)
Source description	Photon point collimated source. Spectrum from detailed modelling of the Esteya x-ray tube (GIS model, see reference)	Valdes-Cortez *et al.* (2019)
Cross-sections	1) Photoelectric from PHOTACS; 2) Rayleigh scattering using non-relativistic perturbation theory; 3) Compton from relativistic impulse approximation; 4) Atomic relaxation with EADL transition probabilities.	1) Sabbatucci and Salvat (2016); 2) Sakurai (1967), Born (1969), Baym (1974), Cullen *et al.* (1997); 3) Ribberfors (1983); 4) Perkins *et al.* (1991), Deslattes *et al.* (2003), Bearden (1967)
Transport parameters	Photon cut-off = 8 keV in all materials in eBT device, 1 keV in ionization chamber and water phantom; Electron cut-off = 1 keV in all materials surrounding sensitive chamber volume and water envelope (PENELOPE parameters C1 = C2 = 0); Electron transport disabled elsewhere.	Valdes-Cortez *et al.* (2019), Sempau and Andreo (2006), Salvat (2019).
Variance reduction tools	1) Interaction forcing: D_w scoring bins and sensitive chamber volume; 2) Splitting particles (penEasy rotational option at the flattening filter).	1) Salvat (2019); 2) Sempau *et al.* (2011).
Scored quantities	Absorbed dose in water and chamber cavity; photon fluence.	
Statistical uncertainties	$\leq 0.1\%$ $(k = 2)$	
Post-processing	None	

of the mean mass-energy absorption coefficients water to air, $(\overline{\mu_{\rm en}/\rho})_{\rm w,air}$, averaged over the energy-fluence spectrum at each depth was calculated as (Ma *et al.* 2001):

$$\left(\frac{\overline{\mu_{\rm en}}}{\rho}(z)\right)_{\rm w,air} = \frac{\int_0^{E_{\rm max}} E\,\Phi_{E,{\rm w}}\left[\left(\frac{\mu_{\rm en}(E)}{\rho}\right)_{\rm w}\right]\,dE}{\int_0^{E_{\rm max}} E\,\Phi_{E,{\rm w}}\left[\left(\frac{\mu_{\rm en}(E)}{\rho}\right)_{\rm air}\right]\,dE}, \tag{1}$$

where $\Phi_{E,{\rm w}}$ is the photon fluence differential in energy in water at a given depth z, and $[(\mu_{\rm en}\,(E)\,/\rho)_{\rm w}]$ and $[(\mu_{\rm en}\,(E)\,/\rho)_{\rm air}]$ are the mass energy-absorption coefficients for water and air, respectively. The photon fluence corresponds to spectra with a bin width of 0.1 keV scored in a cylinder of 1 mm height and 1 mm radius, with its upper surface positioned at the same depth in water as the EPoM$_{\rm man}$. All the above-mentioned factors were consistently evaluated with PEN18.

2.4.2. Determination of the EPoM and correction factors The absorbed dose to water at depth z, $D_{\rm w}(z)$, can be calculated from the mean absorbed dose in the sensitive volume assigned to a point at depth z', $D_{\rm cav}(z')$, through the ratio

$$\frac{D_{\rm w}(z)}{D_{\rm cav}(z')} = \left[\left(\frac{\overline{\mu_{\rm en}}}{\rho}(z')\right)_{\rm w,air}\right] p, \tag{2}$$

where $(\overline{\mu_{\rm en}/\rho})_{\rm w,air}$ is calculated in a volume centered at depth z', and p is an overall factor to correct for the perturbations created by the presence of the chamber in the water phantom.

To determine the dependence of the chamber response on depth and evaluate p, three scenarios have been analyzed following the methodology proposed by Gimenez-Alventosa *et al.* (2018):

(i) A surface correction factor ($p = p_{\rm surf}$) obtained through equation 2 at the water phantom surface using the EPoM$_{\rm man}$ provided by the manufacturer, i.e., the chamber is located with the EPoM$_{\rm man}$ positioned at depth:

$$p_{\rm surf} = \frac{D_{\rm w}(z=0)}{D_{\rm cav}(z'=0)\left[\left(\frac{\overline{\mu_{\rm en}}}{\rho}(z'=0)\right)_{\rm w,air}\right]}. \tag{3}$$

This approach will indicate that a single measurement performed at the water phantom surface would suffice to correlate satisfactorily $D_{\rm cav}$ and $D_{\rm w}$ for all depths. Such procedure will resemble the methodology normally applied in kV beams.

(ii) A global correction factor ($p = p_{\rm glob}$), calculated using the EPoM$_{\rm man}$. Such method will require measuring and/or simulating the chamber response at all depths. To do so one evaluates the ratio:

$$f_i = \frac{D_{\rm w}(z_i)}{D_{\rm cav}(z_i)\left[\left(\frac{\overline{\mu_{\rm en}}}{\rho}(z_i)\right)_{\rm w,air}\right]} \tag{4}$$

for all depths z_i. The correction factor p_{glob} is then obtained by minimizing the differences between D_{w} and D_{cav} using a 1D chi-square distribution

$$\chi^2\left(p_{\mathrm{glob}}\right) = \sum_{i=1}^{N} \frac{\left(f_i - p_{\mathrm{glob}}\right)^2}{{\Delta f_i}^2}, \tag{5}$$

where N is the number of the chamber positions, and Δf_i is the Type A uncertainty of the ratio f_i given in equation 4.

(iii) A shift correction factor ($p = p_{\mathrm{shift}}$) including a modification on the EPoM. We have used the approach proposed by Kawrakow (2006) to find the EPoM that minimizes the effect of depth in the correction factors. This consists on a refinement of case (ii) considering the EPoM as a free parameter to be specified within the ionization chamber sensitive volume.

Starting from a depth $z = \mathrm{EPoM}_{\mathrm{man}}$, we found the Δz value for which the ratio

$$f_i = \frac{D_{\mathrm{w}}(z_i + \Delta z)}{D_{\mathrm{cav}}(z_i)\left[\left(\frac{\overline{\mu_{\mathrm{en}}}}{\rho}(z_i)\right)_{\mathrm{w,air}}\right]}, \tag{6}$$

is as independent of depth as possible. Hence, Δz will provide an improved EPoM value. To accomplish that condition, it is necessary to minimize a 2D chi-square distribution

$$\chi^2\left(p_{\mathrm{shift}}, \Delta z\right) = \sum_{i=1}^{N} \frac{\left(f_i - p_{\mathrm{shift}}\right)^2}{{\Delta f_i}^2}, \tag{7}$$

where N is the number of chamber positions, and Δf_i is the Type A uncertainty of the ratio f_i given in equation 6. Further details of the minimization process can be found in e.g. Kawrakow (2006) and Gimenez-Alventosa *et al.* (2018).

2.5. Absorbed dose measurements

As mentioned earlier, the vendor does not report manufacturing tolerances in the chamber sensitive volume. The possible role, played by such tolerances on the absorbed-dose determination, has been evaluated by performing a set of depth-dose measurements using three different PTW T34013 chambers (SN 000810, 000311, and 000146). These measurements were performed by a single person, using a single eBT Esteya unit and a Plastic Water Low Range (PW LR: CIRS, Norfolk, VA, USA) phantom. For the Esteya unit, the water equivalence of plastic phantoms was studied by (Garcia-Martinez *et al.* 2014, Candela-Juan *et al.* 2015b, Valdes-Cortez *et al.* 2019), reporting differences between the absorbed dose to a water voxel located at the surface of a water-equivalent plastic phantom and the absorbed dose to a water voxel located at the surface of a water phantom to be less than 0.2%.

Plastic Water LR phantom consists out of slabs with different thickness from 1 mm up to 20 mm. One 20 mm slab has a groove for inserting the T34013 chamber and its cable (see figure 2, left), so that the top surfaces of the chamber and the slab are aligned. Five 20 mm slabs were placed under the chamber to provide full backscatter conditions. Two kinds of measurements were carried out: reference absorbed dose (D_{ref}) at 3 mm depth (typical

reference depth used in clinical practice) to establish the output and relative depth-dose curves (PDD), normalized at 3 mm depth (Ouhib *et al.* 2015, Guinot *et al.* 2018). D_{ref} was calculated according to the TRS-398 Code of Practice, using the method described in (Candela-Juan *et al.* 2015b) and $\mathrm{EPoM}_{\mathrm{man}}$. All measurements were done for the two applicator diameters, $\mathrm{APP}_{10\mathrm{mm}}$ and $\mathrm{APP}_{30\mathrm{mm}}$, used throughout this work. The differences between the three chambers were evaluated through $\{[\mathrm{PDD}(z)_a \times D_{\mathrm{ref},a}] \,/\, [\mathrm{PDD}(z)_b \times D_{\mathrm{ref},b}] - 1\} \times 100$, where the subscripts a and b denote different chambers.

2.6. Estimation of uncertainties

The uncertainties of MC-derived quantities were evaluated according to the GUM recommendations (BIPM 2010), assuming normal distributions. Uncertainties are expressed with a coverage factor $k = 2$ as recommended by the AAPM TG-138 (DeWerd *et al.* 2011). Type A uncertainties were smaller than 0.1% for D_{w}, D_{cav}, $(\mu_{\mathrm{en}}/\rho)_{\mathrm{w}}$, and $(\mu_{\mathrm{en}}/\rho)_{\mathrm{air}}$. Type B and combined uncertainties were estimated as follows:

(i) For $(\overline{\mu_{\mathrm{en}}/\rho})_{\mathrm{w,air}}$, Andreo *et al.* (2012) reported a combined uncertainty of 0.2% (group II for an x-ray beam with an average energy of 34.1 keV).

(ii) Ratio $D_{\mathrm{w}}/D_{\mathrm{cav}}$: Photoelectric cross-section uncertainties (predominant interaction for photons of 30 keV, considering all materials along their path) have been estimated between 2% and 3% for photons below 100 keV, mostly due to the implementation of the Pratt renormalization screening (PRS) in the different MC codes (Seltzer *et al.* 2014). $D_{\mathrm{w}}/D_{\mathrm{cav}}$ was evaluated at selected depths (0 mm, 3 mm, and 10 mm) with and without PRS to estimate the Type B uncertainty associated, obtaining a value of about 0.2%.

(iii) The impact on the uncertainty estimation arising from the simplified source model describing the Esteya unit (see Section 2.4) was estimated by performing additional MC simulations at selected depths using the complete description given in Valdes-Cortez *et al.* (2019). Differences between the two source types were less than 0.02% for $(\overline{\mu_{\mathrm{en}}/\rho})_{\mathrm{w,air}}$ and less than 0.2% for $D_{\mathrm{w}}/D_{\mathrm{cav}}$ at all depths.

(iv) p_{surf}, p_{glob} and p_{shift}: Their combined Type B uncertainties were obtained by adding in quadrature the uncertainty values estimated in (i), (ii), and (iii).

3. Results and discussion

3.1. Mass-energy absorption coefficients

Figure 3 shows the fluence spectra of the $\mathrm{APP}_{10\mathrm{mm}}$ and $\mathrm{APP}_{30\mathrm{mm}}$ applicators at different depths. The maximum variation of $(\overline{\mu_{\mathrm{en}}/\rho})_{\mathrm{w,air}}$ from 0 to 20 mm depth was 0.06%. In addition, the largest difference between the $\mathrm{APP}_{10\mathrm{mm}}$ and $\mathrm{APP}_{30\mathrm{mm}}$ cases, for the entire range of depths, was 0.04%. Hence, $(\overline{\mu_{\mathrm{en}}/\rho})_{\mathrm{w,air}}$ was considered in the following a depth- and applicator-independent quantity, with a value of 1.018 and an uncertainty of 0.2% (see table 2). These values are in good agreement with the data and uncertainty estimates published by (Ma *et al.* 2001, Andreo 2019, Valdes-Cortez *et al.* 2020).

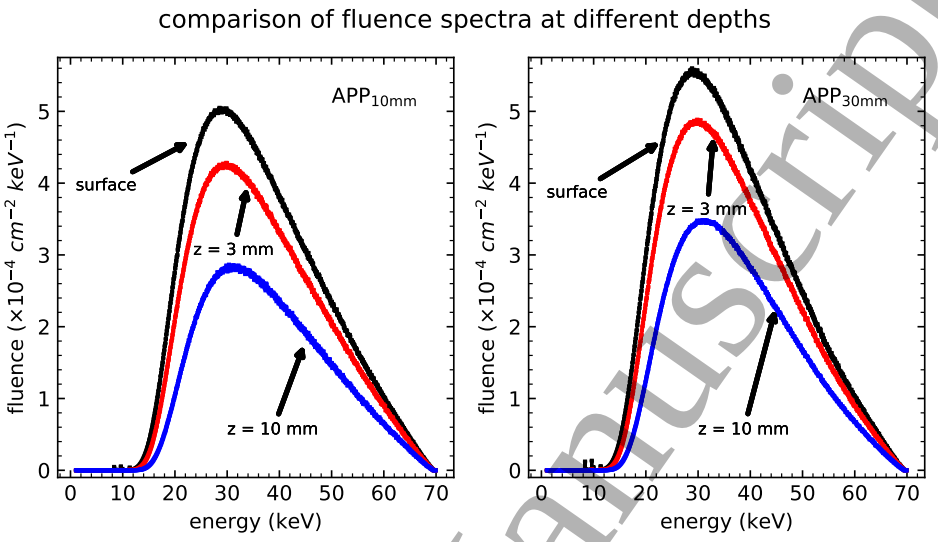

Figure 3: *Fluence spectra for the 10 mm and 30 mm applicators, scored at different depths (z). The spectra were obtained with an energy resolution of 0.1 keV, tallied in cylindrical volumes of 1 mm radius and 1 mm height. The values are normalized to the number of primary particles.*

3.2. Determination of the correction factors and the EPoM

Figure 4 shows the ratio D_w/D_{cav} for both applicators, APP_{10mm} and APP_{30mm}. These ratios were obtained with a Type A uncertainty of 0.1%. Type B uncertainties were evaluated incorporating the sources of uncertainty listed in Section 2.6 (ii) and (iii), leading to a combined uncertainty of about 0.3% (see table 2).

For the applicator APP_{10mm}, a variation in D_w/D_{cav} of about 1% can be observed between the water phantom surface and at a depth of 10 mm, from 1.376 to 1.390. The corrections factors p_{surf} and p_{glob} obtained were 1.351 and 1.359, respectively.

With respect to the third proposed method, p_{shift}(EPoM), equation 7 reaches a minimum at $\Delta z = 0.4$ mm (see figure 5), with a value of p_{shift} = 1.324. Figure 6 shows the differences between D_w and the absorbed dose to water calculated using the three proposed methods, $p_{shift}(EPoM_{man})$, $p_{glob}(EPoM_{man})$, and p_{shift}(EPoM). It can be seen that the $p_{glob}(EPoM_{man})$ method reduces the differences to within [-0.4%, +0.6%], while p_{shift}(EPoM) (with an EPoM at $\Delta z = 0.4$ mm) reduces the differences to within $\pm 0.4\%$ from 0 mm to 15 mm depth.

In the case of the APP_{30mm} applicator, the maximum variation of D_w/D_{cav} was 0.6% at 6 mm depth, from 1.348 to 1.356. The values of p_{surf} and p_{glob} were 1.324 and 1.330, respectively.

With respect to p_{shift}(EPoM), the optimum EPoM value was also found at $\Delta z = 0.4$ mm below $EPoM_{man}$ (see figure 5 and table 3), with p_{shift} equal to 1.300. The use of p_{glob} ($EPoM_{man}$) reduces the differences between D_{cav} and D_w to within 0.5%, while p_{shift} (EPoM)

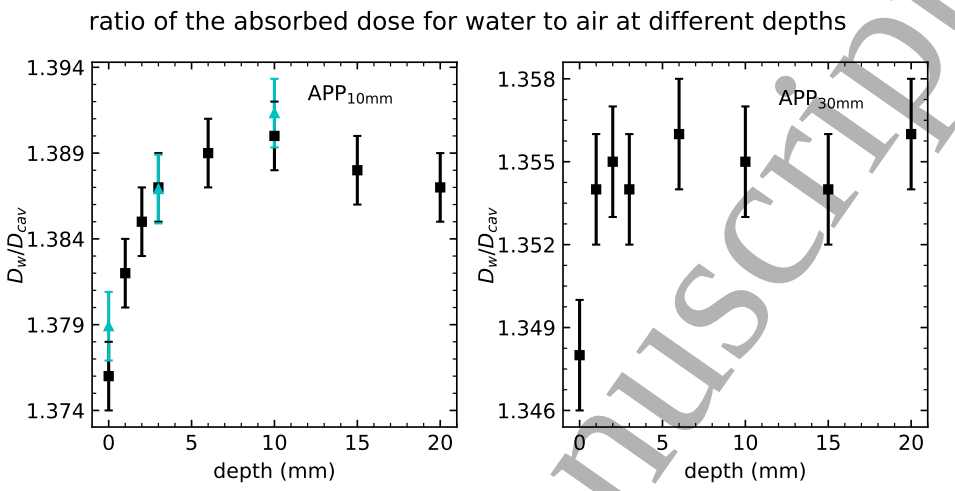

Figure 4: *Ratios of absorbed doses ($D_{\mathrm{w}}/D_{\mathrm{cav}}$) (black squares) as a function of depth, calculated for applicators of 10 mm and 30 mm diameter. Cyan triangles (left image) represent $D_{\mathrm{w}}/D_{\mathrm{cav}}$ simulated without the Pratt's screening renormalization correction at 0 mm, 3 mm, and 10 mm depth. Only Type A uncertainties are shown.*

(EPoM at $\Delta z = 0.4$ mm) reduces the differences to within 0.3%.

For both applicators, p_{surf} (EPoM$_{\mathrm{man}}$), p_{glob} (EPoM$_{\mathrm{man}}$), and p_{shift}(EPoM) were obtained with a combined uncertainty smaller than 0.4%. Table 2 shows the uncertainties estimated in the calculation of the various correction factors. Differences of about 2% were observed between the corresponding correction factors depending on the applicator considered, 10 mm or 30 mm in diameter. Hence, a conservative approach leads us to assume the same value for other applicators with diameters in-between 10 and 30 mm.

A summary of the correction factors and their estimated uncertainties is given in table 3.

Watson *et al.* (2017) explored the response of the T34013 chamber with an unfiltered beam of 50 kV at the same depth intervals as in this work. They reported a modification of about 2.5% in the value of $(\overline{\mu_{\mathrm{en}}/\rho})_{\mathrm{w,air}}$. When using EPoM$_{\mathrm{man}}$ and the nominal geometry provided by the chamber manufacturer, the ratio $D_{\mathrm{w}}/D_{\mathrm{cav}}$ was estimated to be 1.33 (approximated value) at 3 mm depth (first point of the published series), decreasing nearly by 5% at 15 mm depth. On the other hand, when the authors consider possible manufacturing tolerances in the height of the sensitive volume (using EPoM$_{\mathrm{man}}$), they found differences in the ratio $D_{\mathrm{w}}/D_{\mathrm{cav}}$ with depth of about 12%. The authors conclude that changing the EPoM from the manufacturer's recommendation to the midpoint of the sensitive volume may reduce these variations in the chamber response. However, that change would increase the depth dependence of the correction factors of the chamber, from 5% to 15% at 15 mm depth.

Gimenez-Alventosa *et al.* (2018) simulated the response of the T34013 chamber for the case of the Valencia and Large Field Valencia applicators. Both surface applicators use a

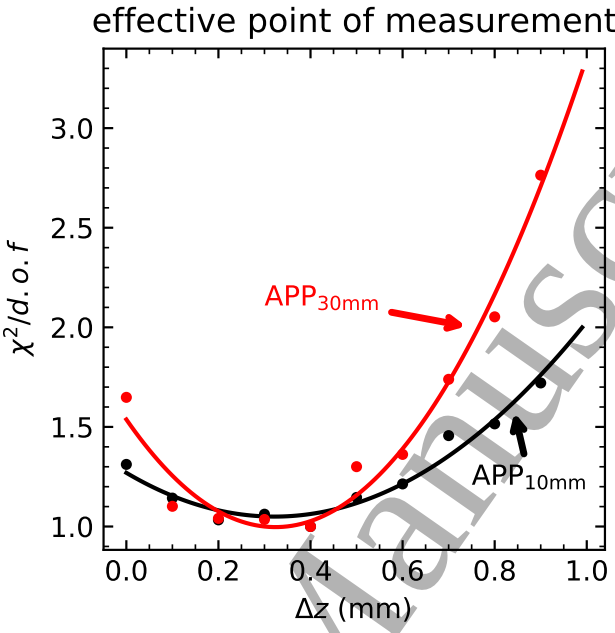

Figure 5: *Values of χ^2 per degree of freedom (normalized to the minimum value of each applicator) vs EPoM shift, calculated for the 10 mm (APP$_{10\mathrm{mm}}$) and 30 mm (AAPP$_{30\mathrm{mm}}$) diameter applicators. The dots correspond to the values obtained with equation 7. The solid lines correspond to a second-degree polynomial fit. CPE is assumed at the water phantom surface. Δz runs toward the bottom of the sensitive volume of the chamber.*

brachytherapy ^{192}Ir source. The authors found spectral variations due to differences in the design of the applicators (i.e., presence of a flattening filter in one of the applicators, different diameters, etc.). In that work, each applicator showed a constant $(\overline{\mu_{\mathrm{en}}/\rho})_{\mathrm{w,air}}$ value (within the statistical uncertainties) for all depths investigated, with a variation of 0.4% in the value calculated between applicators, and 3% in p_{glob} (method I in that work). Furthermore, they found different Δz values for each model of applicator. The filtered beam produces a value $\Delta z = 0.57$ mm, while for the unfiltered beam the optimum Δz was found at EPoM$_{\mathrm{man}}$ (i.e., $\Delta z = 0$).

3.3. Measurement results

The average absorbed dose rates at the clinical reference depth (3 mm) were 2.31 Gy min^{-1} and 2.64 Gy min^{-1} for the APP$_{10\mathrm{mm}}$ and APP$_{30\mathrm{mm}}$, respectively. The absorbed dose rates differences observed between the three chambers were within 1.5% for both applicators. Furthermore, for depth-dose measurements the differences in the relative measurements (up to 20 mm depth) were smaller than 2%, with an average difference within 1% for both

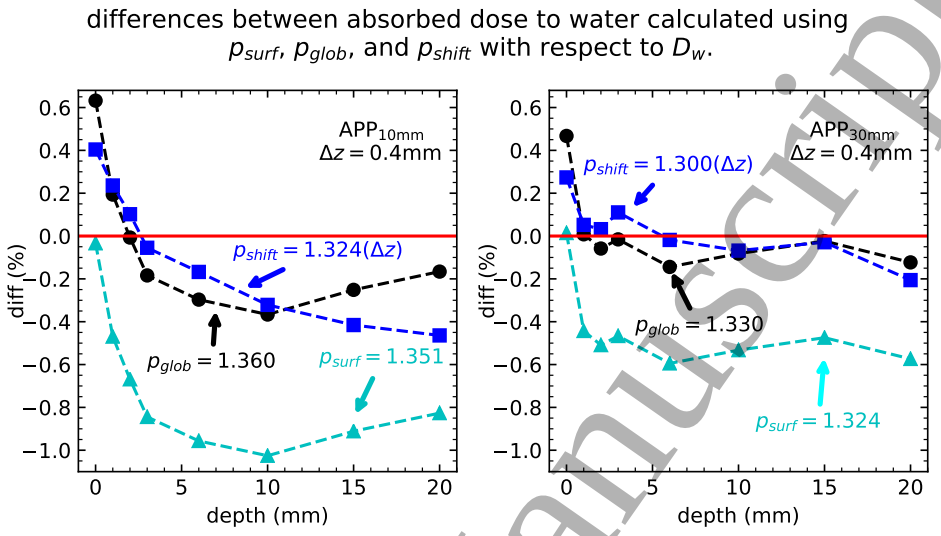

Figure 6: *Differences between absorbed dose to water calculated using* p_{glob} *(black circles),* p_{shift} *(blue squares), and* p_{surf} *(cyan triangles) with respect to* D_{w} *(red line). Uncertainty bars have been removed for clarity.*

Table 2: *Estimated relative uncertainties* ($k = 2$) *for the correction factors and the quantities used in their calculation.*

	Component	Uncertainty (%) Type A	Type B
$(\overline{\mu_{\mathrm{en}}/\rho})_{\mathrm{w,air}}$	Grouping II (50 kV) in Andreo *et al.* (2012)[a]	0.2	
	Effect of point vs full x-ray source		0.02
	MC statistics	0.1	
	u_{c}		0.2
$D_{\mathrm{w}}/D_{\mathrm{cav}}$	Effect of photoelectric cross-section		0.2
	Effect of point vs full x-ray source		0.2
	MC statistics	0.1	
	u_{c}		0.3
Correction factors	u_{c}		0.4

[a] Effect of the photoelectric cross-section uncertainties is also taken into account.

applicators. Therefore, depth-dose measurements uncertainties associated with chamber-to-chamber differences can be estimated to be at most of 2%, a value that also includes the

Table 3: *Summary of the values for the three correction factors proposed along with their combined estimated uncertainties ($k = 2$). The fifth column shows the differences [minimum, maximum] between the absorbed dose obtained from equation 2, using D_{cav} and the perturbation correction factors of the third column, and the simulated D_{w}. The Uncorrected row corresponds to the differences between D_{cav} and D_{w} before applying any of the proposed methods.*

Applicator	Method	Perturbation correction factors (p)	Δz (mm)	Differences (%)
$\mathrm{APP}_{10\mathrm{mm}}$	*Uncorrected*	1	–	[-28.0, -27.3]
	p_{surf}	1.351 ± 0.005	–	[-1.0, 0.0]
	p_{glob}	1.360 ± 0.005	–	[-0.4, +0.6]
	p_{shift}	1.324 ± 0.005	0.4	[-0.5, +0.4]
$\mathrm{APP}_{30\mathrm{mm}}$	*Uncorrected*	1	–	[-26.3, -25.8]
	p_{surf}	1.324 ± 0.005	–	[-0.6, 0.0]
	p_{glob}	1.330 ± 0.005	–	[-0.1, +0.5]
	p_{shift}	1.300 ± 0.005	0.4	[-0.2, +0.3]

uncertainties related with the experimental setup (e.g., alignment and positioning, among others).

Watson *et al.* (2017) evaluated differences due to manufacturing tolerances for an unfiltered 50 kV eBT by performing different MC simulations. They reported that the effect of manufacturing tolerances on the T34013 chamber may generate differences in the absorbed dose of about 5% at 20 mm depth. It can be concluded that the effect of the manufacturer tolerances on the chamber response for an Esteya unit seems to be lower than estimations made in the literature for eBT 50 kV beams.

3.4. Limitations of this study and future research lines

This study relies on state-of-the-art MC simulations for a particular eBT system and an ionization chamber. Therefore, the obtained results depend strongly on the precise description of both the Esteya unit and the PTW34013 ionization chamber provided by the manufacturers. Any subsequent major structural modification implemented by any of the vendors will require repeating this study to rule out any unforeseen change in the correction factors and the effective point of measurement. Hence, the results reported here cannot be directly extrapolated to any other eBT system and/or ionization chamber, for which separate machine- and chamber-specific studies, including a faithful description of the systems involved, will be required.

4. Conclusions

The response of the parallel-plate ionization chamber PTW T34013, recommended by TG-253 for depth-dose measurements in the x-ray beam of 69.5 kVp generated by the Esteya eBT unit, has been evaluated. Three different correction factors have been explored to describe the dependence of the chamber response with respect to depth and applicator size. Of those possibilities, the use of a depth-dependent perturbation factor including a shift of the effective point of measurement, p_{shift}(EPoM), yields the best results. Using this approach, differences between the absorbed dose in water and the corrected absorbed dose in the sensitive volume of the chamber are smaller than $\pm 0.5\%$ and $\pm 0.3\%$ at all depths for the 10 mm and 30 mm applicator respectively. The optimal effective point of measurement was found to be shifted from the one established by the manufacturer by 0.4 mm, being closer to the center of the sensitive volume of the chamber. Uncertainties due to chamber-to-chamber differences have been explored by performing measurements using three different T34013 chambers. Differences were found to be below 2%. The magnitude of these effects is much lower than those reported for other eBT devices using unfiltered beams of 50 kVp. The present results emphasize the importance of carrying out detailed Monte Carlo studies for each electronic brachytherapy device and ionization chamber used for its dosimetry.

Acknowledgments

The authors wish to thank PTW for kindly providing the blueprints required for this study. This work has been partially funded by FEDER/MCIyU-AEI under grants PGC2018-101302-B and FPA2017-84543-P, by the Severo Ochoa Excellence Program under grant SEV-2014-0398, by Generalitat Valenciana through the projects AICO/2019/132 and PROMETEO/2019/087, and by the European Union ERDF funds of the Comunitat Valenciana 2014-2020, with reference IDIFEDER/2018/032. The authors also acknowledge the use of Vives II (University of Valencia), node in the Spanish Supercomputing Network, the Hydrateo and Dresden cluster (University of Valencia), and the IFIC Grid-CSIC computing center.

References

Almansa, J. F., Guerrero, R., Torres, J. and Lallena, A. M. (2017). Monte Carlo dosimetric characterization of the Flexisource Co-60 high-dose-rate brachytherapy source using PENELOPE, *Brachytherapy* **16**(5): 1073–1080.

Andreo, P. (2019). Data for the dosimetry of low- and medium-energy kV x rays, *Phys. Med. Biol.* **64**(20): 205019.

Andreo, P., Burns, D. T., Hohlfeld, K., Huq, M. S., Kanai, T., Laitano, F., Smythe, V. G. and S., V. (2000). *Absorbed Dose Determination in External Beam Radiotherapy: an international code of practice for dosimetry based on standards of absorbed dose to water IAEA Technical Reports Series no. 398*, International Atomic Energy Agency, Vienna.

Andreo, P., Burns, D. T. and Salvat, F. (2012). On the uncertainties of photon mass energy-absorption coefficients and their ratios for radiation dosimetry, *Phys. Med. Biol.* **57**(8): 2117–2136.

Badal, A. and Sempau, J. (2006). A package of Linux scripts for the parallelization of Monte Carlo simulations, *Comput. Phys. Commun.* **175**(6): 440–450.

Ballester, F., Carlsson Tedgren, Å., Granero, D., Haworth, A., Mourtada, F., Fonseca, G. P., Zourari, K., Papagiannis, P., Rivard, M. J., Siebert, F.-A., Sloboda, R. S., Smith, R. L., Thomson, R. M., Verhaegen, F., Vijande, J., Ma, Y. and Beaulieu, L. (2015). A generic high-dose rate ^{192}Ir brachytherapy source for evaluation of model-based dose calculations beyond the TG-43 formalism, *Med. Phys.* **42**(6Part1): 3048–3062.

Ballester-Sánchez, R., Pons-Llanas, O., Candela-Juan, C., de Unamuno-Bustos, B., Celada-Alvarez, F. J., Tormo-Mico, A., Perez-Calatayud, J. and Botella-Estrada, R. (2017). Two years results of electronic brachytherapy for basal cell carcinoma, *J. Contemp. Brachytherapy* **3**(3): 251–255.

Baym, G. (1974). *Lectures in Quantum Mechanics*, Westview Press, Boulder, Colorado.

Bearden, J. A. (1967). X-Ray Wavelengths, *Rev. Mod. Phys.* **39**(1): 78–124.

Berger, M. J., Inokuti, M., Anderson, H. H., Bichsel, H., Dennis, J. A., Powers, D., Seltzer, S. M. and Turner, J. E. (1984). Report 37: Stopping Powers for Elecctrons and Positrons, *J. ICRU* **os19**(2).

BIPM (2010). Evaluation of measurement data — Guide to the expression of uncertainty in measurement, *Technical report*, BIPM.

Born, M. (1969). *Atomic Physics*, Blackie and Son, London.

Candela-Juan, C., Niatsetski, Y., Ouhib, Z., Ballester, F., Vijande, J. and Perez-Calatayud, J. (2015a). Commissioning and periodic tests of the Esteya® electronic brachytherapy system, *J. Contemp. Brachytherapy* **2**(2): 189–195.

Candela-Juan, C., Vijande, J., García-Martínez, T., Niatsetski, Y., Nauta, G., Schuurman, J., Ouhib, Z., Ballester, F. and Perez-Calatayud, J. (2015b). Comparison and uncertainty evaluation of different calibration protocols and ionization chambers for low-energy surface brachytherapy dosimetry, *Med. Phys.* **42**(8): 4954–4964.

Chica, U., Anguiano, M. and Lallena, A. (2009). Benchmark of PENELOPE for low and medium energy X-rays, *Phys. Medica* **25**(2): 51–57.

Croce, O., Hachem, S., Franchisseur, E., Marcié, S., Gérard, J.-P. and Bordy, J.-M. (2012). Contact radiotherapy using a 50kV X-ray system: Evaluation of relative dose distribution with the Monte Carlo code PENELOPE and comparison with measurements, *Radiat. Phys. Chem.* **81**(6): 609–617.

Cullen, D., Hubbell, J. and Kissel, L. (1997). EPDL97: the evaluated photo data library '97 version, *Technical report*, Lawrence Livermore National Laboratory (LLNL), Livermore, CA.

Deslattes, R. D., Kessler, E. G., Indelicato, P., de Billy, L., Lindroth, E. and Anton, J. (2003). X-ray transition energies: new approach to a comprehensive evaluation, *Rev. Mod. Phys.* **75**(1): 35–99.

DeWerd, L. A., Ibbott, G. S., Meigooni, A. S., Mitch, M. G., Rivard, M. J., Stump, K. E., Thomadsen, B. R. and Venselaar, J. L. M. (2011). A dosimetric uncertainty analysis for photon-emitting brachytherapy sources: Report of AAPM Task Group No. 138 and GEC-ESTRO, *Med. Phys.* **38**(2): 782–801.

Eaton, D. J. (2015). Electronic brachytherapy—current status and future directions, *Br. J. Radiol.* **88**(1049): 20150002.

Fulkerson, R. K., Micka, J. A. and DeWerd, L. A. (2014). Dosimetric characterization and output verification for conical brachytherapy surface applicators. Part I. Electronic brachytherapy source, *Med. Phys.* **41**(2): 022103.

Fulkerson, R. K., Perez-Calatayud, J., Ballester, F., Buzurovic, I., Kim, Y., Niatsetski, Y., Ouhib, Z., Pai, S., Rivard, M. J., Rong, Y., Siebert, F., Thomadsen, B. R. and Weigand, F. (2020). Surface Brachytherapy: Joint Report of the AAPM and the GEC-ESTRO Task Group No. 253 (Submitted), *Med. Phys.* .

Garcia-Martinez, T., Chan, J.-P., Perez-Calatayud, J. and Ballester, F. (2014). Dosimetric characteristics of a new unit for electronic skin brachytherapy, *J. Contemp. Brachytherapy* **1**(1): 45–53.

Gimenez-Alventosa, V., Gimenez, V., Ballester, F., Vijande, J. and Andreo, P. (2018). Correction factors for ionization chamber measurements with the 'Valencia' and 'large field Valencia' brachytherapy applicators, *Phys. Med. Biol.* **63**(12): 125004.

Guinot, J. L., Rembielak, A., Perez-Calatayud, J., Rodríguez-Villalba, S., Skowronek, J., Tagliaferri, L., Guix, B., Gonzalez-Perez, V., Valentini, V. and Kovacs, G. (2018). GEC-ESTRO ACROP recommendations in skin brachytherapy, *Radiother. Oncol.* **126**(3): 377–385.

Hill, R., Healy, B., Holloway, L., Kuncic, Z., Thwaites, D. and Baldock, C. (2014). Advances in kilovoltage

x-ray beam dosimetry, *Phys. Med. Biol.* **59**(6): R183–R231.

Ibanez-Rosello, B., Bautista-Ballesteros, J. A., Candela-Juan, C., Villaescusa, J. I., Ballester, F., Vijande, J. and Perez-Calatayud, J. (2017). Evaluation of the shielding in a treatment room with an electronic brachytherapy unit, *J. Radiol. Prot.* **37**(2): N5–N12.

Kawrakow, I. (2006). On the effective point of measurement in megavoltage photon beams, *Med. Phys.* **33**(6Part1): 1829–1839.

Ma, C.-M., Coffey, C. W., DeWerd, L. A., Liu, C., Nath, R., Seltzer, S. M. and Seuntjens, J. P. (2001). AAPM protocol for 40-300 kV x-ray beam dosimetry in radiotherapy and radiobiology, *Med. Phys.* **28**(6): 868–893.

Ouhib, Z., Kasper, M., Perez Calatayud, J., Rodriguez, S., Bhatnagar, A., Pai, S. and Strasswimmer, J. (2015). Aspects of dosimetry and clinical practice of skin brachytherapy: The American Brachytherapy Society working group report, *Brachytherapy* **14**(6): 840–858.

Perkins, S. T., Cullen, D. E., Chen, M. H., Hubbell, J. H., Rathkopf, J. and Scofield, J. H. (1991). Tables and Graphs of Atomic Subshell and Relaxation Data Derived from the LLNL Evaluated Atomic Data Library (EADL), Z = 1-100, Technical Report UCRL-ID-50400, *Technical report*, Lawrence Livermore National Laboratory, Livermore, CA.

Pratt, R. H., Ron, A. and Tseng, H. K. (1973). Atomic Photoelectric Effect Above 10 keV, *Rev. Mod. Phys.* **45**(2): 273–325.

Ribberfors, R. (1983). X-ray incoherent scattering total cross sections and energy-absorption cross sections by means ofsimple calculation routines R., *Phys. Rev. A* **27**(6): 3061–3070.

Sabbatucci, L. and Salvat, F. (2016). Theory and calculation of the atomic photoeffect, *Radiat. Phys. Chem.* **121**: 122–140.

Sakurai, J. J. (1967). *Advanced Quantum Mechanics*, 1 edn, Addison and Wesley, New York.

Salvat, F. (2019). PENELOPE-2018: A Code System for Monte Carlo Simulation of Electron and Photon Transport.

Scofield, J. H. (1973). *Theoretical Photoionization Cross Sections from 1 to 1500 KeV*, Livermore, CA.

Sechopoulos, I., Rogers, D. W., Bazalova-Carter, M., Bolch, W. E., Heath, E. C., McNitt-Gray, M. F., Sempau, J. and Williamson, J. F. (2018). RECORDS: Improved Reporting of montE CarlO RaDiation transport Studies: Report of the AAPM Research Committee Task Group 268, *Med. Phys.* **45**(1): e1–e5.

Seltzer, S. M., Fernandez-Varea, J. M., Andreo, P., Bergstrom, P. M., Burns, D. T., Krajcar-Bronic, I., Ross, C. K. and Salvat, F. (2014). Report 90: Key Data for Ionizing-Radiation Dosimetry: Measurement Standards and Applications, *J. ICRU* **14**(1).

Sempau, J. and Andreo, P. (2006). Configuration of the electron transport algorithm of PENELOPE to simulate ion chambers, *Phys. Med. Biol.* **51**(14): 3533–3548.

Sempau, J., Badal, A. and Brualla, L. (2011). A PENELOPE -based system for the automated Monte Carlo simulation of clinacs and voxelized geometries-application to far-from-axis fields, *Med. Phys.* **38**(11): 5887–5895.

Tom, M. C., Hepel, J. T., Patel, R., Kamrava, M., Badiyan, S. N., Cohen, G. N. and Shah, C. (2018). The American Brachytherapy Society consensus statement for electronic brachytherapy, *Brachytherapy* **18**(3): 292–298.

Valdes-Cortez, C., Niatsetski, Y., Perez-Calatayud, J., Ballester, F. and Vijande, J. (2019). A Monte Carlo-based dosimetric characterization of Esteya ® , an electronic surface brachytherapy unit, *Med. Phys.* **46**(1): 356–369.

Valdes-Cortez, C., Niatsetski, Y., Ballester, F., Vijande, J., Candela-Juan, C. and Perez-Calatayud, J. (2020). On the use of the absorbed depth-dose measurements in the beam calibration of a surface electronic high-dose-rate brachytherapy unit, a Monte Carlo-based study, *Med. Phys.* **2**: 693–702.

Vijande, J., Granero, D., Perez-Calatayud, J. and Ballester, F. (2013). Monte Carlo dosimetric study of the medium dose rate CSM40 source, *Appl. Radiat. Isot.* **82**: 283–288.

Watson, P. G. F., Popovic, M. and Seuntjens, J. (2017). Determination of absorbed dose to water from a miniature kilovoltage x-ray source using a parallel-plate ionization chamber, *Phys. Med. Biol.* **63**(1): 015016.

Ye, S.-J., Brezovich, I. A., Pareek, P. and Naqvi, S. A. (2004). Benchmark of PENELOPE code for low-energy

photon transport: dose comparisons with MCNP4 and EGS4, *Phys. Med. Biol.* **49**(3): 387–397.